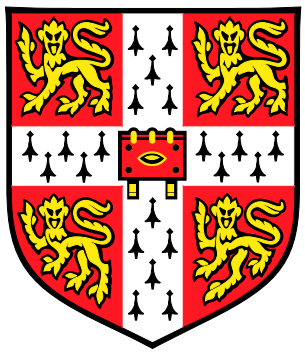

The impact and rupture of a water-filled balloon on a rigid surface

Hugh Michael Lund

This dissertation is submitted for the degree
of Doctor of Philosophy

Robinson College
and
Department of Applied Mathematics and Theoretical Physics
University of Cambridge

November 2013

Preface

This dissertation is the result of my own work and includes nothing which is the outcome of work done in collaboration except where specifically indicated in the text. No parts of this dissertation have been submitted for any other qualification.

Acknowledgements

I would like to thank my supervisor, Dr Stuart Dalziel, for his constant support and guidance, and for always being available to answers any questions I had. I gratefully acknowledge the financial support of both the Engineering and Physical Sciences Research Council, and my parents. I would like to thank all members of the GEFD research group, particularly those I shared an office or lab with, for making my time spent conducting research fun and interesting, and distracting me whenever I was working too hard. Thanks, also, to all the friends I have met in both Robinson College and the wider university, for helping to make my time in Cambridge enjoyable. Special mention should go to the laboratory technicians David Page-Croft, Colin Hitch, Neil Price, and John Milton, both for helping to design and manufacture all of the equipment I have needed, and for supporting worse football teams than Arsenal. Finally, I would like to thank my family, without whom none of this would have been possible.

Abstract

The dropping of a water-filled latex balloon onto a flat, rigid surface is an experiment that is known and has been performed by many, but on which there is no existing published work. High-speed images taken of the process revealed a range of phenomena, many of which had not been previously observed. After release, a water-filled balloon accelerates down and impacts with the tank floor. Upon impact, the balloon deforms through the propagation of waves up the balloon from the impact point. If the balloon does not rupture during this deformation, it then bounces up off the surface, the whole process similar to that when a water droplet bounces on a hydrophobic surface. Often, however, the balloon ruptures. This occurs through the propagation of one or more cracks through the balloon, leading to the rapid retraction of the membrane over the water's surface, and consequent ejection of a fine spray of water droplets behind it. If there are any waves on the balloon at the moment of rupture, a larger-scale growth of the interfacial amplitude occurs, of the same wavelength as the preburst waves. Eventually, gravity dominates, as the water slumps down and spreads over the flat surface.

In this thesis, the process described above is examined in detail, both experimentally and theoretically. To gain some insight into the behaviour of the latex balloons, their static and quasi-static behaviour is examined. A experimental method better than simply dropping the balloons was derived, permitting the accurate quantitative measurement of the process. In this new method, the balloons were held stationary, forced at a set frequency, then ruptured with a pin. The pre-burst waves are then shown to be accurately modelled by linear theory, with tension in the membrane acting much like a fluid surface tension. The behaviour of the rubber in retraction from large initial stretches is shown to be disperse, in contrast with that observed for retractions from small initial stretches, due to both non-linearity in the rubber and drag from the water on the strip. The spray ejected behind the rubber is explained as consequence of the inherent instability of the Gaussian velocity field in the wake. Finally, the late-time growth of the interfacial amplitude is examined, and argued to be closely-related to the Richtmyer-Meshkov instability. A model is then derived for the case of a balloon oscillated and burst with water both inside and outside, and is shown to be in approximate agreement with experiments.

Contents

Chapter 1

Introduction

Filling up a balloon with water and then throwing it at something (or someone) is a game enjoyed by children both young and old throughout the world. The reason for this popularity is simple: water balloons allow a large amount of water to be accurately delivered to a target over distances of several metres, without the need for a high-speed jet. At first glance, the process would appear straightforward; the rubber membrane stretches as it fills, before being tied up to prevent water escaping. The membrane then keeps the water together as it moves through the air towards its target, before breaking up as it deforms on impact. The water then spreads out over the target, covering it in water. This simple explanation shows why it is popular with children, but not why it is of interest to scientists. Yet within this apparently simple process lies a wealth of complicated physics that, thanks to modern high-speed imaging, can now be observed. Many such videos can be found on the Internet, with a simple search of the video-sharing website Youtube revealing videos of water balloons bouncing, bursting, or both, on a wide range of surfaces. These videos may garner hundreds of thousands of views, demonstrating that even the small-scale details of a bursting water balloon fascinate many of us.

However, despite this evident public interest, no evidence of serious scientific research into this process can be found in the literature. Consequently, our initial motivation for this research was not the published work of others, but some basic experiments doing exactly what has just been described: dropping a water balloon onto a rigid surface.

1.1 Basic experiment

The following sequence of pictures (figure 1.1) are of a full water balloon being dropped onto a rigid surface, causing it to burst. The balloon is what may be regarded as a standard party balloon, with a maximum diameter when fully inflated of 300mm; it was dropped from a height of 1m, bursting on impact. The whole process was captured using a high-speed camera. Further description of the equipment and method used is given in chapter 3, but the specifics are not important here as we wish to give only an overview of the problem.

The behaviour of the balloon is displayed in figure 1.1. A brief description of what is occurring in each image is as follows (times are all accurate to the nearest millisecond, with $t = 0$ms being the moment of first contact between the balloon and tank):

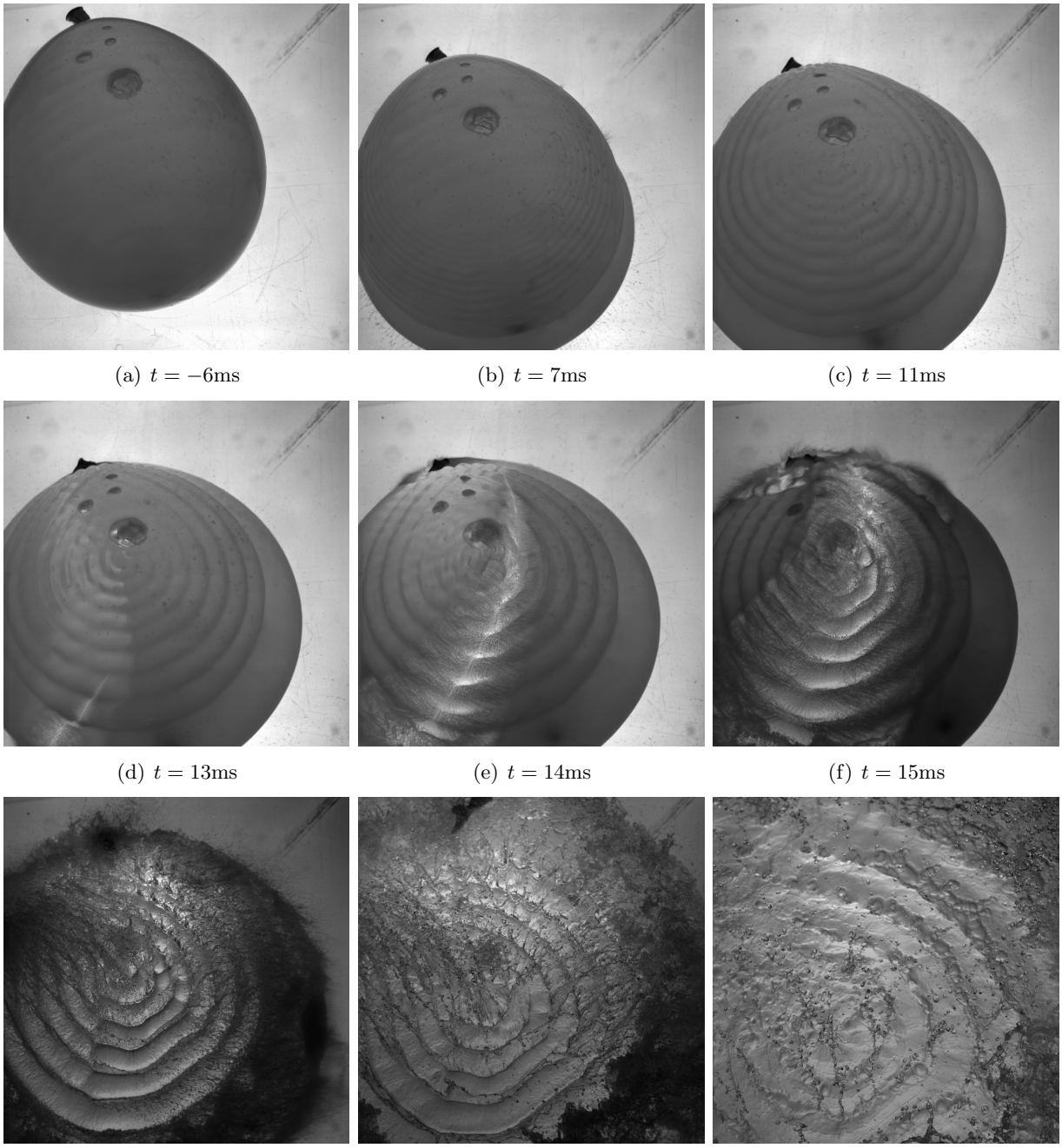

(a) $t = -6$ms (b) $t = 7$ms (c) $t = 11$ms

(d) $t = 13$ms (e) $t = 14$ms (f) $t = 15$ms

(g) $t = 20$ms (h) $t = 31$ms (i) $t = 58$ms

Figure 1.1: The behaviour of a 300mm-diameter water balloon upon impact with a rigid surface. The first image is taken approximately 500ms after the balloon was released, by hand, from a height of 1m.

(a) The balloon is in free-fall. A fully-inflated balloon with no density difference between the fluids inside and outside is approximately pear-shaped due the way it was made. When in free fall, the balloon inflated with water also assumes this shape, as gravity can no longer influence the shape. This is distinct from its sessile shape, the shape it formed when full of water but resting on a flat surface. Both shapes will be discussed in more detail in chapter 2. Water is added through a small opening that is tied once the balloon is full - the knot is visible near the top of the image. As the balloon was released by hand, there is likely to be a rotational element to its motion, though this is insignificant compared to its downward speed. The deformation of the balloon, when held prior to release, likely created small amplitude waves on the membrane, though these have died away by now to the extent that they are not visible. Small bubbles of air may be viewed inside the balloon near the top of the membrane, an unfortunate artifact of the filling of the balloon directly from a tap. In later experiments requiring quantitative measurements, this problem was alleviated by filling the balloon when completely submerged in water; here, it suffices to say that such bubbles did not have any significant qualitative effect on the experiment.

(b) The balloon starts to deform shortly after initial impact with the tank floor. First contact with the tank occurs at $t = 0$ms, causing the surface to flatten. Waves are created on the elastic membrane that travel up the balloon from the point of impact. Waves of a wide range of wavenumber are created, with the short wavelengths travelling faster. Here, so soon after the initial impact, only relatively short waves are seen, with wavelengths around one millimetre. No shorter wavelengths are seen, as they have been suppressed by the bending stiffness of the membrane. The shape of the wavefronts approximately follows the pear-like shape of the balloon.

(c) The balloon continues to deform due to the tank floor. At this later time ($t = 11$ ms), the shorter waves seen earlier have reached the top of the balloon, reflected and undergone significant decay. Now, it is the larger wavelength, larger amplitude waves that are seen; the wavelengths are of the order of centimetres. As before, the waves travel from bottom to top of the balloon, though at a slower rate than those with shorter wavelengths. By now, the shape of the balloon no longer approximates a pear, becoming flatter as it spreads out over the tank floor. Consequently, the total surface area of the balloon has increased, despite the volume within it remaining fixed.

(d) The balloon continues to spread out, with the waves seen in the previous images still present at $t = 13$ ms. However, the further increase in surface area and consequent increase in stress within the elastic membrane has caused it to fail at a point out of view. This has led to a crack (seen near the bottom of the image) propagating through the elastic membrane. Either side of the crack, the membrane starts to retract away from the initial position of the crack.

(e) Over only a millisecond, the crack has taken a curved path across nearly half the membrane. While the waves seen earlier persist away from the crack, much of the elastic membrane is now in retraction. Behind the membrane, water is being ejected from the surface as a small length-scale spray.

(f) One millisecond later at $t = 15$ ms, the crack has now spread round the whole membrane, deviating significantly from its initial path as it nears the tied end of the balloon. Most of the membrane is now in retraction; the fine spray from the water's surface is now seen everywhere away from

the path of the crack. This spray is water ejected from the main body of water previously within the balloon that travels upwards with a slight lean in the direction to which the membrane is retracting. This spray has a characteristic length scale of the order of tenths of millimetres.

Throughout the short time the crack was propagating (around three milliseconds), the larger pre-burst waves persisted wherever the membrane was still present, with the balloon as a whole continuing to flatten and spread out.

(g) At $t = 20$ ms, the water surface is now almost completely uncovered by the membrane. The full retraction of the membrane from the initial formation of the crack took around eight milliseconds. Some of the fine spray seen in images **(e)** and **(f)** remains, though mainly near the edge of the water, where the membrane was last to retract. Elsewhere, larger scale undulations in the water's surface are clearly visible, of approximately the same shape and wavelength as the pre-burst interfacial waves.

(h) The water has spread out and thinned significantly by $t = 37$ ms, while the fine spray has now almost disappeared. This has been replaced by thin crown-like structures of the same wavelength as the pre-burst waves propagating upwards into the air, with the water surface between them approximately flat. These structures are thin sheets of water that are almost axisymmetric at their bottom; this axisymmetry is lost near their leading edge, where they break up into small droplets.

(i) Much later, gravity has come to dominate the flow. This has caused the fine spray and crown-like structures to retract back into the main body of water, which is now spread thinly over the tank floor. The dominant motion of the water is now radially outwards from where the balloon landed. After this image, the water continues to spread until it reaches the tank walls. It then sloshes around until finally coming to rest as a thin, flat layer over the tank floor.

It is easy to see from a description of just one such experiment that the drop and consequent burst of a water balloon involves a deep and complex range of non-trivial physical phenomena. As stated earlier, no known research has been published to examine this situation, and little on fluid-filled balloons in any situation. Despite this, there is relevant literature about each of the phases, rubber and water, that should first be explored.

1.2 Quasi-static behaviour of rubber

The theory of linear elastic motions has long been known, dating back to the work of Hooke [1678] in deriving what is now known as Hooke's Law - that the applied stress is proportional to the strain. This idea was then developed by Navier [1821] and Cauchy [1832] into the theory for linear elasticity still used today to describe small deformations in rubber, as by Long et al. [1996] and Vermorel et al. [2007]. A detailed overview of the development of linear elasticity theory is given by Rajagopal [2011].

Rubber is unusual amongst solids, in that it may undergo deformations several times its initial length without failure. Linear elasticity theory for natural rubber, however, only applies below extensions of around 100%. The earliest attempts at describing the non-linear behaviour of rubber came from Kuhn [1934], Meyer and Ferri [1935] and Kuhn [1936]. They came up with what is known as

the kinetic theory for rubber, based on probabilistic arguments about the motions of the individual chains of molecules. This theory led to the development of the hyperelastic Neo-Hookean model, that was found by Stein [1958] to accurate for extensions less than 300% in rubber balloons.

However, the kinetic theory of rubber relied on the assumption that the molecules do not approach their maximum extension, and the experiments of Treloar [1944] demonstrate that this leads to inaccuracy at higher strains. Treloar [1947] went on to propose that the earlier, general non-linear theory of Mooney [1940] might provide a better fit for the stress-strain relation of rubber. This theory was then expanded upon by Rivlin and Saunders [1951], and so became known as the Mooney-Rivlin theory. This proved more accurate, for extensions up to 400%, though it required a second experimentally determined parameter. Nevertheless, this theory is still studied today, as it provides relatively straightforward analytical demonstrations of many non-linear effects in rubber.

Later on, Ogden [1972] came up with a hyperelastic model for rubber that could be accurate for all extensions, and fitted it well to the data of Treloar [1944]; it is known as the Ogden's model. However, this model was phenomenologically derived, and relied on the finding of three experimentally determined parameters.

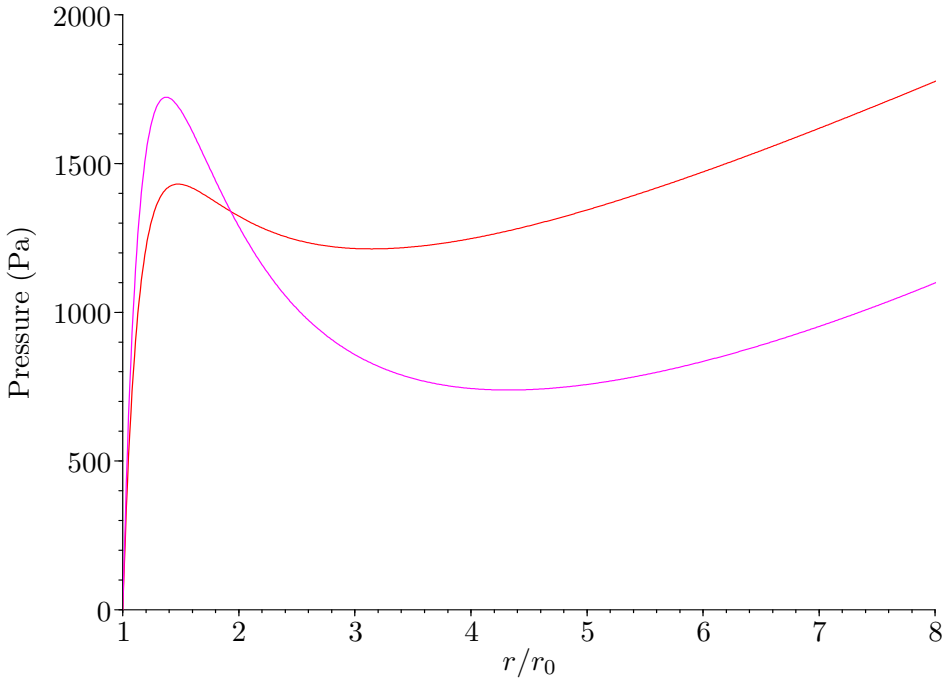

Figure 1.2: The pressure-radius relations for an inflating spherical membrane, as predicted by the Mooney-Rivlin (red) and Ogden's (magenta) models using the parameters given by Muller and Strehlow [2004] and Ogden [1972], respectively. Here, r is the radius of the membrane, with r_0 the radius when the membrane is in its stress-free reference configuration.

The application of non-linear rubber elasticity to a spherical shell was first considered by Adkins and Rivlin [1952], who derived the pressure-radius relation for an inflating Mooney-Rivlin spherical

shell. This derivation is easily extended to the Ogden's model, with its validity confirmed by the experiments of Muller and Strehlow [2004]. Both relations are shown in figure 1.2. One prediction of these theories is that the membrane will become unstable part way through inflation, where the pressure-radius relation is decreasing with increasing radius. Consequently, the membrane will spontaneously stretch. During this motion, it has been shown by Alexander [1971] (amongst others) that an initially spherical balloon may lose symmetry. At higher strains, on the upwards part of the stress-strain curve, the initial spherical shape is recovered.

The non-linear loading-unloading cycle for rubber is further complicated by a loss of symmetry: the unloading stress-strain curve does not follow the loading curve, but instead lies beneath it. This effect is known as hysteresis, and the difference between the two curves corresponds to energy lost during the cycle, as explained by Muller and Strehlow [2004] (chapter 10). The stress-strain behaviour of rubber may change over repeated loading-unloading cycles, as discovered by Mullins [1969] and now known as the Mullins' effect. However, as Diani et al. [2009] describe, forty years on from that initial discovery, there is little agreement over the physical mechanisms behind the effect, nor a good predictive model.

Thorough reviews of the non-linear quasi-static theory of rubber, including theory for inflated spherical shells of rubber, are given in Muller and Strehlow [2004] and Treloar [2005].

1.3 Dynamic Retraction of Rubber

The dynamic behaviour of natural rubber and, in particular, the dynamic behaviour of natural rubber in retraction, is not a straightforward consequence of the quasi-static behaviour. The first investigations into the retraction of a strip of stretched natural rubber were performed by Stambaugh [1944] and Mrowca et al. [1944], who examined the displacement-time behaviour of such strips for extensions up to 400% (though in little detail). Accompanying analysis for the linear case was provided by James and Guth [1944], who showed that, for an elastic strip stretched then released at one end, linear theory predicts a stress-wave to travel down the material at the longitudinal wave-speed. In front of the wave, the material is fully stretched; behind the wave, the material is fully retracted. Mason [1963] examined the retraction of rubber strips in the non-linear regime experimentally and theoretically, uncovering the dispersive nature of the unloading waves for strips of a sufficiently high initial extension. Through theoretical consideration of the force on a section of the retracting strip, it was explained how the change in nature of the wave corresponded to a change in curvature of the stress-strain relationship: where the curvature was positive, the wave was dispersive, and where the curvature was zero (as in linear theory) or negative, the wave was non-dispersive and shock-like. Physically-speaking, positive curvature of the stress-strain relationship meant that high strains travelled faster than low strains, thus the wave was dispersive; where the curvature was negative, low strains travelled faster so the retraction was unstable, and the wave took the form of a non-dispersive shock wave. For a single retraction, both behaviours could occur: the behaviour would initially be dispersive, until the curvature changed sign and a shock formed, behind which the material was fully retracted. The experimental observations then matched the theory, at least qualitatively. Mason [1963] also found that once the main phase of retraction was complete and the material was stress-free, it retained a 'residual' deformation up to 23% of its initial length. The relaxation time for this residual extension was around three times longer than for the main retraction, and was attributed to viscoelastic effects within the rubber. Gent and Marteny [1982] later performed similar tests to determine the wave and material velocities within

retracting natural rubber strips, and found, as expected, that such velocities depended strongly on the initial strain. However, they also found that viscoelastic effects were unimportant in the main phase of retraction. Bogoslovov and Rowland [2007] used the relation between material velocity and strain given by Mason [1963] to determine the stress-strain behaviour of retracting rubber strips observed experimentally. While the speed of the retraction pulse was found to be dependent only on the elastic modulus (gradient of the stress-strain curve) of the material in front of the pulse, they also uncovered significant qualitative and quantitative differences between the quasi-static and dynamic stress-strain response of rubber. They, too, found that viscoelasticity was negligible for the main phase of retraction of natural rubber, but that it did lead to a non-zero residual strain.

More recently, Niemczura and Ravi-Chandar [2011a], Niemczura and Ravi-Chandar [2011b] and Niemczura and Ravi-Chandar [2011c] described tests performed on natural rubber strips retracting from high initial strains, in which the behaviour of the rubber within the dispersive region was examined. Attempts to match their results to quasi-static predictions for the stress-strain relationship failed; a new power-law relationship was proposed, based on their experimental observations, that predicted the material displacement to be algebraically dependent on space and time. After two experimentally-determined parameters were determined, the model displayed excellent agreement with those experimental results. The authors also argued that the change between a shock-like wave and a dispersive wave did not depend directly on the change in curvature of the stress-strain relationship, but on the maximum dissipation criterion - that the retraction proceeds so as to locally release the maximum possible of energy. Assuming this to be true, the shock-like behaviour may occur for higher-strains than predicted by Mason [1963].

The behaviour of retracting strips of natural rubber after the stress wave front has reached the other, fixed end was studied by Vermorel et al. [2007]. Considering only initial extensions within the linear regime ($< 100\%$), they found that the stress wave front rebounds from the fixed end, behind which the material is in compression. This caused the thin strips to buckle. The authors derived a relation between the buckling wavelength, initial extension and strip thickness that matched experimental data well. They also considered the effect of the rubber strips immersed in fluid: whilst water had negligible effect on the retraction within this linear regime, more viscous fluids were found to significantly affect the motion. A theory was derived based on the assumption (backed by some experimental evidence) that flow in the boundary layer near the strip was laminar. From this theory, predictions were made for the asymptotic behaviour of the material behind the wavefront during retraction in a viscous fluid that gave the material velocity behind the wavefront no longer constant but decaying in time like $t^{3/4}$. This prediction agreed well with their experimental data. A prediction was then obtained for the buckling wavelength in a viscous fluid that again matched the experimental data well.

There has been a small number of investigations into the dynamic behaviour of bursting balloons that are held stationary prior to rupture. Stevenson and Thomas [1979] examined the bursting of an air-filled balloon with (biaxial) strains up to 400%. Filming the burst at only 8000 frames per second, they were unable to detect any dispersion in the stress waves, obtaining only average values of the material velocities. Soto and Belmonte [2009] looked at the bursting of air-filled balloons submerged in liquids of a range of viscosities. The rapid retraction of the rubber membrane created what they termed 'striated wrinkles' on the air-liquid interface, whose wavelength appeared to increase with increasing viscosity of the surrounding liquid. No attempt at an in-depth analysis of these wrinkles

was made.

Both Stevenson and Thomas [1979] and Soto and Belmonte [2009] burst their rubber balloons by pricking them with a sharp object when inflated. This caused a mode I crack - also known as an opening crack, with tensile stress applied normal to the crack - to propagate around the balloon in two directions, away from which the material retracted. As given by Broberg [1999], classical elastic fracture theory predicts that such a crack should propagate no faster than the Rayleigh-wave speed of the material, and so slightly less than the shear-wave speed. However, Stevenson and Thomas [1979] examined the crack propagation in some detail, finding that the cracks propagated around the balloon three times faster than the material retracted, and thus much faster than the shear-wave speed. They argued that this crack propagation speed was set by the stress-state near the tip of the crack. Recent experimental work by Petersan et al. [2004] on biaxially-stretched, flat rubber sheets has also found crack propagation speeds in excess of the shear-wave speed, though less than the longitudinal-wave speed; they termed these cracks 'intersonic'. They also observed that the shape of the crack-tip was not parabolic as predicted by classical theory, but was instead sharp, resembling a Mach cone. Marder [2006] demonstrated that the neo-Hookean non-linear elasticity model for rubber does predict both intersonic crack growth and the correct, cone-like shape for the crack-tip. Chen et al. [2011] found that, for sufficiently low extensions, the cracks were subsonic, with parabolic shape tips and speed scaling with the elastic energy density as predicted by linear elastic fracture theory. For sufficiently high stretches, the cracks became intersonic with speed scaling with the stretches and sharp, cone-like tips.

In their study, Stevenson and Thomas [1979] found that their cracks took undulating paths, with typical wavelength and amplitude of around one centimetre. The wavelength and amplitude of these undulations decreased as the initial strain increased. Wave-like crack paths were also found in biaxially-stretched rubber sheets by Deegan et al. [2002], in the form of approximately sinusoidal deviations from the main path. The wavelengths were found to scale linearly with the stretch, while the amplitude scaled with its square-root. More recently, Endo et al. [2012] demonstrated both experimentally and numerically that wavy cracks could also be found in rubber in uniaxial extension, going on to argue that non-linear elasticity plays an important role in this phenomena. Despite this work, the mechanisms behind these wave-like cracks remain poorly understood.

1.4 Droplets

The connection between tension in a balloon membrane and surface tension in a droplet was first made by Condon and Fryd [1958], who showed that for moderate extensions, this tension (as on a fluid droplet) could be regarded as constant. This analogy was also used by Muller and Strehlow [2004] who showed that, while far from perfect (particularly away from moderate extensions), it is useful to understand the physics of fluid-filled balloons. Furthermore, whilst the impact and rupture of a water balloon on a rigid surface has not been explicitly studied before, a large amount of work has been done on the impact of a water droplet on rigid surfaces, a review of which is given by Rein [1993]. The case explored by Richard and Quere [2000] is of particular note, where a droplet impacting a suitably hydrophobic surface may 'bounce': after impact the droplet remains together, spreads, then retracts and eventually lifts completely off the surface. This is similar to a balloon bouncing on a rigid surface, particularly when considering energy: in both cases, initial kinetic energy is converted into surface

energy (in the form of elastic energy for the balloon), that is then converted back into kinetic energy as the droplet or balloon lifts off the surface.

Falling droplets have also been seen to create crown-like structures: a droplet impacting another liquid may lead to the formation of a crown around the impact crater, as first described by Worthington [1882]. This crown is a thin, circular liquid sheet ejected almost vertically from the free surface near the boundary of the impact crater, upon whose leading edge capillary instabilities soon develop before the sheet falls back into the liquid. However, as will be discussed in detail in chapter 6, the mechanism for the creation of the crown for the bursting balloon is very different.

1.5 Interfacial instabilities

A significant amount of work has been done on waves and instabilities on an interface between two fluids. The creation of a perturbation on such an interface with stabilising acceleration will lead to the formation of waves there - for example, a perturbation on an interface similar to that seen in figure 1.3 (without the shock), in a gravitational field acting down the page, would produce waves provided $\rho_2 > \rho_1$.

The situation in which the acceleration is no longer stabilising (for instance, with the acceleration acting down the page but $\rho_2 < \rho_1$ in figure 1.3) is significantly different. Assuming no interfacial tension exists, stable waves are no longer produced. Instead, the amplitudes of any interfacial perturbations grow. The theory is no different than for the stable waves discussed above, but whereas previously the wave frequencies were real, here they become complex. The rate of this growth is well-known to be initially exponential in time, although nonlinearities soon dominate, leading to much more complicated behaviour. This growth in perturbation amplitudes is known as the Rayleigh-Taylor instability (RTI), as discussed in Acheson [1990].

A related effect is known as the Richtmyer-Meshkov instability (RMM), as introduced by Richtmyer [1960] and Meshkov [1969]. This may occur on any interface between two compressible fluids of differing density; unlike RTI, reversing the ratio of densities only changes the phase of the interfacial amplitude growth. This growth is classically understood to develop as a result of the passing of a shock wave through a perturbed interface. The perturbations on this interface may lead to a misalignment of the density and pressure gradients at the surface, causing the instability to develop. As can be seen from the $\nabla\rho \times \nabla p$ term of the (inviscid) vorticity equation

$$\frac{D\boldsymbol{\omega}}{Dt} = \frac{1}{\rho^2}\left(\nabla\rho \times \nabla p\right) + \left(\boldsymbol{\omega}\cdot\nabla\right)\mathbf{u} - \boldsymbol{\omega}(\nabla\cdot\mathbf{u}),$$

this misalignment leads to the deposition of vorticity upon the interface that leads to growth in the amplitude of perturbations.

Richtmyer [1960] derived an approximate linear relation for the initial growth of a single mode due to this instability,

$$\dot{\eta} = Ak\triangle V\eta_0, \tag{1.1}$$

where k is the (dimensional) wavenumber of the interfacial wave, $\triangle V$ is the difference in the surface velocity immediately before and after the shock passes, η_0 is the initial amplitude of that disturbance and A is a parameter known as the Atwood number. This non-dimensional number is a measure of

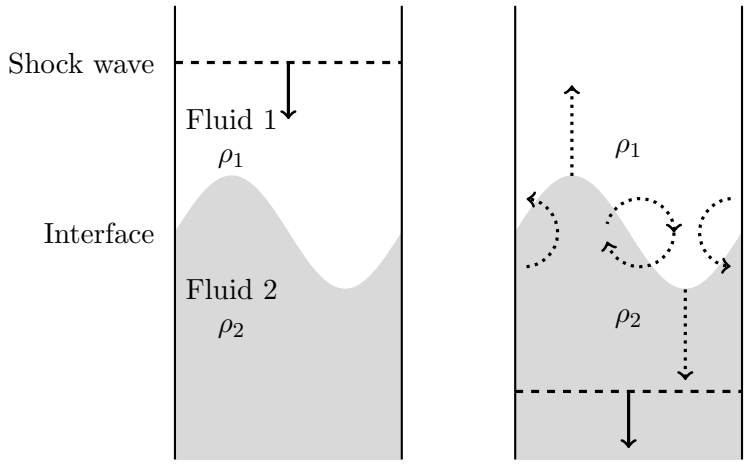

Figure 1.3: Diagram illustrating the appearance of Richtmyer-Meshkov instability after shock passes through a perturbed interface, as Baroclinic vorticity generation on the surface leads to growth in the amplitude of the interface. In this example $\rho_2 > \rho_1$, while the dotted lines represent the direction of flow.

the relative difference in densities between the two phases, and is defined by

$$A = \frac{\rho_2 - \rho_1}{\rho_1 + \rho_2},$$

where the shock is initially transmitted through fluid 2, before passing through the interface into fluid 1. Thus, for $\rho_2 > \rho_1$ the amplitude of the perturbations will grow in approximate agreement with 1.1. In the situation where $\rho_2 < \rho_1$ (and hence $A < 0$), the phase of the interfacial perturbations will first invert before growing in amplitude.

It should be noted that we have referred to this effect as an instability as that is how it is commonly referred to in the literature. While the precise mathematical definitions of instability are less restrictive, in fluid mechanics literature a system is typically referred to as unstable if it includes exponentially-growing modes. Under such a definition, RMI is not a true instability: the initial growth from infinitesimal perturbations is not exponential in time (as for RTI), but linear, and the interface only experiences a positive acceleration momentarily, after which it decelerates. It is, therefore, best regarded as mechanism for interfacial growth, not as an interfacial instability. Consequently, throughout this thesis, we shall often refer to the Richtmyer-Meshkov mechanism (RMM), by which we mean the physics responsible for the flow that is usually called the Richtmyer-Meshkov instability. Any reference to RMI will refer to the growth of a shock-accelerated interface. By these definitions, RMM is more general than RMI, and may applied to situations that do not include shock acceleration.

Non-linearities soon become important, and the late-time growth of the interfacial amplitude is believed to follow a power law - though there is little agreement as to what the exponent of this power law should be. Predictions range from $t^{0.2}$ to t^1, with many in between, whilst experiments also fail to give a universal answer. A detailed review of the models available for planar geometry is given in Brouillette [2002].

A significant amount of numerical work has been carried out on RMM on curved (Glimm et al. [2000]) and spherical (Dutt et al. [2004]) surfaces. These involve the simulation of shocks passing through compressible fluids, and give estimates for the instability growth rates based on the strength of the shock.

A large number of experimental studies have also been conducted into both compressible and incompressible RM instability. Of particular interest are the incompressible experiments of Jacobs and Sheeley [1996], Niederhaus and Jacobs [2003], and Jacobs and Krivets [2005], who conducted a detailed investigation into RMM created by a sled containing two miscible liquids falling onto a spring. Their results for the instability growth rate show good agreement with both Richtmyer's linear theory, and with the models for longer time growth given by Zhang and Sohn [1997] and Sadot et al. [1998].

For RMM created in a finite container, there is also the possibility of a re-shock of the interface, as the initial shockwave reflects off a wall of the container and passes through the interface once more. This phenomena was studied by Brouillette and Sturtevant [1994] and later Chebotareva et al. [1999], who found that though the shock is likely to be weaker by this time, it may still cause secondary instabilities on the interface through the same mechanism as before. This is also relevant for shock-generated RMM in a spherical geometry, as inward-travelling shock waves (that may be created by an outward-travelling shock partially reflecting from the interface) will create a pressure singularity at the origin, from which they reflect outwards. This is discussed in Dutt et al. [2004]. All future references to RMM, however, will only be referring to the single shock case, as this provides the closest link to our experiments.

1.6 Outline of this thesis

In this thesis, an attempt will be made to analyse each of the significant phenomena involved in the drop, distortion, and rupture of a water balloon, with three being of particular interest: the pre-burst interfacial waves, the retraction of the membrane and consequent creation of a fine spray from the water's surface, and the later growth of the crown-like structures on the water's surface. In chapter 2, an exploration of the rubber in the membranes in static situations is given. The membranes were key to the whole process, yet relatively little was known about them in advance. We then move on to discuss in more detail the process described above. Unfortunately, obtaining accurate quantitative data from experiments dropping water balloons in air was near-impossible; they were, however, highly instructive in revealing the physical phenomena involved. A detailed, qualitative description of these phenomena is given in chapter 3. In terms of obtaining accurate quantitative data, it proved far more effective to consider water balloons held stationary, forcibly oscillated by a rod attached to a speaker, then burst with a long needle. Using this new setup, the pre-burst waves of figure 1.1 **(c)-(e)** are studied in detail in chapter 4, and compared to the predictions of linear potential theory for axisymmetric capillary waves on a spherical interface with constant surface tension. The retraction of the membrane is investigated in chapter 5, with both the behaviour of the rubber and the shear instability seen in the figure 1.1 **(e)-(g)** examined experimentally. Finally, the late-time interfacial growth of figure 1.1, **(g)-(h)** is considered in chapter 6, and a model is derived in an attempt to explain the interfacial growth of an oscillated then burst water balloon itself held underwater. Chapter 7 draws these threads together to discuss again the dynamics of dropped water balloons, in the conclusions.

1.7 Terminology used throughout the thesis

Lagrangian coordinates are denoted by upper-case letters, and Eulerian coordinates by lower-case letters. Time is always denoted by a lower-case t. All vectors are in bold font and lower case, and second-order tensors are bold and uppercase.

The two main coordinate systems used are Cartesian coordinates (x, y, z) and spherical polar coordinates (r, θ, ϕ) defined as in figure 1.7. For chapter 6, cylindrical polar coordinates given by (r, θ, z) are used. In all situations, θ will be the azimuthal angle, and ϕ the polar angle.

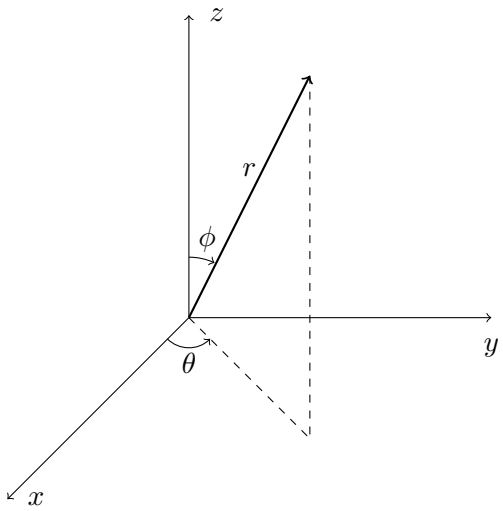

Figure 1.4: The Cartesian and spherical polar coordinate systems as used in this thesis. Here, θ is the azimuthal angle and ϕ is the polar angle.

The fluid velocity vector is $\boldsymbol{u}$, with components $(u(\boldsymbol{x}, t)$, $v(\boldsymbol{x}, t)$, $w(\boldsymbol{x}, t))$ for whichever coordinate system $\boldsymbol{x}$ is in use. Vorticity is $\boldsymbol{\omega}$, circulation Γ with circulation density at an interface (the integral of the vorticity in the normal direction) given by γ. Frequency (the inverse of the period) is denoted f, with angular frequency given by ω. The physical properties of fluids are given by density ρ, surface line tension σ, and kinematic viscosity ν.

For elastic deformations, the position of the point $\boldsymbol{X}$ in the deformed configuration is given by $y(\boldsymbol{X}, t) = \boldsymbol{X} + \boldsymbol{a}(\boldsymbol{X}, t)$. The deformation is thus expressed by the vector $\boldsymbol{a} = (a(\boldsymbol{X}, t)$, $b(\boldsymbol{X}, t)$, $c(\boldsymbol{X}, t))$ for whichever (Lagrangian) coordinate system is in use. All linear elastic deformations will be expressed in terms of the Young's modulus E and the shear modulus μ that have the dimensions of pressure. These may be related to the Lamé parameter λ, Poisson's ratio ν and bulk modulus K as in table 1.7.

When strain is referred to in this thesis, it is the engineering strain (the change in length divided by the undeformed length) that is meant. This will be used only for linear elastic deformations; for larger deformations, the stretch ratio (defined to be the deformed length divided by the undeformed length) shall be used, in line with common practice for the modelling of non-linear rubber elasticity.

All strains are written $\boldsymbol{\epsilon} = \epsilon_{ij}$, with stretches written as λ_i. Both are dimensionless. Stress is given by $\boldsymbol{\tau} = \tau_{ij}$, and has units of pressure. Within a membrane of thickness h, the line tension in the i direction is $T_i = h\tau_{ii}$ and has the units of surface tension, force per unit length.

	(λ, μ)	(E, ν)	Typical value
λ	λ	$\frac{E\nu}{(1+\nu)(1-2\nu)}$	$1950 \times 10^6\,\text{Pa}$
μ	μ	$\frac{E}{2(1+\nu)}$	$0.5 \times 10^6\,\text{Pa}$
E	$\frac{\mu(3\lambda+2\mu)}{\lambda+\mu}$	E	$1.0 - 2.0 \times 10^6\,\text{Pa}$
ν	$\frac{\lambda}{2(\lambda+\mu)}$	ν	0.49987
K	$\lambda + \frac{2}{3}\mu$	$\frac{E}{3(1-2\nu)}$	$1950 \times 10^6\,\text{Pa}$

Table 1.1: The relation between several common parameters used to describe linear elasticity, along with their typical values for natural rubber as given by Mark [2009]. Only two of these (or any other linearly independent combination of them) are needed to fully describe any linear elastic deformation.

Chapter 2

Quasi-static behaviour of the rubber balloons

In this chapter, the physical properties of the rubber balloons used in later experiments are explored. An in-depth study into their properties was necessary as all that was known about the balloons in advance was that they were made of natural rubber. First, a brief review of the history, manufacturing and molecular make-up of natural rubber is given, followed by descriptions of the range of tests performed under quasi-static loading and unloading. From these tests, we hoped to gain a good insight into how the rubber behaved at times when our ability to obtain accurate data was restricted, such as under dynamic conditions - as when a water balloon bursts.

2.1 Rubber

The following detailed description is based on Muller and Strehlow [2004] and the website `http://www.balloonhq.com/`.

Rubber is a solid that is both common in everyday life, yet is far from easy to model scientifically. Its molecular structure leads to a range of phenomena that do not occur in many other materials; it is the most extensible solid known, as well as being near incompressible. The behaviour of rubber undergoing linear deformations is similar to that of many other materials, and relatively simple to model. However, here we are concerned with the behaviour under non-linear deformations, that turns out to be far from simple. In particular, we are concerned with how rubber behaves when stretched and released, and so it is important to know which phenomena arise from the behaviour of the rubber itself, and which arise from other factors such as drag from the surrounding medium. As the non-linear behaviour of rubber is determined on a molecular level, we shall a give a brief overview of the chemistry of rubber in this section, so that the physical processes driving any non-linear phenomena may be explained.

Natural rubber, also known as latex, has the chemical formula $Cis - 1,4 - polyisoprene$, and is traditionally obtained from the sap of the tree Hevea brasiliensis. Raw natural rubber is well-known to be sensitive to temperature: one of the first commercial uses of natural rubber was in the fabrication of raincoats by the Scottish chemist Charles Macintosh in the nineteenth century, but these coats were known for becoming stiff in cold weather, and sticky in warm weather. This remained a problem until

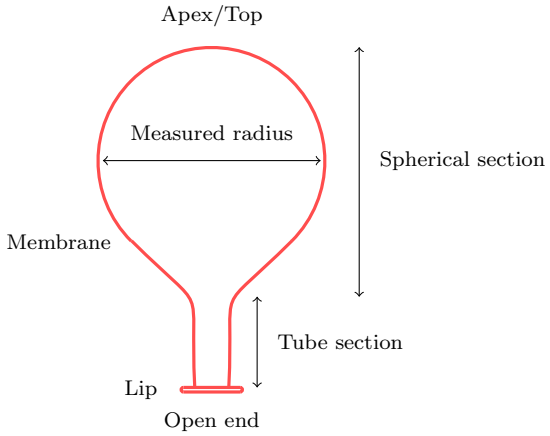

Figure 2.1: Common terms related to a balloon that will be used throughout this thesis.

the development of vulcanised rubber by Charles Goodyear. The process of vulcanising rubber involves adding curing agents and colouring pigments to rubber sap, before baking it in an oven at around 200 degrees Centigrade. Vulcanisation makes the sap into the dry, flexible material that is only weakly responsive to heat that we know today as rubber. It may also be synthesised artificially, though most synthetic rubbers are subtly different, being either polybutadiene, or a mixture of polyisobutylene and polychloroprene known as butyl rubber or neoprene. These artificial rubbers may display significantly different behaviour, including during rapid retraction (see Mrowca et al. [1944]).

According to Robertson [1978], the first rubber balloons were made by Michael Faraday in 1824 to experiment with helium, by simply gluing two sheets of non-vulcanised rubber together. The modern method derives from the work of J.G. Ingram in 1847 in London. Balloons are made by dipping a mold into a bath of the liquid sap that has had curing agents added to it, before it is slowly withdrawn. Though this fluid is very viscous, there will still be a slight tendency for the rubber to gather near the bottom of the mold before it dries. This part becomes the apex of the balloon, opposite the open end, where the balloons are often thickest. The open end of the balloon is then rolled to make the lip, before it is baked for twenty minutes then dried.

When a balloon is inflated, the rubber in the membrane is stretched; the exact physical processes occurring when a piece of rubber is stretched are numerous and complicated. Rubber consists of long chains of isoprene molecules. In the unstretched state, these molecules are very jumbled up; when stretched they untangle, and it is this untangling that provides the initial resistance to stretching. The extension and retraction of rubber is thus entropy (rather than energy)-driven, a fact rubber has in common with only gases. When stretched, entropy decreases and heat is given out; so much so that a stretched rubber band may be warmer to the touch than it was pre-stretch. When the stretch is released, the rubber takes back in heat energy to recover its previous form, and so may feel cold. A more detailed explanation of this effect was given by Stein [1958].

The approximate form of the stress-strain relation for a uniaxially-stretched piece of rubber is shown in figure 2.2, based on data given by Muller and Strehlow [2004]. For small extensions, the behaviour may be regarded as approximately linear. Above $\lambda \approx 1$ this is no longer the case; for $1 < \lambda < 3$, the stress-strain relationship follows that predicted by the neo-Hookean model, based on

probabilistic arguments for the untangling of molecule chains. Around $\lambda \approx 3$, some chains start to become fully stretched out (the finite chain length effect), so the stress rises more sharply with strain. Eventually, a point is reached (around $\lambda = 8$) when all the chains are fully stretched out, at which point the stress theoretically would increase indefinitely for a negligible increase strain. In practice, however, the large stresses will cause the material to crack and tear, and bonds between different molecules break.

The rubber need not follow the same stress-strain path in retraction as it took in extension - indeed, a notable hysteresis is observed. This hysteresis represents the energy lost as heat as a result of the stretch and release. The retraction process is further complicated by what is known as strain-induced crystallisation. When the rubber is in its stress-free state, there are a small number of bonds between different molecules as they lie all jumbled up together. Once near full extension, however, the chains lie parallel alongside each other, pushed closer together by the Poisson effect. New bonds between neighbouring molecules quickly form, a process that is known as crystallisation. This affects the rubber in retraction, causing an initial large loss of stress for relatively small loss of strain. Eventually, the crystallisation 'melts' (see Stevenson and Thomas [1979]) as these new bonds are broken, and so for low stresses, the behaviour nears that for extension. This crystallisation, combined with the loss of heat energy given out in extension, leads to a significant hysteresis in the stress-strain behaviour of rubber in extension and retraction. The initial stretch of the rubber therefore influences both the quantitative and qualitative behaviour in retraction; the same is true for the rate of retraction. Significant differences in the stress-strain behaviour were noted by Bogoslovov and Rowland [2007] between dynamic (with the rubber simply released at one or both ends) and quasi-static (controlled) retractions, that were argued to be a consequence of crystallisation, as the stress-wave speed in crystalline rubber is of a similar order to the rate at which the crystallisation melts. Therefore, while for a quasi-static retraction, the molecular structure has time to adjust to any changes in the stretch, for dynamic retraction it does not. The stress-strain behaviour is thus qualitatively different. Another issue to consider is that the stress-free strain to which the rubber returns may not be the same as pre-stretch; if some of the heat given out in extension has dissipated away, then there is not the energy available to recover its previous level of entropy. This change is not permanent, however; heating the rubber suitably, even if only a few degrees above the ambient temperature, will cause it to recover its pre-stretch strain again.

Rubber also displays some evidence of viscoelasticity: holding a piece of rubber in extension will lead to stress-softening, as the stress slowly decreases (to a non-zero value) over time. For natural rubber, however, the timescale for this stress softening to become significant is on the order of hours and days. Unlike some types of synthetic rubber, natural rubber also has low internal friction - resistance to motion by the movement of molecules within the material, akin to viscosity in a fluid - so that it should not be important for its dynamic retraction (as confirmed by the work of Gent and Marteny [1982]). An examination of potential viscoelastic effects in the rubber we used is given in section 2.7.

2.2 Types of balloons

In our experiments, a variety of natural rubber balloons were tried, of varying shape and from a range of manufacturers. For our purposes, the best balloons were those most consistent in terms of the shape

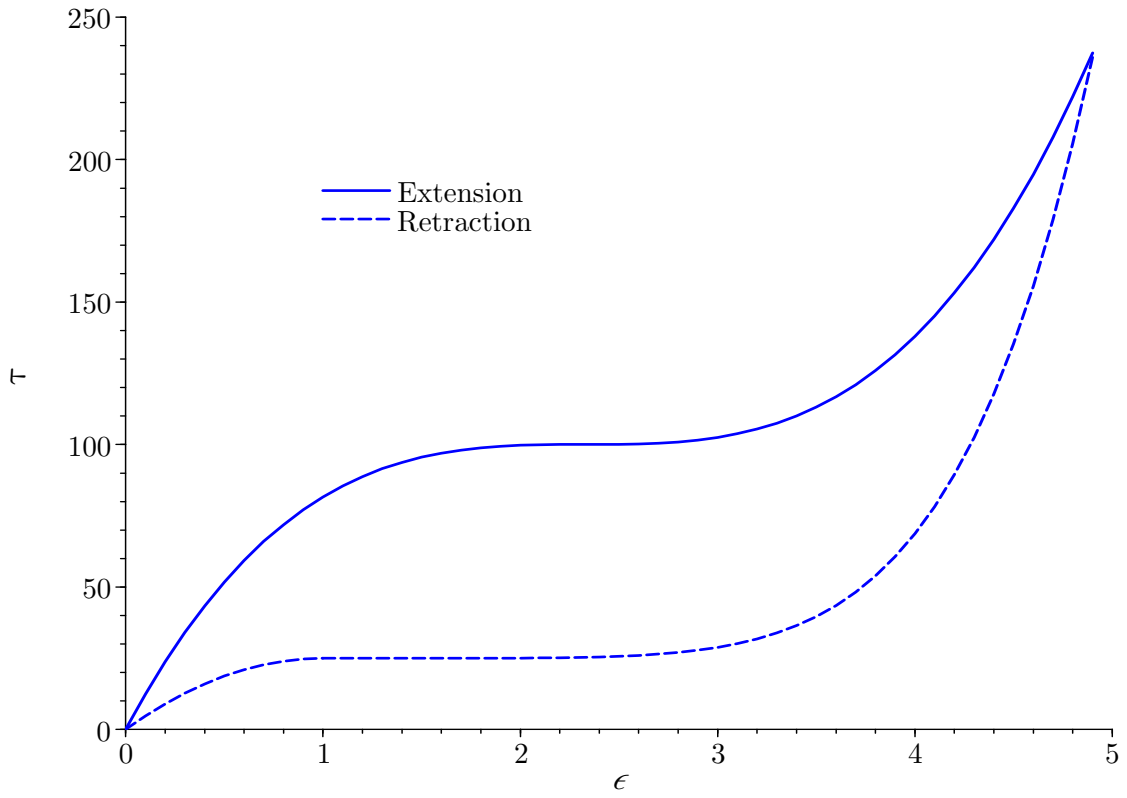

Figure 2.2: The approximate shape of the stress-strain relationship for rubber in uniaxial extension and retraction. The hysteresis is evident, with the area between the two curves representing the energy lost as heat during the process.

and tension at which rupture occurred. After trying a number of high-street brands, the best were found to be those made by the company Pioneer Balloons out of what they branded Qualatex. All subsequent experiments were conducted using these Qualatex balloons. Although the exact make-up of the rubber used in Qualatex balloons was not available, the packaging of the balloons stated that they were

> made from 100% latex,

meaning natural rubber. It was also stated that the balloons were

> biodegradable and sensitive to light and heat.

However, the balloons were never subjected to extreme conditions in lighting or heat, and no differences were noticed in behaviour of the balloons between those freshly purchased and those kept for several months in our laboratory. It is likely that these effects would only become significant in extreme conditions or long timescales. As the balloons were kept inside a laboratory away from sunlight, there was no risk of degradation due to uv light.

A range of sizes and shapes of balloons were tested, though only four were used extensively. Balloons of the standard, 'party balloon' shape are near-spherical when fully-inflated; they are known by their diameter when fully inflated (when it is at the point of bursting). The size of balloon most commonly available for purchase in shops, 300mm, were used for some experiments, but far more were conducted on 130mm balloons. These smaller balloons were used primarily because their size made them easier to manipulate. Cylindrical balloons are known by a number representing their diameter and length when fully inflated; a 646 balloon, for instance, is approximately 6 inches (0.15 m) in diameter and 46 inches (1.16 m) long when fully inflated. Common sizes are 160, 260 and 646; all experiments in this thesis on cylindrical balloons were conducted on 646 balloons (as explained in section 2.14).

Unfortunately, beyond the information given above, nothing else was known about the physical properties of the balloons (and no attempt was made to contact the manufacturer). Though parameters for natural rubber have been determined by other authors, there is little agreement between them. We were thus left to determine the properties of the rubber in the balloons ourselves, experimentally.

2.3 Membrane thickness

Knowing the thickness of the membranes was necessary if we wished to match theoretical models to experimental data. Measurements were taken of a 130mm balloon both before it was inflated, and after it had been fully inflated then deflated, with results given in figure 2.3. No measurements were taken of the thickness of the balloon when inflated, as we had no means of doing so. As stated in chapter 1, the method by which the balloons were made led to inconsistencies in the thickness from top to bottom, though we could expect them to be symmetric about the vertical axis. Consequently, several measurements were taken of the balloon at different places. The measurements were made using a constant torque micrometer screw gauge, that took measurements by compressing the rubber sheet between two metal surfaces. Due to the elastic nature of rubber, this method is likely to underestimate the thickness, though by the same proportion each time. Consequently, it should accurately reveal the variations in the thickness around the balloon, but only approximate the exact values.

The measurements revealed that the balloons were approximately axisymmetric, with variations in the horizontal (azimuthal) direction being typically less than 0.01 mm, and thus far smaller than those in the vertical direction. Pre-inflation, the thickness was monotone increasing up the 130mm balloon, from 0.19mm near the open end to 0.26mm at the apex, an increase of nearly 50%. After inflation, however, the thickness was much more uniform, with the spherical section of the balloon approximately 0.15mm thick. Consequently, for all experiments on 130mm balloons not previously inflated, 0.22mm will be taken to be the uninflated thickness, whereas for previously inflated balloons, 0.15mm will be used as the uninflated thickness. For cylindrical 646 balloons, the thickness was uniform away from the open end, with average values 0.35mm pre-inflation and 0.20mm post-inflation.

2.4 Rubber density

The density of the rubber was also unknown in advance, with the website `http://www.engineeringtoolbox.com/density-solids-d\_1265.html` giving the range of possible values between 910kg/m^3 and $1,200\text{kg/m}^3$. Consequently, an attempt was made to estimate it experimentally, as it was important to estimate

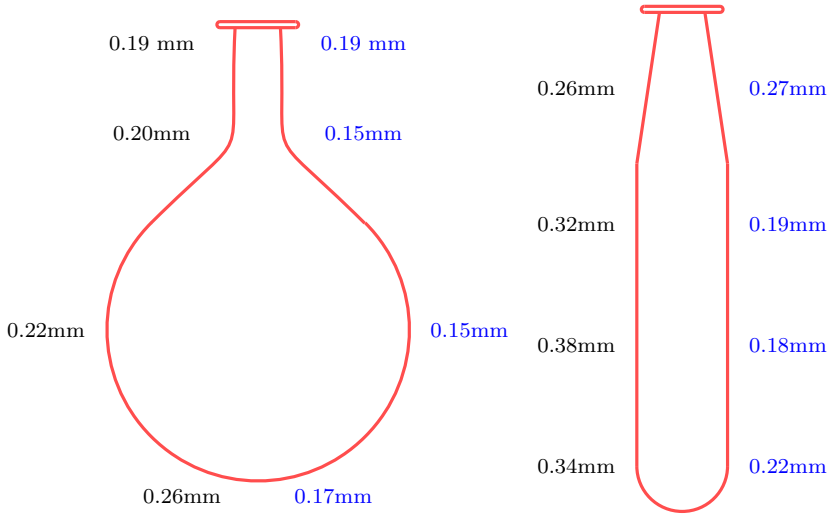

(a) 130mm spherical (b) 646 cylindrical

Figure 2.3: The thickness of the balloons used in later experiments at several locations over a vertical cross-section, both pre-stretch (black) and post-stretch (blue).

the influence of gravity on all our experiments, but also to determine the inertia of such rubber strips in retraction, as in chapter 5. Unfortunately, the only samples of such rubber we could obtain were the balloons themselves, and their thickness (and variations in thickness) made it very difficult to determine the volume of a sample. Nevertheless, an attempt was made by measuring directly the size and weight of a strip cut out of a 646 balloon (a more accurate estimation of the rubber density could have been obtained by floating a piece of the rubber in a density gradient, but this was not performed). This strip was 205mm long and 20mm wide, with the thickness assumed to be 0.35mm, the average thickness of a 646 balloon found in section 2.3. The volume of this strip was therefore 1435mm^3, and with its weight of 1.4g, the density estimate was

$$\rho = 976\text{kg/m}^3. \tag{2.1}$$

This is very close to the density given in Mark [2009] of 970kg/m^3, and due to the inaccuracy of the estimation techniques used here, it is this value of 970kg/m^3 (found using more accurate methods) that shall be used for rubber density throughout this thesis. As rubber is incompressible, this density should be independent of the strain, and thus accurate throughout all our experiments. Importantly, the fact that the density of the rubber was close to 1000kg/m^3 meant we could reasonably ignore differences in density between the rubber and water.

2.5 Pressure, stress and tension

It is common, when attempting to determine the stress-strain response of materials like rubber, to conduct simple uniaxial force-extension tests. However, given that our equipment was already set-up to examine the inflation of the rubber balloons, it proved more straightforward to determine the

response of the rubber by measuring the change in internal pressure against change in the balloon radius. It is detailed in Muller and Strehlow [2004] how the relation between the overpressure $[p]$, line tension σ, stress τ and radius r in a thin, incompressible, isotropic, spherical, elastic shell may be found, and a summary is given here.

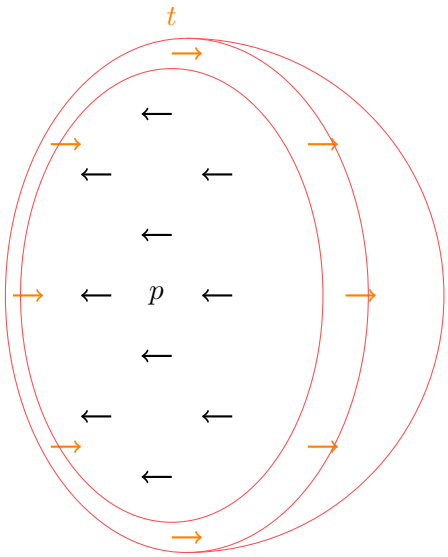

Figure 2.4: Free-body diagram for one hemisphere of a spherical pressure vessel.

Consider a uniform, spherical membrane, of reference thickness h_0 and inner radius r_0. In the deformed configuration, the thickness is given by h and the inner radius by r. When inflated, the membrane is in a state of biaxial stress, with circumferential stretch λ given by

$$\lambda = 1 + \epsilon = \frac{2\pi r}{2\pi r_0} = \frac{r}{r_0}.$$

The (Cauchy) stresses are then

$$\tau_{\phi\phi} = \tau_{\theta\theta} = \tau,$$

$$\tau_{rr} = \tau_{ij} = 0$$

for all $i \neq j$. Following the free body diagram of figure 2.4, we consider a cross-section that splits the balloon into two hemispheres. Assuming the balloon is in static equilibrium, the total force from the increased pressure above ambient $[p]$ of the air inside the balloon must be balanced by the total stress within the membrane. This balance gives

$$\pi r^2 [p] = \left(\pi(r+h)^2 - \pi r^2\right)\tau$$

that, after linearising about $h/r = 0$, reduces to

$$[p] = \frac{2h}{r}\tau. \tag{2.2}$$

The line tension σ is just the total stress over the thickness of the balloon,

$$\sigma = h\tau, \tag{2.3}$$

so the relation between pressure and tension is

$$[p] = \frac{2}{r}\sigma. \tag{2.4}$$

This is the Laplace-Young equation for a spherical fluid interface with constant surface tension σ and radius r. Indeed, the Laplace-Young equation for an interface of curvature κ upon which acts a surface tension of strength σ, and across which exists a pressure difference $[p]$, is

$$[p] = \sigma\kappa. \tag{2.5}$$

This may be used to model the tension within elastic membranes more generally, provided the thickness of the membrane is much less than its radius of curvature. As described in Parnes [2001], the tension within such a membrane may be reliably approximated as acting only tangentially; the derivation of equation (2.5) then follows the same path as for a fluid interface.

From the Laplace-Young equation, it is easy to see that for a static, spherical (in the absence of gravity) droplet of water in air of radius R, the pressure inside above the ambient is given by

$$p = \frac{2\sigma}{R}. \tag{2.6}$$

However, for a soap bubble of radius R, the internal pressure above the ambient is given by

$$p = \frac{4\sigma}{R}. \tag{2.7}$$

This is double the pressure inside a droplet, as a soap bubble has two water-air interfaces separating the inside from the outside, whereas a droplet has only one. It is important to note here that the correct equation for tension within a spherical membrane is equation (2.4) as stated by Adkins and Rivlin [1952]. It is not equation (2.7) as is given in Muller and Strehlow [2004], where it was argued that as there are two rubber-fluid interfaces between the interior and exterior of a balloon, the situation is analogous to a soap bubble. However, for an inflated balloon, it is not the rubber-fluid surface tension that supports the pressure difference between the interior and exterior fluids, but the tension within the rubber. There is, therefore, only one surface supporting the pressure jump across the interface, the situation is analogous to a droplet of one fluid in another fluid, and thus the tension in an inflated balloon is correctly approximated by equation (2.4). This result will be used throughout this thesis to calculate the tension within a membrane from knowledge of the pressure inside.

2.6 Experimental method

All of the experiments in this chapter were performed with the balloon held stationary within a transparent acrylic tank with base 1m×1m and height 0.6m. Unless explicitly stated otherwise, the tank was then filled to a depth of approximately 500 mm with water. This was done before the balloon

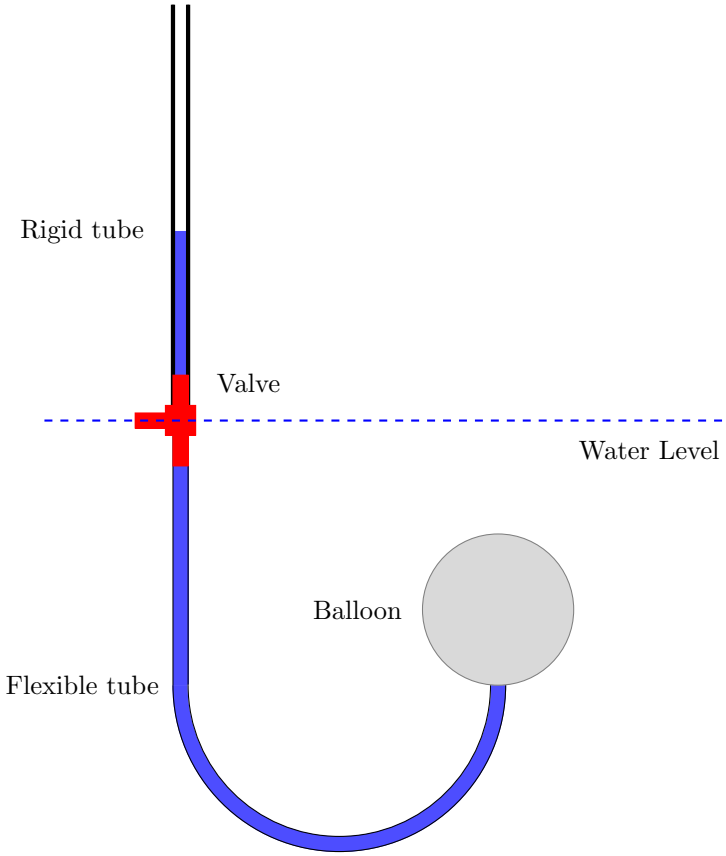

Figure 2.5: The experimental set-up used to measure the pressure-radius response and shape of our balloons when held underwater.

was filled, to minimise the amount of air in the system. The balloon was attached to the end of a 6 mm diameter flexible plastic tube, the other end of which was in attached to a three-way valve of tubes. One exit to this valve opened onto air; the other end was secured to a 1500 mm-long, 14 mm diameter rigid plastic tube held vertical. This set-up is diagrammed is figure 2.5.

The balloon was then filled by closing off the exit to the valve not connected to a tube, and pouring water down the rigid tube. By measuring the height of water in this rigid tube, an estimate of the tension in the membrane could be obtained, as follows: first, the pressure within the balloon was calculated by assuming it was in balance with the hydrostatic pressure within the 14 mm tube. When the experiment was being conducted with air external to the balloon, the height of the water-column was measured from the centre of the balloon; with water external to the balloon, the height of water column was taken from the surface of the water within the tank. Following section 2.5, the tension within the balloon could be estimated from these pressure measurements using the Laplace-Young equation for a spherical interface

$$\triangle p = \frac{2\sigma}{R},$$

where $\triangle p$ is the pressure difference across the interface, R is the average of the horizontal and vertical radii of the (approximately) spherical balloon, and σ is the (assumed constant) tension within the balloon. Conducting these experiments with the balloon underwater minimised the effects of gravity and meant the membrane's shape was as close to spherical as possible. This, in turn, meant the Laplace-Young equation was more accurate. This difference in behaviour arose because with air outside the membrane, it could not balance the hydrostatic pressure within the balloon (a consequence of gravity), and so the membrane had to deform to balance it instead. With water outside the membrane, the hydrostatic pressure was balanced between the fluids; there was, therefore, no need for the membrane to deform, and so it remained more spherical.

Images of the balloon were captured using a Photron Fastcam SA1.1 High-Speed Camera, as seen in figure 2.6. For each inflation measurement, a small amount of water was added to the top of the rigid tube. For each deflation measurement, a small amount of water was released out of the system via the switch. In both cases, the system was left for approximately 1 min to settle, before the height of the water in the rigid tube was recorded concurrently with the capturing of an image of the membrane. From this image, we used the program DigiFlow to determine the shape and approximate radius of the balloon. From the height and density of water in the rigid tube, we could determine the pressure (and hence the tension) in the balloon.

2.7 Viscoelasticity

Rubber is well-known to display some features of viscoelasticity. According to Lakes [2009], a viscoelastic material is one for which the relationship between stress and strain depends on time. This is well-known to be true for rubber; holding a stretched piece of rubber at room temperature will lead to stress-softening, where the stress in the rubber decreases over time despite the fixed strain (as described in section 2.1). However, the time-scales required for viscoelastic effects to become significant are far greater than those relevant to our experiments; according to Lakes [2009], a piece of rubber held stretched with $\epsilon = 1.5$ at room temperature for an hour will experience a change in stress of around 4%. We conducted our own test for stress-softening: using the set-up described in section 2.6,

Figure 2.6: Equipment used to perform the experiments.

a 130mm balloon was filled with water then held stationary, before the stress was recorded regularly over the course of an hour while the volume of water within the system remained constant. This meant that the volume of water within the balloon, and hence the stretch of the membrane, did increase by a small amount during the course of the experiment. The results are displayed in figure 2.7, and reveal a drop in stress of around 11% over the course of an hour. Such long time-scales mean that we would not expect viscoelasticity to play a role in the dynamic retraction of stretched rubber, which occur over fractions of a second. For some of our experiments, such as those used to determine the dispersion relation for the pre-burst waves as in chapter 4, a single balloon was held filled (and thus with the rubber in extension) for a period of several minutes. However, any stress-softening as a result of the viscoelasticity of rubber was mostly accounted for by measuring the pressure in the balloon, and hence the stress, concurrently with any other measurements or recordings. It is also possible that the presence of air instead of water inside the membrane may also affect the timescale for relaxation, though as all experiments in this thesis were conducted with water inside, any change in behaviour would not affect our results. Consequently, we do not expect viscoelasticity to have been a siginificant factor in any of our experimental results.

2.8 Mullins effect

The Mullins effect, as discussed in chapter 1, is a well-known phenomenon in rubber whereby the stress-strain relationship changes over repeated extensions and retractions. This change is dependent on the maximum strain previously applied to the rubber. However, as stated by Diana et al. [2009], even now, forty years on from the initial review by Mullins [1969], we are still far from a universally accepted physical explanation for this phenomenon, or indeed an accurate predictive model. Fortunately, despite the stress-strain relationship for the initial extension often being vastly different from that of the following extensions, over many such tests with the same maximum strain, the stress-strain relationship

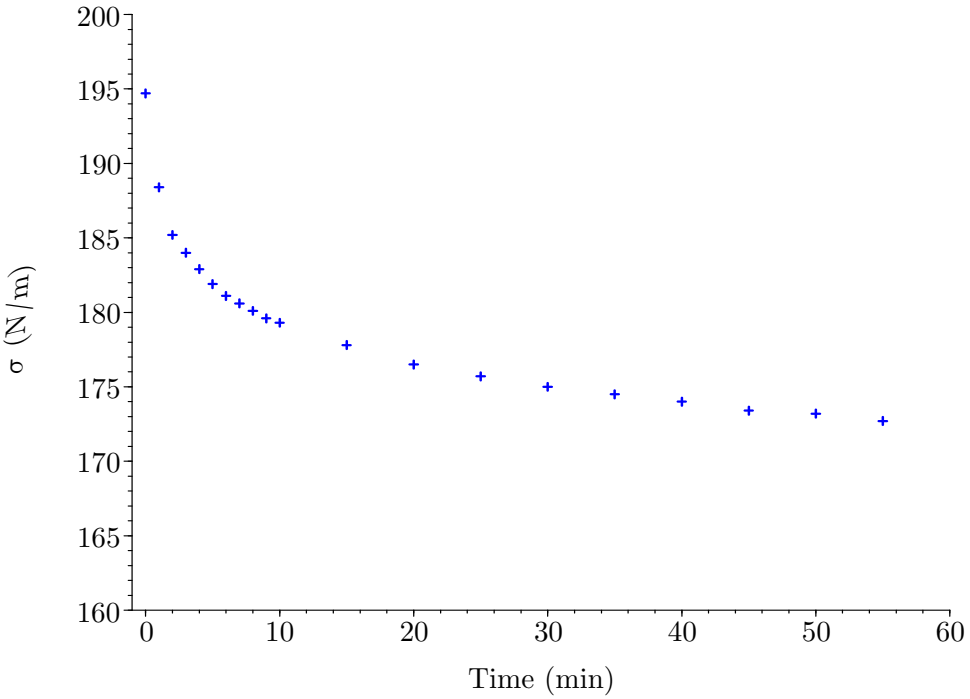

Figure 2.7: The change in the tension within a filled 130mm over time.

becomes repeatable. It should be noted here that this does not take into account external heating of the rubber, which may cause the rubber to return to something near its state before the initial deformation.

To see whether the Mullins effect was present in the rubber we were using, quasi-static stress-strain data was taken for up to five fillings and unfillings of a single balloon. The experimental method described in section 2.6 was used; the process of adding water and taking measurements continued until the height of water in the rigid tube reached around 700 mm, at which point measurements were taken as the balloon was quasi-statically emptied.

The effect of the previous maximum stretch on the stress-strain relationship is revealed in figure 2.8, with the behaviour on second filling of a balloon with maximum stretch on first filling of $\lambda = 4$ compared to that of a balloon with maximum stretch on first filling of $\lambda = 6$. In all cases, both here and throughout this thesis, stretches are determined relative to the rubber prior to its first filling. There is a significant discrepancy in the stress-strain relationship, particularly when the tension in the membrane was low. To simplify later experiments, all balloons were filled to $\lambda = 6$ on first filling unless explicitly stated otherwise.

The change in the stress-strain behaviour for a 130mm membrane on repeated fillings and unfillings is given in figure 2.9, where it clearly demonstrates the presence of the Mullins effect. However, after the initial filling, any difference between subsequent fillings, and between all unfillings, were minimal. As a result of this, in all future experiments the membrane was filled and unfilled at least once before being filled again for the actual experiment.

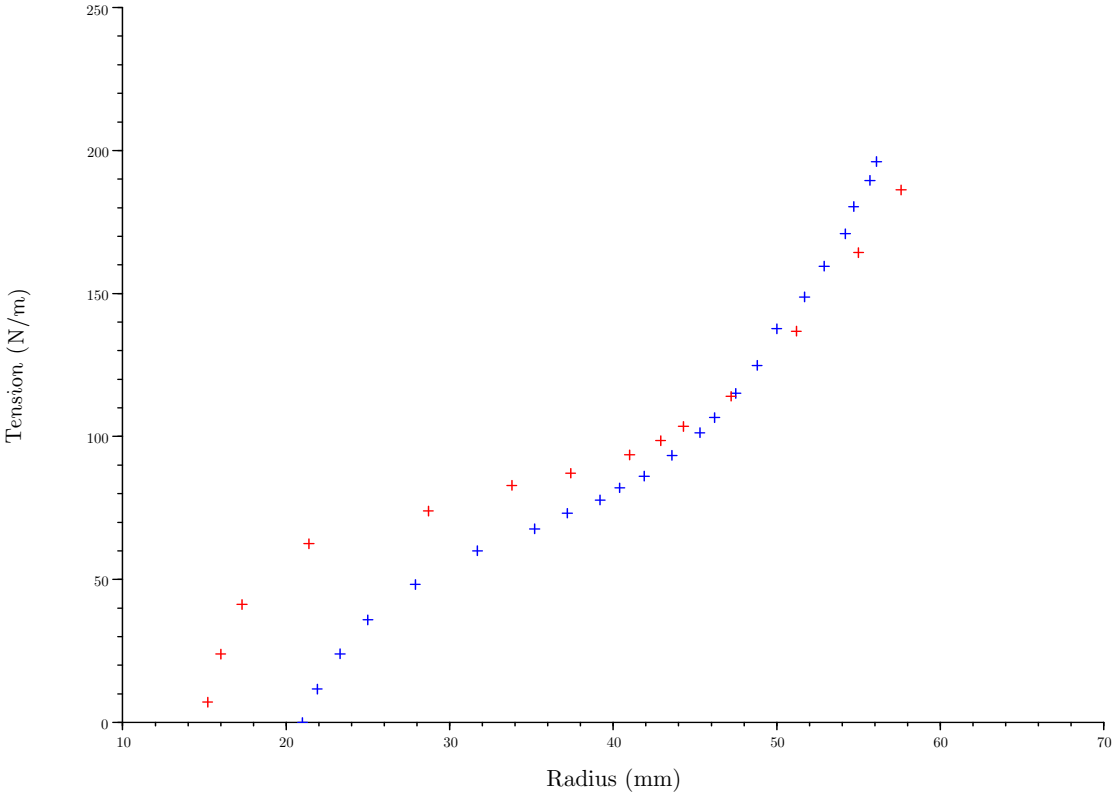

Figure 2.8: The response of two 130mm balloons on second inflation, one filled to $r = 40$mm on first filling (red) and the other filled to $r = 60$mm on first filling (blue).

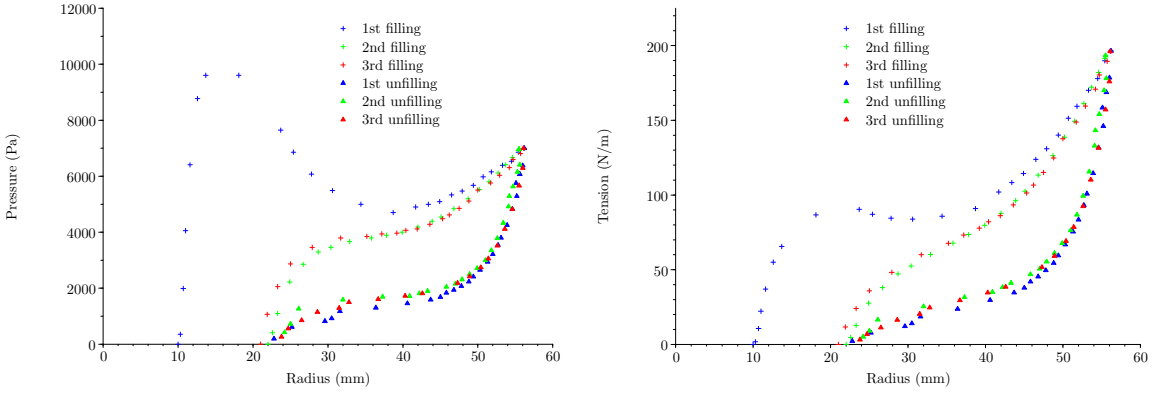

Figure 2.9: The response of a 130mm membrane over three consecutive quasi-static fillings and unfillings.

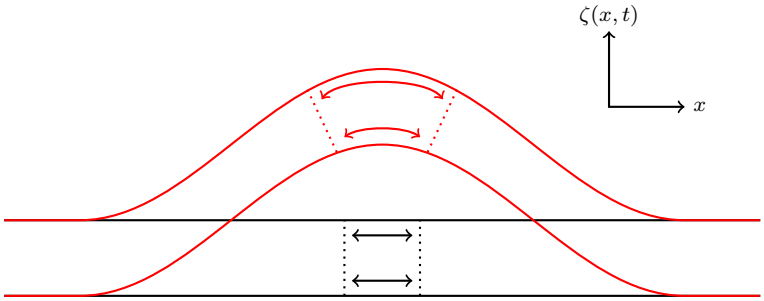

Figure 2.10: An illustration of the creation of bending stresses within an elastic membrane. The out-of-plane deformation causes the top part of the strip to extend further than the bottom section. The consequent gradient in tension through the strip creates a net force that resists such deformations.

2.9 Bending stiffness

For in-plane deformations of an elastic membrane in a vacuum, it is the in-plane stresses that determine the membrane's response. These in-plane stresses may also act as the restoring force for out-of-plane (transverse) deformations, such as the surface waves seen in chapter 1 when a water balloon impacts a rigid surface. For such waves, however, a further effect must be considered: bending stiffness. A good demonstration of this effect is illustrated in figure 2.9 for an elastic sheet, where due to the out-of-plane deformation of the sheet the top of the sheet is stretched further than the bottom. The consequent shear in the stress acts to restore the sheet to the horizontal, and thus may act as a restoring force for waves. For a one-dimensional elastic plate with Young's modulus E, density ρ, and thickness h, Vermorel et al. [2007] give the linear equation for the small transverse displacement $\zeta(x,t)$ as

$$\rho\frac{\partial^2\zeta}{\partial t^2} = \tau\frac{\partial^2\zeta}{\partial x^2} + \frac{Eh^2}{12}\frac{\partial^4\zeta}{\partial x^4}, \tag{2.8}$$

where τ represents the (assumed constant) in-plane stress. This is known as the Euler-Bernoulli theory of buckling. For a stretched elastic sheet, this will be $O(E)$ or greater, whereas the bending stress is $O(E(h/\lambda)^2)$ for wavelength λ. Consequently, for thin membranes in extension (such as our filled balloons) bending stiffness will not be significant. The assumption that bending effects are negligible for a thin elastic sheet in extension is known as the membrane approximation, a topic covered in detail by Ventsel and Krauthammer [2001]. Note that bending stiffness will become important when $\lambda \approx h$, so that tension-driven waves of such short wavelengths will be suppressed. This implies a high k cut-off for the pre-burst waves seen on dropped water balloons, as was observed in chapter 1.

Bending stresses only become significant when the in-plane stresses within a membrane are negative. The dispersion relation for the transverse waves given by equation (2.8) is

$$\omega^2 = \frac{\tau}{\rho}k^2 + \frac{Eh^2}{12\rho}k^4.$$

Thus when $\tau >> 0$, stable tension waves form. For $0 < \tau << 1$, the primary transverse response will be stable waves for which the restoring force is bending stiffness in the membrane. However, when $\tau < 0$, there exists a range of wavenumbers for which the transverse waves are unstable, causing the

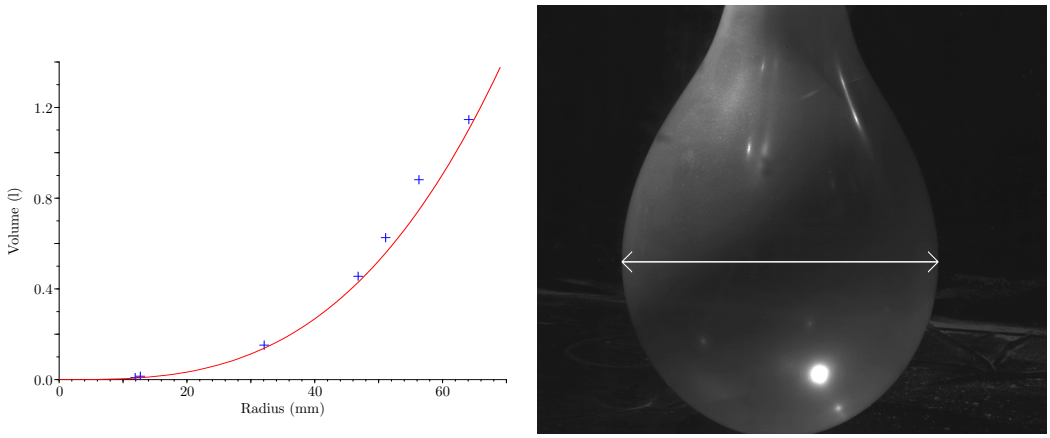

(a) (b)

Figure 2.11: Figure (a) shows the volume of water inside a balloon as it is quasi-statically inflated while held underwater. The blue marks represent the volume found by weighing the balloon, plotted against the greatest horizontal radius r_g as displayed in (b). The red-line represents the estimate of the volume gained from assuming the balloon is a sphere of radius r_g.

amplitude of out-of-plane deformations to grow - as is seen when you push two ends of a rubber band together and it buckles. The wavelength of these waves is set by the ratio of the compressive stress to the bending stiffness, with the surrounding medium having little effect (see Vermorel et al. [2007]). More discussion of this effect will be given in chapter 5.

2.10 Volume

The volume of our balloons when inflated was another unknown. The most accurate method available to us to determine the volume of water within a balloon was to simply weigh the balloon. This was done for one of our 130mm balloons, by filling it up to the required size underwater, capturing an image of it, then removing it from the water and weighing the water within on a set of digital scales. The weights were then plotted against the greatest horizontal radius r_g of the balloon, as depicted in 2.11(b), with the results shown in figure 2.11(a).

Knowing r_g gave us an alternative method for estimating the volume - if we assumed the balloon is perfectly spherical, the volume would be given by $4/3\pi r_g^3$. This prediction is given in figure 2.11(a) by the red line, and appears to consistently underestimate the volume by around 10%. The reason for this is simple: fully inflated balloon does not remain spherical, but becomes more pear-shaped as the tube-like region near the open end inflates. A more detailed investigation of the static shape of the balloons when static is given in the following sections. We would therefore expect a more accurate estimate for the volume of the balloon to be obtained by finding the outline of the balloon digitally and assuming axisymmetry; however, such a method was not attempted.

2.11 Sessile shape of a spherical balloon

The shape of a static water-filled balloon, both when lying on a flat, rigid surface in air and when held underwater, is determined in part by the response of the rubber in extension. By finding and analysing this shape, it would shed more light on the behaviour of the rubber, and in particular reveal whether the tension is near constant throughout the membrane. We note here that, as discussed in section 2.9, we expect bending stiffness to play no significant part in determining the shape of our balloons. This is further demonstrated through consideration of the non-dimensional tensioned-beam parameter (as used by Srinil et al. [2009]), $\epsilon = L^2\tau/EI$ where L is a relevant length scale. This parameter gives a comparison between the stress and bending stiffness within the membrane. Taking relevant values thickness $h \approx 0.0002$ m, radius $L \approx 0.1$ m, $E \approx 500,000$ N/m^2, $\tau = ELh$, and $I = Lh^3/12$, implies $\epsilon = 30,000$, strongly suggesting that tension is the dominant force in determining the shape of the balloons.

To examine the sessile shape of our 130mm balloons, the method given in section 2.6 was used. The first set of experiments were performed with the balloons supported by a rigid surface surrounded by air; in the next set, the water surrounding the balloons was reintroduced. After the experiments were complete, the images were analysed using DigiFlow to determine the shape and radius of the balloons.

In air

First, we considered a water balloon lying on a flat surface surrounded by air. If the tension within the balloon itself was uniform for a set volume, we would expect its shape to obey the same equation as that which describes the shape of an axisymmetric water droplet lying on a flat surface in air, known as the sessile drop equation:

$$\frac{\sigma\eta''}{(1+\eta'^2)^{\frac{3}{2}}} - \frac{\sigma}{\eta(1+\eta'^2)^{\frac{1}{2}}} + \rho g z - \lambda = 0. \tag{2.9}$$

Derived by Wang and Lannutti [1968], $\eta(z)$ is the displacement of the balloon's free surface from its central axis, σ represents the (constant) surface tension, ρ represents the water's density and λ is a Lagrangian multiplier that arises from the fact that a finite volume of water is being considered. The value σ was determined using the method described in section 2.6. The natural boundary condition at the top of the balloon are

$$\eta(h) = 0, \tag{2.10}$$

$$\eta'(h) = \infty, \tag{2.11}$$

where h is the height above $z = 0$ of the balloon's apex. Specifying the volume of the balloon V and the radius of the contact area between the balloon and the flat surface $\eta(0)$, means that the Lagrangian multiplier λ is given by

$$\lambda = -\frac{1}{\pi\eta^2(0)}(\rho g V + 2\pi\eta(0)\sigma\sin(\theta)), \tag{2.12}$$

where θ is the contact angle between the balloon and the flat surface.

We are therefore left a second-order ordinary differential equation for $\eta(z)$, three unknown parameters h, θ and λ, and five boundary conditions for $\eta(0)$, $\eta'(0)$, $\eta(h)$, $\eta'(h)$, and V. Therefore, specifying

V and $\eta'(0)$ as is typically done for droplets, equation (2.9) could in principle be solved numerically. Here, however, $\eta'(0)$ could not be easily identified from either the conditions so far derived or experimental observation. However, $\eta(0)$ could be determined experimentally, so the equation was solved by using a shooting method, iterating over $\eta'(0)$ for given V and $\eta(0)$, and taking as the solution the iteration that gave $\eta(h)$ as close to zero as possible. We employed matlab's inbuilt Runge-Kutta (4,5) solver, ode45. Equation (2.9) was solved starting at $z = 0$ and working towards $z = h$, for given initial conditions $\eta(0)$ (the contact radius) and $\eta'(0)$ (the wettability of the balloon/solid surface interface). The value of V used was that given by a sphere whose radius was an average of half the greatest horizontal and vertical sections of the sessile balloon. We did not use just the greatest horizontal radius as suggested by figure 2.11, as the sessile shape of the balloons was far less spherical than the pear-like shape they assumed when fully inflated underwater. Consequently, using just the greatest horizontal radius led to the volume being greatly over-estimated.

The theoretical results for water-filled balloons resting horizontally on a flat, rigid surface in air may be viewed in figure 2.12, for two different cross-sections. They reveal a close agreement to the predicted shape, suggesting that the tension is indeed close to constant away from the tube end. Small discrepancies are seen near the top of balloon, that could perhaps be removed by more accurate choice of the input parameters V and $\eta(0)$. The boundary conditions at the top (2.10) and (2.10) may not be changed, however, as they are theoretically specified, and the height h is an unknown to be determined.

However figure 2.13, depicting such a balloon held vertically, shows that the tube section of the balloon strongly affects the shape of a very full balloon, as its inflation makes the overall shape of the balloon pear-like.

There exists the possibility that this lack of sphericity at high strains is the result of an inherent instability in rubber. It is well-known that biaxially stretched flat sheets of rubber, once over a certain critical strain, become asymmetric - the strain is greater in one direction than the other, despite symmetrically applied stresses. Indeed, this is even predicted by the several common non-linear models of rubber, such as the Mooney-Rivlin model discussed in section 2.13.1. Inflated balloons are also biaxially-stretched membranes, and the critical strain estimated in Muller and Strehlow [2004] to be around 3.17 - well within the range of extension considered in our experiments. However, Muller and Strehlow [2004] go on to consider a spherically-inflated Mooney-Rivlin membrane, and find that theoretically the strain should remain symmetric for all strains. Consequently, as they suggest and as is described in section 2.1, the observed departures from the spherical are likely a result of the manufacturing process used to create these membranes, and not a sign of an inherent instability in spherical, isotropic rubber membranes.

In water

The simplest case to consider is to examine the shape of the balloons from above, in water. As the tube region should not affect the outline significantly, we would expect them to appear circular. As figure 2.14 reveals, this was indeed the case throughout inflation, for the full range of strains from 0 to 6. This provides good justification for assuming that the balloons were axisymmetric, as is done in later chapters to simplify modelling.

The side-on shape of a stationary balloon held underwater was also examined, by determining the circular harmonics of a silhouette of the balloon. Images were taken of a back lit balloon during filling,

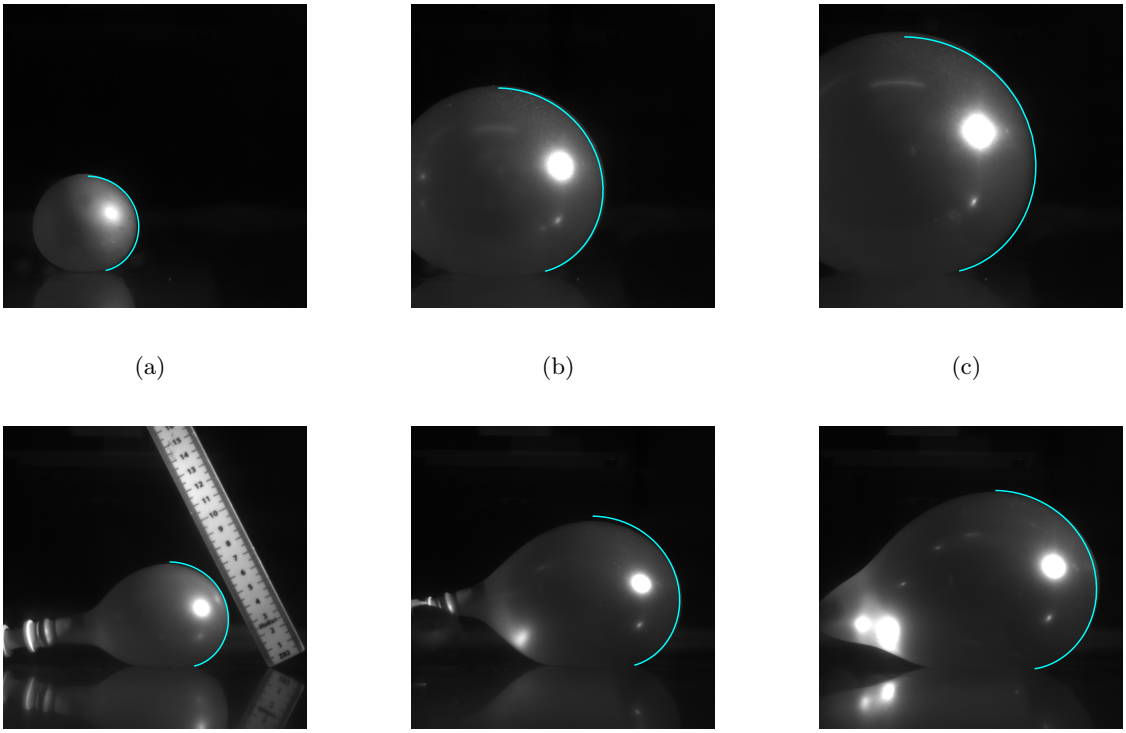

(a) (b) (c)

(d) (e) (f)

Figure 2.12: A sessile 130mm balloon matched against the theoretical predictions of equation (2.9), given by the cyan line. Figures **(a)** to **(c)** are for such a balloon viewed head-on, while **(d)** to **(f)** are the same balloon viewed from the side.

from which the shape and radius of the balloon was later determined by finding the intensity contour giving the outline of the balloon. For this, we wished to ignore the tube region of the balloon, as this would greatly distort the results for the rest of the balloon. Whilst it was not possible for us to accurately determine how much of an influence this tube region has to the response of the balloon away from this region under inflation and oscillation, its relatively small size suggests that this influence would not be significant. The contour was thus chosen to follow a small circle fitted where the end of this neck region met the rest of the balloon such that the new contour was smooth at these points. For each point on this contour, the angle θ and distance r to the contour's centroid was determined. This radius r was then Fast Fourier Transformed and coefficients found for the description of the contour, for r as a function of θ, as

$$r = \sum_{0}^{\infty} a_n \cos\left(n\theta + \phi_n\right). \tag{2.13}$$

The coefficient a_n represents the amplitude of the harmonic, with ϕ_n representing the phase. For instance, a perfect circle of radius R has coefficients $a_0 = R$, $a_n = 0 \; \forall \, n > 0$.

We can get some measure of how similar two shapes are by taking the Euclidean distance between

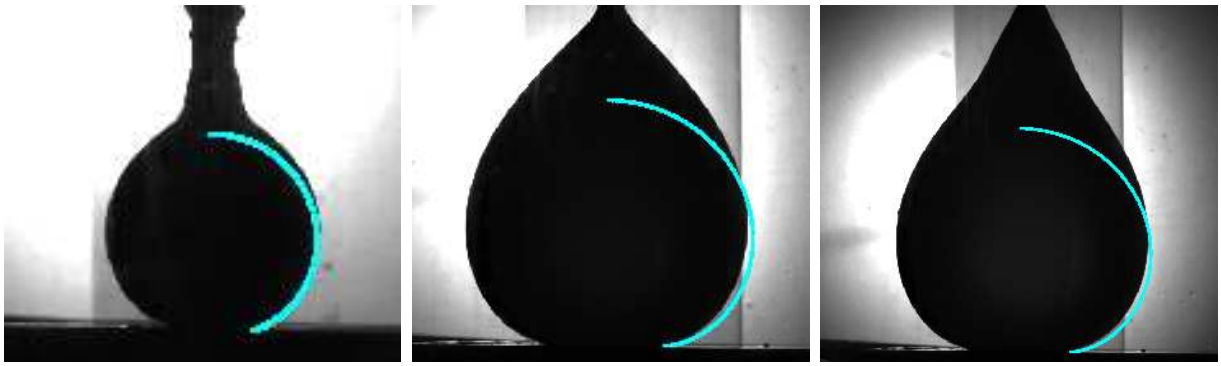

(a) $\sigma = 75$ N/m (b) $\sigma = 133$ N/m (c) $\sigma = 194$ N/m

Figure 2.13: Comparison of the sessile shapes of a balloon held vertical during filling. The theoretical predictions of the sessile drop equation are given by the light blue lines.

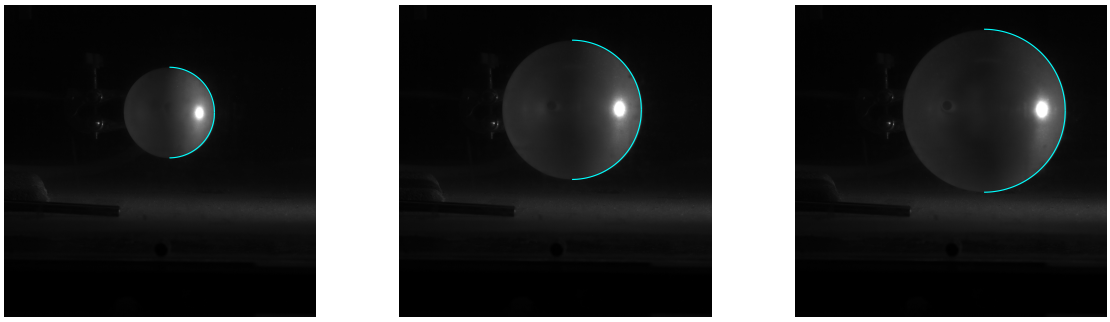

(a) $[p] = 4,300\,\text{Pa}$ (b) $[p] = 5,200\,\text{Pa}$ (c) $[p] = 6,900\,\text{Pa}$

Figure 2.14: The shape of a 130mm balloon looking down on the top. The light blue line is a circle.

the vectors consisting of the amplitude coefficients of their Fourier decomposition as described above, after being in some way scaled. For a closed contour, one obvious choice for this scaling is the area enclosed by the contour, and this scaling is used in all subsequent examples. Thus, for two contours A and B whose amplitude coefficients (after being scaled by the square root of the area enclosed by the contour) are found to be a_n and b_n respectively, the distance between the shape of these contours may be estimated as

$$D_{AB} = \sqrt{\sum_{0}^{N} (a_n - b_n)^2},$$

for some large $N > 0$. In the examples to follow, we used $N = 16$, as no discernible difference was seen when introducing higher harmonics. The description of a shape A by the vector $< a_n, n = 0, ..., N >$ is useful to us as it ignores all rotation, translation and scaling of the contour which may arise due irregularities in the balloons or experimental procedure.

Each experimentally-found outline was compared to that of an ideal, spherical balloon, as this

would be the shape taken by a balloon for which the tension was the same everywhere. Once a suitable contour had been found, the circular harmonic coefficients ($\tilde{a}_n$) were determined before being scaled. This scaling was performed using the area A_r enclosed by the contour, so that the final coefficients used for comparison were $a_n = \tilde{a}_n/\sqrt{A_r\pi}$. The Euclidean distance was then found between the vector $< a_n, n = 0, ..., N >$ and that formed from the coefficients expected for a perfect sphere, namely $< a_0 = 1, a_n = 0 \,\forall\, n > 0 >$. This measure, s, could then be used to compare the shape of a balloon as it was quasi-statically inflated, and at different parts of the phase of a wave during oscillation. Results depicting s for a twice pre-filled, unoscillated balloon whilst being filled for a third time are given in figure 2.15; the relation is u-shaped, due to the varying influence of the tube region as depicted in figure 2.16. For radii r less than 30 mm (figure 2.16(a)), the tube region remained uninflated as the rest of the membrane was ellipsoid; this is also seen when the balloon is uninflated, and is a consequence of variations in thickness of the membrane. As the radius increased (figure 2.16(b)), the tube remained uninflated but the spherical region inflated; variations in thickness were now relatively small, so the outline contour was at its closest to circular. As r increased from 40 mm to 70 mm (figure 2.16(c)), the change in shape was noticeable by the naked eye, as the tube region also inflated. The balloon consequently took its familiar pear-like shape, as the outline contour deviated significantly from the circular.

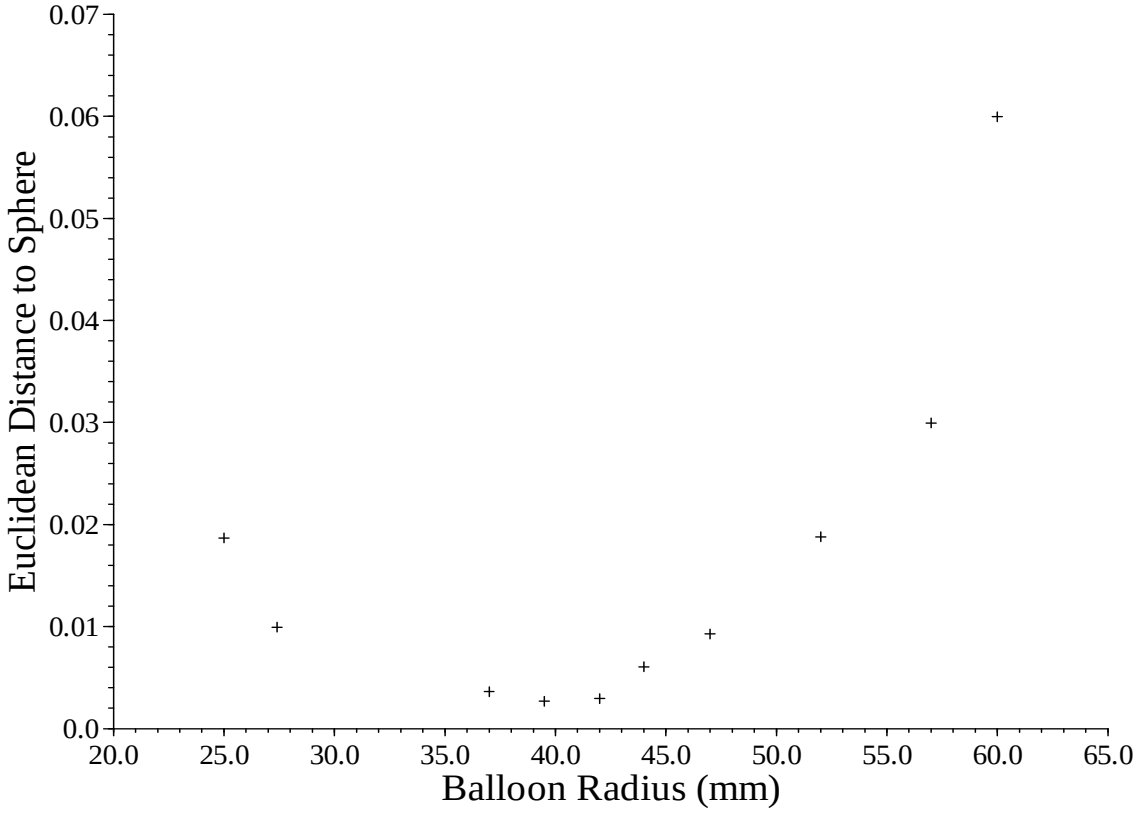

Figure 2.15: The Euclidean distance to a sphere of a quasi-statically filled balloon.

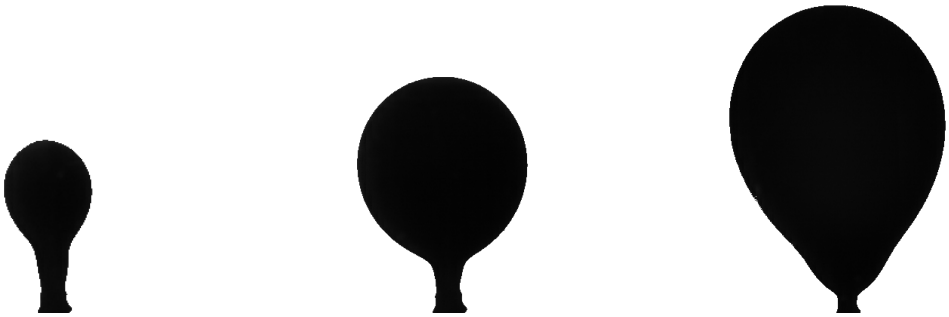

(a) $r = 25$mm (b) $r = 40$mm (c) $r = 57$mm

Figure 2.16: The silhouette of a 130mm balloon over a single inflation.

In summary, we have found that the balloons are axisymmetric; if the tube region is ignored, the shape of the main inflated region varies over its inflation, but is always close to spherical. The initial non-sphericity in the membrane is likely a consequence of variations in membrane thickness, while the later deviations arise from the influence of the tube region at the bottom.

2.12 Sessile shape of a cylindrical balloon

A water-filled cylindrical balloon viewed end-on underwater would be expected to appear circular; figure 2.12 shows this to indeed be true for our balloons.

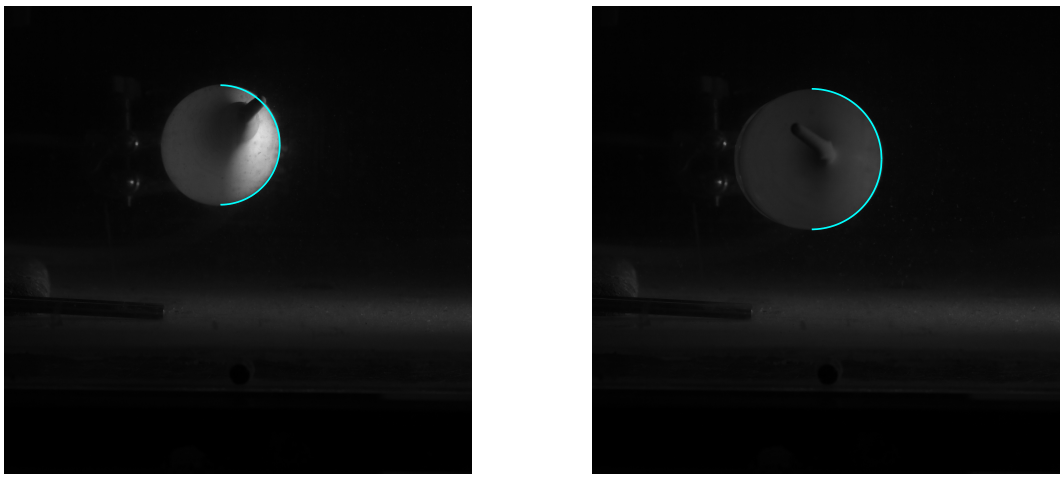

(a) $[p] = 5,500\,\mathrm{Pa}$ (b) $[p] = 6,400\,\mathrm{Pa}$

Figure 2.17: The shape of a water-filled 321 balloon underwater, looking at it end-on. The light blue line is a circle.

However, as for a spherical balloon, a water-filled cylindrical balloon in air resting on a horizontal surface and viewed end on will have a different, more complicated shape. As in section 2.11, this shape arises due to a balance between the (circumferential) tension in the balloon and gravity acting on the water within it, so we modify the analysis of Wang and Lannutti [1968] to model cylindrical droplets. We consider a vertical cross-section of the balloon parallel to the plane $y = 0$. The equation of interest is now

$$\frac{\sigma\eta''}{(1+\eta'^2)^{\frac{3}{2}}} + \rho g z - \lambda = 0, \tag{2.14}$$

where $\eta(z)$ is the displacement in the x-direction of the balloon's free surface from its central plane, σ represents the (constant) surface tension, ρ represents the water's density and λ is a Lagrangian multiplier that is a consequence of the fact that a finite cross-section of water is being considered. The natural boundary conditions are, as before,

$$\eta(h) = 0 \tag{2.15}$$

$$\eta'(h) = \infty, \tag{2.16}$$

where h is the height above $z = 0$ of the balloon's apex. An equation for the Lagrangian multiplier λ is then

$$\lambda = -\frac{1}{\eta(0)}\left(\frac{1}{2}\rho g S + \sigma\sin(\theta)\right), \tag{2.17}$$

where S is the area of the cross-section.

This system may then be solved as in section 2.11, and sample results are shown in figure 2.18. For all but the largest volumes, equation (2.14) appears to give a good estimate of the cross-sectional shape of a sessile water-filled 646 balloon in air.

2.12.1 Side-on view

The side-on view of our cylindrical balloons was complicated by an instability in shape that did not occur for the spherical balloons. As may be viewed in figure 2.19, when partially filled, the radius was not constant all along the balloon, but instead there were two distinct regions of differing radii, with a sharp transition region between them. The appearance and growth of such aneurysms, as they are known, occurs dynamically, yet this situation is statically-stable. It is a consequence of the non-linear stress-strain relationship in rubber at high strains, and has been seen and described by many others authors, including by Kyriakides and Chang [1990] and Yin [1977]. As for the balloon outline, it is approximately rectangular away from the curved ends for small and large inflations, but much more complicated at medium inflations where no simple theory exists to describe it.

2.13 Stress-strain relationship for the quasi-static inflation of spherical balloons

We also wished to determine the pressure-radius response of the balloons as they were quasi-statically inflated. A similar experimental investigation was conducted on balloons by Muller and Strehlow [2004]; we repeat their investigation, but using our balloons. As discussed in section 2.5, doing so

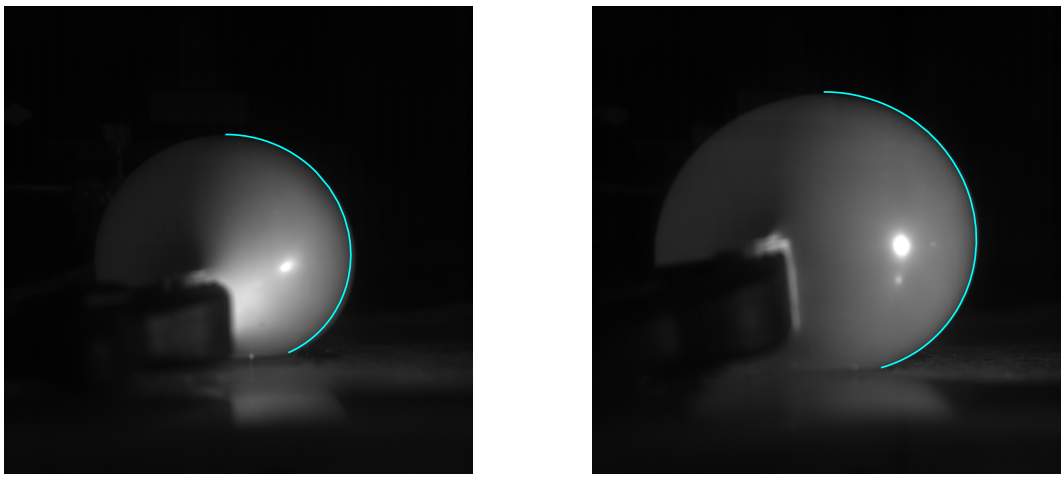

(a) $[p] = 3,900\,\mathrm{Pa}$ (b) $[p] = 5,300\,\mathrm{Pa}$

Figure 2.18: The shape of a sessile water-filled 646 balloon, looking at it end-on. The light blue line is the prediction of equation (2.14).

would allow us to determine the property of rubber most important for our work: its stress-strain response.

2.13.1 Theoretical models for the quasi-static stress-strain behaviour of rubber

Rubber is, in many respects, a simple material to model: it is approximately incompressible, isotropic, and at small strains ($\lambda < 2$) the stress-strain relation is approximately linear. Indeed, our results show nothing to dispute these statements. However, its high extensibility (up to $\lambda = 8$ according to Mark [2009]) means that this is far from a full description of its behaviour. At higher strains the stress-strain relationship clearly becomes non-linear, with the rate of deformation also having a significant impact. Even for quasi-static deformations, there exists no universally-used physically-derived theory to predict the behaviour for $\lambda > 2$. All the most commonly used and accurate models are phenomenologically derived, with the accuracy determined by how many experimentally-derived parameters one is willing to accept.

Once a model for the stress-strain response has been chosen, it is possible to derive the pressure-radius and tension-radius response for a thin, incompressible elastic spherical membrane, as detailed in Muller and Strehlow [2004]. As before, we consider a uniformly spherical membrane, of reference thickness h_0 and inner radius r_0. In the deformed configuration, the thickness is given by h and the inner radius by r. When inflated, such a shell is in a state of biaxial stress, so that the circumferential stretch λ is given by

$$\lambda = 1 + \epsilon = \frac{2\pi r}{2\pi r_0} = \frac{r}{r_0}.$$

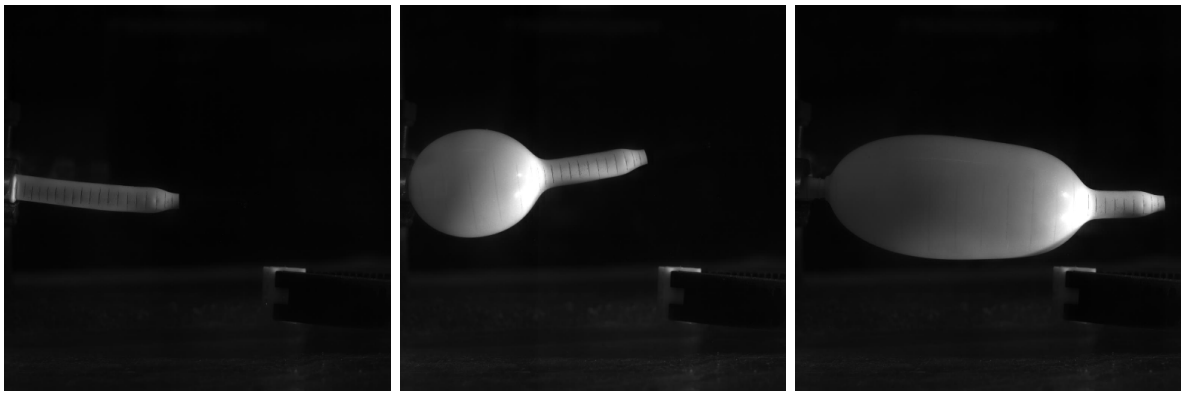

Figure 2.19: The shape of a water-filled 321 balloon underwater, as it inflates. As the volume increases, the inflation loses symmetry due to the appearance of an aneurysm that then spreads along the balloon.

As the material is incompressible, conservation of volume means

$$4\pi\left[(r+h)^3 - r^3\right] = 4\pi\left[(r_0+h_0)^3 - r_0^3\right]$$

that after linearisation gives

$$hr^2 = h_0 r_0^2,$$

and thus

$$h = h_0\lambda^{-2}.$$

Hence, using (2.2), the pressure jump is given by

$$[p] = 2\frac{h_0}{r_0}\lambda^{-3}\tau. \tag{2.18}$$

All that is then left is to propose a model for the stress, τ. There are a number of possible models. We consider here only the four types most commonly used to model rubber: the standard linear model of elasticity, and neo-Hookean, Mooney-Rivlin, and Ogden's non-linear hyperelastic models.

Linear theory

We shall start by considering linear theory, as it is the simplest theory. For a spherical linear balloon, we expect the stress to be linearly dependent on strain, namely

$$\tau_{\phi\phi} = \tau_{\theta\theta} = G(\lambda - 1)$$

for some constant G (with coordinates ϕ and θ as defined in section 1.7). Consequently, equation (2.18) gives the pressure jump as

$$[p] = 2\frac{h_0}{r_0}G\left(\lambda^{-2} - \lambda^{-3}\right)$$

and thus the tension as

$$T = h_0 G\left(\lambda^{-1} - \lambda^{-2}\right).$$

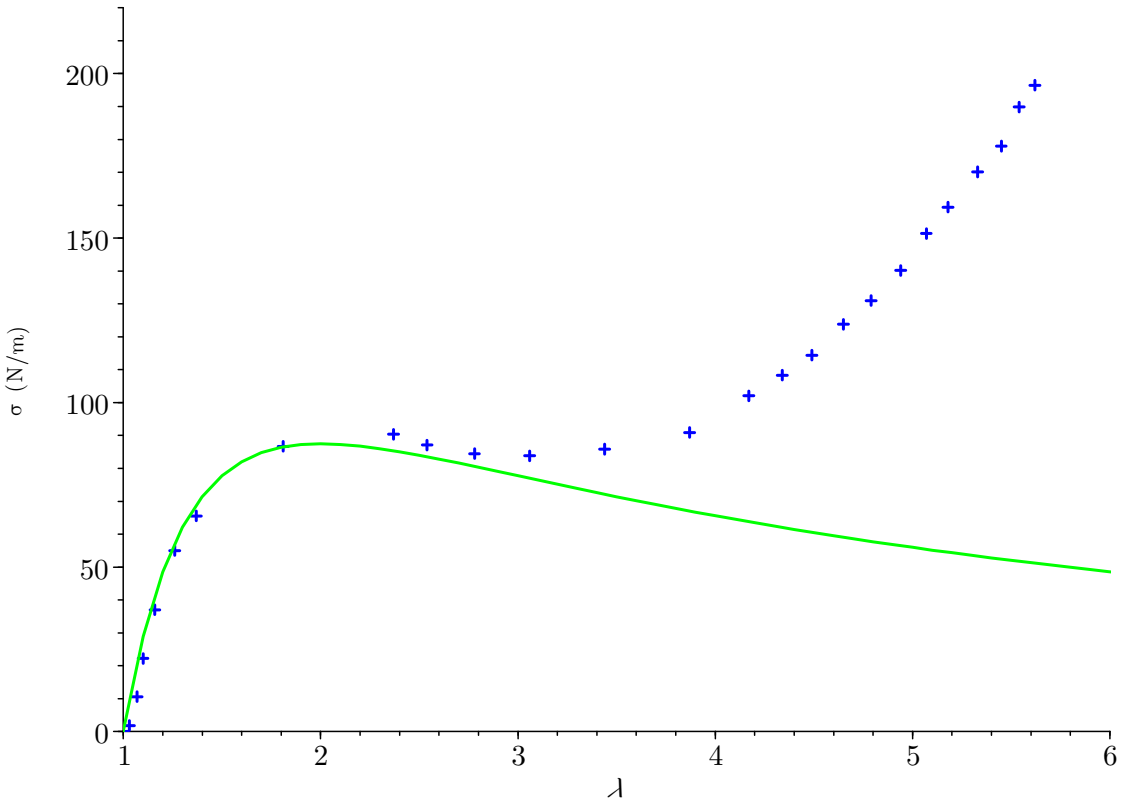

Figure 2.20: Experimental results (blue crosses) for the first filling of a 130mm balloon plotted against the best-fit prediction of linear theory (green line).

The fit of this equation with our experimental results is shown in figure 2.20. There is good agreement for $\lambda < 2$, with the Young's modulus found to be $E = G/2 = 0.8 \times 10^6$Pa, with corresponding shear modulus $\mu = E/3 = 267,000$Pa. However, at higher extensions the theory is far from accurate, quantitatively and qualitatively; it predicts the tension decreases like $1/\lambda$ to zero, while the experimental results show the tension continuing to increase. This suggests the linear theory fails to take into account some significant phenomena.

Non-linear hyperelasticity theory

As the linear theory is inadequate to model the balloons beyond small strains, we must consider more complex, non-linear models. A number of models detailing the stress-strain response of an elastic material at high-strains have been developed based on the continuum theory for finite deformations, as outlined in Ogden [1984]. Here, we consider only the models most commonly used for rubber, those of the form proposed by Ogden [1972].

For non-linear deformations, a distinction must be made between the reference and deformed configurations. By convention, such deformations are described using Lagrangian coordinates $\mathbf{X} =$

(X, Y, Z), where a point $\mathbf{X}$ in the unstressed reference configuration is moved to the position $\mathbf{x} = \mathbf{X} + \mathbf{a}(\mathbf{X})$ in the deformed configuration. The vector $\mathbf{u}(\mathbf{X}) = (a(\mathbf{X}), b(\mathbf{X}), c(\mathbf{X}))$ is referred to as the displacement of the point $\mathbf{X}$. The displacement gradient of a deformation, given by the tensor F, is defined to be

$$F_{ij} := \frac{\partial x_i}{\partial X_j}. \tag{2.19}$$

The strain tensor is then defined as

$$E = \frac{1}{2}\left(F^T F - I\right).$$

The value

$$J = \det(F)$$

gives the local change in volume of the deformation, and is the Jacobian of the transformation from the deformed coordinates to the reference coordinates. For an incompressible material such as rubber, $J = 1$ everywhere.

The left and right stretch tensors U and V, and the left and right Cauchy-Green strain tensors B and C, are defined by

$$B = V^2 = F^T F, \tag{2.20}$$

$$C = U^2 = F F^T. \tag{2.21}$$

The (strictly positive) eigenvalues of U (or V) are denoted λ_1, λ_2, and λ_3 and are known as the principal stretches of the deformation. For a purely biaxial deformation, the stretch in direction i, λ_i, is related to the initial length L_i and deformed length l_i by $\lambda_i = l_i/L_i$. For the spherical deformation described in section 2.5, the principal stretches are $\lambda_\phi = \lambda_\theta = \lambda$, and the change in thickness λ_r. For an incompressible deformation, $\lambda_1\lambda_2\lambda_3 = 1$, so that $\lambda_r = (\lambda_\phi\lambda_\theta)^{-1} = \lambda^{-2}$.

The stress on the material in the reference configuration is given by the first Piola-Kirchoff stress tensor, τ_R. The stress in the deformed configuration is called the Cauchy stress, and is denoted τ. The two are related by

$$\tau_R = JF^{-1}\tau. \tag{2.22}$$

Note that τ is symmetric, but τ_R is not necessarily. These tensors must be found by posing a constitutive relation for the material.

Two further definitions are required to complete the picture of non-linear elasticity theory. A material is called elastic if $\tau_R = \tau_R(x, F)$, and hyperelastic if there exists a function $W(x, F) \in \mathbb{R}$ such that the derivative of W with respect to the strain gives the stress, namely

$$[\tau_R(x, F)]_{ij} = \frac{\partial W(x, F)}{\partial F_{ij}}. \tag{2.23}$$

Here, W also represents the elastic energy stored in a deformed body, so is known as the stored-energy or strain-energy density function. The total elastic energy within a body is given by

$$\int_V W dV = \int_v W J^{-1} dv. \tag{2.24}$$

This formulation of non-linear elasticity, with the scalar potential function W, is known as Green elasticity. Though other forms of elasticity have been developed, we following Ogden [1984] in considering only Green elasticity, as it has proven most useful in modelling the behaviour of rubber.

For an isotropic material, such as the rubber used in our experiments, the strain-energy function W may be regarded as a symmetric function of the principal stretches. Only this form of W will be used in this thesis, and will be denoted

$$W(x, F) = W(\lambda_1, \lambda_2, \lambda_3).$$

For an incompressible deformation, equation (2.23) gives τ_R as

$$[\tau_R]_{ii} = \frac{\partial W}{\partial \lambda_i} - \lambda_i^{-1} P \tag{2.25}$$

for some arbitrary hydrostatic pressure function P, and so equation (2.22) gives

$$\tau_{ii} = \lambda_i \frac{\partial W}{\partial \lambda_i} - P. \tag{2.26}$$

A biaxial deformation is one for which constant stretch is applied in two principal directions (say 1 and 2), with the other direction stress-free. Mathematically, this is written

$$\tau_{33} = \lambda_3 \frac{\partial W}{\partial \lambda_3} - P = 0,$$

and thus

$$P = \lambda_3 \frac{\partial W}{\partial \lambda_3}.$$

If the stress applied in directions 1 and 2 is the same, the deformation is said to be equibiaxial; thus for an incompressible equibiaxial deformation,

$$\lambda_1 = \lambda_2 = \lambda, \quad \lambda_3 = \lambda^{-2}$$

and hence we may define $\tilde{W}$ such that

$$\tilde{W}(\lambda) = W\left(\lambda, \lambda, \lambda^{-2}\right).$$

The non-zero stresses are then

$$\begin{aligned} [\tau]_{ii} &= \lambda_i \frac{\partial W}{\partial \lambda_i} - P \\ &= \lambda_i \frac{\partial W}{\partial \lambda_i} - \lambda_3 \frac{\partial W}{\partial \lambda_3} \\ &= \lambda \frac{\partial W}{\partial \lambda_i} - \lambda^{-2} \frac{\partial W}{\partial \lambda_3}. \end{aligned}$$

As W is symmetric in in the principal stretches, so

$$\frac{\partial W}{\partial \lambda_1} = \frac{\partial W}{\partial \lambda_2},$$

giving

$$\begin{aligned}[\tau]_{11} = [\tau]_{22} &= \frac{1}{2}\lambda\left[\frac{\partial W}{\partial \lambda_1} + \frac{\partial W}{\partial \lambda_2} - 2\lambda^{-3}\frac{\partial W}{\partial \lambda_3}\right] \\ &= \frac{1}{2}\lambda\left[\frac{\partial \lambda_1}{\partial \lambda}\frac{\partial W}{\partial \lambda_1} + \frac{\partial \lambda_2}{\partial \lambda}\frac{\partial W}{\partial \lambda_2} + \frac{\partial \lambda_3}{\partial \lambda}\frac{\partial W}{\partial \lambda_3}\right] \\ &= \frac{1}{2}\lambda\frac{d\tilde{W}}{d\lambda}. \end{aligned} \tag{2.27}$$

Combination of equations (2.18) and (2.27) then gives the overpressure as

$$[p] = \frac{h_0}{r_0}\lambda^{-2}\frac{d\tilde{W}}{d\lambda}. \tag{2.28}$$

Using this relation along with equation (2.4) gives the tension in the balloon as

$$\sigma = \frac{1}{2}h_0\lambda^{-1}\frac{dW}{d\lambda}. \tag{2.29}$$

These formulae are valid for any hyperelastic model of a thin, incompressible, spherical membrane of rubber.

All that is left is to pose a constitutive relation for W. A full description of the models available is given by Ogden [1984]. Different non-linear models have different ranges of validity with, generally speaking, accuracy at higher strains coming at the cost of introducing more experimentally-determined parameters.

The most often studied and used models are all examples of an Ogden's model. Such a model is defined by its strain energy density function W for an incompressible material taking the form

$$W(\lambda_1, \lambda_2, \lambda_3) = \sum_{k=1}^{N} \frac{\mu_k}{\alpha_k}\left(\lambda_1^{\alpha_k} + \lambda_2^{\alpha_k} + \lambda_1^{-\alpha_k}\lambda_2^{-\alpha_k} - 3\right), \tag{2.30}$$

for any material constants N, $\mu_k \in \mathbb{N}$, $\alpha_k \in \mathbb{R}$. To ensure consistency with linear elasticity, the shear modulus μ is given by

$$\mu = \frac{1}{2}\sum_{k=1}^{N}\mu_k\alpha_k. \tag{2.31}$$

Two particular choices of N and α_k lead to two well-known and long-studied models for non-linear incompressible elasticity in rubber: the neo-Hookean model, and the Mooney-Rivlin model.

The neo-Hookean model is an Ogden's model with $N = 1$, $\alpha_1 = 2$. Unlike the other models described here, it can actually be derived from physical principles; its validity, according to Ogden [1984], is based on the statistical thermodynamics of cross-linked polymer chains, as are found in rubber. The strain energy density function is

$$W = \frac{\mu}{2}\left(\lambda_1^2 + \lambda_2^2 + \lambda_3^2 - 3\right), \tag{2.32}$$

with the tension in a spherical membrane given by

$$T = h_0\mu\left(1-\lambda^{-6}\right). \tag{2.33}$$

Treloar [2005] found μ to be 390,000Pa for natural rubber. Notably, the model predicts that as $\lambda \to \infty$, the tension will tend to the upper limit $h_0\mu$. Though this model has some applicability in the non-linear regime, it is still only accurate for rubber in biaxial tension for $\lambda < 4$, far less than that for an inflated rubber balloon.

The Mooney-Rivlin model has been proposed by Mooney [1940] and Rivlin and Saunders [1951] as a better model for the non-linear behaviour of rubber. This has material constants $N = 2$, $\alpha_1 = 2$, $\alpha_2 = -2$, and is based entirely on empirical evidence. The strain energy density function is

$$W = \frac{\mu_1}{2}\left(\lambda_1^2+\lambda_2^2+\lambda_3^2-3\right) + \frac{\mu_2}{-2}\left(\lambda_1^{-2}+\lambda_2^{-2}+\lambda_3^{-2}-3\right), \tag{2.34}$$

with the tension in a spherical membrane given by

$$\sigma = h_0\left[\mu_1\left(1-\lambda^{-6}\right)-\mu_2\left(\lambda^2-\lambda^{-4}\right)\right]. \tag{2.35}$$

Typical values for the remaining free parameters in natural rubber are $\mu_1 = 300,000$Pa, $\mu_2 = -30,000$Pa as in Muller and Strehlow [2004]. The introduction of this extra experimental parameter does increase its range of validity, though it is still only accurate for rubber in biaxial tension when $\lambda < 5$. Unfortunately, a fully inflated rubber balloon experiences strains in the region of $\lambda \approx 7$, so a further model is required.

One model that is known to be accurate in predicting the stress-strain response in rubber up to strains of 600% may be found by considering an Ogden's model with $N = 3$, and thus introducing a further experimentally determined parameter. This model was first proposed by Ogden [1972] to fit data found by Treloar [1944], with $\alpha_1 = 1.3$, $\alpha_2 = 5$, and $\alpha_3 = -2$, and thus

$$\begin{aligned} W &= \frac{\mu_1}{1.3}\left(\lambda_1^{1.3}+\lambda_2^{1.3}+\lambda_3^{1.3}-3\right) + \frac{\mu_2}{5}\left(\lambda_1^{5}+\lambda_2^{5}+\lambda_3^{5}-3\right) \\ &\quad + \frac{\mu_3}{-2}\left(\lambda_1^{-2}+\lambda_2^{-2}+\lambda_3^{-2}-3\right) \end{aligned} \tag{2.36}$$

with the tension in a balloon given by

$$T = h_0\left[\mu_1\left(\lambda^{-0.7}-\lambda^{-4.6}\right)+\mu_2\left(\lambda^3-\lambda^{-12}\right)+\mu_3\left(\lambda^{-4}-\lambda^2\right)\right]. \tag{2.37}$$

The suggested values of the remaining material constants were $\mu_1 = 617,400$Pa, $\mu_2 = 1,176$Pa, $\mu_3 = -9,800$Pa. Later, the same form of model was found by Jones and Treloar [1975] to fit their data, only now with $\alpha_2 = 4$, and $\mu_1 = 690,000$Pa, $\mu_2 = 10,000$Pa, $\mu_3 = -12200$Pa. This form of model may accurately predict the stress-strain response of rubber for $\lambda > 5$, the region of interest in the inflation of our balloons. Unfortunately, despite its accuracy, its complicated form and empirical derivation mean that it reveals little deeper insight into how and why rubber behaves as it does.

2.13.2 Comparison between theory and experiment

Experimental data for a typical 130mm balloon that has not been pre-inflated is plotted in figure 2.21(a), along with the best-fit for the three hyperelastic theories described previously.

The parameters for these models were determined by finding the least-squares fit to the greatest range of the data for which the model could be regarded as accurate. The reference thickness h_0 was taken to be the average post-stretch thickness 0.22mm determined in section 2.3.

All three models show good agreement for small stretches, $\lambda < 4$. For the neo-Hookean model, $N = 1$, $\alpha_1 = 2$, with the statistically-determined parameter

$$\mu_1 = 307,800\,\text{Pa}. \tag{2.38}$$

This was accurate only for $\lambda < 4$, as while it captures the initial levelling out of the stretch-tension relationship, it fails to predict the subsequent increase in gradient. This is because the derivation of the model did not account for the finite length of the individual molecules.

For the Mooney-Rivlin models, $N = 2$, $\alpha_1 = 2$, $\alpha_2 = -2$, with parameters

$$\mu_1 = 268,000\,\text{Pa}, \qquad \mu_2 = -29,700\,\text{Pa}. \tag{2.39}$$

This was accurate for $\lambda < 5$.

For the Ogden's model, $N = 3$ with the best fit parameters

$$\alpha_1 = 1.3, \qquad \alpha_2 = 5, \qquad \alpha_3 = -2, \tag{2.40}$$

$$\mu_1 = 536,800\,\text{Pa}, \qquad \mu_2 = 3,700\,\text{Pa}, \qquad \mu_3 = -1,000\,\text{Pa}. \tag{2.41}$$

This was accurate for all our data, up to $\lambda = 7$. Note that, unlike the other two models, a local minimum in the tension is predicted for $\lambda = 2.5$. This is just an artifact of finding the parameters that provide the best fit to the data; in reality, stress should always increase with strain, and thus the stretch-tension relation should be monotone increasing.

These experimentally determined parameters are consistent with those previously published, if allowing for discrepancies introduced by differences in the exact type of rubber used, and experimental error.

Section 2.8 revealed that filling then unfilling a balloon changes the stress-strain behaviour within the rubber significantly. Fits of the three models discussed above with the stress-strain behaviour of a balloon pre-filled (either once or twice) are displayed in figure 2.21(b). Unlike for the initial inflation, we could find no published data to compare our values to. Compared to first inflations, the behaviour is qualitatively similar, though the local minimum seen for $\lambda \approx 4$ on first inflation is not present in the data for subsequent inflations. Quantitatively, the data is significantly different at lower stretches, though similar at higher stretches. Note that $\lambda = 1$, the stress-free state, is different to before - $r_0 = 21$mm here, compared to $r_0 = 10$mm for the first case - so that the maximum extension is given as $\lambda = 2.67$, despite representing the same actual balloon radius.

The parameters for the neo-Hookean model were found to be

$$\mu_1 = 394,600\,\text{Pa}, \tag{2.42}$$

and thus only a small increase on the value for the first inflation.

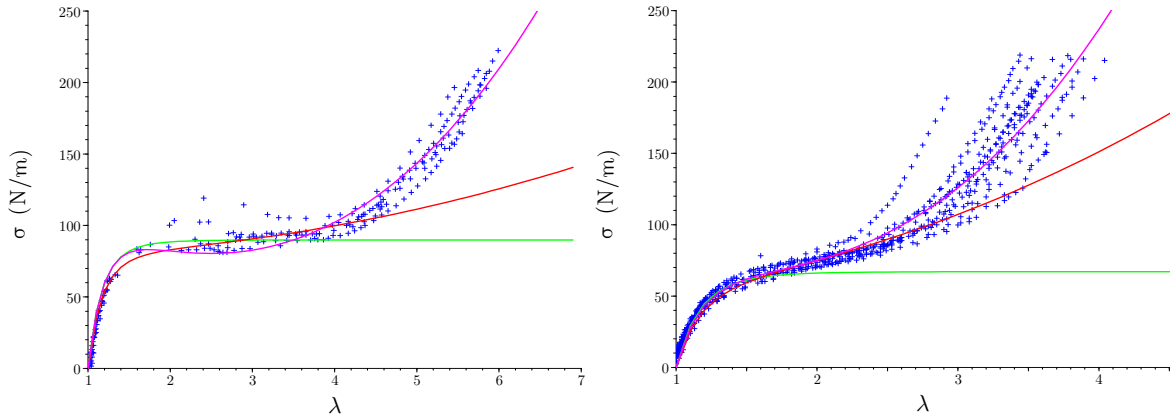

(a) First filling

(b) Subsequent fillings

Figure 2.21: The tension-radius response of a quasi-statically filled 130mm balloon. Experimental data (blue marks) is plotted against the best-fit neo-Hookean (green), Mooney-Rivlin (red) and three-parameter Ogden (magenta) models.

For the Mooney-Rivlin model on subsequent inflations,

$$\mu_1 = 237,500\,\text{Pa}, \qquad \mu_2 = -74,400\,\text{Pa}. \tag{2.43}$$

While the value for μ_1 represents only a small decrease from the first inflation, but the value for μ_2 represents a significant decrease, with $|\mu_2|$ more than doubling.

For the Ogden's model, the data for subsequent inflations implies

$$\alpha_1 = 1.3, \qquad \alpha_2 = 5, \qquad \alpha_3 = -2, \tag{2.44}$$

$$\mu_1 = 491,300\,\text{Pa}, \qquad \mu_2 = 105,000\,\text{Pa}, \qquad \mu_3 = 146,300\,\text{Pa}. \tag{2.45}$$

As for the other models, μ_1 experiences only a relatively small change. However, there is a significant increase in both $|\mu_2|$ and $|\mu_3|$, with μ_3 also changing in sign.

It is clear that the Ogden's model is the most accurate, though that is perhaps to be expected given that it has the most free parameters. The neo-Hookean model is good enough for the early stages of extension ($\lambda < 2$), but plateaus at late-times, never exceeding the value $h_0\mu$. The Mooney-Rivlin model is accurate for twice the range ($\lambda < 3$), and predicts unbounded growth in the tension with radius. However, it is unable to attain accuracy at high-strains while maintaining accuracy at low strains with a single set of parameters. However, the significant scatter seen in the data for $\lambda > 2.5$ means that even the Ogden's model must be regarded as approximate. This scatter likely originates from the sensitivity of the behaviour to the maximum stretch it has previously been inflated to, as revealed in section 2.8. Though attempts were made to ensure this was approximately the same for every balloon, around $\lambda = 6$, it was impossible to ensure perfect accuracy as the stretch could only be determined once the experiment had been completed. Consequently, the maximum previous stretch was somewhere between 5 and 6 for most balloons. The data from a single experiment significantly above the rest in figure 2.21(b) was likely from a balloon with maximum previous stretch significantly less, around $\lambda = 4$.

2.13.3 Quasi-static deflation

It is worth briefly considering the stress-strain behaviour of the 130mm balloon when quasi-statically unfilled, as it is arguably more relevant to the retraction of the membrane following bursting. As stated in chapter 1, there is known to be significant hysteresis in the stress-strain relationship, so that it differs from that for inflation. Unfortunately, there is little evidence in the literature of a concerted attempt to model this behaviour. Our own attempts to fit the Ogden's model for inflation to the stretch-tension relationship were far from successful, as shown in figure 2.22; the fitted curve is qualitatively different from the experimentally-observed behaviour. While one could, no doubt, propose an analytical stress-strain relation that would provide a good fit, this was not attempted; as chapter 1 revealed, the dynamic retraction behaviour of rubber differs significantly from the quasi-static behaviour, so whatever the quasi-static relationship, it is likely to be irrelevant to the (fast) rupture and retraction of a water balloon.

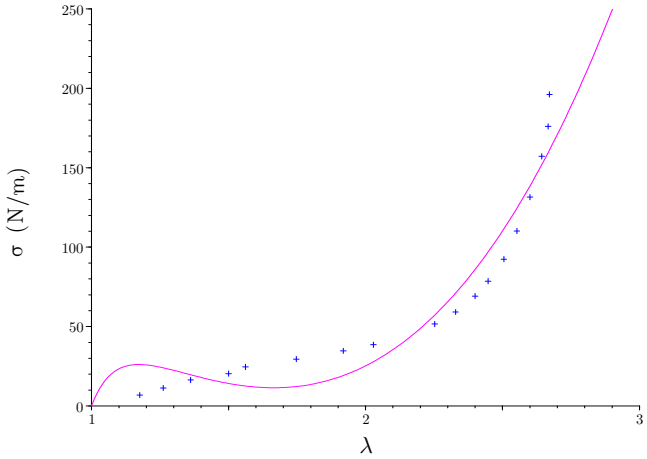

Figure 2.22: The quasi-static unfilling stress-strain behaviour of a 130mm balloon. The magenta line represents the best-fit Ogden's model.

2.14 Quasi-static inflation of cylindrical balloons

In this section, a similar investigation to that for 130 mm spherical balloons is conducted into the quasi-static stress-strain behaviour of cylindrical balloons. There is no evidence in the literature of any such experimental studies on cylindrical balloons having been performed before.

2.14.1 Non-linear hyperelasticity theory

The high-strains present in these experiments meant that, once again, linear theory is invalid. Instead, the non-linear theory outlined in section 2.13.1 may be used to model the quasi-static inflation of cylindrical balloons, though the situation here is slightly more complicated: the balloons will still be in a state of biaxial stress, but the stresses (and corresponding strains) will not be equal. Nevertheless,

the theory may be fully derived as before, following the derivation for cylindrical balloons given in Muller and Strehlow [2004], then matched to experimental data. This derivation assumes that the balloons are much longer than they are wide, so that the influence of the ends of the balloon may be ignored (save that they stop the interior fluid escaping).

We consider a perfectly cylindrical elastic container, of reference thickness h_0, inner radius r_0 and length L_0. In the deformed configuration, the thickness is given by h, the inner radius by r and the length by L. As for a spherical membrane, the cylindrical membrane will be in a state of biaxial stress, but unlike before, the two tangential principal stretches are not necessarily the same. The axial stretch is given by

$$\lambda_z = 1 + \epsilon_z = \frac{L}{L_0}$$

and the circumferential stretch by

$$\lambda_\theta = 1 + \epsilon_\theta = \frac{2\pi r}{2\pi r_0} = \frac{r}{r_0}.$$

The Cauchy stresses are then given by

$$\tau_{zz} = \tau_z,$$

$$\tau_{\theta\theta} = \tau_\theta,$$

$$\tau_{rr} = \tau_{ij} = 0$$

for all $i \neq j$. We then consider the two free-body diagrams of figure 2.23. As before, for both situations the pressure acting over the internal cross-section must be balanced by the stress in the membrane. Thus, the force balance for the cross-section shown in figure 2.23(a) gives

$$[p]\pi r^2 = \tau_z[\pi(r+h)^2 - \pi r^2].$$

Linearising about $h/r = 0$ leads to

$$\tau_z = \frac{1}{2}\frac{r}{h}[p]. \tag{2.46}$$

The force balance for the cross-section shown in figure 2.23(b) gives

$$[p]2rL = \tau_\theta 2hL$$

and hence

$$\tau_\theta = \frac{r}{h}[p]. \tag{2.47}$$

By conservation of volume of the membrane, we expect

$$[\pi(r+h)^2 - \pi r^2]L = [\pi(r_0+h_0)^2 - \pi r_0^2]L_0$$

which after linearising gives

$$h_0 r_0 L_0 = hrL,$$

or equivalently

$$h = h_0 \lambda_\theta^{-1} \lambda_z^{-1}. \tag{2.48}$$

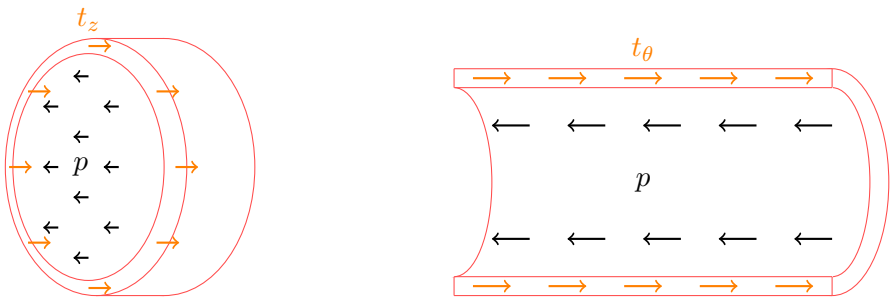

(a) (b)

Figure 2.23: Free-body diagrams of a cylindrical pressure vessel. All arrows are parallel to the normal vector to the cross-section plane.

This implies

$$[p] = \frac{h_0}{r_0}\lambda_\theta^{-1}\lambda_z^{-1}\tau_\theta \tag{2.49}$$

and thus that the pressure jump scales inversely with the initial radius r_0. Consequently, for the same thickness, those cylindrical balloons with the largest initial radius should be the easiest to inflate - as was indeed found to be the case with our 160, 321, and 646 balloons. As a consequence of this, all quasi-static inflation/deflation tests had to be conducted on 646 balloons. We were using the experimental set-up described in section 2.6, so the balloons were inflated by the pressure from the water in the tube held above the water's surface, but tube was not long enough to hold a great enough height of water to provide enough pressure to inflate the 160 and 321 balloons beyond $\lambda = 1.5$.

It is clear from equations (2.47) and (2.46) that

$$\tau_\theta = 2\tau_z, \tag{2.50}$$

an equation known as the boiler formula.

For each theoretical model, the predicted individual stresses may be found as before from the proposed strain energy function $W(\lambda_z, \lambda_\theta)$ by

$$\tau_z = \lambda_z \frac{\partial W}{\partial \lambda_z},$$

$$\tau_\theta = \lambda_\theta \frac{\partial W}{\partial \lambda_\theta}.$$

It is then straightforward to write $[p]$ as a function of λ_z and λ_θ. However, equation (2.50) together with these relations may be solved for λ_z as a function of λ_θ. Using this new relation, we may in fact get a prediction for $[p]$ as a function of λ_z or λ_θ alone.

For the neo-Hookean model,

$$W(\lambda_z, \lambda_\theta) = \frac{\mu}{2}\left(\lambda_z^2 + \lambda_\theta^2 + (\lambda_z\lambda_\theta)^{-2} - 3\right).$$

Equation (2.50) then gives

$$\lambda_z = \frac{1}{2}\sqrt{\lambda_\theta^2 - \sqrt{\lambda_\theta^4 + 8\lambda_\theta^{-2}}}, \tag{2.51}$$

so as $\lambda_\theta \to \infty$,

$$\lambda_z \to 2^{-1/2}\lambda_\theta.$$

Equation (2.51) may then be used to find that the pressure jump is given by

$$[p] = 2\frac{h}{r}\tau_z = 2\mu\frac{h_0}{r_0}\lambda_z(\lambda_\theta)^{-1}\lambda_\theta^{-2}(\lambda_\theta^2 - \lambda_\theta^{-2}\lambda_z(\lambda_\theta)^{-2}). \tag{2.52}$$

Equations (2.51) and (2.52) are plotted as the green curves in figure 2.24.

For the Mooney-Rivlin model,

$$W(\lambda_z, \lambda_\theta) = \frac{\mu_1}{2}\left(\lambda_z^2 + \lambda_\theta^2 + (\lambda_z\lambda_\theta)^{-2} - 3\right) + \frac{\mu_2}{-2}\left(\lambda_z^{-2} + \lambda_\theta^{-2} + (\lambda_z\lambda_\theta)^2 - 3\right).$$

Writing

$$K = -\frac{\mu_1}{\mu_2}$$

and solving for λ_z reveals

$$\lambda_z = \sqrt{\frac{1}{2}\frac{K\lambda_\theta^2 - \lambda_\theta^{-2}}{2K + \lambda_\theta^2} + \sqrt{\left(\frac{1}{2}\frac{K\lambda_\theta^2 - \lambda_\theta^{-2}}{2K + \lambda_\theta^2}\right)^2 + \frac{K\lambda_\theta^{-2} + 2}{2K + \lambda_\theta^2}}}. \tag{2.53}$$

Notably, this predicts that λ_z is bounded above by $\sqrt{K}$, to which it tends as $\lambda_\theta \to \infty$. For the parameters found earlier, this equates to

$$\lambda_z^{max} = 3.00$$

for the first inflation, and

$$\lambda_z^{max} = 1.79$$

for subsequent inflations. This means that for large inflations, the length of the balloon remains constant, with only the radius of the balloon increasing in response to increased internal pressures.

The pressure jump is then given by

$$[p] = 2(-\mu_2)\frac{h_0}{r_0}\lambda_z(\lambda_\theta)^{-1}\lambda_\theta^{-2}\left[\lambda_z(\lambda_\theta)^2 - \lambda_z(\lambda_\theta)^{-2}\lambda_\theta^{-2}\right]\left[K + \lambda_\theta^2\right]. \tag{2.54}$$

Equations (2.53) and (2.54) are plotted in figure 2.24 in red.

For Ogden's model,

$$\begin{aligned} W(\lambda_z, \lambda_\theta) \;=\; & \frac{\mu_1}{1.3}\left(\lambda_z^{1.3} + \lambda_\theta^{1.3} + (\lambda_z\lambda_\theta)^{-1.3} - 3\right) \\ & + \frac{\mu_2}{5}\left(\lambda_z^5 + \lambda_\theta^5 + (\lambda_z\lambda_\theta)^{-5} - 3\right) \\ & + \frac{\mu_3}{-2}\left(\lambda_z^{-2} + \lambda_\theta^{-2} + (\lambda_z\lambda_\theta)^2 - 3\right). \end{aligned}$$

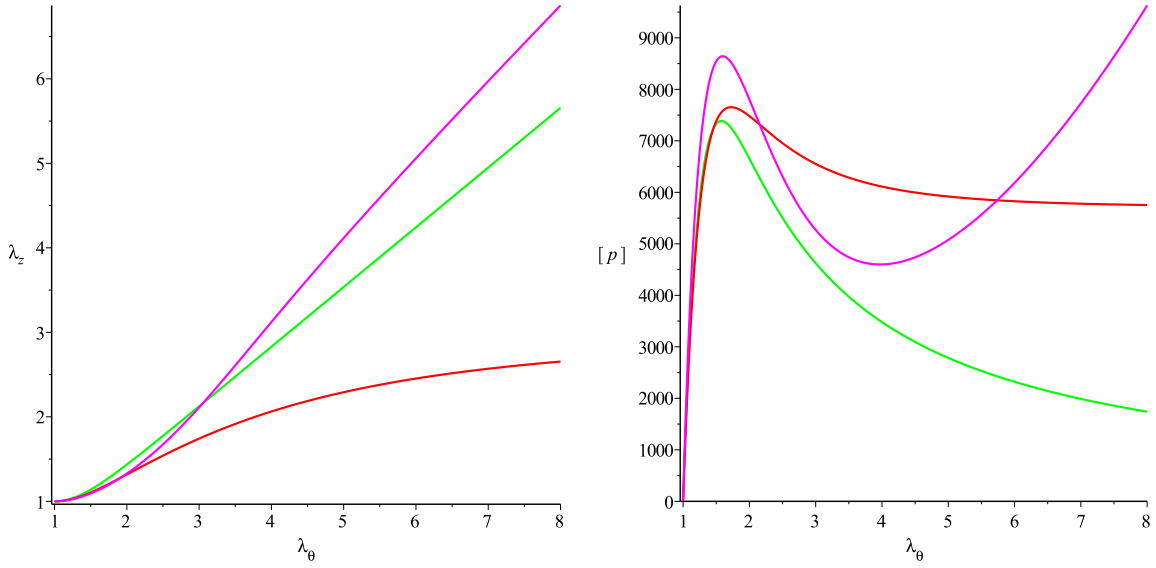

(a) λ_z v λ_θ (b) $[p]$ v λ_θ

Figure 2.24: The theoretical predictions of the neo-Hookean (green), Mooney-Rivlin (red) and Ogden's model (magenta) using the parameters determined in the previous section. For the neo-Hookean and Ogden's models, both stretches increase as the volume of the balloon increases; for the Mooney-Rivlin model, however, the length of the balloon is limited above. All three models, however, show similar pressure-radius behaviour at low stretches, initially increasing before decreasing. After this, however, they diverge: the pressure in a neo-Hookean balloon continues to decrease for increasing stretch, in a Mooney-Rivlin balloon tends to a constant value for all high stretches, and in an Ogden's balloon increases again with stretch.

Equation (2.50) must then be solved numerically. In the limit $\lambda_\theta \to \infty$,

$$\lambda_z \to 2^{-1/5}\lambda_\theta,$$

so that both the length and radius of the balloon continue to increase for large volumes. The pressure jump may also be determined numerically using equations (2.49) and (2.50). The behaviour of the Ogden's model is shown in figure 2.25 by the magenta lines.

The pressure-radius behaviour predicted by each of the models is distinct. The neo-Hookean model predicts the pressure reaches a maximum near $\lambda_\theta = 1.5$ before tending to 0 as $\lambda_\theta \to \infty$, written here as

$$[p]_\infty = 0.$$

This could, potentially, lead to an instability, particularly with an ideal gas within the balloon: if the pressure decrease due to an increase in volume of the balloon is greater the pressure drop due to the expanding gas, runaway expansion will occur. However, it was not possible to test this idea, as the neo-Hookean model was no longer valid for our rubber in the high-stretch region where such behaviour may have occurred.

The Mooney-Rivlin also predicts the pressure reaches a maximum near $\lambda_\theta = 1.5$, but then tends to a constant value as $\lambda_\theta \to \infty$. This constant value is

$$[p]_\infty = 2(-\mu_2)\frac{h_0}{r_0}\sqrt{K}.$$

Using the previously determined values of these parameters, this is predicted to be

$$[p]_\infty = 3900\,\text{Pa}$$

for the first inflation, and

$$[p]_\infty = 2100\,\text{Pa}$$

for subsequent inflations. Physically, these two two values for $[p]_\infty$ should be the same. That they are not further reinforces the idea that the Mooney-Rivlin model should not be regarded as physically relevant for high stretches.

The Ogden's model predicts that near $\lambda_\theta = 1.5$, the pressure jump flattens off, and may even decrease depending on the exact values of the parameters. This would lead to a local minimum, and consequently allow the existence of equilibrium states where λ_θ may hold two different values on the same balloon with a constant internal pressure. Such states were indeed observed and discussed in section 2.12.1, and are known as aneurysms. As $\lambda_\theta \to \infty$, the pressure jump tends to infinity, so

$$[p]_\infty = \infty.$$

Due to the previously determined accuracy of the Ogden's model over the others for a 130mm balloon, and to avoid cluttering up the graphs, in the next section only the predictions of the Ogden's model will be shown with the experimental data. However, when the models were compared, the Ogden's model indeed proved to be the most accurate again.

2.14.2 Quasi-static experiments

Our cylindrical quasi-static inflation experiments were conducted solely on 646 balloons, as their large initial radius made them far easier to inflate (as discussed in the previous section). In figure 2.25, the experimental measurements for such a balloon on its first and second inflations are recorded, together with the theoretical predictions of the Ogden's model using the parameters determined for 130mm balloons. The initial thickness was taken to uniformly 0.32mm, as determined for 646 balloons in section 2.3. The axial stretch was determined by measuring the change of separation between lines drawn on the balloon pre-inflation; the circumferential stretch was found by measuring the radius.

For the first inflation, both the λ_z v λ_θ and $[p]$ v λ_θ relationships are in good agreement with the Ogden model up to $\lambda_\theta = 5$. Beyond this value, the λ_z v λ_θ relationship in particular shows a significant qualitative difference with the theory. This lack of accuracy is possibly a consequence of the fact that the radius increases more than the axial stretch, meaning that at high extensions, the curved ends become significant, despite being ignored in the theoretical model. Consequently, the assumption that the balloon is an infinite cylinder may no longer be accurate. For this first inflation, there should be no anisotropy in stress-strain behaviour, as the material has undergone no previous extension.

For the second inflation of the balloon, figure 2.25(b) shows that the Ogden's model is far from accurate, both quantitatively and qualitatively. While the reason for this is unknown, it is possibly a consequence of the rubber losing isotropy during its first inflation. Although the stress-strain behaviour of rubber does become consistent after multiple stretches and unstretches, it also depends on its maximum previous stretch, as explained in section 2.8. As figure 2.25 shows, a fully-inflated 646 balloon reaches a maximum radial stretch of 6, but a maximum axial stretch of only 4.5. Thus, it is likely that during subsequent inflations, the key assumption that the rubber is isotropic is no longer valid; the theory based on that assumption is therefore likely to be inaccurate.

The pressure-volume relationship for two 646 balloons were also found, and displayed in figure 2.26. Quantitatively, the theory proved to be inaccurate much beyond $\lambda_\theta = 4$, yet the experimental relationships do show the qualitative features necessary for the aneurysm instability discussed in section 2.12.1. The pressure initially climbs with volume to a maximum, before sharply decreasing to a local minimum, then rising again. It is this decrease in pressure with increasing volume that, as explained by Kyriakides and Chang [1990] amongst others, leads to the elastic instability that forms aneurysms. That these aneurysms form near the open end of the balloons is likely a consequence of their method of manufacture, as it causes them to be thinner there.

2.15 Summary

In this chapter, the balloons used for all later experiments were examined under quasi-static conditions, to allow determination of their physical properties. First, a brief review of the molecular properties of rubber was given in 2.1. The exact type of balloons used were described in section 2.2, with experimental measurements of the thickness of both 130mm and 646 balloons given in section 2.3. An estimate of the density of the rubber was found in section 2.4, though with large experimental error. The relations between internal pressure, stress and tension in a thin spherical shell were derived in section 2.5, where it was shown that, due to the thinness of the balloons, the tension in the membrane could by approximated by the well-known Laplace-Young equation. The experimental method used to find the quasi-static stress-strain behaviour of the membranes was outlined in section 2.6; using this method, it was demonstrated in section 2.7 that viscoelastic effects could be ignored over the short time-scales of our later experiments. The existence of the Mullins effect in our balloons was established in section 2.8. It was also observed, however, that the stress-strain behaviour became repeatable over subsequent fillings and unfillings. The effects of bending stiffness in the membrane were shown to be minimal in section 2.9.

We then went on the examine the shape of our balloons. Estimating the volume by assuming the balloon was a perfect sphere when underwater was shown to underestimate the true value in section 2.10 by approximately 10%, as it failed to take into account the tube-like region near the open end. Sections 2.11 and 2.12 examined how the shape of the 130mm and 646 balloons changed as they were filled with water both in air and underwater. This supported the theory that the tension in the membranes was approximately the same everywhere. Linear and non-linear theory for the relation between internal pressure and stretch of a spherical balloon was derived in section 2.13 and matched to experimental data, with the three parameter non-linear theory of Ogden shown to provide the best fit. Finally, section 2.14 repeated the analysis of the previous section for cylindrical 646 balloons, showing the non-linear theory to be a reasonable predictor of behaviour for the initial inflation. However,

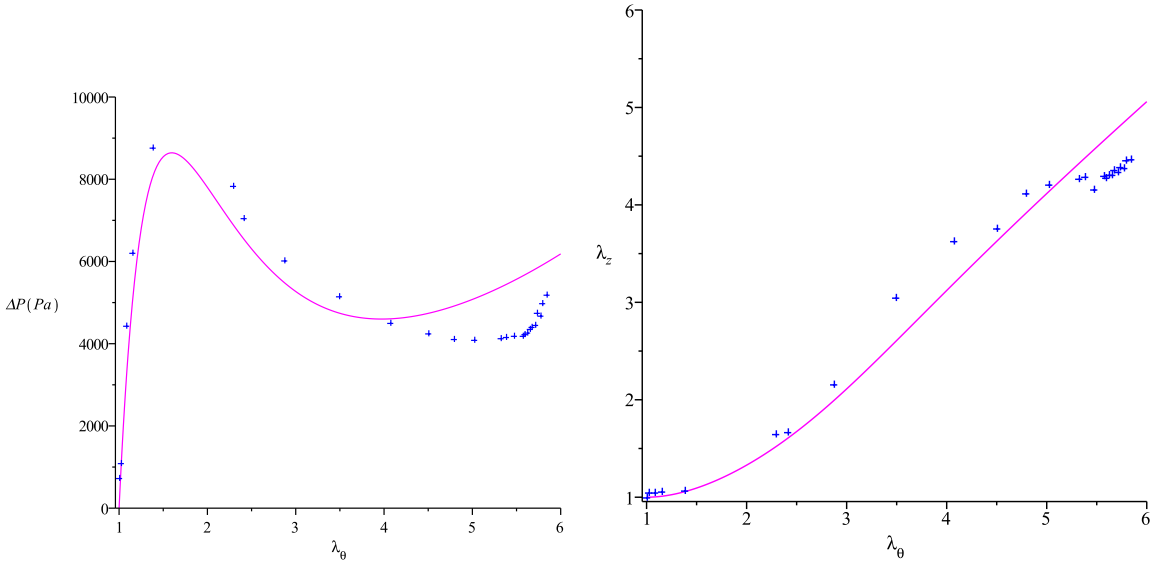

(a) First inflation

(b) First inflation

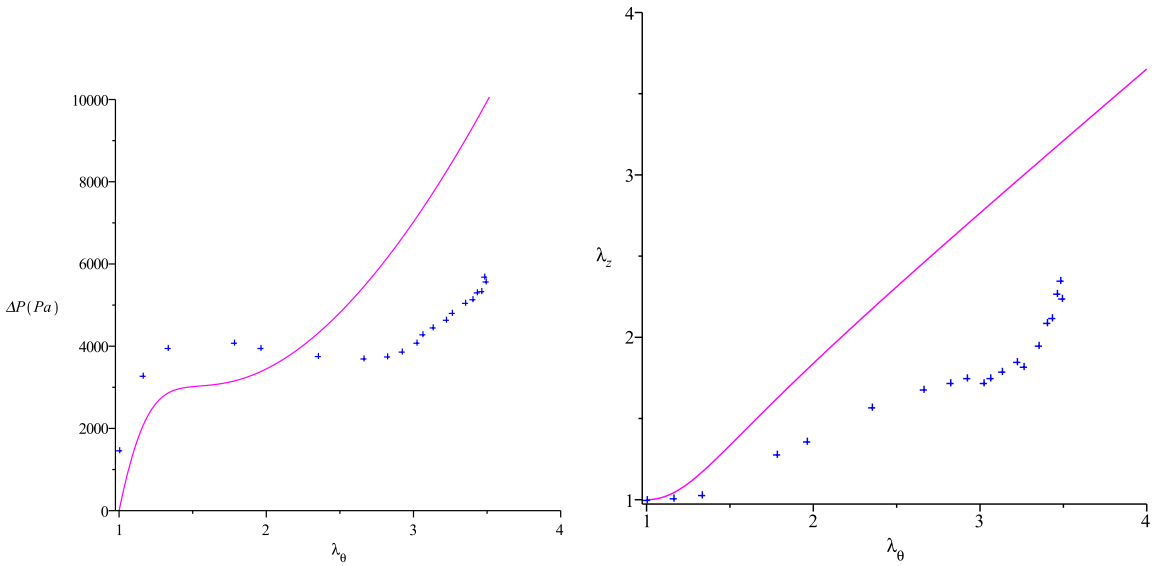

(c) Second inflation

(d) Second inflation

Figure 2.25: Experimental data for quasi-statically filled 646 balloons, on first and second inflation. The experimental data is denoted by the blue crosses, while the theory for the Ogden's model (using the physical constants found in section 2.13.1) is given by the magenta line.

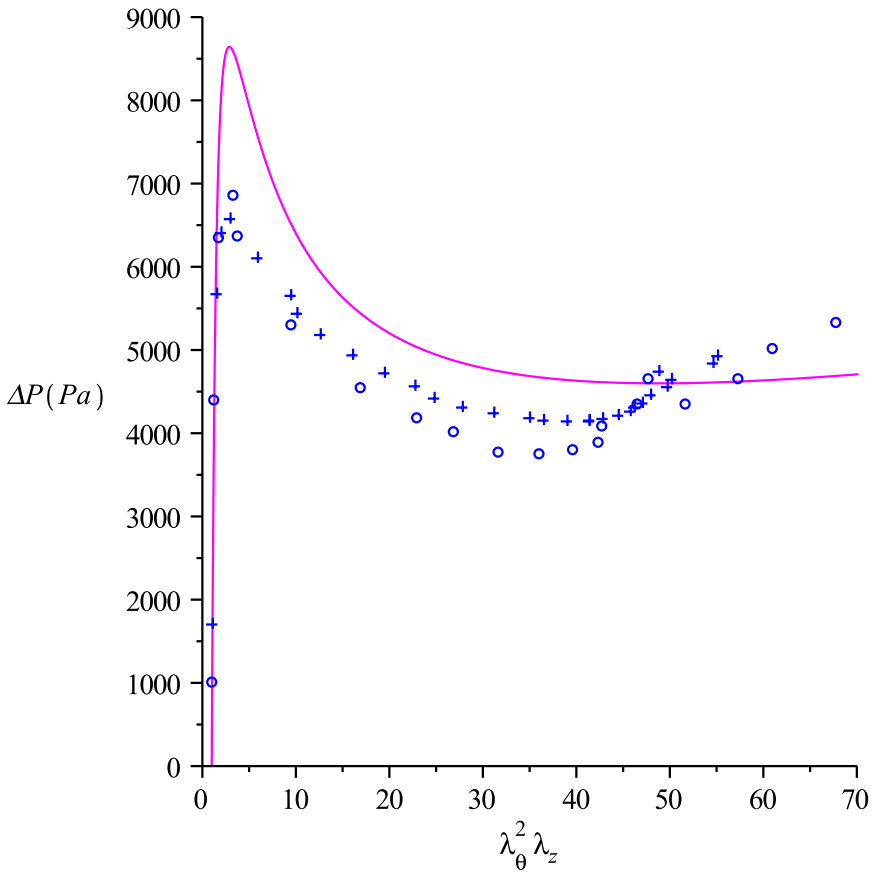

Figure 2.26: Experimental data for two quasi-statically filled 646 balloons. The experimental data is denoted by the blue crosses and circles, while the theory for the Ogden's model (using the physical constants found in section 2.13.1) is given by the magenta line. The volume V is represented here using the stretches, $V = \lambda_\theta^2 \lambda_z$.

subsequent inflations deviated significantly from this theory, likely due to a loss of isotropy in the rubber membranes.

Chapter 3

Water Balloons Dropped in Air

The motivation for this thesis came from a very basic experiment: dropping water balloons onto a rigid surface, and filming the resulting behaviour with a high-speed camera. Though it proved to be near impossible to extract quantitative data, these experiments displayed vividly the significant phenomena that may occur. In this chapter, these phenomena and the physical reasons behind them are discussed in detail.

3.1 Experimental Setup

Every experiment involving the dropping of a water balloon was conducted within the same transparent perspex tank as described in chapter 2. This consisted of a flat, rigid base to ensure the impact of all dropped balloons were similar, high sides to protect the surrounding electronic equipment from contact with water, and a small hole in one corner to allow water to drain from the tank between experiments. A range of light sources were used, though most experiments were illuminated by two 250 W halogen dichroic projection lamps arranged to project light into the tank through a diffuser attached to either the tank's base or side. The experiments were filmed using the Photron Fastcam SA1.1 High-Speed Camera shown in chapter 2; for frames-rates of 5400fps and below, the maximum resolution was 1024×1024, with frame-rates above this forcing a reduction in resolution. Most videos were recorded at 5400fps with resolution 1024×1024, though the frame-rate was occasionally reduced if the intensity of the lighting was not great enough to allow the acquisition of clear images, or increased to observe the balloon's retraction closely. The images captured by the camera were stored on the its internal memory when activated using a post-event trigger, before the section of video of interest would then be saved to the hard-disk of laboratory computer. This meant the amount of data (and hence number of frames) was limited by the camera's internal memory, which for our purposes was effectively 5.3GB. This corresponded to just over a two second's worth of images when recording at 5400fps at 1024×1024.

As for the latex balloons, both the 300 mm and 130 mm diameter balloons were used. As revealed in chapter 2, they both assumed a pear-like shape when fully inflated with air; more spherical 430 mm balloons were also tested but rarely used, as their greater maximum volume made them very difficult to manoeuvre when filled full enough with water to rupture on impact.

Calibration of distances in the camera's current set-up would be performed before the dropping of

a balloon, a process that was almost always necessary as it proved far easier to move and adjust the camera than many other items of equipment in use (including the balloons themselves). The balloons would then be filled with water from a tap to near their maximum volume, before being dropped by hand from a height of approximately 1 m onto the floor of the tank. The camera was triggered by hand soon after impact, ideally within a second so that the full dynamics of the burst were saved to the camera's internal memory.

3.2 Pre-rupture evolution

Between release by hand and rupture upon impact, the behaviour of the balloon followed a fairly repeatable path. The initial gravitational potential energy was converted into kinetic energy as it accelerated towards the tank floor. Upon impact, the balloon deformed, flattening and spreading over the tank floor as waves on the membrane traveled from the point of impact to the top; at the same time, kinetic energy was converted into elastic energy in the membrane. In fact, if the balloon did not rupture, it would eventually reach its maximum extension (and hence have maximum elastic energy) before high pressures near the outer edge accelerated the fluid there inwards, causing the balloon to retract and lift off the surface once more, as the elastic energy was converted back into kinetic energy. This whole process is depicted in figure 3.1.

Of course, the simple description given above hides a variety of physical phenomena, both significant and insignificant. Before release, the balloon was supported by hand, necessarily deforming it from its gravity-free equilibrium shape; to release the balloon those hands were removed as quickly and smoothly as possible, after which the balloon entered free-fall. One consequence of this release mechanism was the creation of waves on the balloon's surface moments after release, as the tension in membrane sought to restore the balloon to its equilibrium shape. However, as the balloons were dropped from a large height (one metre or more) to encourage rupture on impact, the relatively long time the balloons were in free fall meant that these waves had decayed away by the moment of impact, to the point of imperceptibility. Consequently, they had no effect on the subsequent evolution of the balloon.

Attempts were also made to ensure the balloon impacted the surface with a certain orientation. Unfortunately, our release method meant that this was not always possible, with a small amount of angular momentum often imparted to the balloons on release. This had not decayed away by impact; yet any rotations were so slow as to be insignificant compared to the speed of the other phenomena occurring. The exact orientation of the balloon on impact could, however, influence the subsequent behaviour: as explained in chapter 2, the balloons were pear-shaped when full, so that first impact near the open end led to different behaviour from first impact near the top. Though interfacial waves were created for impact at any orientation of the balloon, their shape, amplitude and path around the balloon did depend on orientation. Different wavefronts could then interact as in figure 3.2, which would not happen if the balloon were perfectly spherical and the wavefronts all traveled straight up the balloon. This, in turn, could affect the path of the crack around the membrane, as well as the late-time interfacial growth. However, these differences were only be small; the same phenomena would still occur, but in slightly altered locations. Furthermore, as (for a variety of reasons as discussed in section 3.5) no quantitative measurements were taken of water balloons dropped in air, so no concerted attempt was made to study the effect of balloon orientation on impact in detail. Later experiments to

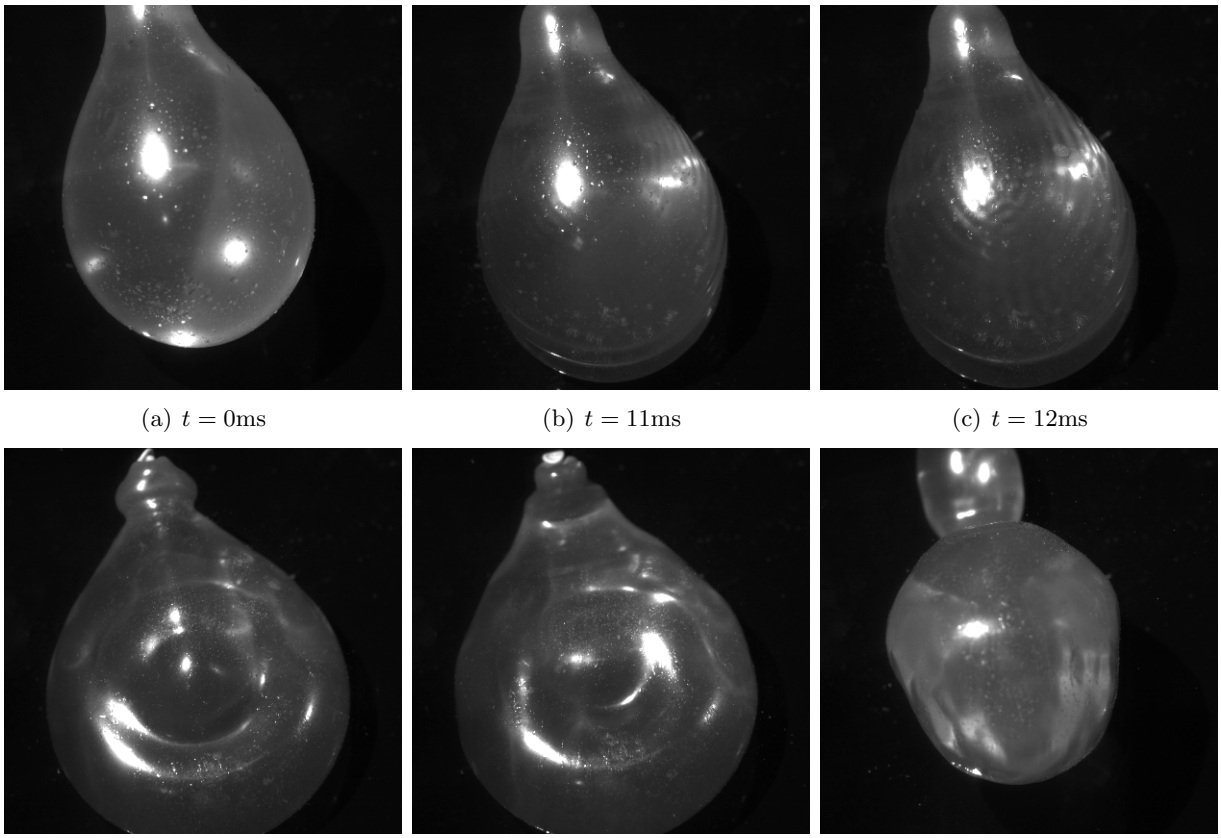

(a) $t = 0$ms (b) $t = 11$ms (c) $t = 12$ms

(d) $t = 23$ms (e) $t = 28$ms (f) $t = 71$ms

Figure 3.1: The behaviour of a 130mm balloon impacting on a flat, rigid surface. Time $t = 0$ms is approximately 500ms after the balloon was released from a height of approximately 1 m.

obtain accurate quantitative data of the interface were all performed with the balloon fixed in same orientation, which proved to be a great simplification.

Detailed modeling of the interfacial waves created upon impact was difficult, as the deformation of the balloon made the geometry complicated, and led to significant changes in the tension in membrane. However, the reason for their appearance was clear, as will be discussed in-depth in chapter 4; a brief description is given here. The restoring force for these waves was tension with the membrane, which acted to minimise the surface area of the balloon. In this way, the tension was acting very much like the surface (capillary) force of a liquid; indeed, it is shown in chapter 4 that modelling the tension as a capillary force is approximately valid. Interfacial waves of a wide range of wavenumber were created by the impact, that traveled up the balloon from the point of impact to the top. The shorter the wavelength, the faster they traveled - as is the case for true capillary waves (see Lamb [1932], page 457), where for wavelength λ, phase speed $c_p \propto \lambda^{-1/2}$.

Of course, unlike a fluid surface free from surfactants, rubber membranes do exhibit some bending stiffness (as discussed in section 2.9). However, it is revealed there that for transverse waves such as these, the bending force is $O((h/\lambda)^2)$ in comparison to that resulting from the in-plane tension. As

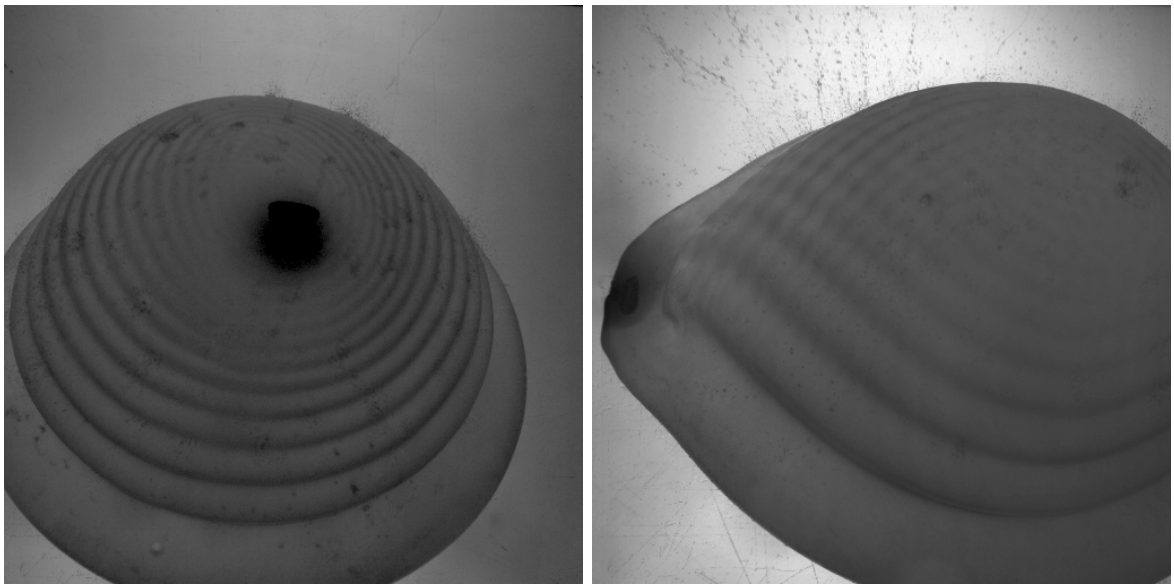

Figure 3.2: The effect of balloon shape on the interfacial waves. In image (a), the balloon is dropped on its top, so that circularly symmetric waves propagate up it. In image (b), the balloon is dropped on its side, causing the waves to interfere near the open end.

the thickness $h = 0.00016$m, bending is only significant for the waves of the smallest wavelength, those that traveled the fastest and had decayed away by the time the membrane ruptured. Consequently, the bending stiffness of the membrane had little effect on the pre-burst behaviour of the balloon.

3.2.1 Water droplet analogy

The capillary-like nature of these interfacial waves suggests a clear analogy with capillary waves on a fluid droplet. Richard and Quere [2000] studied the impact of water droplets on a hydrophobic surface, with the behaviour of the droplets closely mirroring that of the non-rupturing (and hence bouncing) water balloon shown in figure 3.1. To demonstrate this similarity clearly, the experiments of Richard and Quere [2000] were recreated by releasing water droplets from a pipette onto a thin, flat layer of Pliolite particles. Together, tihs layer of particles acted as a hydrophobic surface. Images from one such experiment are displayed in figure 3.3.

It is clear from comparison between figures 3.1 and 3.3 that the two situations are qualitatively similar. This is no coincidence; the behaviour of the droplet was determined by gravity and capillary forces, while the behaviour of the balloon was controlled by gravity and elastic tension in the membrane that, as explained previously, acted to a good approximation as a capillary force. When a droplet was released above the flat, hydrophobic surface, it initially accelerated, losing some of its initial gravitational potential energy to kinetic energy. Small fluctuations in its shape appeared when in free fall, as a consequence of the droplet's deformation during release from the pipette, and the effects of the surrounding air. Upon impact, the droplet flattened as it spread, increasing its contact area with the flat surface and converting some kinetic energy into surface energy. Simultaneously, capillary

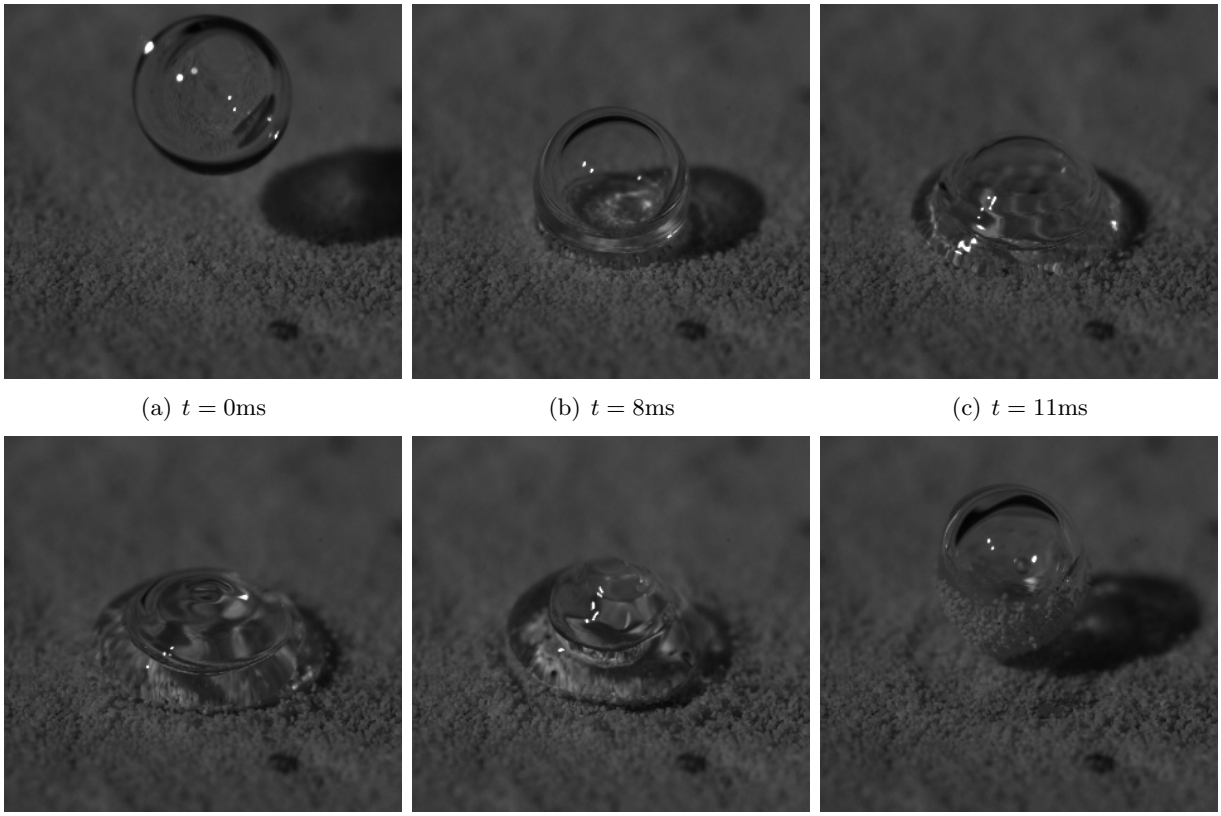

(a) $t = 0$ms (b) $t = 8$ms (c) $t = 11$ms

(d) $t = 14$ms (e) $t = 17$ms (f) $t = 31$ms

Figure 3.3: The behaviour of a water droplet impacting on a layer of Pliolite particles that together act as a hydrophobic surface. Time $t = 0$ms is approximately 100ms after the droplet was released.

waves of a wide range of wavenumber were formed on the droplet's free surface. These waves moved upwards over the surface from the initial point of contact to the droplet's highest point. They were dispersive, with waves of highest wavenumber having the greatest phase speed. Eventually, the droplet reached its maximum extension (and hence maximum surface energy) before the high pressures near the contact line associated with the high curvature there forced it to retract and lift off the surface once more, with most of the surface energy converted back into kinetic energy. This process, then, is very similar to that of a bouncing water balloon, as described at the beginning of this section.

The description given above demonstrates clearly the similarities between a bouncing water balloon and bouncing water droplet, yet it also ignores several differences between the two cases that relate to the size and distribution of their respective surface forces. For instance, for a small water droplet in the absence of significant initial deformation or external forces such as gravity, surface tension will always act to make it spherical; for a full water balloon in such a situation, chapter 1 revealed that the tension acts to make it more pear-shaped. This, in turn, will affect the shape of the wavefronts created on impact as they travel over the surface, though only near the open end of the balloon. The tension within the membrane of a water balloon is also far stronger than the surface forces of a water droplet.

As a consequence of this, while a water balloon dropped from a height of several metres is likely to remain close to its equilibrium shape for most of the fall, water droplets released from large heights are known to deform significantly and even break up into smaller droplets (see Fletcher [1962]).

The higher tension in the membranes also prevents the fingering of the contact line and splashing seen for droplets impacting at high speed, as the outer edge of the expanding balloon always remains approximately pear-shaped. This suppression of fingering will also be enhanced by the fact that the membrane tension, unlike water surface tension, increases as the surface area increases (due to the membrane stretching). During the early stages of impact, any increase in tension will be small, as the change in the balloon's surface area will be small compared to the initial increase from filling the balloon. Thus, the tension within the membrane will remain close to its initial value. At later times during the impact, however, the change in surface area becomes large, leading to big increases in the tension. This, in turn, will affect the surface waves, and the rate and extent of overall deformation of the balloon.

The presence of the membrane also affects the nature of the interaction between the balloon and the flat surface, in particular affecting the frictional force between the balloon and surface, that dissipates kinetic energy within the flow. For a spreading water droplet, a no-slip condition is imposed on the flow where it meets the surface. A boundary layer therefore will be created, in which energy is dissipated due to the friction between the water and the surface. For a spreading balloon, however, flow is possible along the surface, as the membrane may 'slip' along it. There will still be friction between the balloon and the surface, and thus energy will be dissipated, but this friction will not prevent all flow where they meet. Unfortunately, as no investigation was undertaken to quantify the magnitude of this frictional effect for bouncing balloons, it is not possible to compare its relative impact between the bouncing droplet and balloon. Furthermore, it was not possible from our experimental videos to determine whether any slip between the membrane and the flat surface occurred at all. We do expect some slip to have occurred, however, as while attempts were made to dry the equipment between experiments, the presence of moisture on both the balloon and flat surface may have made such slipping more likely to occur than for perfectly dry surfaces.

Differences also arise due to the exact nature of the surface forces. Tension in the membrane does, to a first approximation, act like a fluid capillary force. However, unlike a normal fluid/fluid interface, the membrane has elasticity. This means that, unlike fluid surface tension, the tension increases when the surface area increases. This does not greatly influence the frequency or wavelength of the waves on the membrane, as their linearity means the changes in surface area they induce are small. It does, however, significantly affect the behaviour of the fluid adjacent to the interface. Essentially, differences arise because water is not truly inviscid. Continuity of tangential velocity and stress at the interface implies the existence of a boundary layer there within both fluids (as discussed by Rood [1995]), that contains vorticity. The total vorticity summed over both sides of the membrane will always be the same, but how it is distributed within that region will not. As stated by Craik [1985], the boundary layer is of the same thickness ($O(Re^{-1/2})$ and thus small) in both cases. However, the strength of vorticity in the water at the interface is only $O(1)$ for the droplet, but $O(Re^{1/2})$ for the balloon. Consequently, the total circulation at the interface in the water is $O(Re^{-1/2})$ for the free surface of a droplet, but $O(1)$ for the membrane-covered surface of a balloon. The reason for this difference is that for a water droplet in air, the shear is directly between the fluids. Consequently, the greater density of the water means that the vorticity is far greater in the air, the water being almost free to move, as

it feels little resistance from the less dense air. For the water balloon in air, shear at the interface is dominated by tension gradients within the membrane created by changes in the surface area, being far greater than shear stresses in either fluid. Consequently, both fluids experience equal shear, so the vorticity is split equally between both fluids.

The elasticity in the membrane also affects the viscous decay time of the interfacial waves, the greater shear within the water for the membrane-covered interface leading to far quicker decay of the waves. As given by Miller and Scriven [1968], the amplitude of a capillary wave of wavenumber k on the spherical free surface of radius a of a fluid with kinematic viscosity ν, decays exponentially with modulus $\tau_{free} = [(2k+1)(k-1)\nu/a^2]^{-1}$. This decay is associated with energy losses purely in the outer flow, away from the interfacial boundary layer, as no significant shear occurs at the interface. For a wave on an interface covered by an inextensible membrane (one with infinite elasticity, so that no change in surface area is permitted) with tension σ, its amplitude decays exponentially with modulus $\tau_{membrane} = [\nu^{1/2}\omega^{1/2}(k-1)^2/2\sqrt{2}a(k+1)]^{-1}$. This greater rate of decay occurs because now the decay is dominated by energy losses within the interfacial boundary layer, where the shear is significant. For a wave of wavelength 0.01m on a balloon with radius 0.06m (giving $k \approx 38$, $\sigma \approx 200$N/m and $\omega \approx 6100$), the moduli are

$$\tau_{free} \approx 1.27\text{s},$$

$$\tau_{membrane} \approx 0.06\text{s},$$

clearly demonstrating the effect of the membrane in causing enhanced decay of the interfacial waves, and explaining the decay of waves generated by the release of the balloon. Going further, such a wave has phase speed $c_p \approx 10$m/s, with half the circumference of the balloon $C = 0.06\pi \approx 0.2$m. Thus, it takes the wave approximately 0.02 s to travel from the bottom to the top, roughly a third of the decay modulus. This explains why the waves are far more difficult to see after they reach the top of the balloon- in part due to interference with other waves, but in part because they have undergone significant decay. As for a surface tension-driven wave, $\omega \propto k^{3/2} \propto \lambda^{-3/2}$, the decay modulus $\tau_{membrane} \propto \omega^{-1/2}\lambda^1 \propto \lambda^{7/4}$, predicting that the largest wavelengths will persist for longer, coming to dominate over the smaller, reflected wavelengths at late-times; this proved to be the case for our dropped balloons, as shown in figure 3.1**(e)**.

All of the differences discussed above, while potentially creating differences between the impact of a water droplet on a hydrophobic surface and that of a water balloon on a rigid surface, do not affect the behaviour in a significant qualitative way. There is, of course, one such phenomenon that does do this: the rupturing of the membrane, the effects of which will be discussed in the following sections.

3.3 Rupture and and retraction of the balloon

Were the balloon to be filled to a sufficient volume and then dropped from a great enough height, the increase in tension in the membrane generated by the deformation on impact caused it to fail. The full process of the rupture and retraction of the membrane is studied in detail in chapter 5, but we shall give a summary for water balloons dropped in air here.

Rupture of the membrane occurred through the propagation of usually one (though occasionally more) cracks though the membrane, as displayed in figure 3.4. The path of the crack(s) varied from balloon to balloon, though often they traveled from bottom to top of the balloon, likely a consequence

of the bottom of the balloon impacting and thus experiencing increases in strain (and hence stress) before the top. The cracks rarely traveled in a straight line, more often taking curved paths. This was to be expected, in part due to natural variations in the tension within the membrane, but also in part because cracks in rubber sheets under biaxial tension have been known to follow wave-like paths, as in Deegan et al. [2002].

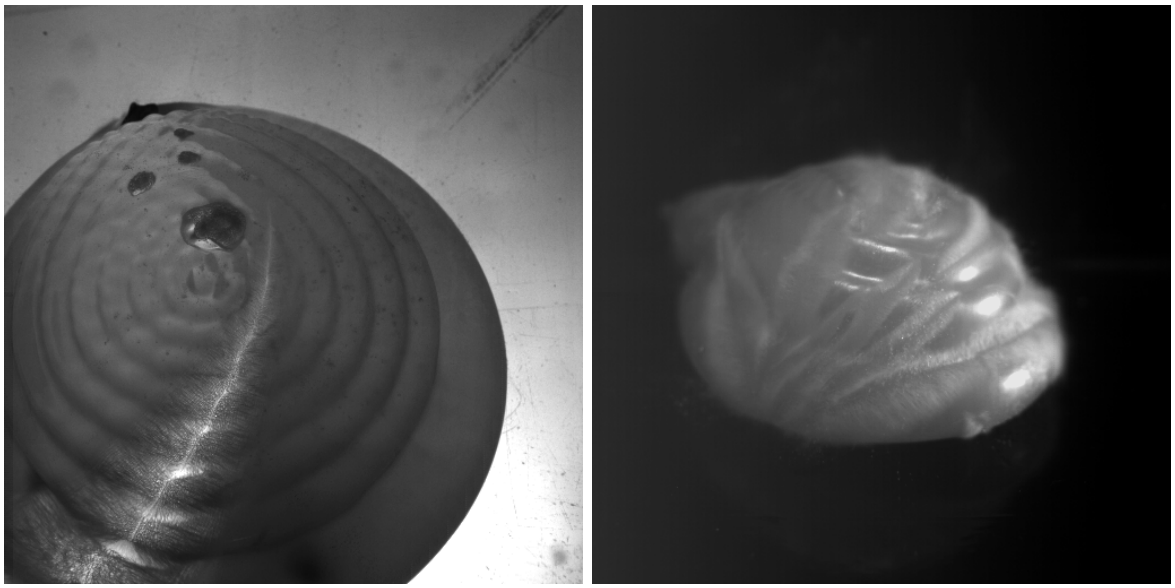

(a) (b)

Figure 3.4: Examples of membrane failure through **(a)** one and **(b)** several cracks.

The presence of the crack led to the rapid retraction of the membrane over the water's surface. In brief, this occurred because the crack edges were stress-free (in contrast to the high stresses in the rest of the membrane), causing a quasi-longitudinal stress wave to propagate into the rubber. The material in front of this wavefront was stationary; the material behind was in motion, retracting away from the crack. This wave was dispersive, a consequence of both the non-linear behaviour of rubber at high strains, and shear stress between the rubber and the water. As the membrane was in a biaxial state of stress pre-burst, the Poisson effect (whereby an incompressible material, such as rubber, when stretched in one direction retracts in the other two) would only enhance the speed of retraction; the stresses and strains tangential to the crack would remain after rupture, contracting the material in the direction normal to the crack. In total, the time from crack formation to full elastic retraction was around 5ms.

A summary of the processes occurring for a retracting balloon membrane in water is given in figure 3.5. The rapid retraction of the membrane over the water caused the appearance of a shear instability on the air/water interface. This instability, as shown in figure 3.6 and previously observed by Soto and Belmonte [2009], was also observed during the rupture of stationary water balloons. Thin jets of water were ejected from the surface of the water into the air, while wider regions of air penetrated into the water. Such asymmetry (non-Boussinesq behaviour) of interfacial growth is similar to that observed for Rayleigh-Taylor instability (RTI) or the Richtmyer-Meshkov instability (RMI) at high

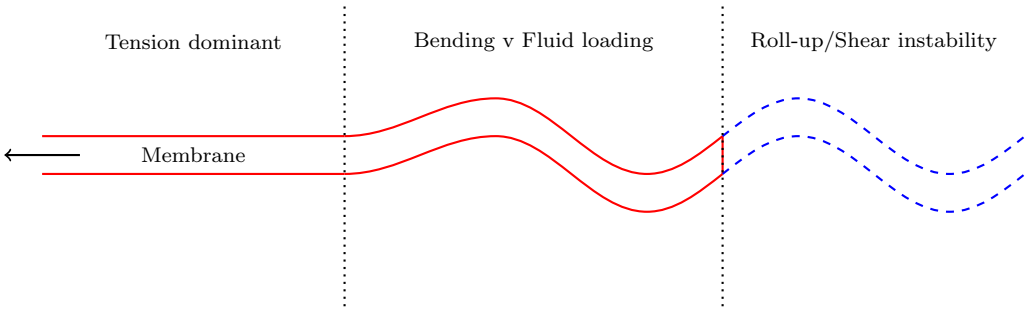

Figure 3.5: Diagram of the transverse wave phenomena created by a retracting rubber membrane.

Atwood numbers. This instability was certainly caused by the interaction between the membrane and the water, through two possible ways. If we neglect any transverse (normal to the plane of retraction) motion of the membrane as it retracts, the situation is similar to the flow behind an impulsively started rigid plate. As the membrane retracted over the water, it created a thin viscous boundary layer adjacent to it, containing vorticity of opposite signs either side of the membrane. As the fluid within the boundary layer passed into the wake, the boundary condition at the interface changed from no-slip with the retracting membrane, to zero tangential stress (as the air/water interface could be regarded as a free surface). The consequent adjustment to the velocity profile within the boundary layer made it susceptible to inviscid shear instabilities of the Kelvin-Helmholtz type, leading to the formation of sinusoidal waves on the wake. These deformations subsequently rolled up into discrete vortex patches of alternating sign, the flow then showing similarities to a von-Karman vortex street. Due to the density differences between the water and air phases, the flow then lost symmetry, causing the jets of water to be ejected from the surface.

The above discussion assumed that there was no transverse motion on the retracting membranes. In reality, however, this proved not to be an accurate assumption: transverse waves were observed on the membrane near the free edge, running parallel to it, of wavelengths of order 1 mm. Examples of such waves are shown in figure 3.7. The waves arise because of fluid loading effects: the water imparts lift to the moving membrane, a consequence of the large difference between the membrane's velocity and that of the stationary water away from it. Away from the free edge, the tension in the membrane is sufficient to suppress any transverse deformations. However, as discussed previously, the stress and hence tension at the free edge must be zero. This, in turn, means there must be a region near the free edge where the tension is not great enough to overcome the fluid loading, leading to the creation of waves there. Their wavelength and growth-rate is then set by a balance between the fluid loading, and tension and bending stiffness in the membrane. The influence of bending stiffness is clear from the fact that these waves have similar wavelength and amplitude to the bending waves observed as the membrane undergoes compression once fully retracted. This creation of these waves is then closely related to a flag flapping in the wind, as the mean fluid velocity creates bending waves on the flag. These transverse waves then influence the wake: vorticity of a single sign was shed for each half-period of the free edge, the sign then alternating for the next half-period. The consequent vorticity distribution in the wake would then roll up into alternately signed patches, and the flow would continue as described for the flat membrane. The wavelength of the instability would therefore

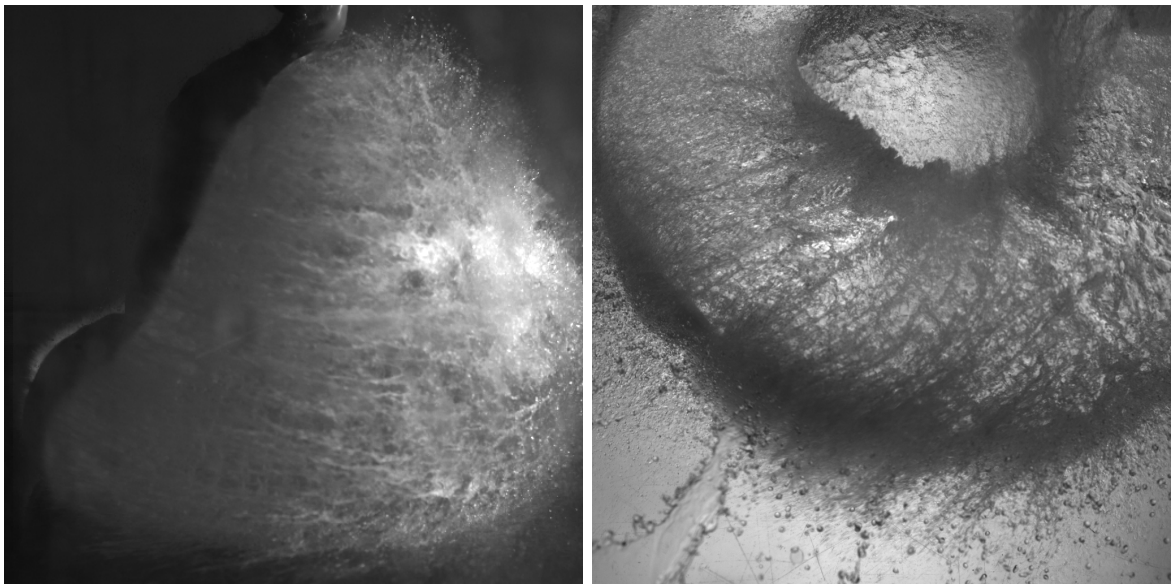

Figure 3.6: Shear instabilities on the water surface created by the retracting latex, after the impact of 300 mm diameter balloons on a rigid tank floor in air.

be set by the wavelength of waves on the membrane, typically around 1 mm. The roll-up due to the flapping of the membrane occurred before any other instability, such as that described above, could develop in the wake. However, the waves on the membrane would only develop when it was traveling faster enough. Consequently, the shear instability seen for retracting balloons is likely a combination of both effects: instability in the wake itself at early and late times when the membrane is traveling slowly, shedding of vorticity due to waves on the membrane at intermediate times.

In fact, the free edge waves and instability in the wake could be regarded as examples of the same phenomenon: the retraction of the membrane caused a large momentum difference between the material at the interface (the membrane for the waves, the wake itself for the instability) and the stationary outer flow. This momentum difference lead to inviscid shear instability of the Kelvin-Helmholtz type, and consequently transverse deformations, due to a centrifugal force on the interface exerted by the outer fluid. Tension and bending stiffness in the membrane restricted the growth of the instability when the membrane was present. This was not the case in the wake, however, leading to the roll-up of the vorticity and consequent non-linear behaviour on the water's surface, as seen in figure 3.6.

Once the membrane was close to returning to its initial unstretched state, it would undergo buckling, as shown in figure 3.8. As discussed in 1, there are two stages to the retraction of rubber from high strains: a fast elastic retraction, and a slow viscoelastic retraction. Once the elastic (but not viscoelastic) retraction was complete, the membrane buckled, as its inertia created compressive in-plane stresses that, as it was thin, it could not sustain without undergoing out-of-plane deformation. As given by Vermorel et al. [2007], for the linear retraction of a rubber band, these buckling waves depend on the ratio between the compressive and bending stresses. Consequently, their wavelengths are independent of the Young's modulus E, and are $O(h)$ in the strip thickness h. This would appear

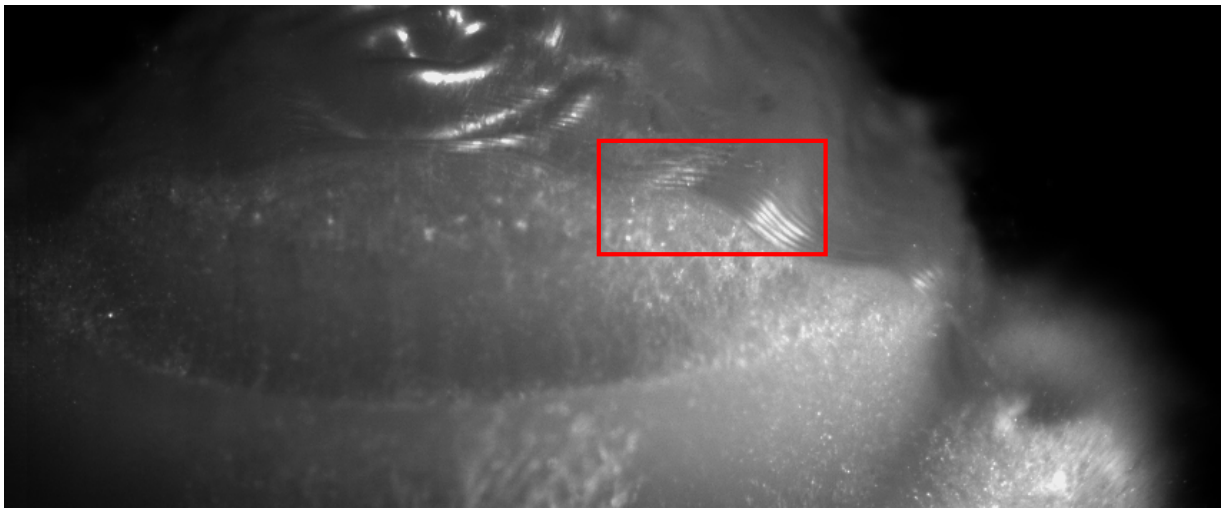

Figure 3.7: Waves seen near the free edge of the retracting membrane. The waves are present on the 10 mm of membrane closest to the free edge and run parallel to it, with wavelength approximately 1 mm. The red box highlights the region in which they are most clearly visible.

to be true for our balloons too; the buckling wavelengths are around $0.1 - 1$mm, with the thickness of the membrane around 0.2mm. The formation of the buckles was not simultaneous everywhere on the membrane, as the compressive stresses depended on the local state of strain. On average, it took around 1ms for them to spread over the entire membrane.

3.4 Late-time interfacial growth

Whenever a water balloon was burst, the shear instability discussed in the previous section was observed. However, if any capillary-like waves were present on the membrane at the moment of rupture, a later, significant growth in the amplitude of the interface occurred, as may be seen in figure 3.9. From our search of the literature, it would appear this phenomenon has not previously been observed. The wavelength of this interfacial growth was set by the wavelength of the capillary-like waves present on the balloon at the moment of rupture, and was thus much larger than the length-scale of the shear-like instabilities described previously. The time-scale was much greater too, with significant growth of interfacial amplitude taking approximately 50ms.

A simple explanation for this growth is that it is a direct consequence of the removal of the restoring force on the capillary-like waves within the water, as the flow continued to evolve according to the flow field present immediately prior to rupture without the tension in the balloon to restrict it (as in figure 3.10). The kinetic energy associated with the waves was no longer restricted by the membrane, being instead diverted into growth of the interfacial amplitude. Yet a deeper explanation may given: that while the mechanism for this growth of the interface may not have been explicitly seen before, it is in fact a manifestation of the mechanism driving RMI, that we shall refer to as the Richtmyer-Meshkov mechanism (RMM).

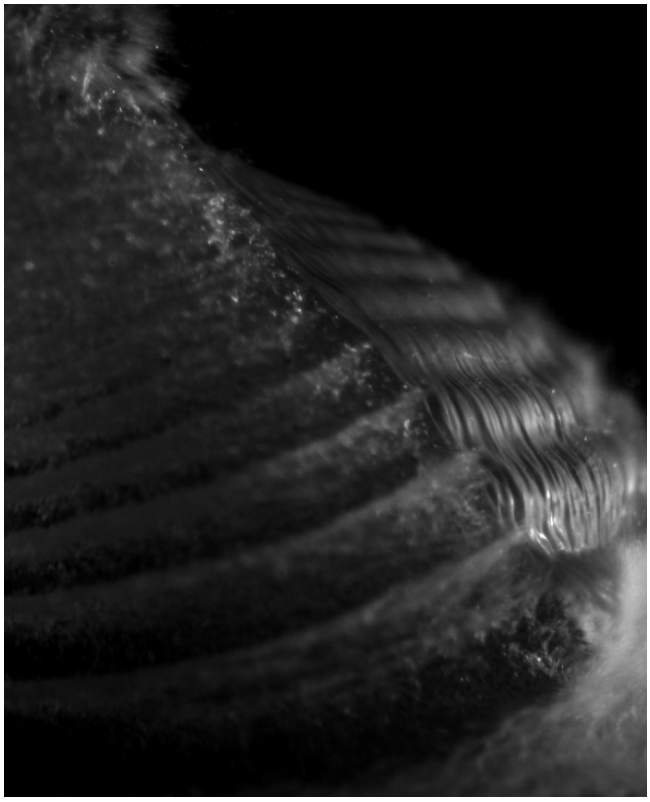

Figure 3.8: Bending waves on the membrane as it undergoes compression after fully retracting.

As discussed in chapter 1, RTI and RMI are closely related. Consider, as a starting point, the sinusoidally-perturbed density interface as shown in figures 3.11(a) to 3.11(c), with no acceleration acting on the system. Applying a constant acceleration g on the density field down the page, the perturbations will oscillate as classical gravity waves (see Batchelor [1967]), all while retaining their initial amplitude (in absence of viscosity). If this acceleration is instantaneously reversed at $t = 0$ (say) the system is now unstably stratified, causing the amplitude of the interfacial perturbations to grow exponentially. This was discovered by G.I.Taylor [1950], and is a manifestation of RTI. In this way, RTI may be regarded as a consequence of the instantaneous of the reversal of the acceleration on a density interface: $g \propto \text{sgn}(-t)$, as shown in figure 3.11(d).

Classical RMI is a consequence of a shock passing through a density interface. Consider the system of figure 3.11(b) with the shock travelling up or down the page through the interface (changing the direction of the shock only changes the phase of amplitude growth). The only time a force is applied to interface is when the shock instantaneously passes through it at $t = 0$; as described in chapter 1, this leads to the baroclinic generation of vorticity there that causes the interfacial amplitude to grow linearly in time. RMI can therefore be seen as a consequence of the momentary application of acceleration to a density interface: $g \propto \delta(t)$, as shown in figure 3.11(e).

Now consider the density interface covered by a thin elastic membrane. Tension in the membrane will act as an acceleration on the interface, causing the interfacial perturbations to stably oscillate as

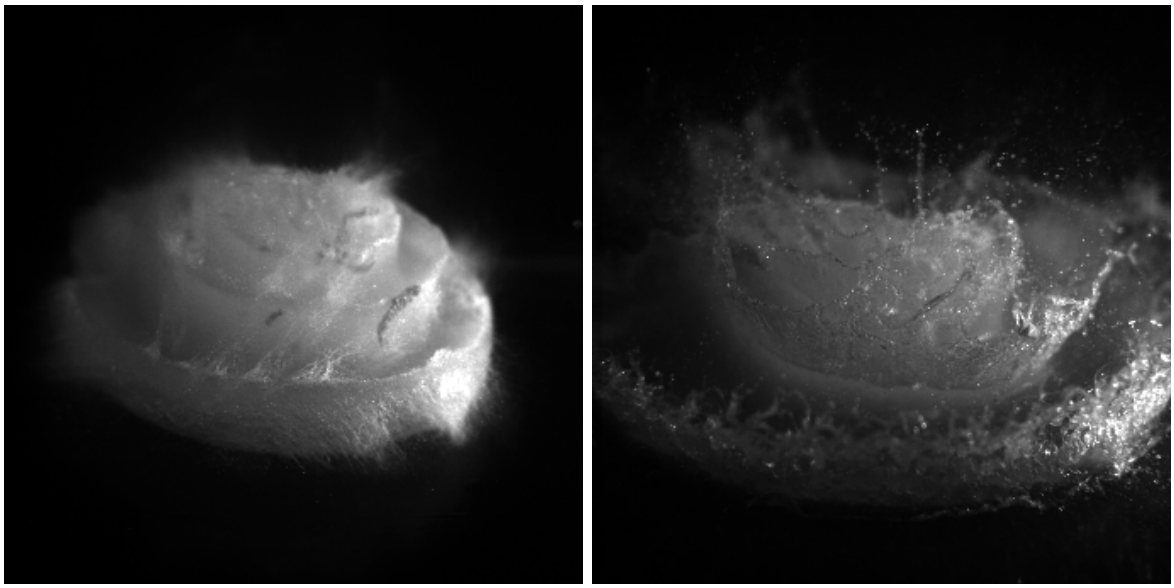

Figure 3.9: An example of the late-time growth of the interfacial amplitude caused by the impact and rupture of a 130mm water balloon on a rigid surface in air. The water contains milk powder to aid visualisation of the free surface.

capillary-like waves (as described in section 3.2). If the membrane is instantaneously removed at $t = 0$, the tension within it is no longer able to act as a restoring force for the interfacial waves (note that the rupture of the membrane around a water balloon may be accurately approximated as its instantaneous removal from the interface here, as the time-scale for the late-time growth was far greater than that for the retraction of the membrane). However, the interfacial vorticity associated with the pre-burst waves (that will be revealed in section 3.2 to be significant) remains at the interface, and leads to the growth of the interfacial amplitude. In this way, the late-time growth of the interfacial amplitude in bursting water balloons may be seen as a consequence of the instantaneous removal of the restoring force on an interface: $g \propto H(-t)$, as shown in figure 3.11(f).

From the above descriptions, it is not obvious that the interfacial growth after bursting a balloon is a manifestation of RMM; the accelerations applied to the interface are different, one a delta function and the other a step function. However, a delta function may be regarded as limit of step functions,

$$\delta(t) \propto \lim_{\triangle t \to 0} \frac{H(t + \triangle t)H(-t)}{\triangle t} \tag{3.1}$$

with $\triangle t > 0$. In this way, the connection between the two cases may be clearly seen mathematically; the connection may also be explained physically. The delta function acceleration for classical RMM actually consists of two distinct stages separated by an infinitesimal amount time: the instantaneous application of acceleration to the interface, and its instantaneous removal. It is during the application stage that vorticity is baroclinically generated at the interface, but it is only after the acceleration is instantaneously removed that this vorticity causes the amplitude to grow. For the balloon case, acceleration is applied to the interface and hence vorticity is generated for an infinite time (by which

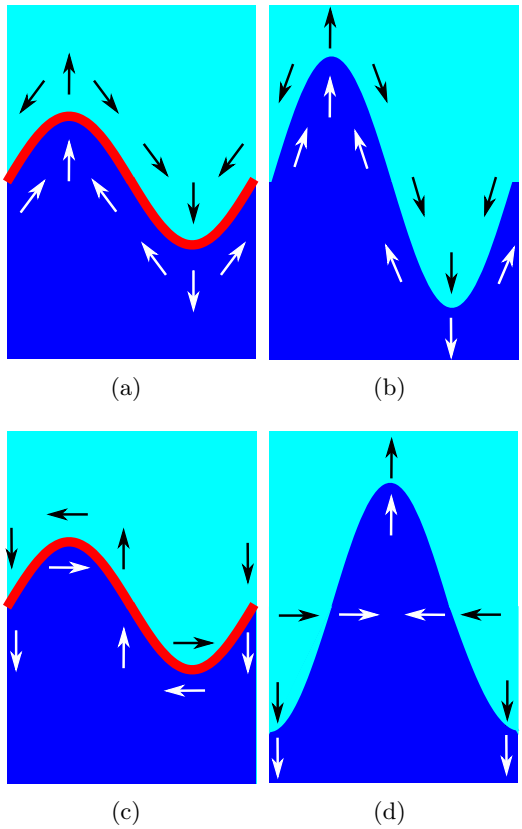

Figure 3.10: The motion of the fluid (given by the arrows) due to waves on an interface covered by an elastic membrane, and the subsequent evolution of the flow after the membrane is removed. Diagrams **(a)** and **(b)** describe a standing wave, diagrams **(c)** and **(d)** describe a travelling wave going from left to right; the difference in the phase of growth is clear. With no motion in the fluid prior to removal of the membrane, no large-scale growth of the interfacial amplitude will occur.

we mean far longer than a single wave period) before rupture, yet it is only after that acceleration is removed that the interfacial amplitude grows, in accordance with the vorticity present at the moment of rupture. Thus in both cases, the instantaneous removal of the acceleration from the interface allows the vorticity there to increase the interfacial amplitude; this growth is independent of how long the acceleration acted on the interface. In this way, the growth of the interfacial amplitude seen in figure 3.9 is a manifestation of RMM.

In fact, the only significant difference between the balloon RMM and classical RMM is the mechanism for creation of the interfacial vorticity (before the acceleration is removed): baroclinic generation of vorticity for classical RMM as in chapter 1, wave-generated velocity shear within the interfacial boundary layer for balloon RMM as in section 3.2. One simple consequence of this difference is that, while classical RMM will occur irrespective of the motion of the interface at $t = 0$ (it requires only that the interface is perturbed), balloon RMM requires the interface to be in motion, with the nature of this motion (for example, standing or travelling waves) affecting the phase of growth of the

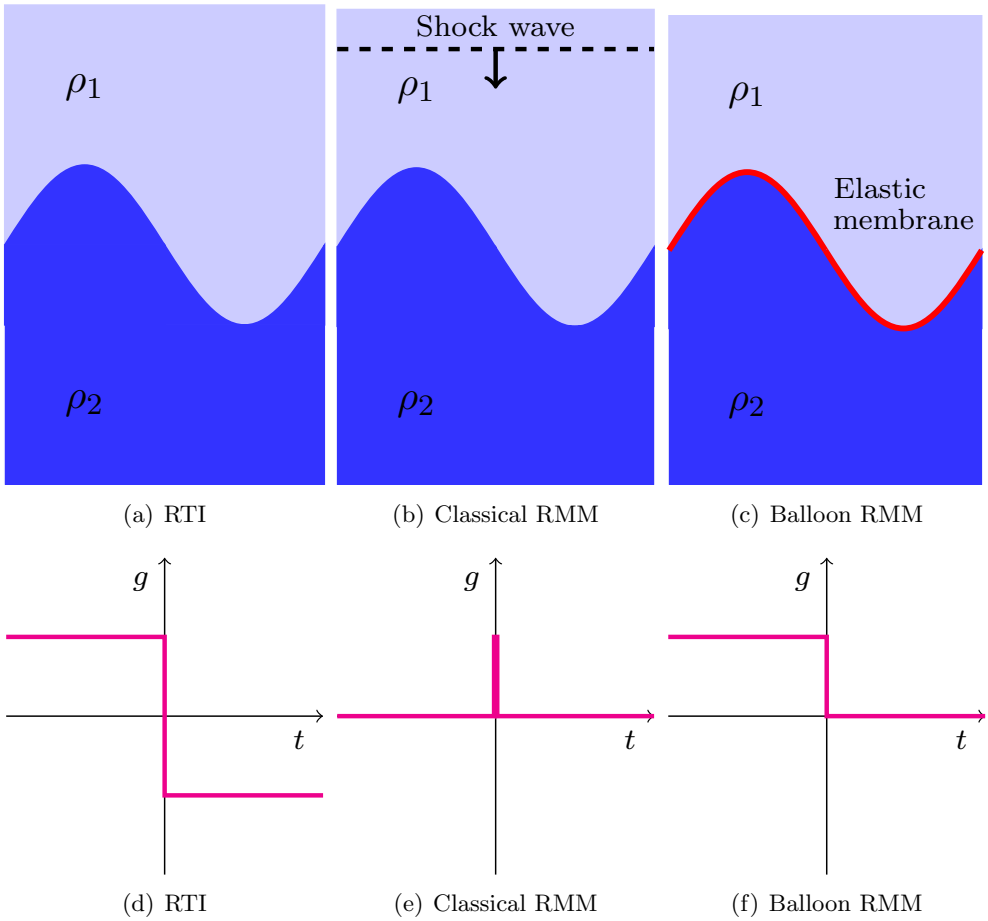

(a) RTI (b) Classical RMM (c) Balloon RMM

(d) RTI (e) Classical RMM (f) Balloon RMM

Figure 3.11: Images (a)-(c) depict the physical set-up required for Rayleigh-Taylor instability (RTI), classical shock-generated Richtmyer-Meshkov mechanism (RMM), and wave-generated balloon RMM, respectively, on a perturbed density interface. Images (d)-(f) show the form of the acceleration g over time t acting on the interface. For RTI, we need $\rho_1 > \rho_2$, and for classical RMM, $\rho_1 \neq \rho_2$. For balloon RMM, however, the densities may take any value.

interfacial amplitude; this is made clear in figure 3.10. There is a more significant difference, however: while classical RMM requires a density difference between the phases, balloon RMM does not. Consequently, while classical RMM fails when $A = 0$, bursting an oscillated balloon with $A = 0$ should lead to interfacial growth. Though this is clearly impossible to test dropping water balloons as described in section 3.1, a new experimental method was devised to test this hypothesis. This is described in chapter 6, but suffice to say here that it proved successful: balloon RMM does cause interfacial growth even when $A = 0$.

For water balloons dropped in air, the late-time interfacial growth was asymmetric (see figure 3.9). Where the water was moving into the air, each region of growth took the form of a thin, axisymmetric sheet ejected from the water's free surface. The water's own surface tension acted to round off the leading edge of the thin sheets, where eventually further small-scale capillary instabilities could be observed. Between these sheets, the air penetrated into the water; the interface took the form of a wide, shallow depression, whose amplitude grew far more slowly than that of the sheets of water penetrating into air.

The asymmetric structure of the interfacial growth demonstrates that this is a clearly non-Boussinesq process: despite gravity being too weak to affect the growth, the density difference between the phases has a significant effect on the behaviour. Such asymmetric behaviour is also seen for classic density-driven interfacial instabilities such as RTI and RMI at high Atwood numbers; the sharp, faster-moving sheets of denser fluid penetrating into the lighter fluid are known as 'spikes', whilst the wide, slow moving intrusions of lighter fluid into the denser phase are known as 'bubbles' as they approximate the shape of air bubbles moving through water. For RMM at short times, the growth rate of both bubbles and spikes will be approximately linear, as theorised by Richtmyer [1960]. At late-times, however, non-linearities become important and the situation becomes far more complex to model. As explained by Brouillette [2002], even for classical RMI, no one universally accepted theory exists, with the best models phenomenological. For the bursting of water balloons in air, the growth rate is further complicated by gravity, which over longer timescales must be taken into account, and the overall motion of the balloon when spreading out over the tank floor. Many of these issues are a consequence of a density difference between the phases; yet balloon RMM works for $A = 0$, when the effects of gravity are negligible and the flow is Boussinesq. $A = 0$ also corresponds to symmetric growth, with both phases assuming bubble-like shapes; if the same fluid is used both inside and outside balloon, any effects of fluid surface tension would also disappear. The shape of the balloons would also be closer to the spherical (see chapter 2). This suggested that modelling the interfacial growth for $A = 0$ would be a far more tractable problem, as was done by Jacobs and Sheeley [1996] for classical RMI. Consequently, unlike dropped water balloons in air, the interfacial growth for balloon RMM with $A = 0$ will examined in detail experimentally and theoretically in chapter 6.

At very late-time, gravity came to dominate the interfacial growth, which together with the water's inertia caused the entire mass of water to slump down and spread out. The water then sloshed around the tank until coming to rest as a thin, flat layer of water above the tank floor.

3.5 Limitations of this experiment

After conducting numerous experiments using the experimental method discussed here, its limitations became apparent: detailed quantitative study of the rupture of a dropped water balloon in air proved

impossible. The experiment involved a large number of unknowns, including where the balloons would land, in what orientation and when exactly they would burst. This affected both the shape of the balloon and the nature of the capillary-like waves present at the moment of rupture, as well as making it difficult to take accurate measurements. We would also always get a range of wavenumbers for the capillary-like waves, when it would be a great simplification to consider only the single-mode case. Additionally, little was known about the membranes themselves, as they had simply been purchased straight from a commercial retailer. Together, these effects made the experiments practically unrepeatable. Furthermore, this experimental method also greatly limited the range of Atwood numbers we could examine to those close to 1, when arguably the most interesting case was for $A = 0$.

An attempt was made to regulate the rupture by placing a small, sharp pin at the point of impact of the balloon. The pin created the initial failure from which a crack propagated up through the membrane. The membrane then retracted away from this crack, and so away from the bottom of the balloon. The water then slumped out across the rigid surface as a gravity current. An example of such an experiment is shown in figure 3.12, and reveals that only one of the three phenomena of interest, the shear instability, was present in these experiments - as the membrane under tension did not impact the rigid surface, no capillary-like waves formed and so there was no larger-scale interfacial growth. Even as a way of studying just the shear instability, this method was clearly inferior to simply bursting a stationary water balloon.

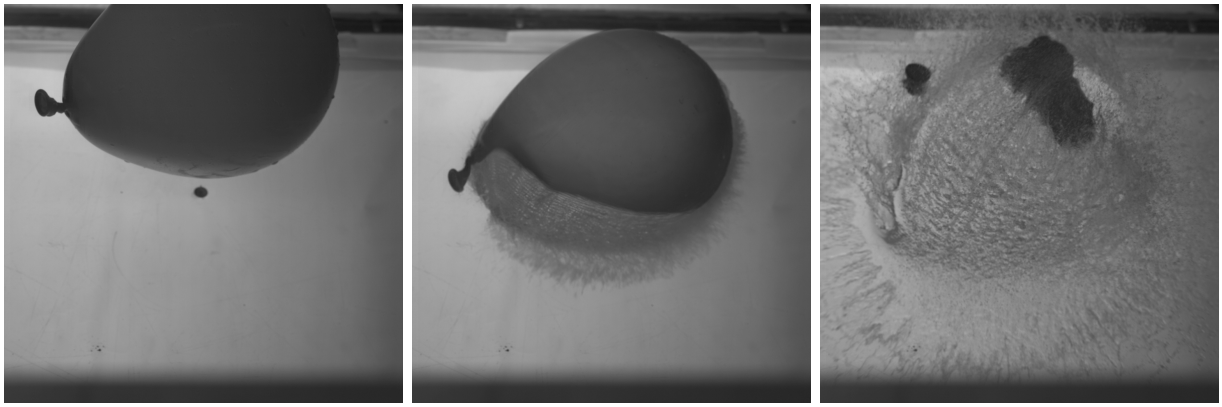

(a) $t = 0$ (b) $t = 0.02s$ (c) $t = 0.03s$

Figure 3.12: The impact of a 300mm water balloon onto a 5mm-long pin resting on a rigid surface, after being dropped from a height of approximately 1m. Notably, no capillary-like waves have formed by the time the membrane ruptures, preventing the later large-scale interfacial growth occurring.

3.6 Summary

In section 3.1, a description is given of the experimental procedure used to capture high-speed images of a water-filled membrane impacting upon a flat, rigid surface, where three main phenomena were observed. Section 3.2 described how capillary-like waves were created on the membrane upon impact for which the restoring force was elastic tension in the membrane. The balloon would then continue

to spread horizontally and flatten, leading to an overall increase in the tension within the membrane. Should the membrane not fail, the membrane would then retract and the balloon would bounce off the surface, with the whole process analogous to a water droplet impacting a hydrophobic surface. In section 3.3 it was explained how, if the membrane did fail whilst spreading, the process changed dramatically. One or more cracks propagated through the membrane, leading to the rapid retraction of the membrane over the water's surface. This created a shear instability at the air/water interface, causing thin jets of water to be ejected from the interface. The large number of such jets created a 'spray' effect. In section 3.4, it was demonstrated that, should there be capillary-like waves present on the membrane at the moment of rupture, a larger-scale interfacial growth was observed on a much longer time-scale than the shear instabilities. The denser water phase propagated into the air as 'spikes', while the less dense air phase propagated into the water as 'bubbles', at a much slower rate. This growth had the same form as other well-known instabilities at high Atwood number, and was explained to be a manifestation of the Richtmyer-Meshkov mechanism. Finally, it was explained in section 3.5 why no quantitative measurements were taken of water balloons dropped in air onto a flat surface.

Chapter 4

Capillary-like waves on the membrane

In this chapter, a detailed investigation of the pre-burst capillary-like waves observed in chapter 3 is undertaken. An improved experimental method is outlined that, in combination with Particle Image Velocimetry (PIV), allowed accurate qualitative measurements of the flow to be taken. The predictions of linear theory are then derived, and shown to be in good agreement with the experimental results.

4.1 Improved Experimental Method

A significantly improved experimental method was developed in response to the issues described in section 3.5. Instead of dropping the balloons, they were oscillated while held stationary, before being ruptured with a sharp object. This allowed us to isolate and examine each of the three phenomena separately, and permitted accurate measurements of the flow to be taken from images captured on a high-speed camera. With the exception of irregularities in the membranes themselves, all the issues raised in section 3.5 were significantly mitigated. This method also worked when the balloon was submerged in water, permitting us to study the behaviour of a perturbed and burst balloon when there was no density gradient across the membrane. This meant that our statement in chapter 3, that the Richtmyer-Meshkov mechanism (RMM) for a balloon would lead to interfacial growth even when $A = 0$, could be tested.

The experimental lay-out is given in figure 4.1. Experiments were conducted with both air ($A \approx 1$) and water ($A = 0$) external to the balloon. The only latex balloons used were 130 mm diameter, whereas the most commonly-available size of balloon has a maximum diameter nearer 300 mm. This was a necessity, due to the scale of the other equipment. No experiments were performed on cylindrical balloons for the same reason, namely the large size of even the smallest such balloons when fully inflated. As stated in chapter 2, all balloons were filled and unfilled once before any experiment were performed on them. The balloon was connected to the same system of tubing as in chapter 2 that allowed measurement of the pressure inside the balloon. Additionally, the balloon was now supported by a section of 60mm-diameter pipe that helped to support it when fully inflated, with the open end being the lowest point of the balloon, within the pipe. This support pipe restricted the overall movement of the balloon when oscillated, helping to ensure that its centre remained approximately stationary. However, where the balloon was in contact with the pipe, the displacement of the balloon was fixed at zero, and so the presence of the support pipe did play a role in setting the resonant modes

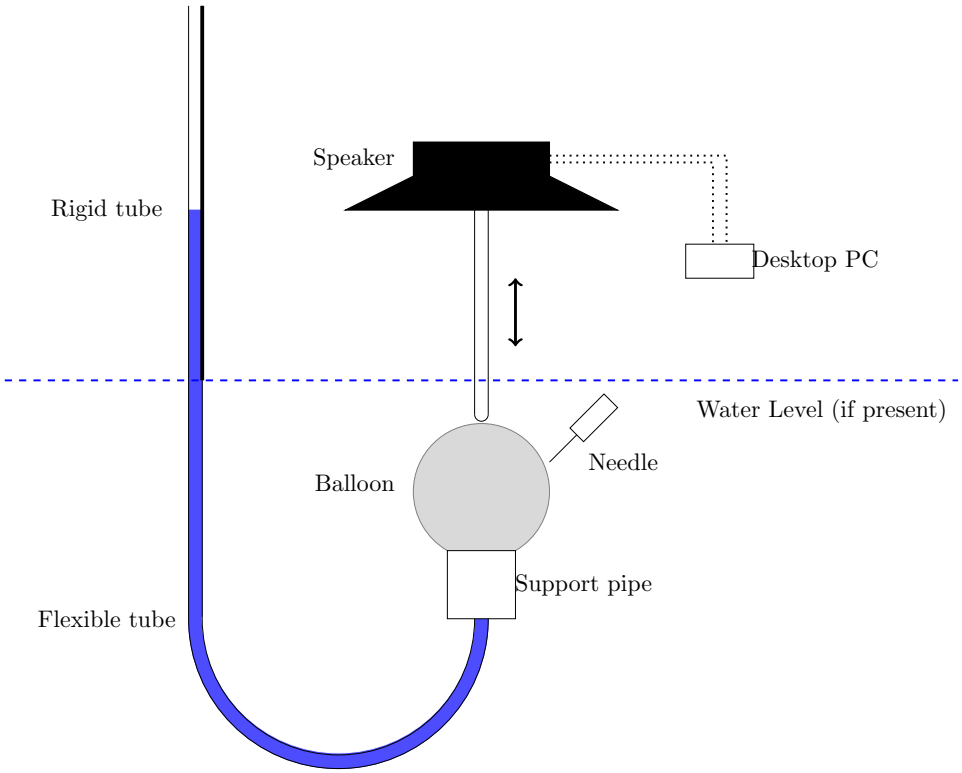

Figure 4.1: The experimental set-up used to oscillate 130 mm balloons at a fixed frequency before they were ruptured by the needle.

of oscillation. To create the required capillary-like waves on the balloon, it was subjected to periodic forcing before being deliberately ruptured. This forcing was achieved using a 70 W loud speaker with an impedance of 8 Ohm and polypropylene cone of diameter 200 mm. A cut-away plastic beaker had been glued to the speaker, with a 350 mm long rigid rod firmly attached to the beaker. The whole apparatus was then suspended approximately 500 mm above the tank floor. An analogue output card installed in a computer was used to drive the position of the speaker via an 80 W audio amplifier. A balloon was then put in place and filled as described above, and the speaker adjusted so that the rod was aligned with the balloon's axis of symmetry and in contact with the top of the balloon (see figure 4.1) such that it created a static deformation in the surface approximately 10 mm in depth, to ensure that it remained in contact with the balloon for as greater part of the period of oscillation as possible. Once the balloon was in position, the frequency of oscillation was chosen and the speaker activated. The balloons were then forced at the requisite frequency for at least 2 s to ensure only waves of the correct frequency were present on the balloon.

These experiments were all performed using the same tank and high-speed camera as described in section 3.1, with the camera recording at either 2000fps or 5400fps. By observing the motion of the interface in the recorded videos, the wavelength and amplitude of the interfacial waves could be determined. For information about the rest of the flow, it was necessary to perform Particle Image Velocimetry (PIV). For this, approximately neutrally-buoyant $180 - 212$ μm Pliolite particles were used, after being mixed with rinse aid to overcome their hydrophobic nature. A number of such particles were then poured into the balloon, the water outside (if present), or both. The experiments were illuminated using a 700 W arc lamp projecting light through a slit formed on the tank's side using two blackened metal strips and black, self-adhesive film. After the images had been saved to hard-disk as before, they were analysed using the PIV facility within the program DigiFlow.

4.2 Qualitative Experimental Results

First we give a qualitative overview of the results of our new experimental method. There were two free input parameters that we could vary: the volume of the balloon (and hence tension in the membrane), and the input frequency f. Both were limited in range by the experimental equipment available to us. The volume was limited at the lower end by the need to have waves of a sufficient wavelength and amplitude (while remaining linear) to enable good flow visualisation, and at the upper end by the likelihood of spontaneous bursting of the balloon. The input frequency was limited at the lower end by the appearance of higher harmonics in the forcing below 50 Hz, and at the upper end by the power of forcing available - the greater the frequency of forcing, the smaller the amplitude, limiting forcing to frequencies under 180 Hz.

Sample qualitative results are displayed in figure 4.2 for a balloon forced at 105Hz; while the exact magnitude of the flow quantities changed with membrane tension and forcing frequency, the qualitative features were the same for all experiments conducted within the ranges given above.

As seen for dropped water balloons, waves were created on the membrane. The tension in a rubber balloon may act as a restoring force for both traveling and standing waves in the balloon, and knowing which is present at the moment of rupture is important. As was explained in the previous chapter, the late-time interfacial growth was a consequence of kinetic energy in the waves present pre-rupture. With travelling waves, there will always be such kinetic energy present at the point of rupture, and

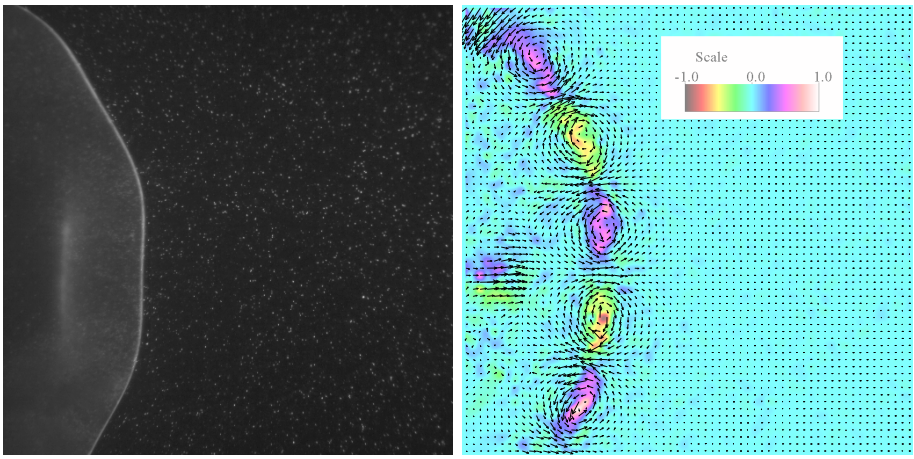

(a) $t = 0.0$ms

(b) $t = 2.5$ms

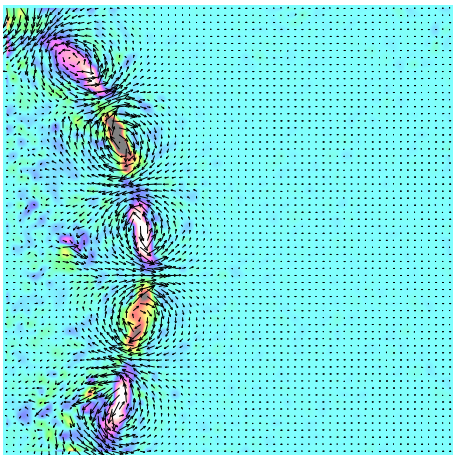

(c) $t = 5.0$ms

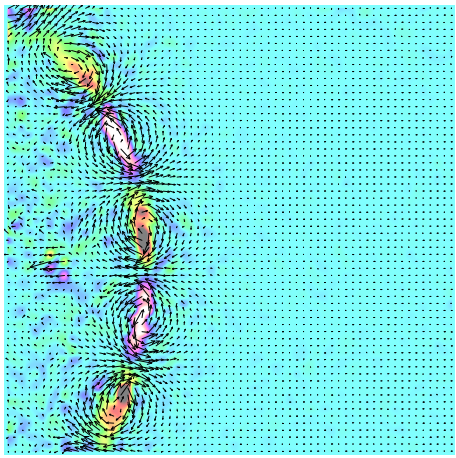

(d) $t = 7.5$ms

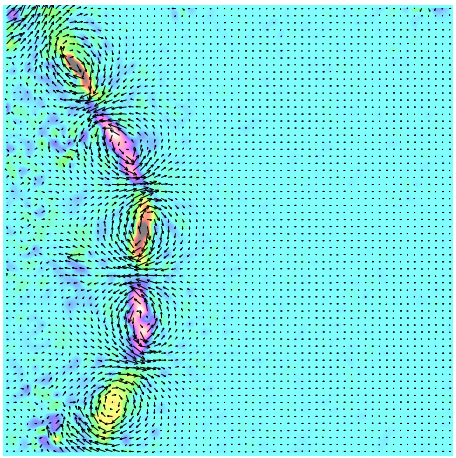

(e) $t = 10.0$ms

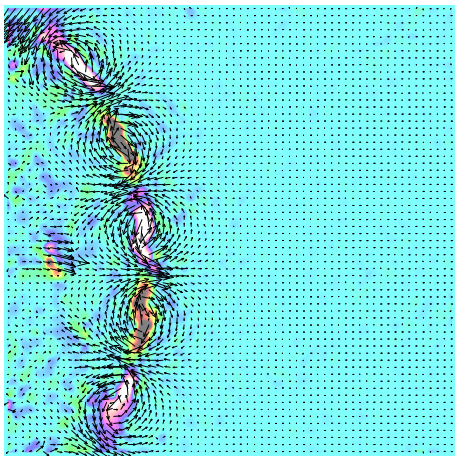

(f) $t = 12.5$ms

Figure 4.2: The flow field created by a water-filled 130mm membrane oscillated underwater at 105Hz over one forcing period. Image **(a)** shows the set-up used, with particles both inside and outside the membrane and a light sheet shone vertically through it. Images **(b)** - **(f)** show the results of PIV performed on the resulting video, with the arrows representing the velocity field and the colours representing the vorticity: purple for positive vorticity, cyan for zero, green for negative. The scale given is dimensionless, with all values scaled by the maximum magnitude of vorticity in the sequence.

thus the late-time growth will always occur, and at the same rate, whenever rupture begins (though the location of the subsequent growth will be unknown); with standing waves, the amount of kinetic energy present in the waves depends on their phase at the moment of rupture, and thus growth will not always occur (though the location of any subsequent growth will be fixed). For the dropped balloons as in chapter 3, it was waves traveling up the membrane that were seen as the balloon landed and deformed. Similarly with the held and oscillated balloons, when the forcing began it was traveling waves that were seen. Yet after a few oscillations, the traveling waves created by the oscillated rod formed a steady interference pattern, so that standing waves were seen. Some traveling waves persisted, but were negligible in their impact. For the range of parameters used in our experiments, the time for a single wave to travel to the bottom of the balloon and back up again, was between 0.05s and 0.15s. This meant that after 0.5s the perturbations on the interface were effectively standing waves. As in all experiments with oscillated balloons, the balloons were left to oscillate for at least 1s before measurements were taken, only standing waves were seen. There was the potential for some beating of the standing waves to occur: if the oscillation frequency was not an exact resonant frequency, the standing waves would not be steady (so that the position of nodes was fixed) but instead would oscillate position. Similarly, dissipation would also mean that the waves were not perfect standing waves. However, no significant variation of the position of nodes was observed experimentally, so that the interfacial waves could be approximately regarded as steady standing waves.

The wavelength λ of the interfacial waves varied between 10 and 100mm, while the amplitude $\tilde{A}$ of the waves lay in the range $1 - 10$mm. For a spherical interface, a linear wave is one for which the amplitude of the wave is much smaller than both their wavelength and the radius of the sphere R. In our experiments, R lay between 40mm and 60mm, clearly giving $\tilde{A}/R \ll 1$ for all the experiments. It was also true that $\tilde{A}/\lambda \ll 1$ in every experiment, as our choice of experimental equipment meant that $\tilde{A}$ and λ were not independent - increasing the frequency of forcing (and thus decreasing the wavelength) led to a corresponding decrease in the maximum available forcing amplitude (and thus that of the waves).

As a further consequence of the linearity of these waves, the relative change in surface area was small: with the amplitude around a tenth of the wavelength, the change in surface area was around one per-cent. This, in turn, meant that the balloon was never perturbed far from its initial, near-spherical shape.

The preceding observations could be found simply by considering the movement of the interface. However, our ability to perform PIV permitted us to uncover far more information about the flow. As figure 4.2 clearly demonstrates, the velocities were greatest near the interface, decaying quickly as you move away from it. The same is true of the vorticity, being restricted to a narrow region near the interface of a thickness much less than the amplitude of the waves. Within this region, the vorticity alternates in sign around the interface, in phase with the interfacial waves.

Importantly, experiments conducted in this way and in which the balloon was at some point burst, showed all the same phenomena as seen for a dropped and burst balloon, as discussed in chapter 1. Consequently, we could restrict our analysis of the pre-burst waves to the much-simplified linear case, without neglecting any important physical mechanisms.

4.3 Linear theory for capillary waves

Here, we shall derive a model for the surface waves on a water balloon based on the linearized Navier-Stokes equations, neglecting any overall motion of the balloon and the influence of gravity. To the best of our knowledge, this represents the first attempt to model surface waves on water-filled balloons, as no evidence of such a study is found in the literature. This model will be accurate for the oscillated stationary balloons as described in the previous section. For dropped balloons in air, the agreement will not be as good, as the balloon will deform far from spherical during impact, the assumption of linearity then no longer applying. Nevertheless, it will still capture the essential features of the flow (particularly at early times, for waves of short wavelength), but qualitative comparisons must be regarded as only approximate.

To simplify the derivation of the theory for our interfacial waves, we must make several assumptions: that the water is incompressible (a common assumption), of low viscosity, that the balloons are spherical (a reasonable assumption, as shown in chapter 2), and that the flow is axisymmetric. For the balloons forced at a single on-axis point, deviations from axisymmetry of the flow will only arise from non-axisymmetry of the balloon. For dropped balloons, the non-sphericity of the balloons means that their orientation upon impact will affect the axisymmetry of any waves created; any horizontal motion of the balloon through the air may also have the same effect.

We consider here only capillary waves. While gravity clearly plays a role in generating the waves on a dropped balloon, causing its acceleration through the air, the small typical wavelength of these waves means that tension in the membrane will be the dominant restoring force as they propagate, for all but the few waves of greatest wavelength. We also neglect bending stiffness because, as discussed in section 2.9, it will be negligible for waves of wavelength much greater than the membrane thickness $h = 0.16$ mm. For oscillated balloons, only waves of a single frequency and therefore wavelength were formed in each experiment. The shortest of these waves had a wavelength of the order of 10 mm, so bending stiffness was always unimportant. For the dropped balloons in air, the impact of the balloon created waves on the full spectrum of frequencies, and therefore wavelengths. The bending stiffness would therefore play a significant role in limiting the amplitude of the waves of shortest wavelength, as was noted in chapter 1. The following analysis should therefore only be regarded as accurate for waves of wavelength over 1 mm.

The final assumption we make is that the interfacial waves are linear; that is, that their amplitude A is much less than both their wavelength λ and the radius of the balloon a. This assumption may not hold for all the waves seen on a dropped water balloon, particularly those of largest wavelength (see figure 3.1). Yet it is true for many such waves, and as figure 1.1 revealed, the presence of linear waves on the interface at rupture does lead to interfacial growth. Consequently, we may neglect second-order terms in the interfacial amplitude, velocity field, and their derivatives.

Based on these assumptions, a large volume of work has been conducted into the interfacial waves that they permit. We shall seek to recover these results, and extend the analysis to derive the full flow field for spherical interfaces in the limit of small fluid viscosities. In doing so, we shall also make clear what impact the presence of the membrane has, in comparison with a true fluid/fluid interface.

	2D	Spherical
Free surface	$\sqrt{\frac{\sigma k^3}{\rho}}$	$\sqrt{\frac{\sigma k(k-1)(k+2)}{a^3\rho}}$
Two-fluid interface	$\sqrt{\frac{\sigma k^3}{\rho_1+\rho_2}}$	$\sqrt{\frac{\sigma(k+1)k(k-1)(k+2)}{a^3[(k+1)\rho_1+k\rho_2]}}$
One-fluid inextensible	$\sqrt{\frac{\sigma k^3}{\rho}}$	$\sqrt{\frac{\sigma k(k-1)(k+2)}{a^3\rho}}$
Two-fluid inextensible	$\sqrt{\frac{\sigma k^3}{\rho_1+\rho_2}}$	$\sqrt{\frac{\sigma(k+1)k(k-1)(k+2)}{a^3[(k+1)\rho_1+k\rho_2]}}$

Table 4.1: The angular frequency of oscillation ω for low-viscosity waves on an interface, to lowest order in kinematic viscosity ν. Here, σ is surface tension, k the wavenumber, and ρ density. The fluids in the 2D cases are infinitely deep. For the spherical cases, the unperturbed radius is a. Subscript 1 denotes fluid quantities below or inside the interface, subscript 2 the fluid above or outside.

4.3.1 Previous work

Viscous capillary waves on an interface has been a topic of research for over one hundred years. A summary of the early results is given by Lamb [1932], who gives a detailed description of the problem for a pure air/water interface in both 2D and spherical geometry. Miller and Scriven [1968] considered 2D and spherical interfaces between two fluids of non-negligible density, deriving the dispersion relations in the limit of both low and high viscosity.

Classical theory of capillary waves concerns flow near a pure fluid-fluid interface; a water balloon, whether in air or underwater, is clearly not a pure fluid-fluid interface. There are a great number of similarities, yet also some significant differences. These differences arise because for the capillary interfaces considered in the preceding section, only a constant surface tension acted on the interface - the surface itself was free to expand and contract without change in tension. For an interface covered in rubber, this is clearly not true: as revealed in chapter 2, stretching the membrane will cause the tension in it to increase significantly. Such gradients in tension will act to limit tangential motion of the interface, making the interface act as something akin to a rigid boundary. The relevant theory has received a lot of attention, due to the way oil slicks on an ocean surface may act as a thin elastic interface (that this theory is equally applicable to an actual elastic membrane has been noted by Christensen [2005], amongst others). A useful summary is given by Christensen [2005], while a complete review is given by Lucassen-Reynders and Lucassen [1969]. The basic equations for the flow are the same as for the fluid-fluid case, namely the linearised Navier-Stokes equations. The differences arise through the boundary conditions. When the stress required to expand or contract the membrane is far less than shear stresses in the fluid, the effect of the membrane on the flow is negligible, and the interface may be regarded as a pure fluid-fluid interface. When the stress required to expand or contract the membrane is far greater than shear stresses in the fluid, the influence of the membrane becomes significant and the interface is referred to as inextensible. Lamb [1932] considered an inextensible air/water interface in 2D, while Miller and Scriven [1968] went further and derived the dispersion relations for both planar and spherical inextensible interfaces with two fluids of non-negligible viscosity and density.

	2D	Spherical
Free surface	$2\nu k^2$	$\frac{(2k+1)(k-1)\nu}{a^2}$
Two-fluid interface	$\frac{2k\rho_1\rho_2\sqrt{\nu_1\nu_2\omega}}{\sqrt{2}(\rho_1+\rho_2)[\sqrt{\nu_1}\rho_1+\sqrt{\nu_2}\rho_2]}$	$\frac{(2k+1)^2\rho_1\rho_2\sqrt{\nu_1\nu_2\omega}}{2\sqrt{2}a[(k+1)\rho_1+k\rho_2][\sqrt{\nu_1}\rho_1+\sqrt{\nu_2}\rho_2]}$
One-fluid inextensible	$\frac{k\sqrt{\omega\nu}}{2\sqrt{2}}$	$\frac{(k-1)^2\sqrt{\omega\nu}}{2\sqrt{2}a(k+1)}$
Two-fluid inextensible	$\frac{k\sqrt{\omega}[\sqrt{\nu_1}\rho_1+\sqrt{\nu_2}\rho_2]}{2\sqrt{2}[\rho_1+\rho_2]}$	$\frac{\sqrt{\omega}[\sqrt{\nu_1}\rho_1(k-1)^2+\sqrt{\nu_2}\rho_2(k+2)^2]}{2\sqrt{2}a[(k+1)\rho_1+k\rho_2]}$

Table 4.2: The temporal decay rate β for low-viscosity waves on an interface, with the symbols as defined in table 4.1. Where used, ω denotes the relevant angular oscillation frequency as given in table 4.1

A summary of the lowest-order approximations in the kinematic viscosity ν as derived by Lamb [1932] and Miller and Scriven [1968] for the angular frequency of oscillation ω is given in table 4.1, and for the temporal decay rate β in table 4.2. The frequency is shown to depend only on the densities of two fluids, and so the nature of the interface is unimportant. The viscosity is also unimportant in determining the frequency, with those given in 4.1 identical to those found when assuming inviscid flow. The decay rates, however, prove not to be independent of either the interfacial behaviour or the viscosity. Lamb [1932] provides the full solution for a 2D air/water interface, in particular showing that vorticity in the water is concentrated in a layer of thickness $\sqrt{2\nu/\omega}$ near the interface, of strength order ν^0. The circulation density at the interface γ, defined to be the integral of the vorticity across this layer, will therefore be order $Re^{-1/2}$ and hence small. Unfortunately, Miller and Scriven [1968] do not derive the full solution to the spherical flow field, or give explicit scalings for the interfacial vorticity. However, Craik [1985] does state that the interfacial vorticity for both an interface between two fluids of non-negligible density and for an inextensible interface is again restricted to a layer of thickness $\sqrt{2\nu/\omega}$, but is of strength order $\nu^{-1/2}$ on both sides. Hence, the circulation density will be order Re^0, significantly higher than for a free surface. The reason for this difference with the free surface case is that the fluid is now constrained by the no-slip condition at the interface, whereas for a free surface it is free to move unhindered. This distinction will be discussed in greater detail in the following sections.

As will be explained later, a balloon membrane may be accurately regarded as a inextensible spherical interface. Though the correct dispersion relation for this flow was given by Miller and Scriven [1968], they do not give full expressions for the flow field. Consequently, we shall re-derive their result here, though using a slightly different method: instead of simplifying the problem into solving for one component of velocity and one component of vorticity, we shall follow the work of Lamb [1932] on more simplified situations, and introduce a velocity potential and stream function. The interfacial conditions for an elastic interface are then algebraically different from those given by Miller and Scriven [1968] (though the physically they are the same), and so we are required to derive the interfacial conditions ourselves, as they do not appear anywhere in the literature. Furthermore, Miller and Scriven [1968] do not give expressions for the full flow field, as we require; we are therefore required to do so ourselves, to obtain another result not given in the literature. The reason we follow

Lamb [1932] and introduce a velocity potential and stream function is that we wish to examine the influence of vorticity in detail. The velocity potential will describe the inviscid and irrotational part of the flow, whereas the stream function will describe the viscous and rotational part of the flow. This method will allow us to easily and clearly isolate the viscous interfacial boundary layer. This is important because, as will be described in chapter 6, the vorticity within this boundary layer may drive the late-time growth of the interfacial amplitude. This explicit derivation of the vorticity near an elastic, spherical interface is also not found in any other published work that we have seen.

4.3.2 Equations of motion

For all the cases we will consider, the basic equations for the velocity field are the same: the linearised Navier-Stokes equations

$$\frac{\partial \boldsymbol{u}}{\partial t} = -\frac{1}{\rho}\nabla p + \nu \nabla^2 \boldsymbol{u}, \tag{4.1}$$

$$\nabla . \boldsymbol{u} = 0, \tag{4.2}$$

where ν is the kinematic viscosity. The dynamic viscosity is denoted $\mu = \rho\nu$.

We then follow Lamb [1932], and introduce a scalar velocity potential ξ and vector $\boldsymbol{\psi}$ such that the velocity $\boldsymbol{u}$ is given by

$$\boldsymbol{u} = \nabla \xi + \nabla \times \boldsymbol{\psi}. \tag{4.3}$$

Inserting (4.3) into (4.2) implies ξ satisfies Laplace's equation,

$$\nabla^2 \xi = 0. \tag{4.4}$$

Taking the curl of (4.1), and using the vector identity

$$\nabla \times \nabla \times \boldsymbol{f}(\boldsymbol{x}) = \nabla(\nabla . \boldsymbol{f}(\boldsymbol{x})) - \nabla^2 \boldsymbol{f}(\boldsymbol{x}) \tag{4.5}$$

for any $\boldsymbol{f}(\boldsymbol{x})$, leads to

$$\nabla^2 \left(\boldsymbol{\psi}_t - \nu \nabla^2 \boldsymbol{\psi} \right) = 0. \tag{4.6}$$

The vector $\boldsymbol{\psi}$ will then be a solution if it satisfies

$$\boldsymbol{\psi}_t = \nu \nabla^2 \boldsymbol{\psi}. \tag{4.7}$$

It is important to note that ∇^2 in the above equation is the vector Laplacian, that is only equal to simply applying the scalar Laplacian to each component in Cartesian coordinates. Otherwise, it is effectively defined by equation (4.5).

As we are investigating periodic waves, we shall assume the flow is harmonic in time and use separation of variables, so that

$$\boldsymbol{X_i} = X_i(x_1) Y_i(x_2) Z_i(x_3) e^{-nt} \tag{4.8}$$

for (Eulerian) spacial variables $\boldsymbol{x}$ and time dependence n. Equations (4.1) and (4.2) then determine the functions $\boldsymbol{X_i}$, while the boundary conditions determine the constants. The wavenumber, when it arises, will be denoted k.

Here, we assume in advance that k is real and n complex. The angular frequency of oscillation ω is then given by the imaginary part of n, and the temporal damping coefficient (denoted β) by the real part of n. This is relevant to a dropped balloon, when traveling waves are created at a single moment in time. Later, we shall consider the opposite case of n purely imaginary and k complex. The imaginary part of k then gives the spacial damping coefficient α that is relevant to the oscillated balloons, where energy is constantly being put into the system by the forcing to create a system of standing waves.

As it was shown in chapter 2 that the shape of our balloons when inflated may be reasonably approximated by a sphere, we work in spherical polar coordinates (r, θ, ϕ) where θ is the azimuthal angle, and ϕ is the polar angle. We also assume axisymmetry, neglecting all flow in the θ direction, so that $\xi = \xi(t, r, \phi)$ and the vector $\boldsymbol{\psi} = (0, \psi(t, r, \phi), 0)$. We note that the scalar function ψ is not itself a stream function, but is related to the Stokes stream function Ψ by

$$\psi = -\frac{\Psi}{r \sin \phi}. \tag{4.9}$$

In spherical coordinates, (4.4) becomes

$$\nabla^2 \xi = \frac{\partial^2 \xi}{\partial r^2} + \frac{2}{r}\frac{\partial \xi}{\partial r} + \frac{1}{r^2}\frac{\partial^2 \xi}{\partial \phi^2} + \frac{\cot \phi}{r^2}\frac{\partial \xi}{\partial \phi} = 0. \tag{4.10}$$

In equation (4.7) with $\boldsymbol{\psi} = (0, \psi(t, r, \phi), 0)$, the r and ϕ components are identically zero, with the θ component giving

$$\frac{\partial \psi}{\partial t} = \nu \left(\frac{\partial^2 \psi}{\partial r^2} + \frac{2}{r}\frac{\partial \psi}{\partial r} + \frac{1}{r^2}\frac{\partial^2 \psi}{\partial \phi^2} + \frac{\cot \phi}{r^2}\frac{\partial \psi}{\partial \phi} - \frac{1}{r^2 \sin^2 \phi}\psi \right). \tag{4.11}$$

Note that the right-hand side is equal to $\nabla^2 \psi - \psi / r^2 \sin^2 \phi$, and not simply $\nabla^2 \psi$.

As given by Lamb [1932] and Miller and Scriven [1968], the full solution to the above equations using separation of variables may be written as

$$\xi = \sum_{k=0}^{\infty} R_k(r) F_k(\phi), \tag{4.12}$$

$$\psi = \sum_{k=0}^{\infty} \tilde{R}_k(r) \tilde{F}_k(\phi), \tag{4.13}$$

where k is the wavenumber. To ensure that the solution is π-symmetric (so that the solution is continuous at $\phi = 0$ and π), it is required that $k \in \mathbb{N}$. Unlike for the planar case, k here is non-dimensional and approximately equal to $2\pi a/\lambda$ (though as λ varies with ϕ, this is not a proper definition); k is more accurately regarded as double the number of waves on the balloon. The individual functions are then

$$R_k(r) = A_1 r^k + A_2 r^{-k-1}, \tag{4.14}$$

$$\tilde{R}_k(r) = B_1 j_k \left(\sqrt{\frac{n}{\nu}} r \right) + B_2 y_k \left(\sqrt{\frac{n}{\nu}} r \right), \tag{4.15}$$

$$F_k(\phi) = C_1 P_k(\cos\phi) + C_2 Q_k(\cos\phi), \tag{4.16}$$

$$\tilde{F}_k(\phi) = D_1 \frac{\partial}{\partial\phi}\left[P_k(\cos\phi)\right] + D_2 \frac{\partial}{\partial\phi}\left[Q_k(\cos\phi)\right]. \tag{4.17}$$

The functions P_k and Q_k are the Legendre functions of the first and second kind, respectively; $P_k(\cos\phi)$ is also known as the spherical harmonic of degree k and order 0. The functions j_k and y_k are known as the spherical Bessel functions of the first and second kind, that are defined in terms of ordinary Bessel functions of the first (J_k) and second (Y_k) kind as

$$j_k(r) = \sqrt{\frac{\pi}{2r}} J_{k+1/2}(r), \tag{4.18}$$

$$y_k(r) = \sqrt{\frac{\pi}{2r}} Y_{k+1/2}(r). \tag{4.19}$$

For a spherical interface, unlike a 2D interface, the inviscid theory predicts the amplitude of the wave depends on its position, ϕ, with a maximum amplitude at 0 and π (though the order of the Legendre polynomial will affect whether the two poles are in or out of phase) and minimum amplitude for the anti-nodes nearest to $\pi/2$. Consequently, a simple test of this theory is to measure the variation of wave amplitude around a balloon. Experimental measurements of the standing wave amplitude on two different 130mm balloons held underwater are given in figure 4.3. The results show a good agreement to this theory; only small discrepancies appear as ϕ nears $\pi/2$ (the bottom of the balloon), but this is likely only a consequence of the supporting tube holding the balloon in place.

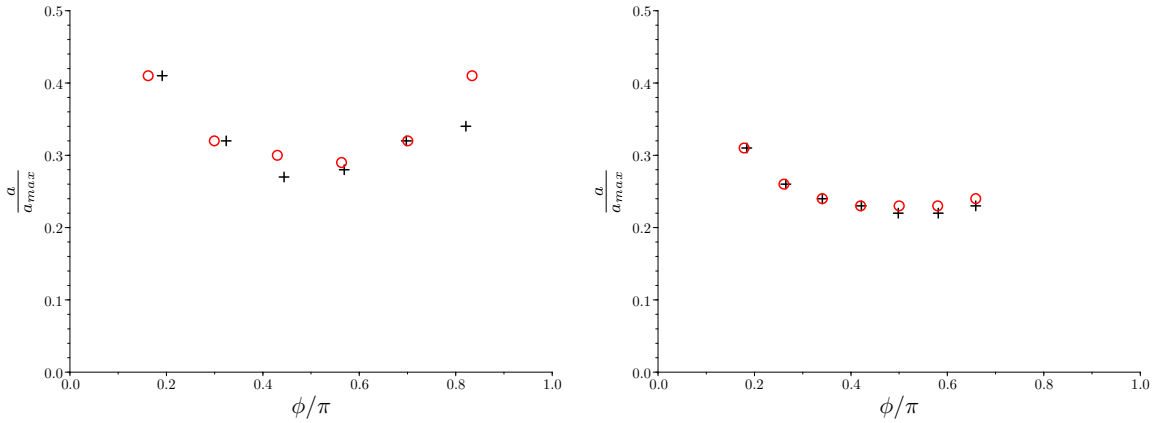

(a) $k = 7$, $\sigma = 111$ N/m

(b) $k = 12$, $\sigma = 114$ N/m

Figure 4.3: The experimental amplitude (scaled against the maximum) around a spherical 130mm balloon held underwater and forced at a set frequency (black) matched against the predictions of linear potential theory (red).

4.3.3 Boundary Conditions away from the interface

We wish to consider waves on a fluid-fluid interface, so the above equations of motion must be satisfied by different potentials in each fluid. Flow quantities inside the interface will be denoted by a subscript 1, with those outside denoted subscript 2.

There are two types of boundary condition: those applied at the interface, and those not. The conditions not applied at the interface are simpler, being

$$\xi_1, \psi_1 < \infty \qquad \text{at } r = 0, \tag{4.20}$$

$$\xi_i, \psi_i < \infty \qquad \text{at } \phi = 0, \pi \text{ for } i = 1, 2 \tag{4.21}$$

$$\xi_2, \psi_2 < \infty \qquad \text{as } r \to \infty. \tag{4.22}$$

From now on, and in the interests of simplicity, we only consider waves of a single, real wavenumber. This is directly applicable to the stationary balloons, as the forcing was of only a single frequency. For the dropped balloons, when a range of wave frequencies is seen, the full solution may be recovered by the linear addition of terms representing each wavenumber.

Applying these boundary conditions to solutions given by (4.12) and (4.13) leads to

$$\xi_1 = A_1 \, r^k \, P_k(\cos\phi) \, e^{-nt}, \tag{4.23}$$

$$\xi_2 = A_2 \, r^{-k-1} \, P_k(\cos\phi) \, e^{-nt}, \tag{4.24}$$

$$\psi_1 = B_1 \, j_k(m_1 r) \, \frac{\partial}{\partial\phi} \left[P_k(\cos\phi) \right] \, e^{-nt}, \tag{4.25}$$

$$\psi_2 = B_2 \, h_k(m_2 r) \, \frac{\partial}{\partial\phi} \left[P_k(\cos\phi) \right] \, e^{-nt}, \tag{4.26}$$

where $m_i = (n/\nu_i)^{1/2}$ and h_k the spherical Hankel function of the first kind, $h_k(r) = j_k(r) + i \, y_k(r)$. Note that h_k appears because m_2 turns out to be proportional to $1 + i$, and as shall be shown in section 4.3.7, $j_k((1+i)r) \sim (1/r)\exp[r]$ but $h_k((1+i)r) \sim (1/r)\exp[-r]$ as $r \to \infty$.

4.3.4 Boundary conditions at the interface

As stated previously, Miller and Scriven [1968] do not use a velocity potential and stream function, and so we cannot use the interfacial conditions they derive. Consequently, we must rederive them ourselves.

We suppose the interface to be given by linear deformations about $r = a$. Deformations in the r direction are given by $\eta(\phi, t)$, with deformations in the ϕ directions given by $\zeta(\phi, t)$. The interface is therefore given by $(a, 0, 0) + \boldsymbol{\eta} = (a + \eta, 0, \zeta)$. After linearisation, however, the interfacial boundary conditions are all applied at simply $r = a$.

The interfacial boundary conditions then arise from the continuity of velocities and stresses across the boundary. Specifically, they are continuity of normal velocity and stress (as commonly used for an interface between inviscid fluids), and continuity of tangential velocity and stress (that are only non-trivial for a viscous interface). Continuity of normal velocity implies

$$\frac{\partial \eta}{\partial t} = u_1 = \frac{\partial \xi_1}{\partial r} + \frac{1}{r^2 \sin\phi} \frac{\partial}{\partial\phi} \left(r \sin(\phi) \psi_1 \right), \tag{4.27}$$

$$\frac{\partial \eta}{\partial t} = u_2 = \frac{\partial \xi_2}{\partial r} + \frac{1}{r^2 \sin\phi} \frac{\partial}{\partial \phi} \left(r \sin(\phi) \psi_2 \right). \tag{4.28}$$

These conditions are commonly referred to as the (linearized) kinematic conditions. The continuity of tangential velocities is equivalent to the condition of no-slip between the fluids and the interface, and may be written as

$$\frac{\partial \eta}{\partial t} = w_1 = \frac{1}{r} \frac{\partial \xi_1}{\partial \phi} - \frac{1}{r \sin\phi} \frac{\partial}{\partial r} \left(r \sin(\phi) \psi_1 \right), \tag{4.29}$$

$$\frac{\partial \eta}{\partial t} = w_2 = \frac{1}{r} \frac{\partial \xi_2}{\partial \phi} - \frac{1}{r \sin\phi} \frac{\partial}{\partial r} \left(r \sin(\phi) \psi_2 \right). \tag{4.30}$$

To satisfy these conditions, the deformations to the interface must be of the form

$$\eta(\phi, t) = C P_k(\cos\phi) e^{-nt}, \tag{4.31}$$

$$\zeta(\phi, t) = D \frac{\partial}{\partial \phi} \left[P_k(\cos\phi) \right] e^{-nt}, \tag{4.32}$$

for some constants C and D.

The final two conditions arise from continuity of stresses, normal and tangential. For fluid stress tensor $\boldsymbol{\tau}$ and interface with normal $\boldsymbol{n}$ and tangent $\boldsymbol{t}$, these conditions, as derived by Batchelor [1967] (p. 69), are

$$[\boldsymbol{n}.\boldsymbol{\tau}.\boldsymbol{n}]_1^2 = -T \nabla.\boldsymbol{n}, \tag{4.33}$$

$$[\boldsymbol{n}.\boldsymbol{\tau}.\boldsymbol{t}]_1^2 = -\boldsymbol{t}.\nabla T, \tag{4.34}$$

to be evaluated at the interface. The first condition is a statement of continuity of the normal stresses, and is also known as the Laplace-Young equation as discussed in chapter 2. The second condition is a statement of continuity of the tangential stresses, with shear stresses within the fluids balancing gradients in tension on the interface. For a pure fluid-fluid interface, where the tension will be constant, this implies that the shear stresses in either fluid will be equal. For a membrane-covered interface, however, gradients in the surface tension may exist. Note that these conditions are derived neglecting shear stresses within the membrane, a suitable approximation when the membrane is thin.

In spherical coordinates, the relevant stresses are given by

$$\boldsymbol{n}.\boldsymbol{\tau}.\boldsymbol{n} = \tau^{rr} = -p + 2\mu \frac{\partial u}{\partial r}, \tag{4.35}$$

$$\boldsymbol{n}.\boldsymbol{\tau}.\boldsymbol{t} = \tau^{r\phi} = \mu \left(r \frac{\partial}{\partial r} \left(\frac{w}{r} \right) + \frac{1}{r} \frac{\partial u}{\partial \phi} \right). \tag{4.36}$$

Continuity of normal stress, given by (4.33), is usually referred to as the dynamic condition. The difference in normal stress is balanced by the interfacial tension T multiplied by the curvature κ:

$$\tau_1^{rr} - \tau_2^{rr} = T\kappa \qquad \text{at } r = a. \tag{4.37}$$

The left hand side may be rewritten as

$$\tau_1^{rr} - \tau_2^{rr} = \left[-p_i + \mu_i \frac{\partial u_i}{\partial r} \right]_2^1. \tag{4.38}$$

The pressures at the interface may be determined using the linearized Bernoulli's equation,

$$\frac{\partial \xi_i}{\partial t} + \frac{p_i}{\rho_i} = C_i(t), \tag{4.39}$$

for some unknown functions C_1 and C_2. This is derived from equation (4.1) (see Lamb [1932] or Lucassen-Reynders and Lucassen [1969]), with the terms relating to viscosity and the stream function dropping out after application of equations (4.4) and (4.7). This suggests that for such a purely rotational flow there is no pressure gradient; this is indeed correct, and an example of such a flow is Couette flow that is driven by the shearing motion of two parallel plates, as described by Lamb [1932].

The left-hand side of (4.37) may therefore be rewritten

$$\tau_1^{rr} - \tau_2^{rr} = [-\rho_i C_i]_2^1 + \left[\rho_i \frac{\partial \phi_i}{\partial t} + \mu_i \frac{\partial u_i}{\partial r}\right]_2^1. \tag{4.40}$$

The curvature of the interface is given by

$$\kappa = -\nabla . \boldsymbol{n} \tag{4.41}$$

where $\boldsymbol{n}$ is the unit normal to the interface. For an interface defined to be $(a + \eta, 0, \zeta)$, the normal is

$$\boldsymbol{n} = \frac{\left(1, 0, -\frac{\eta_\phi}{r}\right)}{\left(1 + \left(\frac{\eta_\phi}{r}\right)^2\right)^{1/2}}, \tag{4.42}$$

and hence the linearised curvature is

$$\kappa = \frac{2}{a}\left(1 - \frac{\eta}{a}\right) - \frac{1}{a^2}\left(\eta_{\phi\phi} + \eta_\phi \cot\phi\right). \tag{4.43}$$

The first term is the curvature term for a spherical surface of radius r, with the rest an adjustment due to the linear perturbation η.

For a pure fluid-fluid interface, the tension T is typically considered to be constant. However, for an interface covered by a thin elastic membrane (such as a water-filled balloon), this is clearly not the case. Instead, we follow the work on covered interfaces detailed by Lucassen-Reynders and Lucassen [1969] and suppose that T takes the form

$$T = \sigma + \tilde{E}(\nabla . \boldsymbol{\eta}), \tag{4.44}$$

where σ and $\tilde{E}$ are constants known as the membrane tension and membrane elasticity, respectively. This supposes the tension is determined by the large uniform tension resulting from the initial inflation of the balloon, together with small changes linearly related to small changes in the local area of the interface. It also assumes that the membrane stress is isotropic. Providing the post-inflation deformations to the interface remain small, our work in chapter 2 does suggest that the tension-strain relationship may indeed be approximated by an isotropic linear relationship. Due to the non-linearity of the stress-strain relation for rubber, the value of E will depend of the value of σ. However, we may use the radius-tension relation for inflation found in chapter 2 for spherical balloons to estimate typical values of σ and $\tilde{E}$: for a fully-inflated balloon, $\sigma \approx 200$ N/m, $\tilde{E} \approx 100$ N/m. As the surface

deformations are small, the constant term σ will then usually be much larger. If we wished to include the effects of visco-elastic nature of rubber, we could include a third term proportional to $\partial(\nabla.\boldsymbol{\eta})/\partial t$, as in the Kelvin-Voigt model (see chapter 5). However, as discussed in chapter 1, we may neglect it here due to the short timescales of the interfacial waves. While the theory described above has been applied to covered interfaces before, there is no evidence in the literature of it being applied directly to model a membrane-covered interface.

Going back to equation (4.37), the right-hand side after linearisation becomes

$$\begin{aligned} T\kappa = \frac{2\sigma}{a} - \frac{\sigma}{a^2}\left(2\eta + \frac{\partial^2\eta}{\partial\phi^2} + \cot\phi\frac{\partial\eta}{\partial\phi}\right) \\ + \frac{2\tilde{E}}{a}\left(\frac{2}{a}\eta + \frac{1}{a}\frac{\partial\zeta}{\partial\phi} + \frac{\cot\phi}{a}\zeta\right). \end{aligned} \tag{4.45}$$

Combining (4.40) and (4.45) gives us the full condition. If we consider the situation when there is no flow, it becomes

$$[-\rho_i C_i]_2^1 = \frac{2\sigma}{a}, \tag{4.46}$$

a restatement of the Laplace-Young equation for a spherical interface of radius a. The constants terms on either side therefore cancel, leaving us with the full normal stress condition:

$$\begin{aligned} \left[\rho_i\frac{\partial\phi_i}{\partial t} + \mu_i\frac{\partial u_i}{\partial r}\right]_2^1 &= -\frac{\sigma}{a^2}\left(2\eta + \frac{\partial^2\eta}{\partial\phi^2} + \frac{\partial\eta}{\partial\phi}\cot\phi\right) \\ &\quad + \frac{2\tilde{E}}{a}\left(\frac{2}{a}\eta + \frac{1}{a}\frac{\partial\zeta}{\partial\phi} + \frac{\cot\phi}{a}\zeta\right) \qquad \text{at } r = a. \end{aligned} \tag{4.47}$$

The final condition is then continuity of tangential stress across the interface, as given by (4.34). This may be written as

$$\tau_1^{r\phi} - \tau_2^{r\phi} = \frac{1}{r}\frac{\partial T}{\partial\phi} \qquad \text{at } r = a. \tag{4.48}$$

Using (4.36), the left-hand side is

$$\tau_1^{r\phi} - \tau_2^{r\phi} = \left[\mu_i\left(\frac{\partial w_i}{\partial r} - \frac{w_i}{a} + \frac{1}{a}\frac{\partial u_i}{\partial\phi}\right)\right]_2^1. \tag{4.49}$$

Using (4.44), the right-hand side is

$$\begin{aligned} \frac{1}{a}\frac{\partial T}{\partial\phi} &= \frac{\tilde{E}}{a}\frac{\partial(\nabla.\boldsymbol{\eta})}{\partial\phi} \\ &= \frac{\tilde{E}}{a^2}\left(\frac{\partial\eta}{\partial\phi} + \frac{\partial^2\zeta}{\partial\phi^2} + \cot\phi\frac{\partial\zeta}{\partial\phi} - (1+\cot^2\phi)\zeta\right). \end{aligned} \tag{4.50}$$

The tangential stress condition in full is thus

$$\begin{aligned} \mu_1\left(\frac{\partial w_1}{\partial r} - \frac{w_1}{a} + \frac{1}{a}\frac{\partial u_1}{\partial\phi}\right) - \mu_2\left(\frac{\partial w_2}{\partial r} - \frac{w_2}{a} + \frac{1}{a}\frac{\partial u_2}{\partial\phi}\right) \\ = \frac{\tilde{E}}{a^2}\left(\frac{\partial\eta}{\partial\phi} + \frac{\partial^2\zeta}{\partial\phi^2} + \cot\phi\frac{\partial\zeta}{\partial\phi} - (1+\cot^2\phi)\zeta\right). \end{aligned} \tag{4.51}$$

These interfacial conditions have all been derived before; their use in modeling a spherical membrane-covered interface (a water balloon) is new, however.

4.3.5 Dispersion relation

There are six interfacial equations: (4.27) - (4.30), (4.47), (4.51). Substituting in the correct form of the potentials, stream functions and interfacial deformations, the functions of ϕ and t may all be cancelled out to leave six homogeneous linear equations for the six unknown constants: A_1, A_2, B_1, B_2, C, and D. These equations may be rewritten as

$$\boldsymbol{M}\boldsymbol{v} = 0, \tag{4.52}$$

where $\boldsymbol{M}$ is a six-by-six matrix, and $\boldsymbol{v} = (A_1, A_2, B_1, B_2, C, D)$. A solution in which the flow velocities are not uniformly zero will only exist if

$$Det(\boldsymbol{M}) = 0, \tag{4.53}$$

an equation known as the dispersion relation. The matrix $\boldsymbol{M}$ may be determined using the conditions derived above; to help simplify it, we use the following relations for spherical Bessel functions taken from *http://dlmf.nist.gov/10*:

$$j_k(r) = \frac{r}{2k+1}[j_{k-1}(r) + j_{k+1}(r)], \tag{4.54}$$

$$\frac{\partial}{\partial r} j_k(r) = \frac{k}{r} j_k(r) - j_{k+1}(r). \tag{4.55}$$

The same form of relations hold for the spherical Hankel function h_k.

In the interests of simplification, we define the following functions

$$Q^j(k) = -\frac{k+1}{a} j_k(m_1 a) + m_1 j_{k+1}(m_1 a), \quad Q^h(k) = -\frac{k+1}{a} h_k(m_2 a) + m_2 h_{k+1}(m_2 a),$$

$$F_1(k) = -n a^k \rho_1 + 2\rho_1 \nu_1 k(k-1) a^{k-2},$$

$$F_2(k) = \frac{n\rho_2}{a^{k+1}} - \frac{2\rho_2\nu_2(k+1)(k+2)}{a^{k+3}},$$

$$G^j(k) = -\frac{2k(k+1)\rho_1\nu_1}{a}(-Q^j(k) - 2j_k), \quad G^h(k) = -\frac{2k(k+1)\rho_2\nu_2}{a}(-Q^h(k) - 2h_k),$$

$$H^j(k) = \left(m_1^2 - \frac{(k+1)(k-2)}{a^2}\right) j_k(m_1 a) - 2\frac{m_1}{a} j_{k+1}(m_1 a),$$

$$H^h(k) = \left(m_2^2 - \frac{(k+1)(k-2)}{a^2}\right) h_k(m_2 a) - 2\frac{m_2}{a} h_{k+1}(m_2 a).$$

The dispersion relation is then

$$\begin{vmatrix} ka^{k-1} & 0 & -\frac{k(k+1)j_k(m_1a)}{a} & 0 & n & 0 \\ 0 & -\frac{k+1}{a^{k+2}} & 0 & -\frac{k(k+1)h_k(m_2a)}{a} & n & 0 \\ a^{k-1} & 0 & Q^j(k) & 0 & 0 & n \\ 0 & a^{-k-2} & 0 & Q^h(k) & 0 & n \\ F_1(k) & F_2(k) & G^j(k) & G^h(k) & \frac{\sigma(k-1)(k+2)}{a^2} - \frac{4\tilde{E}}{a^2} & \frac{2\tilde{E}k(k+1)}{a^2} \\ 2a^{k-2}\rho_1\nu_1(k-1) & \frac{2\rho_2\nu_2(k+2)}{a^{k+3}} & \rho_1\nu_1H^j(k) & -\rho_2\nu_2H^h(k) & 2\tilde{E} & -k(k+1)\tilde{E} \end{vmatrix} = 0. \tag{4.56}$$

Expanding this out, we obtain an equation relating the wavenumber k to the angular frequency ω. In its full form, it is non-linear and highly complicated. There are, however, two simplifications relevant to the bursting of water balloons we may use. One is that the viscosity of both phases will be small, more accurately stated as the Reynolds number being large. This will be discussed later. First, we discuss the other simplification, that our membrane may be regarded as inextensible.

Infinite elasticity approximation

For a pure fluid-fluid interface (where $\tilde{E} = 0$), there will be two physically relevant solutions to (4.56), those corresponding to the capillary waves. Introducing elasticity then has two effects: not only does it affect the capillary waves (as discussed in section 4.3.1), it also introduces two more physically relevant solutions to the dispersion relation. These extra solutions represent a different type of wave known as a dilational wave, that correspond to longitudinal oscillations of the membrane. They make the surface expand and contract without significant transverse motion. As explained by Lucassen [1968], these waves are analogous to longitudinal elastic waves (to be discussed in chapter 5) in a membrane of effective thickness the width of the interfacial boundary layer $\sqrt{2\nu/\omega}$, whereas the capillary waves are analogous to transverse waves in an elastic membrane of effective thickness the wavelength λ.

The relative importance of the capillary and dilational waves is determined by the relevant non-dimensional parameter $\mathcal{E}$, where

$$\mathcal{E} = \frac{\tilde{E}k^2}{a^2\nu^{1/2}\rho\omega^{3/2}}, \tag{4.57}$$

as given by Christensen [2005]. It is determined by the balance between elastic forces in the membrane, and shear forces within the fluid.

Dilational waves may only exist when $\mathcal{E}$ is finite and non-zero, being most significant when $\mathcal{E} = 1$. However, while the frequency of the dilational waves is the same as the capillary waves, their wavelengths and decay coefficients are different. For the dilational waves, Lucassen-Reynders and Lucassen [1969] state that the typical spacial decay length is of similar order to their wavelength. Consequently, even for finite elasticity they are damped out much faster than the capillary waves, usually being significant only near the forcing point. They may therefore be neglected in many situations. There is, however, also another reason why they may be neglected for our experiments.

Rubber is typically considered to be a very elastic material, that permits easy deformation. Yet when compared to the shear stresses within a near-inviscid flow such as that under consideration here, the stresses required to deform a rubber membrane are very large. We therefore consider the so-called inextensible limit, $\mathcal{E} \to \infty$. In this limit, a small extension of interface produces a large restoring force in the membrane, relative to the shear forces within the fluid. Local changes in the area of the interface may therefore be neglected to first order. Consequently, dilational waves may be neglected (as the membrane cannot support them). In 2D flow, there is then no tangential deformation of the interface, and the tangential interface conditions may be simplified to enforcing no tangential flow at the interface. In spherical coordinates, however, the situation is not so straightforward, as a normal deformation may be accompanied by a tangential deformation such that the local surface area is conserved. The limit of infinite elasticity is therefore not the same as assuming no tangential flow at the interface.

For typical values seen in oscillated water balloons, $\mathcal{E} \approx O(10^2) >> 1$, so approximating the membrane as an inextensible film ($\tilde{E} \to \infty$) is appropriate. This means that dilational waves may be neglected. The dispersion relation (4.56) applicable to our membrane-covered interfaces may then be simplified by considering only terms of order $\tilde{E}$ (as the terms of order $\tilde{E}^2$ cancel out). In contrast, the terms of order $\tilde{E}^0$ (equivalent to setting $\tilde{E} = 0$) give the correct dispersion relation for a pure fluid-fluid interface with constant surface tension. Later, in section 4.5.1, we shall also consider the effect of finite membrane elasticity.

Low viscosity limit

The second simplification is that of low viscosity in the fluids, relative to their inertia. That this is accurate to model our experiments may be seen by considering the relevant Reynolds numbers of the flows: a typical Reynolds number for the flow in air will be $Re \approx 10^4$, and for the flow in water, $Re \approx 10^3$. As $Re >> 1$, so the viscosities of all fluids involved will be small relative to the inertia of the fluids. We therefore assume that the kinematic viscosities of the two fluids, ν_1 and ν_2, are both small and of similar order (at room temperature and pressure, $\nu = 1.5 \times 10^7$ m^2/s for air, and $\nu = 1 \times 10^6$ m^2/s for water). As suggested by table 4.2, we may expand either n or k in powers of the small parameter ϵ, where $\nu_1^{1/2} = b_1\epsilon$ and $\nu_2^{1/2} = b_2\epsilon$ for some order 1 constants b_1 and b_2. Focusing first on the time decay, we then have

$$n = n_0 + \epsilon n_1 + \epsilon^2 n_2 + ... \tag{4.58}$$

4.3.6 Angular frequency of oscillation

The first term n_0 is found from (4.56) by setting $\nu = 0$. In the most general case, this is

$$n_0 = i\omega = i\sqrt{\frac{\sigma k(k+1)(k-1)(k+2)}{a^3[(k+1)\rho_1 + k\rho_2]}}, \tag{4.59}$$

where ω is the angular frequency of the oscillation. This relation is accurate to first order for both pure ($\tilde{E} = 0$) and membrane-covered ($\tilde{E} = \infty$) interfaces (and all values of $\tilde{E}$ in between).

We consider in detail the two most relevant cases: air/water interfaces, and water/water interfaces. In our experiments, these interfaces are membrane-covered and hence inextensible. We also consider, to

provide a comparison, what happens for the equivalent pure fluid-fluid interfaces. The air/water case may be simplified by assuming that the density of the fluid outside the membrane may be neglected, $\rho_2 = 0$. Consequently, the external fluid provides no tangential stress and only a constant normal stress to the membrane (what is referred to as a free-surface for such a pure fluid-fluid interface). Using these assumptions, the leading order term for an air/water interface, whether membrane-covered or pure, is

$$n_0 = i\omega_1 = i\sqrt{\frac{\sigma k(k-1)(k+2)}{a^3\rho}}. \tag{4.60}$$

To model a water/water interface, we assume the fluids on either side of the membrane are identical, with equal densities and viscosities. This leads to the leading-order term

$$n_0 = i\omega_2 = i\sqrt{\frac{\sigma k(k+1)(k-1)(k+2)}{a^3\rho(2k+1)}}. \tag{4.61}$$

These frequencies were first found, for a pure fluid-fluid interface, by Rayleigh [1879] and Lamb [1932], respectively. Note that when we refer to a pure water/water interface, we mean one on which a constant but non-zero tension acts. This situation is entirely theoretical, as at a truly pure water/water interface there would be no surface tension (and therefore no restoring force). Consideration of this situation is included for comparison with the membrane-covered case, though it would be applicable to an interface between two immiscible liquids of similar density and viscosity to water.

Experimental confirmation of these dispersion relations in the membrane-covered cases is given in figures 4.4 and 4.5, for the two cases of water and air external to the membrane; there is no evidence in the literature of any such experiments, measuring the properties of surface waves on water-filled balloons, having been done before. The frequency ω was assumed to be given by the frequency of the input, and the tension σ was determined as described in section 2.6. The wavenumber k was found by counting the number of waves around the balloon. It is clear that here, our experimental data closely fits the theoretical prediction of equation (4.59). This suggests that our use of a linear potential flow model is correct, as a first approximation. The goodness of this fit is not affected by introducing the first-order viscous correction to the oscillation frequency, found in the next section as the imaginary part of n_1. As the viscosity of water is so small, any changes to oscillation frequency introduced by viscosity are so small as to be insignificant in comparison to the inviscid approximation. The finite size of the tank also does not influence these results, as flow velocities decay like $(a/r)^{k+1}$ outside the balloon. The walls were typically at a distance 0.4 m from the balloon, implying typical velocities near the walls a factor $(0.1/0.4)^{11} \approx 10^{-6}$ smaller than at the interface. Consequently, the no-flow conditions at the tank walls were approximately satisfied, and thus had no impact on the flow near the balloon.

From these first-order approximations to the frequency, we may estimate the phase speed of waves, $c_p = \omega/k$. In particular, for an air/water interface,

$$c_{p_{air}} = \sqrt{\frac{\sigma(k-1)(k+2)}{ka^3\rho}}, \tag{4.62}$$

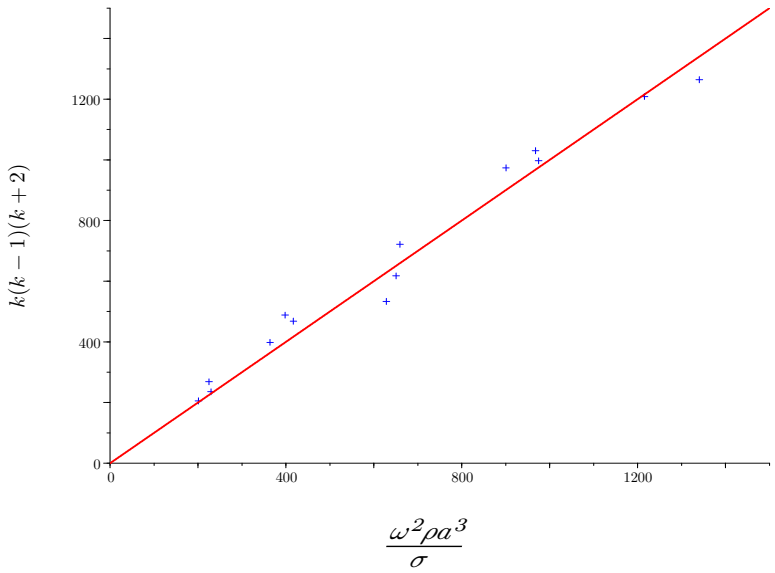

Figure 4.4: The relation between σ, ω and k for water-filled balloons held and oscillated in air ($\rho_1 = 1000\text{Kgm}^{-3}$, $\rho_2 = 0$). Displayed is the experimental data (blue marks) and the theoretical prediction of equation (4.59) (red line)

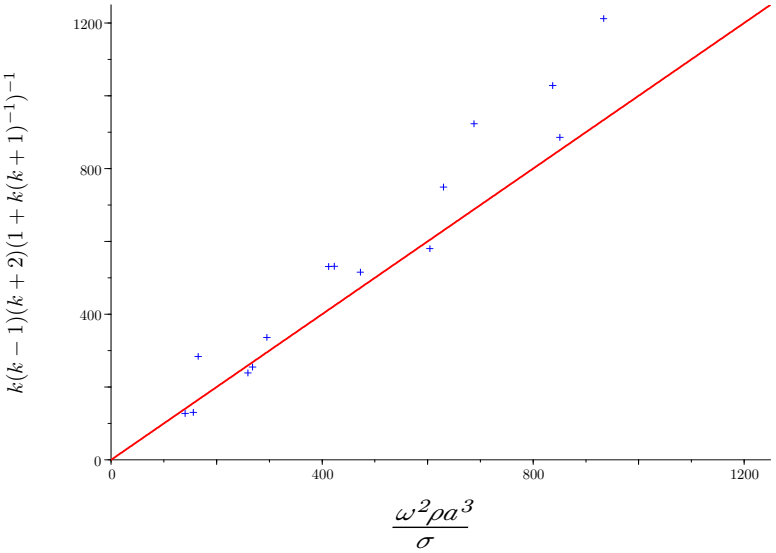

Figure 4.5: The relation between σ, ω and k for water-filled balloons held and oscillated underwater ($\rho_2 = \rho_1 = 1000\text{Kg m}^{-3}$). Displayed is the experimental data (blue marks) and the theoretical prediction of equation (4.59) (red line)

and for a water/water interface

$$c_{p_{water}} = \sqrt{\frac{\sigma(k+1)(k-1)(k+2)}{k(2k+1)a^3\rho}} = \sqrt{\frac{k+1}{2k+1}}c_{p_{air}}. \tag{4.63}$$

For all $k > 1$ these phase speeds are monotone increasing in k. Though more complicated to calculate, the same is true for the group velocities

$$c_g = \frac{\partial\omega}{\partial k}. \tag{4.64}$$

This therefore implies that high wavenumbers travel fastest, or equivalently that short waves travel fastest. This explains our observations from chapter 1 that it is the shorter waves that are visible first when a dropped balloon impacts a rigid surface - waves of all wavenumbers are created at the moment of impact, but it is the shortest ones that travel up the balloon fastest, and thus become visible first.

4.3.7 Temporal decay rate

The second-order term n_1 from the expansion of equation (4.56), is found by considering only terms of order ϵ. To do this, we need to consider the behaviour of the spherical Bessel and Hankel functions in the limit $\nu_i \to 0$. All appearances of these functions in (4.56) are with the input

$$ma = \sqrt{\frac{n}{\nu}}a \approx \sqrt{\frac{n_0}{\nu}}a = \pm(1+i)\frac{\omega^{1/2}a}{\sqrt{2}\nu^{1/2}},$$

to first order in ϵ. The inputs to the Bessel and Hankel functions therefore go to infinity along the line $arg(z) = \pm\pi/4$, and not on the real line. We therefore need the following asymptotic form (again from *http://dlmf.nist.gov/10*):

$$j_k(z) \sim \frac{1}{2z}\exp\left[-i\left(z - \frac{k\pi}{2} - \frac{\pi}{2}\right)\right], \quad \text{for } 0 < \arg(z) < \pi, \tag{4.65}$$

$$j_k(z) \sim \frac{1}{2z}\exp\left[i\left(z - \frac{k\pi}{2} - \frac{\pi}{2}\right)\right], \quad \text{for } -\pi < \arg(z) < 0, \tag{4.66}$$

$$h_k(z) \sim \frac{1}{z}\exp\left[i\left(z - \frac{k\pi}{2} - \frac{\pi}{2}\right)\right], \quad \text{for } 0 < \arg(z) < 2\pi. \tag{4.67}$$

In particular, this implies the asymptotic forms for $r \in \mathbb{R}$:

$$j_k((1+i)r) \sim \frac{1}{2(1+i)r}\exp\left[-i\left(r - \frac{k\pi}{2} - \frac{\pi}{2}\right)\right]\exp[r], \tag{4.68}$$

$$h_k((1+i)r) \sim \frac{1}{(1+i)r}\exp\left[i\left(r - \frac{k\pi}{2} - \frac{\pi}{2}\right)\right]\exp[-r], \tag{4.69}$$

and hence the following useful relations

$$\lim_{r\to\infty}\frac{j_{k+1}(\pm(1+i)r)}{j_k(\pm(1+i)r)} = \pm i,$$

$$\lim_{r\to\infty} \frac{h_{k+1}(\pm(1+i)r)}{h_k(\pm(1+i)r)} = -i.$$

Using these results, we can then find the next non-zero term in the expansion of n. These are easily derived from those given in table 4.2, but we repeat them here for clarity. Where there is a square-root and hence a choice of sign, it is chosen to ensure the real part is positive, which represents decay as opposed to growth of the waves in time.

For all cases we consider here, the highest-order decay rate term is

$$\epsilon n_1 = \frac{(2k+1)^2\omega^{1/2}\rho_1\rho_2\nu_1^{1/2}\nu_2^{1/2}}{2\sqrt{2}a[(k+1)\rho_1 + k\rho_2][\rho_1\nu_1^{1/2} + \rho_2\nu_2^{1/2}]}(1-i), \tag{4.70}$$

For an air/water free surface, n_1 is zero, so the decay is given by the next term,

$$\epsilon^2 n_2 = \frac{(2k+1)(k-1)\nu_1}{a^2}. \tag{4.71}$$

However, for an air/water inextensible surface n_1 is not zero, so the decay is dominated by

$$\epsilon n_1 = \frac{(k-1)^2\omega_1^{1/2}\nu_1^{1/2}}{2\sqrt{2}a(k+1)}(1-i). \tag{4.72}$$

Similar behaviour to (4.72) is seen for both a pure water/water interface

$$\epsilon n_1 = \frac{(2k+1)\sqrt{\omega_2}\nu^{1/2}}{4\sqrt{2}a}(1-i), \tag{4.73}$$

and an inextensible water/water interface

$$\epsilon n_1 = \frac{\sqrt{\omega}(2k^2+2k+5)\nu^{1/2}}{2\sqrt{2}a(2k+1)}(1-i). \tag{4.74}$$

It is the real part of n_1 that corresponds to the decay coefficient; the imaginary part represents a small correction to the angular frequency of oscillation. We consider here only the air/water interface with water inside the balloon and air outside. Due to the geometric asymmetry between the inside and outside of a spherical interface, the case with water outside and air inside is slightly different. It was, however, considered by Miller and Scriven [1968], and showed only small qualitative differences from the situation with water inside and air outside the balloon, the decay rate differing only by a function of k.

The decay proportional to ν is associated with viscous decay in the outer flow, away from the interface. Such terms are therefore present in all flows, whatever the form of the interface. The (greater) decay proportional to $\nu^{1/2}$, where present, is associated with the flow in the interfacial boundary layer, and thus only non-zero when there is some resistance to flow at the interface. Note that decay proportional to $\nu^{1/2}$ mirrors that seen in a viscous boundary layer on a solid wall (see Batchelor [1967], page 311).

From these decay rates, we may see the impact of the inextensible membrane, in accordance with our previous discussions. For the water/water interface, the impact is small, the decay rates differ by a

factor of only $2(2k^2+2k+5)/(2k+1)^2$, that is between 2 and 1 for all $k > 1$. For the air/water interface, however, the impact is significant. The ratio between the membrane-covered and pure interface decay rates is $(k-1)\omega^{1/2}/(2k+1)(k+1)\nu^{1/2} \approx 2.5\times10^4$, large as ν is small. The decay rate for the air/water membrane-covered interface is, in fact, much closer to that a pure water/water interface than for a pure air/water interface.

The above discussion demonstrates the consequences of not considering the problem in full, using only a velocity potential ϕ and neglecting the rotational flow associated with the stream function ψ: doing so would mean that the viscous decay coefficient would be significantly underestimated, by a factor of order $\nu^{1/2}$. As we shall see later, doing similarly for the vorticity would lead to it being underestimated by a similar amount for the case of a membrane-covered air/water interface.

4.3.8 Spacial decay

In the previous theory, we have discussed only waves decaying in time, such as the traveling waves seen on a dropped water balloon in air. For the stationary, oscillated balloons, however, the forcing for the waves was constant in time, and led to standing waves being created on the balloon. Such waves, that do not decay in time, are referred to as stationary waves. Consequently, it is the spacial damping coefficient α that is relevant (though note that it will be dimensionless, as it gives decay per angle in the ϕ direction). Note that this spacial decay gives the decay of pure standing waves (and travelling waves) with distance from the point of forcing. Our standing waves are not pure standing waves, but are formed by the interaction between travelling waves. These waves are incident waves (direct from the point of forcing), and reflected waves from the bottom of the balloon (or where the balloon meets the supporting pipe). Thus, the amplitude of our standing waves will not decay directly in accordance with the spacial decay rate given here; for instance, the standing wave closest to the point of forcing will have the largest contribution from the incident waves, but the smallest contribution from the reflected waves. However, finding the spacial decay should at least give us some idea as to the scale of impact the decay may have on the waves we see in our experiments.

To find the spacial decay rate, we repeat the analysis of section 4.3.5 but with n assumed imaginary and k complex (note that the angular dependence then involves both $P_k(cos(t))$ and $Q_k(cos(t))$, where Q denotes the Legendre function of the second kind). The wavenumber k is then expanded as a series in powers of ϵ,

$$k = k_0 + k_1\epsilon... \tag{4.75}$$

For an air/water membrane-covered interface, this gives the spacial damping coefficient $\alpha = Im(k_1\epsilon)$ as

$$\alpha = \frac{k_0(k_0+2)(k_0-1)^3}{\sqrt{2}a\sqrt{\omega}(k_0+1)(3k_0^2+2k_0-2)}\nu^{1/2}. \tag{4.76}$$

For a water/water membrane-covered interface, it is

$$\alpha = \frac{k_0(k_0-1)(k_0+1)(k_0+2)(2k_0^2+2k_0+5)}{2\sqrt{2}a\sqrt{\omega}(3k_0^4+6k_0^3+2k_0^2-k_0-1)}\nu^{1/2}. \tag{4.77}$$

These decay coefficients may be checked against those given by Lucassen-Reynders and Lucassen [1969] for 2D, and by using the relation found by Gaster [1962] for low viscosity flows,

$$\beta = c_g\alpha, \tag{4.78}$$

where $c_g = \partial\omega/\partial k$ is the group velocity. Applying this relation to the β's found in the previous section does indeed confirm the above values of α.

The typical distances (in radians) of decay are then given by α^{-1}. For an air/water interface, typical values imply $\alpha^{-1} \approx 150$ radians, and for a water/water interface they imply $\alpha^{-1} \approx 100$ radians, much larger than the circumference of the balloon. We therefore would not expect that amplitudes of the standing waves to deviate significantly from their inviscid values. This also implies that any progressive component to the waves arising due to dissipation will be weak, and so have negligible impact on the system of standing waves we observe in experiments.

4.3.9 Constants

We may extend the above analysis to obtain the constants in $\boldsymbol{v}$ as defined by (4.52). Their full form will again be highly complicated, so we expand in powers of ϵ and give the lowest-order non-zero term. The condition $Det(\boldsymbol{M}) = 0$ means that the system will be under-determined. We therefore specify every other constant in terms of C, the amplitude of the normal deformations to the interface, as this we could directly control in our experiments on stationary balloons.

The first-order constants for the potentials, A_1 and A_2, are the same for both pure and inextensible air/water and water/water interfaces (with the relevant angular frequency ω):

$$A_1 \approx -\frac{\omega C}{k a^{k-1}}, \tag{4.79}$$

$$A_2 \approx \frac{a^{k+2}\omega C}{k+1}. \tag{4.80}$$

The remaining constants depend on the form of the interface, however. For a pure fluid/fluid interface, the tangential surface deformation D is, in general,

$$D \approx \frac{[(k+1)\rho_1\nu_1^{1/2} - k\rho_2\nu_2^{1/2}]C}{k(k+1)[\rho_1\nu_1^{1/2} + \rho_2\nu_2^{1/2}]} \tag{4.81}$$

Unlike the other constants, the stream function constants B_1 and B_2 are both zero to first order in ϵ. To second order,

$$B_1 \approx \frac{(2k+1)\omega^{1/2}\nu_1^{1/2}\nu_2^{1/2}\rho_2 C}{2\sqrt{2}k(k+1)j_k(m_1 a)[\rho_1\nu_1^{1/2} + \rho_2\nu_2^{1/2}]}(1-i), \tag{4.82}$$

$$B_2 \approx \frac{(2k+1)\omega^{1/2}\nu_1^{1/2}\nu_2^{1/2}\rho_1 C}{2\sqrt{2}k(k+1)h_k(m_2 a)[\rho_1\nu_1^{1/2} + \rho_2\nu_2^{1/2}]}(1-i). \tag{4.83}$$

For an air/water free surface, where $\rho_2 = 0$, the above equations imply

$$B_1 \approx 0, \tag{4.84}$$

$$B_2 \approx \frac{(2k+1)\omega^{1/2}\nu_2^{1/2} C}{k(k+1)h_k(ma)}, \tag{4.85}$$

$$D \approx \frac{C}{k}. \tag{4.86}$$

The leading-order non-zero term in B_1 is then given by the third-order term in the expansion,

$$B_1 \approx \frac{2(k-1)\nu_1 C}{kaj_k(m_1 a)}. \tag{4.87}$$

For the pure water/water interface,

$$B_1 \approx \frac{(2k+1)\omega^{1/2}\nu^{1/2}C}{2k(k+1)j_k(ma)}(1-i), \tag{4.88}$$

$$B_2 \approx \frac{(2k+1)\omega^{1/2}\nu^{1/2}C}{2k(k+1)h_k(ma)}(1-i), \tag{4.89}$$

$$D \approx \frac{C}{2k(k+1)}. \tag{4.90}$$

However, for any membrane-covered interface the constants become

$$B_1 \approx \frac{(2k+1)\omega^{1/2}\nu_1^{1/2}C}{2k(k+1)j_k(ma)}(1-i), \tag{4.91}$$

$$B_2 \approx \frac{(2k+1)\omega^{1/2}\nu_2^{1/2}C}{2k(k+1)h_k(ma)}(1-i), \tag{4.92}$$

$$D \approx \frac{2C}{k(k+1)}. \tag{4.93}$$

Notably, with a membrane these constants are independent of the densities, thus will not change between an air/water and water/water interface.

Though $j_k(m_1 a)$ and $h_k(m_2 a)$ are themselves functions of ν_1 and ν_2, they will be exponentially large for typical values seen in our experiments. Consequently, B_1 and B_2 will be far smaller than A_1 and A_2, by a factor proportional to ϵ (the equivalent ratio was given by Lamb [1932] for a pure 2D air/water interface, where it was proportional to ν). The stream function also decays exponentially over a distance $\sqrt{2\nu/\omega} \approx 0.1$ mm, whereas the potential decays algebraically over the much-larger distance $a \approx 50$ mm. Consequently, in both cases the outer flow away from the interface will be dominated by the irrotational potential flow given by ξ. The rotational part of the flow will only become important when $j_k(mr)$ is large and of a similar order to $j_k(ma)$, which is in a thin region of thickness $\sqrt{2\nu/\omega}$ near the interface.

4.3.10 Vorticity

Using the above calculated constants, we may then determine the vorticity in the flow. While the vorticity distribution at a 2D air/water interface was found by Lamb [1932], we can find no evidence of it being determined for either spherical or membrane-covered (or both) interfaces anywhere in the literature. Determining the vorticity distribution is important for us, as it is the interfacial vorticity

that dominates the late-time behaviour of the interface, as will be discussed in chapter 6. The vorticity $\boldsymbol{\omega}$ is given by

$$\begin{aligned}\boldsymbol{\omega} &= \nabla \times \boldsymbol{u} \\ &= \nabla \times \nabla \times \boldsymbol{\psi} \\ &= \left(0, -\left(\nabla^2\psi - \frac{\psi}{r^2 \sin^2\phi}\right), 0\right) \\ &= \left(0, -\frac{n}{\nu}\psi, 0\right). \end{aligned} \tag{4.94}$$

In each fluid, the θ component of vorticity is therefore, to highest non-zero order in ϵ,

$$\omega_1^\theta = -\frac{\omega B_1}{\nu_1} j_k(mr) \frac{\partial}{\partial\phi} \left[P_k(\cos\phi)\right] e^{-n_1 t + i\omega t}, \tag{4.95}$$

$$\omega_2^\theta = -\frac{\omega B_2}{\nu_2} h_k(mr) \frac{\partial}{\partial\phi} \left[P_k(\cos\phi)\right] e^{-n_1 t + i\omega t}. \tag{4.96}$$

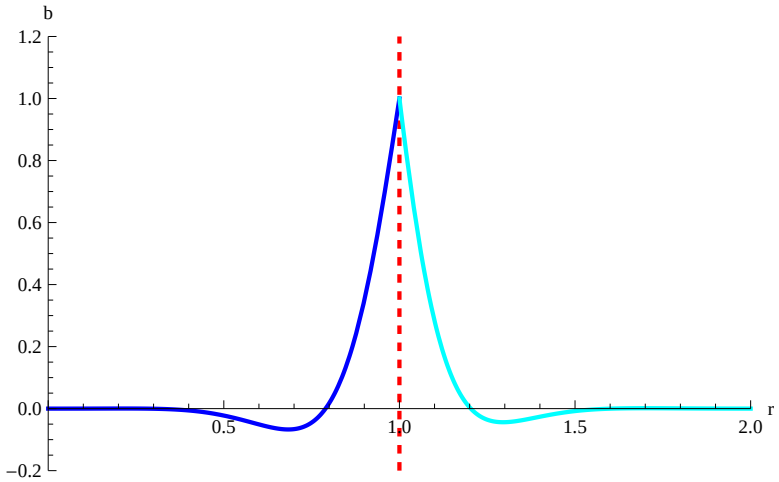

Figure 4.6: The shape of the vorticity distribution (blue lines) near a spherical interface at $r = 1$. Most of the vorticity is contained in a thin region near the interface, decaying rapidly as you move away, in both directions. The thickness of the interface here is $\sqrt{2\nu/\omega} = 0.125$, or equivalently 0.125 times the radius of the interface.

A plot of the r dependence of the vorticity is given in figure 4.6. From it, it is clear to see that most of the vorticity is concentrated in a thin region of width $\sqrt{2\nu/\omega} \ll \lambda$ adjacent to the interface, mirroring the stream function. The vorticity may therefore be approximated as lying only in a sheet at the interface. The strength of this sheet on the inside and outside of the interface is denoted γ_1 and γ_2 respectively, and is also known as the circulation density. The total circulation density is given by $\gamma = \gamma_1 + \gamma_2$. As the viscosities are small, we shall consider only the first-order term for γ, that may only be found by considering the inviscid limit. Then the flow is irrotational everywhere away from the interface, with the stream function zero everywhere. The only vorticity is restricted to an

infinitesimally thin sheet lying not in either fluid, but strictly on the interface. Following Batchelor [1967] (page 97) and applying Stokes' theorem over a small rectangle lying across the interface, we see

$$\gamma(\phi,t) = [u(a,\phi,t)]_1^2 = \left[\frac{1}{a}\frac{\partial\phi}{\partial\phi}\right]_1^2. \tag{4.97}$$

We showed previously that both the form of the potentials and their constants A_1 and A_2 are independent of the type of interface and the viscosities of the two phases, and only depend on their densities through the angular frequency of oscillation ω. Therefore, the total interfacial circulation density in every case may be written as

$$\gamma(\phi,t) = \frac{2k+1}{k(k+1)}\omega C\frac{\partial}{\partial\phi}\left[P_k(\cos\phi)\right]e^{i\omega t}. \tag{4.98}$$

The circulation density at the interface is therefore independent of the type of interface (whether fluid/fluid or membrane-covered) to first order. With regards to the densities, $\gamma \propto [k\rho_2+(k+1)\rho_1]^{-1/2}$, so γ will be approximately $\sqrt{2}$ times greater for the water/water interface as for the air/water interface with the same wavenumber. Nevertheless, the total interfacial circulation will always be zeroth-order in ϵ.

However, the idea that all the vorticity is located exactly on the interface is clearly unphysical, as viscosity means that there can be no discontinuity in tangential velocity. Instead, it diffuses it out into the fluids either side of the interface. As shown above, the vorticity is actually contained within thin boundary layers either side of the interface. The first-order contribution to the interfacial circulation density γ from each fluid may therefore be calculated by integrating the vorticity over the width of the boundary layer in the limit $\nu_i \to 0$. Defining $\tilde{m}_i = \sqrt{2\nu_i/\omega}$, the contributions are

$$\begin{aligned}\gamma_1(t,\phi) &= \lim_{\nu_i\to 0}\int_{a-\tilde{m_1}}^{a}\omega_1^\theta dr \\ &= \left[-\omega\lim_{\nu_1\to 0}\int_{a-\tilde{m_1}}^{a}\left(\frac{B_1}{\nu_1^{1/2}}\right)dr\right]P_k(\cos\phi)e^{i\omega t},\end{aligned} \tag{4.99}$$

$$\begin{aligned}\gamma_2(t,\phi) &= \lim_{\nu_i\to 0}\int_{a}^{a+\tilde{m_2}}\omega_2^\theta dr \\ &= \left[-\omega\lim_{\nu_2\to 0}\int_{a-\tilde{m_2}}^{a}\left(\frac{B_2}{\nu_2^{1/2}}\right)dr\right]P_k(\cos\phi)e^{i\omega t}.\end{aligned} \tag{4.100}$$

Writing

$$\gamma_i = E_i\left[P_k(\cos\phi)\right]e^{i\omega t}, \tag{4.101}$$

for a pure water/water interface we get

$$E_1 \approx \frac{(2k+1)\omega C}{2k(k+1)}(1-i), \tag{4.102}$$

$$E_2 \approx \frac{(2k+1)\omega C}{2k(k+1)}(1-i), \tag{4.103}$$

whereas for a membrane-covered water/water interface we get

$$E_1 \approx \frac{(k-1)\omega C}{k(k+1)}(1-i), \tag{4.104}$$

$$E_2 \approx \frac{(k+2)\omega C}{k(k+1)}(1-i). \tag{4.105}$$

Though the membrane does have an impact for a water/water interface, it is small, becoming negligible as $k \to \infty$. However, as for decay, the impact is significant for air/water interfaces. For the pure free surface,

$$E_1 \approx \frac{2(k-1)\omega^{1/2}\nu_1^{1/2}C}{kaj_k(m_1 a)}, \tag{4.106}$$

$$E_2 \approx \frac{(2k+1)\omega C}{k(k+1)h_k(ma)}, \tag{4.107}$$

and so the vorticity is contained almost entirely within the air. For the membrane-covered air/water interface, however,

$$E_1 \approx \frac{(k-1)\omega C}{k(k+1)}(1-i), \tag{4.108}$$

$$E_2 \approx \frac{(k+2)\omega C}{k(k+1)}(1-i), \tag{4.109}$$

as before, so the circulation is split evenly between the air and water. The physical reason for this discrepancy is that the interfacial vorticity is generated by shear. For a pure fluid/fluid interface the shear arises directly between the two fluids. As the density of the water is so much greater than that of air, the water is not affected by the air and does not experience any drag from it. There is therefore no shear at the interface to generate vorticity in the water. The air, in contrast, feels the influence of the water strongly, and thus significant vorticity is created there. The entire velocity jump between the outer flow in the water and the outer flow in the air is located within the boundary layer on the air side of the interface, and thus that is where the circulation is. For the membrane-covered interface, the assumption of large $\mathcal{E}$ means that the interfacial tangential stresses are dominated by stress in the membrane. The membrane stress is significantly larger than the shear stresses in both fluids, despite the density difference, so that both fluids feel similar effects. Consequently, the jump in velocity is shared between the boundary layers on either side of the interface, and so is the circulation. Note that in every case $E_1 + E_2 = (2k+1)a\omega C/k(k+1)$ as above, so that the total circulation is the same in every case, as expected.

The vorticity created by an oscillated water balloon held underwater was shown in figure 4.2. The velocity and vorticity fields were found using PIV. The images clearly show the vorticity restricted to a narrow region near the interface. This region is thicker than predicted; this could be a result of resolution issues with the PIV, but most likely is because the linear theory does not take into account the amplitude of the waves - beyond the maximum amplitude of the waves, the vorticity only extends into the flow the thickness of the interfacial boundary layer, as predicted by the theory. That the vorticity determined by the PIV is due to the flow, and not due to the movement of the rubber itself, is supported by the fact that no change in the vorticity is detected before and after rupture. Quantitative comparisons of between the vorticity found in experiments using PIV, and the predictions of the above theory, will be given in section 4.7.2, and shown to be in excellent agreement.

4.4 Free surface experiments

We also wished to determine experimentally the flow field and vorticity produced by a membrane-covered air/water interface. Unfortunately, this was not possible to do with water-filled balloon, as diffraction of the light at the air/water interface meant that the particles near the interface could not be seen clearly. Instead, this type of interface was examined using PIV but in a different geometry, that of a flat, 2D interface.

The same tank, camera, lighting and forcing as for the PIV experiments on balloons was used. To create the interface, a thin sheet of natural rubber was stretched over a rigid circular perspex cylinder of radius 0.25 m, and secured to the edges. The tank was filled with fresh water, into which were mixed Pliolite particles of diameter 50 μm. The top of the cylinder, the end covered with the rubber, was then pushed into the water so that it remained flat, before the speaker was lowered so that the rod pushed into the centre of the rubber sheet. This had the secondary benefit of holding the cylinder and rubber sheet in place. The speaker was then oscillated at a set frequency, creating waves of that frequency on the membrane. The camera was then aligned facing the light-sheet, and recorded the movement of the particles in the flow at 2000 fps. A diagram of the experimental set-up is given in figure 4.7.

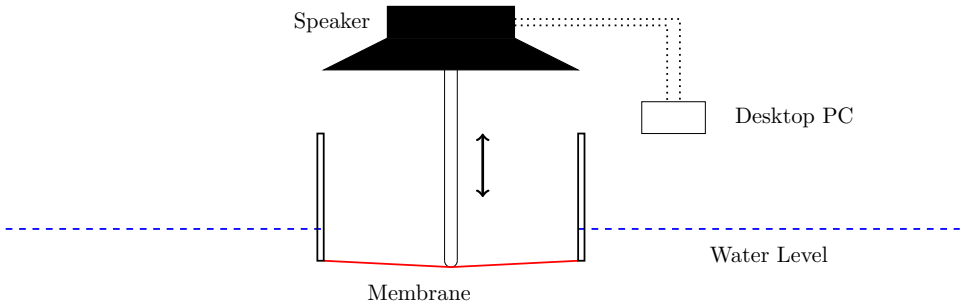

Figure 4.7: A cross-section of the experimental set-up used to investigate waves on a membrane-covered air/water interface. The waves were created using the rod attached to the speaker. The water was contained within a perspex tank. A light-sheet shone in through one side of the tank, with the high-speed camera filming through another at 90 degrees.

4.4.1 Theory for circular waves

The waves produced by the experimental method described above were different again from either the 2D Cartesian or spherical interfacial waves for which theory was derived in section 4.3, being cylindrical in nature. Consequently, we briefly discuss the theory for such waves, which follows closely that given for the other geometries. This is highly similar to the analysis for Rayleigh-Plateau instability, only with the waves travelling in the r, instead of z, direction. Though this analysis has been performed before to examine circular waves on a pure fluid/fluid interface (as created by the impact of a pebble on a pond), we can find no evidence of it being extended to an inextensible interface.

Point forcing on a flat interface produces circular waves, that spread out radially from the point of forcing. For an infinite sheet, these would be progressive waves; however, the radius of the tube over

which our membrane was stretched was of a similar order to the wavelengths created by the forcing, so that a system of standing waves quickly formed. We work in cylindrical polar coordinates (r, θ, z), with $r = 0$ corresponding to the point of forcing. As we are investigating air/water interfaces, we neglect the upper fluid, considering only flow beneath the interface, in the water. We again split the velocity field into irrotational and rotational parts using a velocity potential ξ and vector $\boldsymbol{\psi} = (0, \psi, 0)$. The equations of motion and interfacial boundary conditions are then identical to those for a spherical interface, only in cylindrical coordinates. The regularity conditions here require flow quantities to remain finite at $r = 0$ and as $z \to \pm\infty$ (note that here, the r direction is tangential to the interface, with the z direction normal to it). Consequently, we get

$$\phi = AJ_0(kr)e^{kz}e^{-nt}, \tag{4.110}$$

$$\psi = BJ_1(kr)e^{mz}e^{-nt}, \tag{4.111}$$

where $m = \sqrt{k^2 - n/\nu}$, and A, B are unknown constants. The tangential (ζ) and normal (η) deformations to the surface are then given by

$$\zeta = DJ_1(kr)e^{-nt}, \tag{4.112}$$

$$\eta = CJ_0(kr)e^{-nt}. \tag{4.113}$$

As before, the interfacial boundary conditions then lead to a dispersion relation for n in terms of k. Expanding n is powers of $\nu^{1/2}$,

$$n = n_0 + n_1\nu^{1/2} + n_2\nu + ... \tag{4.114}$$

we find

$$n_0 = \sqrt{\frac{\sigma k^3}{\rho}} \tag{4.115}$$

for both the free ($\mathcal{E} = 0$) and membrane-covered $\mathcal{E} = \infty$ interface, the same angular frequency as for Cartesian waves on a 2D interface.

For a free surface, the decay rate is

$$\beta = 2k^2\nu, \tag{4.116}$$

whereas for an inextensible interface it is

$$\beta = \frac{k\omega^{1/2}\nu^{1/2}}{2\sqrt{2}}, \tag{4.117}$$

again both identical to those for Cartesian waves on a 2D interface. The circulation density at the interface is given by

$$\gamma = i\omega CJ_1(kr)e^{-nt} \tag{4.118}$$

and

$$\gamma = -2k\omega^{1/2}\nu^{1/2}CJ_1(kr)e^{-nt} \tag{4.119}$$

for the free and membrane-covered interfaces, respectively. These expressions will be used in following section to compare linear theory with our experimental results.

4.4.2 Air/water PIV results

In figure 4.8, sample images from our PIV experiments on a membrane-covered air/water interface are shown. They display the structure we would expect, of significant interfacial vorticity concentrated near the interface. In figure 4.9, the experimentally-determined average circulation over one wave half-period within one half-wavelength is plotted against the first order theoretically predicted value of equation 4.119, and the agreement is excellent. In particular, it supports our assertion that the interfacial circulation density within the water for a membrane-covered air/water interface is order ν^0, and thus significantly greater than for an air/water interface not covered by a membrane.

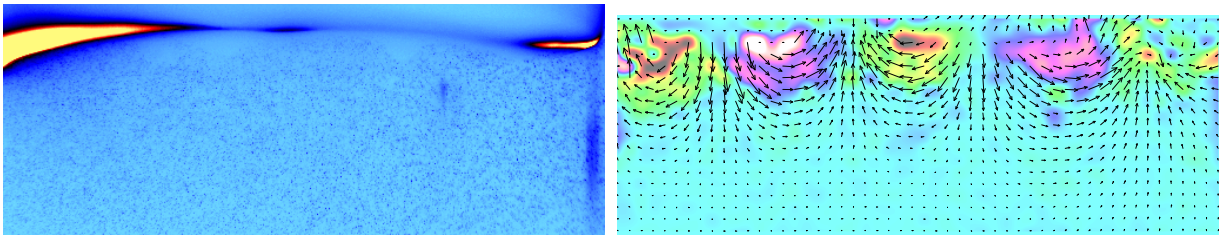

(a) (b)

Figure 4.8: An example of the PIV performed on a flat air/water membrane-covered interface. Image **(a)** is an example of the video taken by the camera, though with false colours to aid visualisation. Image **(b)** shows the results of PIV performed on the video, with the arrows depicting the flow field, and the colours showing vorticity. Green and orange shows negative vorticity, pink and blue positive vorticity.

4.5 Summary of the influence of the membrane

From the derivation of the linear theory throughout the previous section, the physical influence of the membrane becomes clear. For a water/water interface, the impact is minimal, changing flow quantities only in small ways related to the wavenumber k. For an air/water interface, however, the difference is significant, as the presence of the membrane increases both the decay rate of interfacial waves and the magnitude of the interfacial vorticity within the water significantly. This difference in behaviour is ultimately down to shear at the interface. For a fluid/fluid interface, that shear is between the fluids. For a membrane-covered interface, the shear is between the fluids and the membrane, as stresses within the membrane caused by local changes in its area are much greater than shear stresses in either fluid.

For a water/water interface, the fluids either side of the interface are moving in opposite tangential directions in the outer flow, whatever the nature of the interface. Continuity of velocity and tangential stress mean that the flow in the interfacial boundary layer contains significant velocity shear. This, in turn, leads to significant decay and vorticity creation at the interface. Introducing the membrane changes little, as there is already something (the other fluid) to oppose the motion at the interface. There is still some distinction between the two cases, as seen by the different values of both the decay rates (4.73), (4.74) and the tangential interfacial displacement (4.90), (4.93), but the differences are relatively minor.

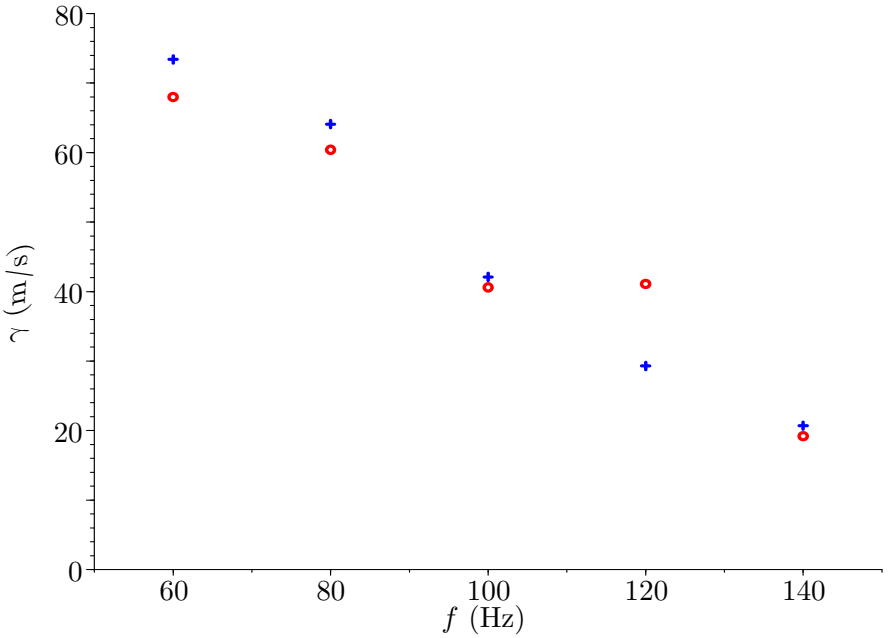

Figure 4.9: Comparison between theory and experiment for an air/water membrane-covered interface. The experimentally-determined average circulation over one wave half-period within one half-wavelength (blue crosses) is plotted against the first order theoretically predicted value of equation 4.119 (red circles). Errors are primarily due to the difficulty in estimating the wave amplitude C, which was often only a few pixels in our videos. This was particularly an issue at the highest oscillation frequencies, when the amplitude of forcing was smallest.

For an air/water interface, we may neglect the influence of the air phase on the water. Thus, without the membrane, there no longer any condition on the interfacial tangential velocity, while the tangential stress need only drop to zero instead of matching with that of a fluid moving in the opposite direction. Consequently, while the tangential stress condition does lead to the creation of an interfacial boundary layer, it is much weaker than for the water/water interface, as there is nothing at the interface to oppose the motion of the outer flow. Introduction of the membrane changes the situation, however. Now, gradients in tension within the membrane, caused by local changes in its area, resist the motion of the outer flow, similar to how a fluid the other side of the membrane would. The fluid velocity goes from being unrestricted at the interface, to a condition of no-slip with the membrane, a membrane who stresses are far greater than viscous shear stresses in the water. Consequently, significantly stronger velocity shear occurs in the interfacial boundary layer, and hence significantly stronger vorticity is created there.

4.5.1 Finite Membrane Elasticity

It was argued in previous sections that the elasticity of the membrane could be regarded as inextensible, with effectively infinite elasticity. This is, indeed, a good approximation to make for our balloons, and

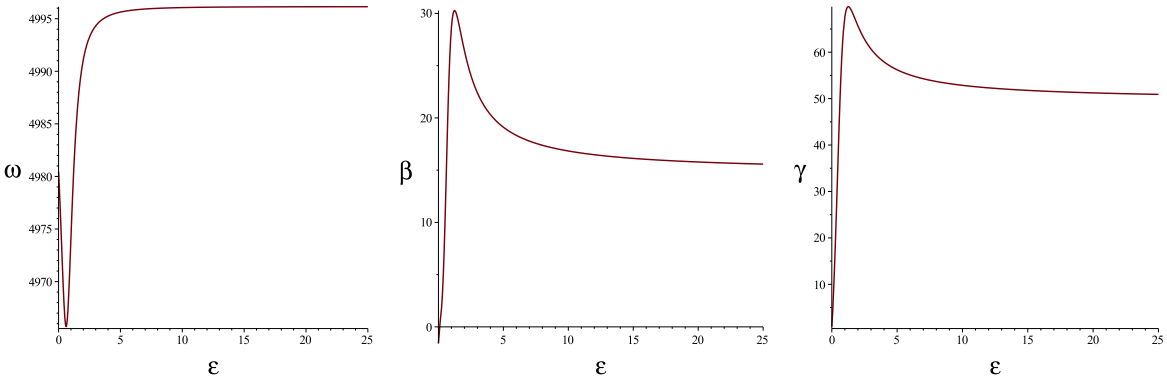

(a) Angular frequency (b) Temporal decay rate (c) Vorticity

Figure 4.10: The angular frequency of oscillation **(a)**, temporal decay rate **(b)**, and circulation density in the water **(c)** as a function of the surface elasticity $\mathcal{E}$ for waves on an air/water interface. Note the peak in vorticity and decay rate occurring near $\mathcal{E} = 1$, beyond which both are approximately constant. This peak occurs due to the presence on dilational waves on an elastic interface.

greatly simplifies the analysis. However, even if the elasticity was finite (but non-zero), the presence of the membrane would still lead to significantly increased decay and vorticity in the water being created at an air/water interface.

At first glance, we may expect the damping in the interfacial boundary layer to be maximum when the membrane is inextensible, as then there would be the greatest shear with the outer flow. However, it has been noted by Lucassen [1968] amongst others that while the damping at $\mathcal{E} = \infty$ is greater than at $\mathcal{E} = 0$, the relation is not monotone increasing. In fact, the damping reaches its maximum at $\mathcal{E} = 1$, before monotone decreasing to its value at infinity. For a 2D air/water interface, the full dispersion relation is

$$n^4\rho^2 + \sigma\rho k^3 n^2 - 4k^2\nu\rho^2 n^3 + 4k^4\nu^2\rho^2 n^2 - 4mk^3\nu^2\rho^2 n^2 + \tilde{E}(mk^5\sigma - k^6\sigma + mk^2\rho n^2) = 0, \quad (4.120)$$

where $m = \sqrt{k^2 - n/\nu}$. A plot of the relationship between n and for typical values of σ, k and ν is given in figure 4.10(a), clearly demonstrating the peak near $\mathcal{E} = 1$. The reason for this peak is because of a resonance between the capillary waves and the dilational waves discussed previously, that exist only when the membrane elasticity is finite. Lucassen-Reynders and Lucassen [1969] give a comprehensive discussion of this phenomenon.

As stated previously, determining the nature of the interfacial vorticity is also important, as it influenced the behaviour of the interface after the balloon burst. We may look directly at the interfacial circulation density in water, using the relation

$$\gamma = -\frac{n}{\nu}\int_{-\infty}^{\infty}\psi dz = \sqrt{\frac{n}{\nu}}\frac{\partial}{\partial\phi}\left[P_k(\cos\phi)\right]e^{-n_1 t + i\omega t}. \quad (4.121)$$

For a 2D air/water interface, the amplitude of γ, denoted $|\gamma|$, is then

$$|\gamma| = \frac{(2mk\nu + 2k^2\nu - n)(-2k^2\nu n\rho + k^3\sigma + n^2\rho)C}{kn^2\rho}. \quad (4.122)$$

Using n as a function of $\tilde{E}$ found using (4.120), this may be solved numerically. The solution is plotted in figure 4.10(c), and shows the same peak near $\mathcal{E} = 1$ and consequent monotonic decrease to its asymptotic value given by (4.106). It clearly demonstrates that the interfacial circulation density will be order ν^0 in the viscosity (and therefore significant) for all $\mathcal{E} > 1$. Given that $\mathcal{E}$ was typically around 100 for our membranes, this shows that the interfacial vorticity will always be significant, whatever the exact conditions or extension of the rubber.

In summary, the important point to be noted here is that the elasticity does not need to be infinite for significant interfacial vorticity to occur. Instead, we only need $\mathcal{E} \geq 1$, a far weaker condition.

4.6 Gravity waves

We discuss briefly here the other common type of interfacial wave, gravity waves, in the interests of comparison, and to facilitate a discussion of the late-time growth in chapter 6. In particular, this linear theory was used by Richtmyer [1960] to determine the initial growth rate for the RMM. As we wish to explore only the basic phenomenology, we consider a 2D fluid-fluid interface. The modeling of the problem closely mirrors that for the capillary waves discussed previously, using both a velocity potential and stream function, with only a few small adjustments: there is an extra body force term ρg in the (Cartesian) Navier-Stokes momentum equation, and all terms relating to the surface tension and its gradients now vanish in the interfacial boundary conditions. This leads to the well-known (see Lamb [1932]) equation for the angular frequency of oscillation (for infinite fluids),

$$\omega = \sqrt{\frac{\rho_1 - \rho_2}{\rho_1 + \rho_2} gk}. \tag{4.123}$$

The stream function in the lower fluid is then, to leading order in ν,

$$\psi_1(x, z, t) = -\frac{2\rho_2 C \omega^{1/2} \nu^{1/2} i}{\rho_1 + \rho_2} e^{mz} \cos(kx) e^{i\omega t}, \tag{4.124}$$

where $m = \sqrt{k^2 - n/\nu}$. Following (4.94), the vorticity is, to leading order,

$$\begin{aligned} \omega_y &= -\frac{n}{\nu}\psi \\ &= \frac{2\rho_2 C \omega^{3/2} \nu^{1/2} i}{\rho_1 + \rho_2} e^{mz} \cos(kx) e^{i\omega t}, \end{aligned} \tag{4.125}$$

and hence the circulation density at the interface is

$$\begin{aligned} \gamma(x, t) &= \int_{-\infty}^{0} \omega_y dz \\ &= \frac{2\rho_2 C \omega i}{\rho_1 + \rho_2} \cos(kx) e^{i\omega t} \\ &= \frac{2\rho_2 C \sqrt{gk} i}{\rho_1 + \rho_2} \left(\frac{\rho_1 - \rho_2}{\rho_1 + \rho_2} \right)^{1/2} \cos(kx) e^{i\omega t}. \end{aligned} \tag{4.126}$$

We can therefore see that, much as for capillary waves, when ρ_2 the term above will disappear and the interfacial circulation will only be order $\nu^{1/2}$. By symmetry, the circulation in the upper fluid will then be the same but with ρ_1 and ρ_2 reversed. We may therefore see that, as for capillary waves, significant interfacial circulation of order ν^0 is always created, and is concentrated in the less dense fluid. However, whereas for capillary waves the maximum vorticity is created when $\rho_2 = \rho_1$, for gravity waves the oscillation frequency and hence vorticity is then zero (as then there is no restoring force for the interfacial waves). Instead, the vorticity increases from being order ν at $\rho_2 = 0$ up to a maximum at $\rho_2 = (1/4)\rho_1$, then decreasing to zero at $\rho_2 = \rho_1$.

We could also consider gravity waves on a membrane-covered interface. Though no detailed analysis has been performed, the qualitative behaviour of such an interface may be inferred from our previous work. Firstly, any tension within the membrane will affect the oscillation frequency of the waves, having a greater influence the shorter the wave. Elasticity in the membrane will also act much as it does for the purely capillary waves considered in previous sections. If the membrane is inextensible, it will again suppress all tangential motion at the interface and thus distribute the interfacial vorticity evenly between the phases either side of the interface, regardless of the density difference between them.

4.7 Estimates for post-rupture behaviour for a water/water interface

The behaviour of a water/water interface post-rupture will be examined in detail in chapter 6. To accurately predict this behaviour, it will be important to determine certain features of the flow qualitatively. In particular, we would need to obtain an estimate for the interfacial velocity, as this set the initial speed of the interface after the balloon has been ruptured, and the vorticity at the interface, as this dominated the late-time behaviour.

4.7.1 Burst velocity

From the previous subsection, we have the interface given by $r = a + \eta(\phi, t)$, where

$$\eta(\phi, t) = C\, P_k(\cos\phi) e^{i\omega t}, \tag{4.127}$$

where the amplitude C and frequency ω (and hence wavenumber k) are set by the forcing. The velocity of the interface v_{int} at time t is

$$\begin{aligned} v_{int} &= \eta_t \\ &= -C\omega\, P_k(\cos\phi) \sin\omega t \end{aligned}$$

It is important to note that the amplitude C here is not the maximum normal displacement from the undisturbed spherical interface for every wave, but only for those waves at the poles. In our experiments, that was equivalent to the amplitude of the forcing. The maximum normal displacement of a particular wave then depends on its position, ϕ. However, the difference between adjacent peaks is small away from the poles.

A good approximation to the relationship between the forcing amplitude and maximum normal displacement near $\phi = \pi/2$ may be found by considering the limit as $k \to \infty$; the lowest value of k in any of our experiments was $k = 6$, making this a not unreasonable assumption. We therefore look here for an appropriate asymptotic form of $P_k(\cos\phi)$ near $\phi = \pi/2$ as $k \to \infty$. In Abramowitz and Stegun [1970] it is given that for $0 < \phi < \pi$,

$$P_k(\cos(\phi)) = \frac{\Gamma(k+1)}{\Gamma\left(k+\frac{3}{2}\right)}\sqrt{\frac{2}{\pi\sin(\phi)}}\cos\left[\left(k+\frac{1}{2}\right)\phi - \frac{\pi}{4}\right] + \mathcal{O}\left(k^{-3/2}\right), \tag{4.128}$$

with

$$k^{b-a}\frac{\Gamma(k+a)}{\Gamma(k+b)} \sim 1 \qquad \text{as } k \to \infty,$$

for all a, $b \in \mathbb{R}$, giving

$$\frac{\Gamma(k+1)}{\Gamma\left(k+\frac{3}{2}\right)} \sim k^{-1/2} \qquad k \to \infty. \tag{4.129}$$

Hence, equation (4.128) may be written as

$$P_k(cos(\phi)) = \sqrt{\frac{2}{k\pi\sin(\phi)}}\cos\left[\left(k+\frac{1}{2}\right)\phi - \frac{\pi}{4}\right] + \mathcal{O}\left(k^{-3/2}\right). \tag{4.130}$$

Now, let us consider the behaviour in the neighbourhood of $\phi = \pi/2$. By writing $\phi = \pi/2 + \psi$ for $|\frac{\psi}{\pi}| \ll 1$, then

$$\begin{aligned}
\sin(\phi) = \sin(\pi/2+\psi) &= \sin(\pi/2)\cos(\psi) + \sin(\psi)\cos(\pi/2) \\
&= \cos\psi \\
&\simeq 1, \\
\cos\left[\left(k+\frac{1}{2}\right)\phi - \frac{\pi}{4}\right] = \cos\left[k\phi + \frac{1}{2}\psi\right] &= \cos(k\phi)\cos(\psi/2) - \sin(k\phi)\sin(\psi/2) \\
&\simeq \cos k\phi.
\end{aligned}$$

Consequently, an asymptotic approximation for $P_k(cos(\phi))$ as $k \to \infty$ near $\phi = \pi/2$ is

$$P_k(\cos\phi) \sim \sqrt{\frac{2}{k\pi}}\cos k\phi. \tag{4.131}$$

An approximate relation between the forcing amplitude C and maximum normal displacement at $\pi/2$, written $\tilde{C}$, is then

$$\tilde{C} \approx \sqrt{\frac{2}{k\pi}}C. \tag{4.132}$$

Hence, in principle, the maximum normal displacement and thus interfacial normal velocity near $\phi = \pi/2$ could be determined from the forcing amplitude. In practice, however, it proved more straightforward to simply measure $\tilde{C}$ directly from the captured video, post-experiment.

The interfacial velocity may therefore be written

$$v_{int} = \omega \tilde{C} \sin \omega t.$$

The term $\tilde{C} \sin \omega t$ is effectively the (time-varying) maximum amplitude of the standing wave at $\phi = \pi/2$. This left the phase of the wave (ωt) at the moment of rupture to be determined experimentally to obtain a theoretical prediction for v_{int}.

The above discussion focused on standing waves. If traveling waves were present on the interface at rupture, the phase would be known pre-rupture (maximum growth occurring $\pi/2$ ahead of the peaks) and thus the maximum velocity of the interface at rupture would be independent of time. However, the location of fastest growth would not be known in advance, and would need to be determined experimentally instead.

4.7.2 Circulation

It will be shown in chapter 6 that it was the vorticity that dominated the non-linear stages of the late-time growth of the interface for the water/water case. Consequently, it was important to obtain an accurate estimate of the vorticity created by the waves on the membrane. We use only the inviscid approximation to the flow to provide the first-order estimate of the vorticity. The circulation of the half-wavelength between anti-nodes N_1 and N_2 is then

$$\begin{aligned}
\Gamma_{N_1}^{N_2} = \int_{N_1}^{N_2} \gamma \, a \, d\phi &= A \left(\frac{2k+1}{k+1} \right) a^k \cos(\omega t) \int_{N_1}^{N_2} \sin(\phi) \, P_k'(\cos\phi) \, d\phi \\
&= A \left(\frac{2k+1}{k+1} \right) a^k \cos(\omega t) \left[P_k(\cos\phi) \right]_{N_1}^{N_2} \\
&= \left(\frac{C\omega a}{k} \right) \cos(\omega t) \left(\frac{2k+1}{k+1} \right) \left[P_k(\cos\phi) \right]_{N_1}^{N_2}. \qquad (4.133)
\end{aligned}$$

The exact value of this final term depends both on k and the particular N_1 and N_2, making it awkward to work with. However, it it may be seen numerically that, as for the amplitude of the waves, the differences in the circulation between different anti-nodes are small away from the poles. As an example, values of $\left[P_k(\cos\phi) \right]_{N_1}^{N_2}$ for $k = 8$ are, in order from $\phi = 0$ to two decimal places: 1.41, -0.72, 0.60, -0.56, 0.56, -0.60, 0.72, and -1.41. The circulation near the poles is much greater than elsewhere, yet near the equator the differences are small, $\approx 5\%$. For higher wavenumbers, these differences will decrease further. Consequently, as most of our post-rupture experimental measurements were taken near $\phi = \pi/2$ with high wavenumbers ($k \geq 6$), it makes sense to consider an approximation to equation (4.133) that simplifies later calculations. In particular, we may use the approximation of equation (4.131) to estimate the interfacial circulation. For the example given above, $\left[P_k(\cos\phi) \right]_{N_1}^{N_2}$ is estimated as $\pi^{-1/2} \approx 0.56$, and so very accurate near $\phi = \pi/2$. The circulation within each half-wavelength is then estimated as

$$\begin{aligned}
\Gamma_{N_1}^{N_2} = \int_{N_1}^{N_2} \gamma \, a \, d\phi &= \int_0^{\frac{2\pi}{k}} \pm C\omega \sqrt{\frac{2}{k\pi}} \left(\frac{2k+1}{k+1} \right) \sin(k\phi) \cos(\omega t) \, a \, d\phi \\
&= \pm 2 \frac{\tilde{C}\omega a}{k} \left(\frac{2k+1}{k+1} \right) \cos(\omega t). \qquad (4.134)
\end{aligned}$$

To test the accuracy of this approximation, the time-averaged absolute value of the circulation within several half-wavelengths near $\phi = \pi/2$ was calculated for a water/water membrane-covered interface, then matched against the equivalent prediction of equation (4.134),

$$|\Gamma_{n_1}^{n_2}| = 2\left(\frac{\tilde{C}\omega a}{k}\right)\left(\frac{2k+1}{k+1}\right)\left(\frac{2}{\pi}\right). \tag{4.135}$$

This comparison was obtained for several 130mm balloons, and over a range of frequencies and wavenumbers. As figure 4.11 reveals, the theoretical estimates were in good agreement with the experimental results near $\phi = \pi/2$. This approximation will be used in chapter 6 to predict the interfacial vorticity at rupture underwater, and hence late-time behaviour of the flow.

4.8 Summary

In this chapter, we have investigated the flow created by waves on the membrane of a water-filled balloon. In section 4.1, a new experimental method was outlined that allowed us to perform Particle Image Velocimetry (PIV) on the flow. Following this, a model for this flow was outlined in section 4.3 that assumed the flow was linear and low viscosity. This model could account for both pure fluid-fluid and membrane-covered interfaces. The outer, irrotational flow was the same in every case, but the flow in the interfacial boundary layer was not: the vorticity on the water side of this boundary layer was significantly weaker for an air/water free surface than for both the water/water and membrane-covered interfaces, due to the lack of shear at the interface. As the interfacial vorticity was important for the late-time interfacial growth, this may mean that the presence of the membrane has a greater impact than merely providing a restoring force for interfacial waves. The predictions for the membrane-covered water/water interface were tested against PIV performed on oscillated balloons, and shown to be accurate. The prediction of greater vorticity at a membrane-covered air/water interface was tested in section 4.4 using a slightly different method, and also shown to be accurate. In section 4.5.1 we showed that it was not necessary for the elasticity of the membrane to be high to produce significant interfacial vorticity. Maximum vorticity is, in fact, created at a relatively low level of interfacial elasticity, above which it decreases monotonically to its asymptotic value. In section 4.6 we determined the conditions in which significant vorticity would be created for gravity waves on a density interface. Finally, in section 4.7 it was described how two characteristics of the flow crucial to the post-rupture behaviour could be determined: the interfacial normal velocity, and the vorticity near the interface. A simple approximation to this interfacial vorticity near the centre of the balloon at high wavenumbers, as all our experiments were, was then shown to be in good agreement with the vorticity found using PIV.

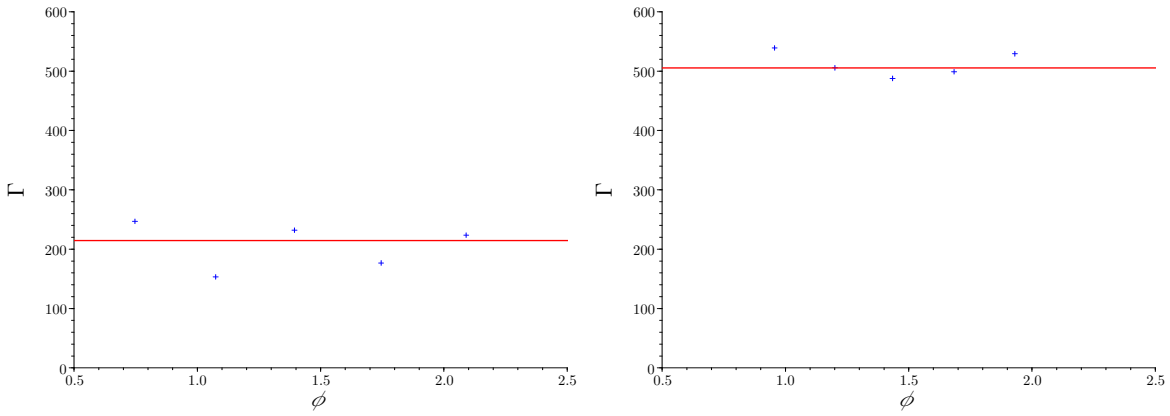

(a) $f = 85\text{Hz}$, $k = 9$

(b) $f = 105\text{Hz}$, $k = 12$

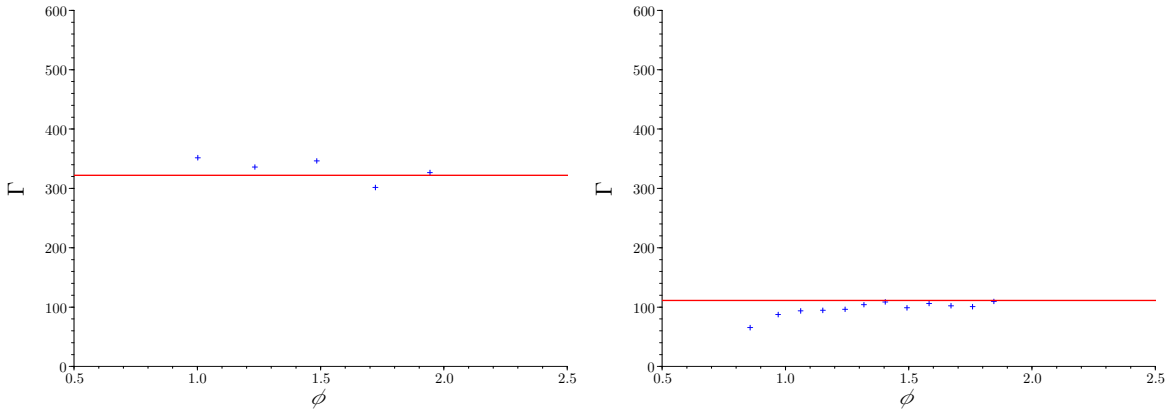

(c) $f = 135\text{Hz}$, $k = 13$

(d) $f = 390\text{Hz}$, $k = 35$

Figure 4.11: The time-averaged absolute value of the vorticity within each half-wavelength plotted against the position of the centre of each half-wavelength, ϕ, for 130 mm balloons oscillated at a range of frequencies and tensions. The blue crosses represent the experimental data acquired using PIV, while the red line is the theoretical prediction of equation (4.135). The angle ϕ is given in degrees, while the circulation is in arbitrary units (pixels^2 per frame).

Chapter 5

Rupture of the membrane

In this chapter, how a water balloon bursts is studied, and linked to the creation of a shear instability on the water's surface. High-speed images reveal the rupture of the membrane to be caused by the passage of one or more cracks through it, that then caused the rubber to rapidly retract. The behaviour of both the membrane and the flow it created are examined in detail, both theoretically and experimentally. Using this analysis, the spray seen when both stationary and oscillated water balloons burst is then explained as a form of shear instability.

5.1 Experimentally observed phenomena

We start by demonstrating the wide range of phenomena that interact during the bursting of a water balloon. In later sections, each of these phenomena will be studied in detail.

Typical images of those bursts are shown in figure 5.1. The experimental equipment and method used to obtain these images is the same as that outlined in section 4.1, only now with the balloon ruptured at some point by the pricking of the membrane with a sharp pin. The phenomena associated with the rapid retraction of the membrane occurred whether or not the balloon was oscillated prior to rupture. In the interests of image clarity, the experiments used to observe the retraction phenomena were performed with unoscillated balloons. The high velocity of the retracting membrane necessitated using higher frame-rates with the camera, typically in the range $10,000$ fps to $100,000$ fps.

As will be discussed in section 5.3, the number of cracks propagating through the membrane for a dropped water balloon could vary widely. However, in the vast majority of cases, including all stationary balloons burst with a pin, only one crack formed. Sample images for such a rupture are displayed in figure 5.1. The crack started from the small hole created by the insertion of the pin into the membrane, propagating away in opposite directions up and down the balloon. The shape of the crack tip was sharp. The rubber retracted away from the crack path, at a speed less than the crack velocity, though not significantly so. The crack traveled in an approximately straight line most of the way around the balloon, only stopping near the open end of the balloon and thus not completing a full diameter. We note here that while this path was typical of many bursts, it was not seen in all: cracks were observed travelling at a wide range of orientations, including near horizontally. The lack of consistency was likely a result of inhomogeneities in the membranes. At the same time, the rubber retracted on either side of the crack, with small transverse waves visible on the membrane near the

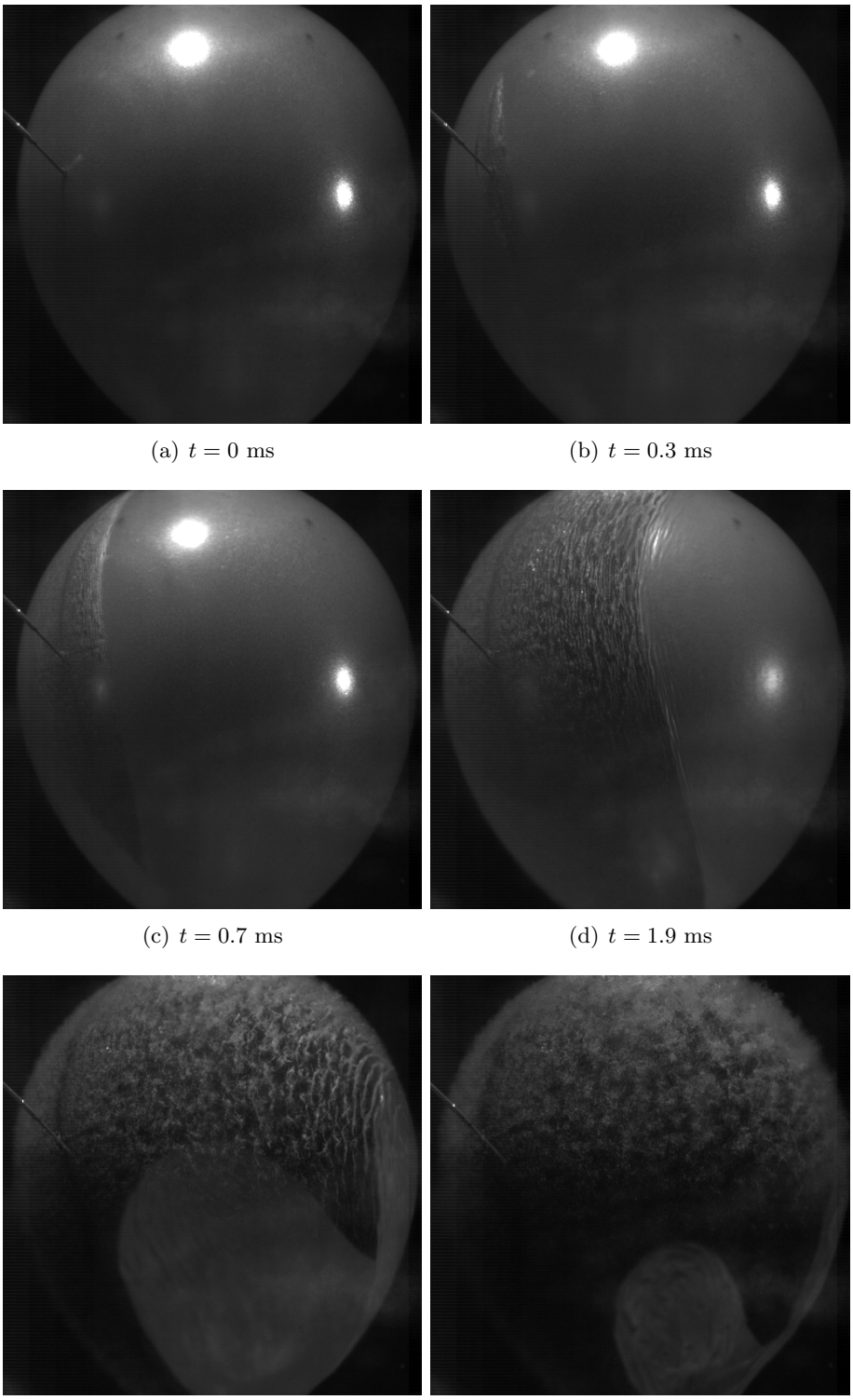

(a) $t = 0$ ms (b) $t = 0.3$ ms

(c) $t = 0.7$ ms (d) $t = 1.9$ ms

(e) $t = 4.3$ ms (f) $t = 7.9$ ms

Figure 5.1: The retraction of a 130 mm water balloon membrane when underwater. The membrane was pricked by the pin, creating a small hole. A crack then started propagating from the hole at $t = 0$ ms. The water inside contains sodium fluorescein to aid visualisation of the interface.

crack faces. Once it had fully retracted, the membrane buckled, as small amplitude transverse waves formed everywhere. Meanwhile, the interface behind the retracting membrane had become unstable. With air surrounding the balloon, this instability took the form of thin sheets of water penetrating far into the air, angled towards the direction of retraction; with water surrounding the balloon, the instability was symmetric, as the water inside and outside the balloon mixed evenly.

The process as displayed in figure 5.1 thus shows five main phenomena that we wish to investigate: propagation of the crack, behaviour of the membrane in retraction, transverse waves near the free edge during retraction, shear instability on the water's surface, and buckling of the membrane after retraction. First, however, we give a brief summary of dynamic elasticity theory, as it proves relevant to explaining most of the phenomena listed above.

5.2 Dynamic elasticity theory

It is assumed in advance that the rubber in the membranes was isotropic and homogeneous, as we found little evidence to the contrary in chapter 2. The fundamental equation of motion for solids is based on conservation of momentum, and known as Cauchy's momentum equation:

$$\rho \boldsymbol{a}_{tt} = \nabla_{\boldsymbol{X}} . \boldsymbol{\tau} + \boldsymbol{b}, \tag{5.1}$$

where $\boldsymbol{X}$ are Lagrangian coordinates moving with the material, and $\boldsymbol{a}$ is the displacement of the material, so that the position of the material in Eulerian coordinates is $\boldsymbol{x} = \boldsymbol{X} + \boldsymbol{a}(\boldsymbol{X})$. The symbol ρ signifies the density of the material in the reference configuration, $\boldsymbol{\tau}$ is the stress tensor for the deformation, and $\boldsymbol{b}$ represents body forces. Note that there are no non-linear inertial terms, as the equation is given in Lagrangian coordinates.

Note that if the stress tensor is assumed to be a function of the strain, $\boldsymbol{\tau} = \boldsymbol{\tau}(\boldsymbol{\epsilon})$, then

$$\nabla_{\boldsymbol{X}} . \boldsymbol{\tau}(\boldsymbol{\epsilon}) = \frac{d\boldsymbol{\tau}}{d\boldsymbol{\epsilon}} \nabla_{\boldsymbol{X}} . \boldsymbol{\epsilon} = \boldsymbol{\tau}'(\boldsymbol{\epsilon}) \nabla^2_{\boldsymbol{X}} \boldsymbol{a} + ... \tag{5.2}$$

and hence the speeds of body waves are given by

$$c = \sqrt{\frac{\boldsymbol{T}'(\boldsymbol{\epsilon})}{\rho}}. \tag{5.3}$$

The wave speeds are therefore determined by the gradient of the stress-strain relationships.

5.2.1 Linear theory

A constitutive relation must then be posed for $\boldsymbol{\tau}$. Here we consider linear theory; though the behaviour of rubber is far from linear at high stretches, it is instructive in demonstrating the types of wave that may occur. The linear limit is applicable for deformations where the strain $|\boldsymbol{\epsilon}| << 1$, and thus all quadratic and higher terms in the derivatives of $\boldsymbol{a}$ are ignored. Any homogeneous isotropic linear elastic material's behaviour may be fully characterized by two parameters. There are several that may be used; here we use the Lamé parameters as defined in 1.7. The model most often used in conjunction

with linear theory is known as the Hookean model, as the material is assumed to obey Hooke's Law with stress proportional to strain. The stress tensor $\boldsymbol{\tau}$ is given by

$$\boldsymbol{\tau} = \lambda\, Tr(\boldsymbol{\epsilon})\, I + 2\mu\, \boldsymbol{\epsilon}, \tag{5.4}$$

where λ and μ are material constants that have the dimensions of pressure. The first term is the hydrostatic stress, a measure of the pressure on a material element that acts to change its volume. The second term is the deviatoric stress, a measure of the shearing on a material volume that acts to change its shape.

Combining equations (5.1) and (5.4) and assuming no body forces gives rise to the Navier equation,

$$\rho \boldsymbol{a}_{tt} = \lambda \nabla_{\boldsymbol{X}} \left(\nabla_{\boldsymbol{X}} . \boldsymbol{a}\right) + \mu \nabla^2_{\boldsymbol{X}} \boldsymbol{a}. \tag{5.5}$$

Together with suitable boundary conditions, this may then be solved using suitable methods for linear equations, such as Fourier series.

This equation permits two types of body wave: longitudinal (change in volume) waves of speed c_p and shear (change in shape) waves of speed c_s, where

$$c_p = \sqrt{\frac{\lambda + 2\mu}{\rho}},$$

and

$$c_s = \sqrt{\frac{\mu}{\rho}}.$$

As λ is always positive, $c_p > c_s$. Both these wave are non-dispersive, meaning that the wave speed is independent of the wavelength. Mark [2009] gives typical values for rubber as

$$\rho = 970\,\mathrm{kg/m^3},$$

$$\lambda = 1950 \times 10^6\,\mathrm{Pa}$$

$$\mu = 0.5 \times 10^6\,\mathrm{Pa},$$

implying

$$c_p = 1420\,\mathrm{m/s},$$

$$c_s = 21\,\mathrm{m/s}.$$

It is important to note that these are the speeds in the reference ($\boldsymbol{X}$) frame. For a material uniformly stretched by a factor of λ_i in the direction of propagation of the wave, the speed of the waves in the Eulerian frame, c_p^E and c_s^E, will be

$$c_p^E = \lambda_i\, c_p,$$

$$c_s^E = \lambda_i\, c_s.$$

With suitable boundary conditions, several types of surface wave may also occur. One important type is known as a Rayleigh wave, that propagates along the free surface of a semi-infinite solid, with the restoring force coming from material elasticity. They are in many ways analogous to water waves on

a free surface: they include both longitudinal and transverse motions, that decay exponentially away from the surface. The speed c_r of Rayleigh waves is given by the solution to the equation

$$\left(2 - \frac{c_r^2}{c_s^2}\right)^2 = 4\sqrt{1 - \frac{c_r^2}{c_s^2}}\sqrt{1 - \frac{c_r^2}{c_p^2}} \tag{5.6}$$

This equation has a unique physical solution, depending on c_p and c_s: for rubber, $c_r \approx 0.95c_s$. This wave speed turns out to be relevant when considering the propagation of cracks through rubber. Other types of surface wave exist, but are not relevant here.

Quasi-longitudinal waves

The longitudinal wave from the previous section describes a motion that is purely compressional, with zero transverse strain. In a finite material, however, equation (5.5) permits another type of longitudinal deformation, one that represents a change in shape but not of volume. These waves are described in detail by Miklowitz [1978]; we give a brief summary in this section. In the interests of simplicity, we consider a deformation of the form $\boldsymbol{a} = (a(t, X), 0, c(t, X, Z))$ and assume the material lies between the region $-h < Z < h$. The equation to be solved is then (5.5), with the added conditions that

$$\nabla.\boldsymbol{a} = 0$$

to ensure the local volume remains constant, and stress-free boundary conditions for u and w at top and bottom boundaries.

As demonstrates, these conditions permit harmonic waves with the dispersion relation

$$(k^2 - \eta_s^2)^2 \left[\frac{\eta_p h \cos(\eta_p h)}{\sin(\eta_p h)}\right] + 4k^2\eta_p^2 \left[\frac{\eta_s h \cos(\eta_s h)}{\sin(\eta_s h)}\right] = 0, \tag{5.7}$$

where

$$\eta_p = \left(\frac{\omega^2}{c_p^2} - k^2\right)^{1/2},$$

$$\eta_s = \left(\frac{\omega^2}{c_s^2} - k^2\right)^{1/2}.$$

The phase speed of these waves is then given by

$$c = \frac{\omega}{k}.$$

Clearly one solution to this equation is just $\eta_p = 0$, which reveals

$$c = c_p$$

and represents the purely compressional longitudinal waves described above. There is another solution to this equation, however, say $c = c_{ql}$, representing longitudinal waves causing transverse strains (hence referred to as quasi-longitudinal waves).

In the limit $h \to 0$, approximating a thin membrane, the dispersion relation becomes

$$(k^2 - \eta_s^2)^2 + 4k^2\eta_p^2 = 0$$

which may be rearranged to show

$$c_{ql}^2 = \frac{\omega^2}{k^2} = 4\left(c_s^2 - \frac{c_s^4}{c_p^2}\right) = \frac{4\mu(\lambda+\mu)}{\rho(\lambda+2\mu)}, \tag{5.8}$$

a non-dispersive wave with phase speed c_{ql} such that $c_s < c_{ql} < c_p$. Written in terms of the Young's modulus E and Poisson's ratio ν, the wave speed is

$$\rho c_{ql}^2 = \frac{E}{1-\nu^2}. \tag{5.9}$$

As the wave motion combines longitudinal and shear components, it may be expected for such waves to travel at the shear wave speed c_s. That they travel faster is a consequence of the top and bottom boundaries of the material acting as a waveguide, focusing any waves traveling along the material. The shear wave speed, $c_s = \mu/\rho$ is the same as for an infinite medium.

As it turns out, it is this second type of longitudinal wave that dominates the motion of retracting natural rubber; the reasons for this are given in the following sections, by using two common approximations for our thin, rubber membranes.

Plane stress approximation

Based on the fact we are considering thin, two-dimensional membranes, we may approximate all stresses transverse to the plane of the membrane as zero. From this, a simplified version of equation (5.5) may be derived, valid for any thin membrane.

This zero-stress assumption is a direct consequence of the membrane being thin. If we Taylor expand the transverse stress near $z = h$,

$$\sigma_{zz} = [\sigma_{zz}]_{z=h} + \left[\frac{\partial \sigma_{zz}}{\partial z}\right]_{z=h}(z-h) + O(h^2). \tag{5.10}$$

Boundary conditions then give $[\sigma_{zz}]_{z=h} = 0$. They also give $\sigma_{zx} = \sigma_{zy} = 0$ on $z = h$ for all X and Y. Consequently, equation (5.1) evaluated at $z = h$ gives

$$\begin{aligned} \rho c_{tt} &= \left[\frac{\partial \sigma_{zx}}{\partial X} + \frac{\partial \sigma_{zy}}{\partial Y} + \frac{\partial \sigma_{zz}}{\partial Z}\right]_{z=h} \\ &= \left[\frac{\partial \sigma_{zz}}{\partial Z}\right]_{z=h}. \end{aligned}$$

Hence $\frac{\partial \sigma_{zz}}{\partial Z} = O(h)$ (as c is), and so as $z = O(h)$,

$$\sigma_{zz} = O(h^2).$$

Thus for $h \ll 1$ we may approximate $\sigma_{zz} = 0$ everywhere for $0 < z < h$. It is then obvious from the condition $\sigma_{zz} = 0$ on $z = -h$ that we may approximate $\sigma_{zz} = 0$ for $-h < z < 0$ too. Using a similar

expansion as in (5.10), it is also easy to show that σ_{xz} and σ_{yz} are order h everywhere, and hence may also be approximated as zero.

Now we consider a deformation of the form $\boldsymbol{a} = (a(t, X, Y, Z), A * Y, c(t, X, Z))$, where we have imposed a constant strain A in the Y-direction to examine its effect on the wave speeds in the X-direction. The condition $\sigma_{zz} = 0$ implies

$$c_Z = -\frac{\lambda}{\lambda + 2\mu}(a_x + A).$$

Consequently, the momentum equation for a becomes

$$\begin{aligned} \rho a_{tt} &= \lambda(a_X + A + c_Z)_X + 2\mu(a_X)_X + \mu(a_Y)_Y \\ &= \frac{4\mu(\lambda + \mu)}{\lambda + 2\mu} a_{XX} + \mu a_{YY}. \end{aligned}$$

The longitudinal wave speed c_l then satisfies

$$\rho c_l^2 = \frac{4\mu(\lambda + \mu)}{\lambda + 2\mu}, \tag{5.11}$$

which is the phase speed of the quasi-longitudinal waves given by equation (5.8). Thus we see that assuming the thickness is small implies any longitudinal waves must be of the quasi-longitudinal type. The compressional longitudinal waves need large transverse stresses that cannot exist in such a thin membrane. Physically, as given by Broberg [1999], any compressional waves decay over distances comparable to the thickness h. They are therefore negligible for any significant motions.

For a thin bar or rod (where the material is thin in both transverse directions) the plane stress approximation is equivalent to $\sigma_{ij} = 0$ for $ij \neq xx$, and leads to

$$\rho c_{ql}^2 = \frac{\mu(3\lambda + 2\mu)}{\lambda + \mu} = E, \tag{5.12}$$

a well-known result (see Love [2013]) often used to model rubber bands (see Vermorel et al. [2007]).

It should be noted that using the plane-stress approximation will almost never give an exact solution: there will always be some transverse stresses with a thin sheet or bar if the Poisson ratio of the material is non-zero. Nevertheless, it is useful approximation that is highly applicable to our experiments, with balloon membranes the order of centimetres in radius, but only tenths of millimeters in thickness.

Incompressibility

Physically, incompressibility means that in response to externally applied stresses, a material cannot change volume, instead only changing shape. Naturally, such a material cannot support compressible waves as described above, that travel at speed c_p. Rubber is only approximately incompressible, but enough that the effect of any pure compression is small. Thus, the large scale longitudinal displacements observed in retracting rubber travel must be accompanied by a change in transverse displacement, as the membrane 'thickens' to maintain the local volume.

Mathematically, the condition that a deformation is incompressible may be expressed as

$$J = det\,(F) = 1, \tag{5.13}$$

with F defined as by equation (2.19). The function J is equivalent to the Jacobian of the transformation from coordinates $\mathbf{X}$ to $\mathbf{x}$.

For a linear deformation $a(\mathbf{X}) = (a, b, c)$,

$$F = \begin{pmatrix} 1 + a_X & a_Y & a_Z \\ b_X & 1 + b_Y & b_Z \\ c_X & c_Y & 1 + c_Z \end{pmatrix}.$$

Thus in the linear limit

$$J = 1 + a_X + b_Y + c_Z,$$

so the incompressibility condition (5.13) is equivalent to

$$\nabla \cdot \boldsymbol{a} = 0. \tag{5.14}$$

It is important to note that (5.14) is only generally true in the linear limit.

Material incompressibility is also equivalent to it having a Poisson ratio $\nu = 1/2$, and $\lambda = \infty$. Hence, incompressibility may also be regarded as the transmission of compressional waves at infinite speed (as $c_p \propto \sqrt{\lambda}$), with changes in pressure transmitted instantly throughout the material accompanied by no change in volume. Effectively, this represents a rigid-body translation of the entire material.

Assuming incompressibility necessitates a change the stress tensor: while the hydrostatic stress is now zero, we must instead introduce an arbitrary function $p = p(t, X, Y, Z)$ such that

$$\boldsymbol{\tau} = -p\boldsymbol{I} + 2\mu\boldsymbol{\epsilon}. \tag{5.15}$$

Physically, p is an arbitrary function as if we apply an equal normal stress to all faces of an incompressible object, no change in its volume (incompressibility) or shape (Newton's first law) would occur, thus causing no change in its motion.

Putting this stress tensor into the Cauchy equation gives

$$\rho\boldsymbol{a}_{tt} = -\nabla p + 2\mu\nabla^2\boldsymbol{a}, \tag{5.16}$$

clearly analogous to the linearised Navier-Stokes equations.

Incompressible plane stress

A good approximation to the waves seen on our thin rubber membranes may therefore be obtained by combining both of these assumptions: incompressibility and plane stress. The plane stress approximation for a deformation $\boldsymbol{a} = (a(t, X, Y), A * Y, c(t, X, Z))$ for some constant A gives

$$p = 2\mu c_Z.$$

Incompressibility gives

$$a_Z + A + c_Z = 0$$

so that

$$p = -2\mu(a_X + A).$$

Equation (5.16) then implies

$$\rho\, a_{tt} = 4\mu\, a_{XX} + \mu a_{YY} \tag{5.17}$$

giving (quasi) longitudinal wave-speed

$$c_{ql} = \sqrt{\frac{4\mu}{\rho}}, \tag{5.18}$$

twice the shear-wave speed c_s. For the Love rod, the equivalent wave speed is

$$c_{ql} = \sqrt{3\mu/\rho}. \tag{5.19}$$

Note that equation (5.18) agrees with (5.11) in the limit $\lambda \to \infty$, as implied by incompressibility.

Given the values of λ and μ previously stated for rubber, we see this gives

$$c_{ql} = 45.4\,\mathrm{m/s},$$

far less than the longitudinal wave speed ($\approx 1,500$ m/s), but double the shear wave speed.

Linear viscoelasticity

As noted in chapter 2, rubber does display some features of viscoelasticity. Lakes [2009] describes a variety of ways to incorporate viscoelastic effects into models of elasticity. One common way is known as the Kelvin-Voigt model, as used by James and Guth [1944] to model retracting rubber strips, where the linear elastic stress tensor $\boldsymbol{\tau} \propto \boldsymbol{\epsilon}$ is replaced by

$$\boldsymbol{\tau} \propto \boldsymbol{\epsilon} + \eta \frac{\partial \boldsymbol{\epsilon}}{\partial t}, \tag{5.20}$$

for some constant η. The extra term in the stress tensor introduces dispersion into the waves. Fortunately, it is well-known (see Gent and Marteny [1982] and Bogoslovov and Rowland [2007]) that the viscoelasticity of natural rubber plays a negligible role during retraction, and thus we may neglect, in general, this term. It is only for other types of rubber, such as Butyl rubber, that viscoelasticity becomes important (see Mrowca et al. [1944]).

5.2.2 Non-linear theory

While the linear theory given above is instructive, chapter 2 revealed that the behaviour of rubber at the large stretches seen in a fully-inflated balloon is highly non-linear. While taking non-linear theories of rubber elasticity into account is complicated in the most general case, the same types of wave may occur, though now they may be dispersive. Here, in the interests of simplicity, we restrict ourselves to examining only the most relevant situation: waves on a thin membrane of biaxially-stretched, incompressible rubber in plane stress. The material is assumed thin in the z direction,

and highly-stretched in the x and y directions. Wave speeds may then be derived from the Cauchy equation (5.1), along with the incompressibility condition

$$J = 1, \tag{5.21}$$

and the plane stress approximation

$$\tau_{ZZ} = 0. \tag{5.22}$$

The Lagrangian wave speeds now depend on the stress-state of the rubber, and thus are different in different directions; those for waves in the x direction are given the subscript x, those in the y direction the subscript y, with the material density given by ρ.

The most common way of modeling non-linear displacements in natural rubber is using the incompressible Mooney-Rivlin model, a phenomenological model previously discussed in section 2.13. For this model, the rubber in the membrane is assumed to be isotropic and hyperelastic, with strain energy density W given by

$$W = \frac{1}{2}\left(\frac{\mu_1}{2} I_B + \frac{\mu_2}{-2} II_B\right), \tag{5.23}$$

where $\boldsymbol{I_B}$ and $\boldsymbol{II_B}$ are invariants of the left Cauchy-Green stress tensor $\boldsymbol{B} = \boldsymbol{F}\boldsymbol{F}^T$ given by

$$\boldsymbol{I_B} = Tr(\boldsymbol{B}), \tag{5.24}$$

$$\boldsymbol{II_B} = \frac{1}{2}\left[Tr(\boldsymbol{B})^2 - Tr(\boldsymbol{B}^2)\right]. \tag{5.25}$$

The constants μ_1 and μ_2 are material constants that need to be determined experimentally, though to ensure continuity with linear theory they must satisfy

$$(\mu_1 - \mu_2) = \mu. \tag{5.26}$$

The wave-speed in a stationary, stretched Mooney-Rivlin material may then be calculated. In the most general (compressible) case its form is highly complicated and nonlinear, and as we have already explained, not relevant to our experiments. Fortunately, the system in the case of incompressible plane stress is far easier to solve. Let us, as before, consider a deformation of the form

$$\boldsymbol{a}(t, X, Y, Z) = (a(t, X, Y), AY, c(t, X, Y, Z))$$

for some constant A, within a thin membrane lying in $-h < Z < h$. The incompressibility condition (5.21) gives

$$c_Z = \frac{1}{(1 + a_X)(1 + A)} - 1. \tag{5.27}$$

The stress tensor is

$$\boldsymbol{\tau} = -p(t, X, Y, Z)\, \boldsymbol{I} + \boldsymbol{\tau_d}$$

for some function p to be determined, with the deviatoric stress given by

$$\boldsymbol{\tau_d} = (\mu_1 - I_B\mu_2)\boldsymbol{B} + \mu_2\boldsymbol{B}.$$

The plane stress approximation (5.22) then leads to

$$p = \frac{\mu_1}{(1+a_X)^2(1+A)^2} - \mu_2\left[\frac{1}{(1+a_X)^2} + \frac{1}{(1+A)^2}\right],$$

so that the momentum equation for a becomes

$$\begin{aligned}\rho a_{tt} &= [\mu_1(1+3(1+A)^{-2}(1+a_X)^{-4}) - \mu_2((1+A)^2+3(1+a_X)^{-4})]a_{xx} \\ &\quad +[\mu_1 - \mu_2(1+a_X)^{-2}(1+A)^{-2}]a_{YY} + Ba_{XY} + h.o.t., \end{aligned} \tag{5.28}$$

where B is a function of μ_1, μ_2, A, a_X and a_Y. From this equation, we see that the quasi-longitudinal wave-speed depends on both X and Y strains in the material (unlike the linear case), and is given by

$$c_{ql(x)} = \left[\frac{[\mu_1(1+3\lambda_y^{-2}\lambda_x^{-4}) - \mu_2(\lambda_y^2+3\lambda_x^{-4})]}{\rho}\right]^{1/2}. \tag{5.29}$$

We note that as $\lambda_x, \lambda_y \to 1$, $c_{ql}^2 \to 4(\mu_1 - \mu_2) = 4\mu$, which agrees with linear theory for small deformations.

The shear wave speed is

$$c_{s(x)} = \left[\frac{\mu_1 - \mu_2(\lambda_x^{-2}\lambda_y^{-2})}{\rho}\right]^{1/2}. \tag{5.30}$$

In the limit $\lambda_x, \lambda_y \to 0$, $c_{s(x)} \to (\mu_1 - \mu_2) = \mu$, in agreement with linear theory.

We note here that these wave speeds agree with those found by Petersan et al. [2004] for thin, highly-stretched, Mooney-Rivlin materials in the limit λ_X, λ_Y are large, and thus neglecting terms $O(\lambda^{-4})$ and higher. Their (simplified) wave speeds are given by:

$$c_{ql(x)} = [\frac{\mu_1 - \mu_2\lambda_y^2}{\rho}]^{1/2}, \tag{5.31}$$

$$c_{s(x)} = [\frac{\mu_1}{\rho}]^{1/2}. \tag{5.32}$$

It was found in chapter 2 that for the highest strains seen in inflated balloons, the behaviour of the rubber was best modelled by the Ogden's model, where

$$W(\lambda_1,\lambda_2,\lambda_3) = \sum_{p=1}^{N}\frac{\mu_p}{\alpha_p}\left(\lambda_1^{\alpha_p}+\lambda_2^{\alpha_p}+\lambda_3^{\alpha_p}-3\right)$$

with N, μ and α_p material constants. For our balloons, the best fit was found using $N = 3$, $\alpha_1 = 1.3$, $\alpha_2 = 5$, $\alpha_3 = -2$. Unfortunately, repeating the analysis presented here for Mooney-Rivlin theory is difficult, due to the more complex nature of the strain energy density. Furthermore, unlike for the Mooney-Rivlin theory, we can also find no evidence of such an analysis being performed for the Ogden's theory in the literature (likely because few authors considered as large extensions as we are

interested in). Nonetheless, the longitudinal wave speed for a biaxially-stretched membrane may be found using the relation given by Mason [1963] for longitudinal stress waves,

$$c_{ql} = \sqrt{\frac{1}{\rho}\frac{d[\tau_R]_{xx}(\lambda_x)}{d\lambda_x}}. \tag{5.33}$$

The theory presented in chapter 2 implies

$$\begin{aligned} [\tau_R]_{XX} &= \frac{\partial W}{\partial \lambda_x} - \frac{1}{\lambda_x} P \\ &= \frac{\partial W}{\partial \lambda_x} - \frac{\lambda_z}{\lambda_x}\frac{\partial W}{\partial \lambda_z} \end{aligned} \tag{5.34}$$

where $\lambda_z = (\lambda_x \lambda_y)^{-1}$ by incompressibility. This leads to

$$c_{ql} = \left[\frac{1}{\rho}\left(\mu_1(0.3\lambda_x^{-0.7} + 2.3\lambda_x^{-3.3}\lambda_y^{-1.3}) + \mu_2(4\lambda_x^3 + 6\lambda_x^{-7}\lambda_y^{-5}) - \mu_3(3\lambda_x^{-4} + \lambda_y^2)\right)\right]^{1/2} \tag{5.35}$$

that in the limit of large λ_x and λ_y becomes

$$c_{ql} \to \left[\frac{1}{\rho}\left(4\mu_2\lambda_x^3 - \mu_3\lambda_y^2\right)\right]^{1/2}. \tag{5.36}$$

The shear wave speed is far more complex to derive, so is not done here. However, the best fit of the Mooney-Rivlin model to our quasi-static data was reasonable for all stretches, thus serves to provide a good estimate of the non-linear behaviour of rubber in extension. Consequently, we shall use the shear wave estimate from the Mooney-Rivlin model where necessary.

5.3 Rupture mechanism

Rupture of the water balloons occurred due to the high tension within the membrane causing the creation of one or more cracks (see figure 3.4) by small defects in the rubber. These cracks would then propagate round the balloon. The faces of each crack was stress-free, so that tension on one side of the crack was no longer balanced by tension on the other side. This imbalance in elastic forces then caused the membrane to retract. For the water balloons dropped in air, the cracks propagated from small defects already present in the membrane, the high tension created as the balloon deformed upon impact causing the cracks to spontaneously form. For the balloons held stationary and oscillated as described in section 4.1, the tension rarely became high enough for spontaneous crack formation to occur. Instead, rupture was initiated by pricking the membrane with a sharp pin; the consequent large defect then lead to the propagation of a crack round the membrane, despite the relatively low membrane tension when compared with dropped balloons.

5.3.1 Crack speed

The exact nature of the cracks we observed on our balloons proved difficult to determine experimentally, even when observing the stationary balloons, due to the curvature of the membranes when

inflated. However, much work has been done on crack propagation in elastic materials, as summarised by Broberg [1999]. The cracks seen in rupturing water balloons are what are known as mode I or opening cracks, where crack propagation is caused by a tensile stress normal to the plane of the crack faces. There two other types of crack: mode II or in-plane shear cracks (where a shear stress is applied parallel to the plane of the crack in the plane of the membrane) and mode III or out-of-plane cracks (where a shear stress is applied parallel to the crack but out of the plane of the membrane). According to linear crack theory, while the propagation speed for each crack depends on the stress conditions, each crack type has a different limiting velocity: c_r for mode I cracks, c_p for mode II cracks, and c_s for mode III cracks. Cracks whose speed c lies in the range $c_s < c < c_p$ are termed intersonic. Physically, these limiting velocities arise because energy is needed to create new surface area, such as the crack faces, and thus for the crack to propagate. This energy comes from the elastic energy in the material, of which there is not enough near the crack tip. It therefore requires energy stored elsewhere, that may only travel into the crack tip as fast as the relevant limiting wave speed. Consequently, the crack itself is limited by the same speed.

According to this linear theory, therefore, as the cracks seen in rupturing water balloons are mode I cracks, their speed should be limited above by the shear wave speed c_s (as $c_s > c_r$). As calculated in the previous section, for rubber experiencing a linear deformation, this is approximately 15.7 m/s; the non-linear Mooney-Rivlin model gives the speed as approximately 16.6 m/s. Yet rubber under high-extension was found by Stevenson and Thomas [1979] (and later by Petersan et al. [2004] and Chen et al. [2011]) to permit crack speeds in excess of the shear wave speed, in the intersonic region. Marder [2006] then proved that this behaviour was in agreement with non-linear (Neo-Hookean) theory. Physically, this intersonic behaviour is permitted here because for rubber under such high extensions, there is enough elastic energy local to the crack tip to permit it to propagate; the crack does not have to 'wait' for energy from far away to travel in for it to propagate.

We have conducted our own experiments into the crack speeds for our bursting balloons. The same equipment as described in section 4.1 was used, with the camera horizontal and focused on the centre of the balloon ($\phi = \pi/2$). The balloons were inflated, held stationary, then pricked with a pin at $\phi \approx \pi/4$, with the ensuing process recorded by the high-speed camera at a frame-rate of 30,000 fps. The speed of the crack was then measured, from the video, as close as possible to $\phi = \pi/2$, and so close to where it was initiated to limit the influence of stress waves that may be propagating faster than the crack itself. This process was performed for a range of inflations, and with air inside and outside the membrane, water inside and air outside, and water inside and outside. Different measurements of the crack speed for one such rupture revealed the crack to be traveling at approximately constant speed, so only one measurement of crack speed was taken for subsequent ruptures.

Results are shown in figure 5.2, along with the theoretical wave speeds $c_s = 16.6$ m/s from the Mooney-Rivlin model, and $c_{ql} = \left[15.3\lambda^3 + 1.0\lambda^2\right]^{1/2}$ ms from the Ogden's model. It should be noted that there is likely to be a reasonable degree of error in these measurements, due to the high speeds and curved shape of the membrane. The results are for stretches in the range $\lambda = 3$ to $\lambda = 7.5$; below this range the cracks would not propagate round the balloon, and the balloon deflated by the inner fluid simply passing out through the small hole created by the pin. Above this range, the balloons would rupture spontaneously, so that the crack path would be unknown and thus difficult to measure. Nevertheless, it is clear that intersonic crack speeds were always seen for cracks at stretches above $\lambda = 5$. This was the case for all cracks with air both internal and external to the membrane. However,

cracks appear to propagate below the shear wave speed for the water/air case when $\lambda < 3.7$, and for the water/water case when $\lambda < 4.7$. Yet it is important to note that this shear wave speed is the speed found when neglecting any medium external to the rubber. Including the added mass effect of the water dragged along with membrane as it retracts may well mean that such cracks are in fact intersonic too. As shall be shown in section 5.4.2, the boundary layer is of the order of fractions of a millimetre within water, thus of similar size and mass to the membrane itself; under this assumption, the wave speeds should be reduced by a factor of 1.4 for water/air, and 2 for water/water, suggesting the cracks observed were, in fact, intersonic.

By way of comparison, the experiments of Stevenson and Thomas [1979] found, for bursting spherical balloons (of unstated size) with air both inside and outside, maximum crack speeds of 133 m/s for $\lambda = 2.3$, 230 m/s for $\lambda = 3.7$, and 285 m/s for $\lambda = 5$. Results for our balloons suggest crack speeds around half those found by Stevenson and Thomas [1979], with the discrepancies likely arising from different types of rubber being used, and inaccuracies in the method of Stevenson and Thomas [1979]. Nevertheless, they are of a similar order. The presence of water around the membrane clearly slowed down the propagation of the crack, decreasing its speed by 25% for the water/air case, and 35% for the water/water case. This occurred because the crack only propagated as the material either side of it retracted. If the retraction of the material is slowed down, then so will the crack slow down. This goes along with the idea of the water's added mass slowing down the crack propagation, as the retracting membrane must drag fluid along with it. The adjustment to the speed will, as argued above, be of the order of 1/1.4 and 1/2 respectively, so in line with what is observed experimentally.

From these experiments, we may estimate the crack speed in a water balloon bursting after impact with a rigid surface. Then, rupture only occurs when natural flaws in the rubber cause a crack to propagate, thus for stretches around $\lambda = 8$. From figure 5.2, this suggests a crack propagation speed around 260 m/s.

5.3.2 Crack tip shape

Linear elastic theory (see Broberg [1999]) predicts that the shape of a crack tip should be parabolic; yet both Petersan et al. [2004] and Chen et al. [2011] observed that when the crack speed in rubber was intersonic, the crack tips became sharp and wedge-like. This was likened to the Mach cone formed when an object exceeds the wave speed in an elastic medium, just as the crack speed exceeded the limiting linear speed, c_R. Marder [2006] confirmed that such cone-like crack shapes were in agreement with non-linear (Neo-Hookean) theory.

Using the same videos as those captured when measuring the crack tip speed in the previous section, it was simple to observe the shape of the crack tips, and sample images are given in figure 5.3. The cracks had sharp, wedge-like tips in every experiment, for the full range of stretches and fluids (water and air) external to the membrane for which a crack propagated. For each experiment, the angle between the faces of the crack at its tip was measured, with results shown on figure 5.4. They clearly show the angle reducing with increasing stretch, with the presence of water reducing the angle further. Another way to consider this is to compare the speed of the crack with the retraction speed of the membrane, as is also displayed in figure 5.4. The ratio of speeds for air inside and outside the balloon matches up with the work of Stevenson and Thomas [1979], found by both them and us to be around 3. The presence of water also outside the membrane increases this ratio to around 4. This shows that the crack speed is enhanced relative to the material speed for higher stretches and the

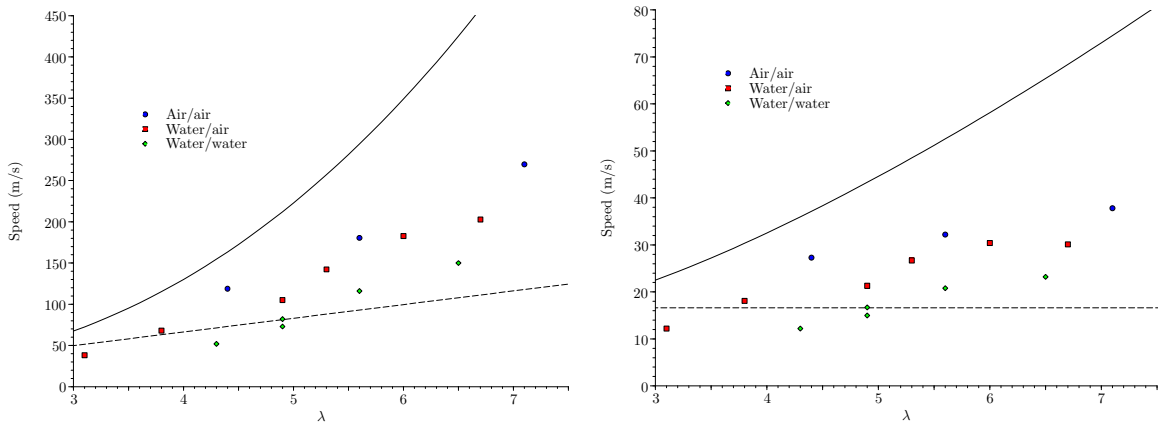

Figure 5.2: The speed of crack propagation in 130 mm balloons, when surrounded by either air, water, or both. Image **(a)** gives the speeds in the Eulerian (laboratory) frame, while image **(b)** gives the speeds in the Lagrangian (reference) frame for the rubber. The quasi-longitudinal wave speed for the Ogden's model is given by the solid black line, the shear wave speed for the Mooney-Rivlin model by the dashed black line.

presence of water. Drag from the water on the membrane thus has a more significant effect on the retracting membrane than on the crack itself, slowing the material down more than the crack. This, in turn, reduced the angle of the crack tip.

5.3.3 Crack path

For an elastic sheet under biaxial tension, Anderson [2004] demonstrated that the crack's path will tend to one perpendicular to the direction of the greatest tension, as this will release the greatest energy. For a cylinder under uniform internal pressure (where the curvature is zero along the cylinder, but positive around its circumference), it was shown in Gere and Timoshenko [1997], and in chapter 2, that the tension around the circumference of a pressurised cylinder is twice that of the tension along its length. Consequently, it would be expected that a crack in a filled cylindrical balloon would travel along its length. Indeed, this was always observed to be the case for our 646 balloons (as in figure 5.5), even when the initial crack direction was almost parallel to the direction of greatest tension.

For our 130 mm balloons, and as demonstrated by the experiments of the previous sections, the crack usually travelled approximately vertically, simultaneously moving from the hole created by the needle to the open end, and from the hole to the apex. This was likely a result of a lack of spherical symmetry in the balloons. As demonstrated in 2.11, a high volume of water inside the balloon corresponded to a loss of symmetry. The balloons became more elongated and 'pear-like' in shape, with the curvature of the surface greater horizontally (in the azimuthal direction) than vertically (polar direction). This, therefore, would correspond to higher tension horizontally than vertically, so the crack would tend to travel vertically. This was not always the case, however, with some (as in figure 5.6) travelling near horizontally. This could occur because the relative difference in horizontal

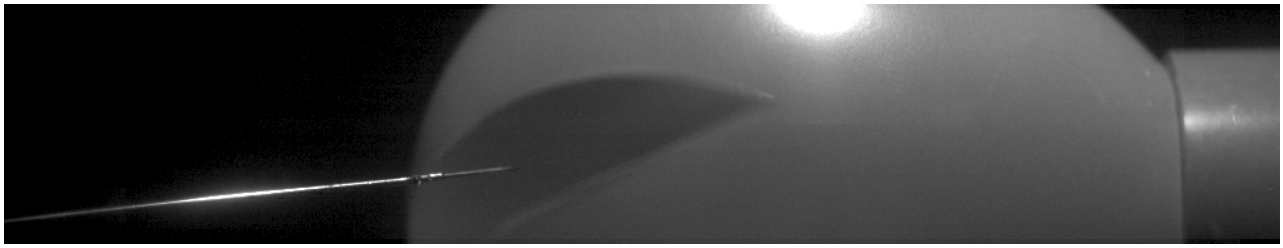

(a) Air/Air, $\lambda = 5.6$

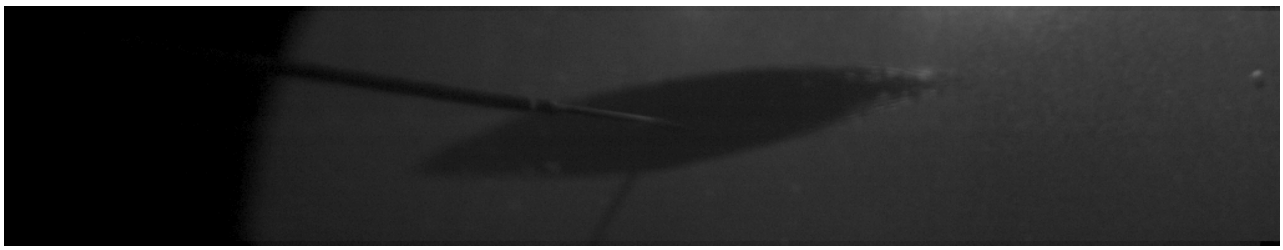

(b) Water/Water, $\lambda = 4.7$

Figure 5.3: The shape of the crack tips propagating through our balloon membranes, as seen in images captured using the high-speed camera recording at $30,000$ fps. In all cases, the tips were observed to be sharp, though the presence of water and higher stretch did reduce the angle between the crack faces.

and vertical curvatures, and hence tensions, was small. Thus, on occasion, factors like details of the structure of the latex due to the manufacturing process, defects in the latex, and the initial crack direction could overcome the crack's tendency to go vertical.

Furthermore, the cracks were not observed to be straight (as evidenced in 5.1), even allowing for a change in direction should they not be initiated vertically. Such 'wavy' cracks have been observed previously in balloons by Stevenson and Thomas [1979], and in flat biaxially-stretched rubber sheets by Deegan et al. [2002]. For the bursting balloons of Stevenson and Thomas [1979], the cracks were macroscopically straight near the initiation point, with oscillations of wavelength and amplitude the order of micrometers, before becoming visibly 'wavy' later on in their propagation round the balloons, with wavelength and amplitude on the order of millimetres. Deegan et al. [2002] found that in biaxially stretched flat sheets, these waves took the form of sinusoidal deviations from the crack path, whose wavelengths scaled linearly with the stretch, while the amplitude scaled with its square-root. Unfortunately, the reasons for this phenomena are unknown, though Endo et al. [2012], who found evidence of wavy cracks in uniaxially stretched rubber sheets, argued that it was strongly linked to the non-linearity of rubber at high extensions. Petersan et al. [2004] also suggested that the fact the cracks were intersonic (a consequence of non-linearity) could play a role.

Observations of the crack paths in our balloons revealed little evidence of the macroscopic waviness found by Deegan et al. [2002], but showed similar behaviour to that of Stevenson and Thomas [1979]: the crack propagated initially in an approximately straight line, usually vertically, as can be seen in figure 5.3. If the rupture was initiated near the top of the balloon, the crack propagated symmetrically down either side to the tube region at the bottom; as this region was cylindrical, the crack propagated

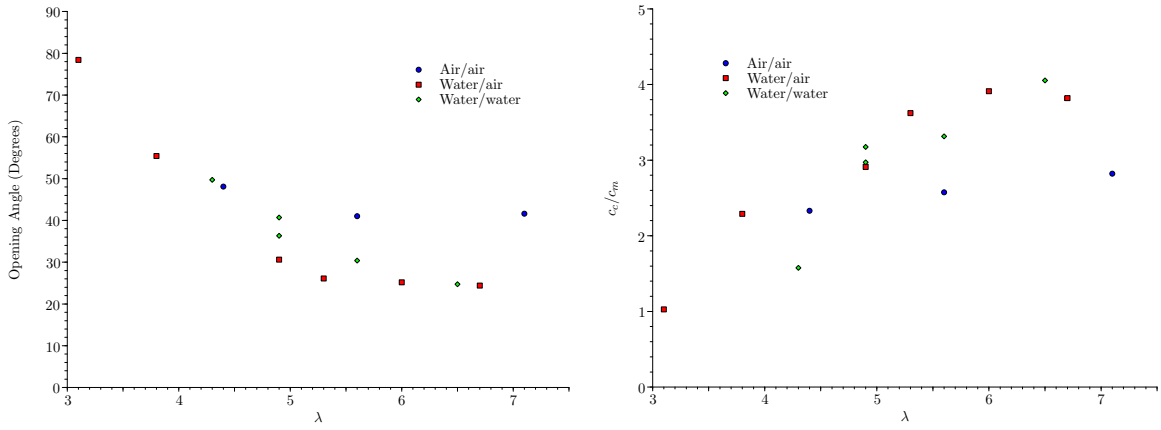

(a) (b)

Figure 5.4: For cracks propagating through a balloon membrane, the tips were always sharp. Image **(a)** shows the angle between the faces at the tip, while image **(b)** shows the ratio between crack speed and the speed of the membrane retracting away from the crack.

straight down it, parallel to the axis of the tube, until it stopped a few millimetres from the open end. Though the crack paths were not perfectly straight, there was little clear evidence of a stable oscillation in the crack path. Such deviations that there were were just as likely to have been caused by imperfections in the membrane.

Cracks that were initiated away from the top did show more interesting behaviour, as is shown in figure 5.7. For most of our experiments, including those of the previous sections, the membrane was ruptured at around $\phi = \pi/4$, thus a quarter of the way down the balloon from the top. The crack then, as always, propagated in two directions away from the initial hole. The half propagating downwards behaved as described above for a balloon ruptured at the top, traveling in a near straight line to the open end. The half propagating upwards travelled in a near straight line over the top of the balloon and down the other side. However, around half way down the other side, it then deviated sharply, to propagate horizontally around the balloon. Often, though not always, it would meet the other half of the crack, causing one section of membrane to be completely separated from the rest. This behaviour occurred whatever fluid surrounded the membrane.

The reason for this deviation is unclear, though it may be a consequence of the fact that, for the large, non-linear stretches we were considering, the speed of the stress waves was far greater than the speed of the crack (as will be discussed in section 5.4). Consequently, by the time the crack was low on the opposite side of the balloon from the initiation point, the material it passed through had been significantly relaxed by stress waves from the other half of the crack. These stress waves had reduced the tension in the horizontal (θ) direction, meaning the greater tension is now in the vertical (ϕ) direction. As the crack wanted to travel perpendicular to the direction of greatest tension, it therefore changes direction to become horizontal.

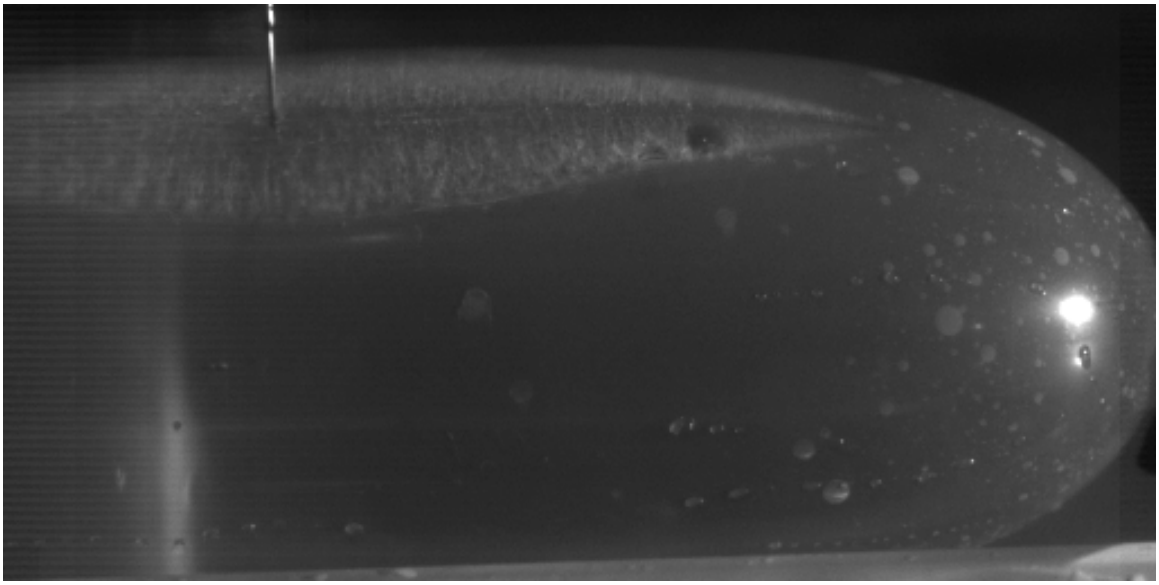

Figure 5.5: A crack propagating through a 646Q cylindrical membrane. The crack propagated parallel to the axis of the balloon, behaviour observed for all ruptures of cylindrical balloons.

5.4 Retraction of the membrane

Once the crack had initiated and propagated around the membrane, the rubber either side then retracted away from the crack. This retraction continued until the membrane had returned to its undeformed state (or close to it, due to viscoelastic effects), when all its elastic tension had been relaxed. For balloons with air both inside and outside, the crack propagation speed was around three times the propagation speed of the membrane. With water present, the crack propagation speed was around four times the propagation speed of the membrane. Consequently, when considering the behaviour of the rubber in retraction, we neglect the propagation of the crack, and instead assume it is instantaneous. Including a moving crack would great complicate the analysis, while not introducing any significant qualitative differences. We also neglect the waviness of the crack, as little evidence of significant waviness was found. As the faces of the crack were stress-free, these assumptions were equivalent to instantaneously applying a stress-free condition at $t = 0$ along a straight line within the membrane. By symmetry, we need only consider the behaviour one side of the crack, at least in the early stages of retraction. This situation is then directly related to the one-dimensional retraction of rubber strips. We focus on this simplified geometry (the curvature of balloon membranes made it difficult to observe the entirety of a single retraction), as the algebra is vastly simpler, while the main phenomena are the same. The small differences that do arise due to geometry are addressed at the end of this section.

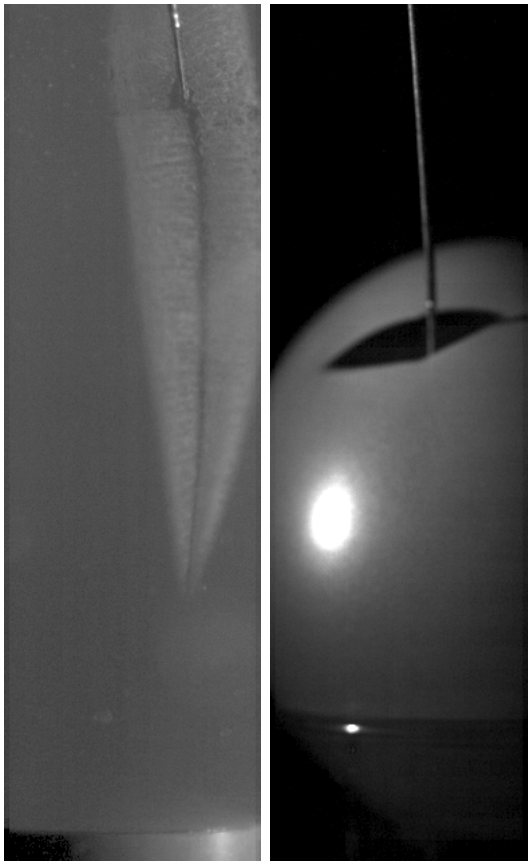

(a) (b)

Figure 5.6: The direction of crack propagation in 130 mm spherical balloons. Cracks in spherical 130 mm balloons usually travelled vertically, as in **(a)**. However, image **(b)** shows a crack traveling near horizontally.

5.4.1 Retraction in air

We first consider the retraction of rubber in air, as it permits direct comparison with the work of others, such as Stambaugh [1944], Mrowca et al. [1944], Mason [1963], Gent and Marteny [1982], Bogoslovov and Rowland [2007], Vermorel et al. [2007] and Niemczura and Ravi-Chandar [2011c]. By assuming air external to the membrane, it permits us to neglect drag from the fluid external to the rubber; the effect of the surrounding fluid will be addressed in section 5.4.2.

As before, we consider first the linear theory, as while it is not applicable to the high extensions seen in our balloons, it is instructive through its simplicity.

Linear Retraction

The theory for a linear rubber strip in retraction was first derived by James and Guth [1944], from equation (5.5) in conjunction with suitable boundary conditions. Only quasi-longitudinal motions are

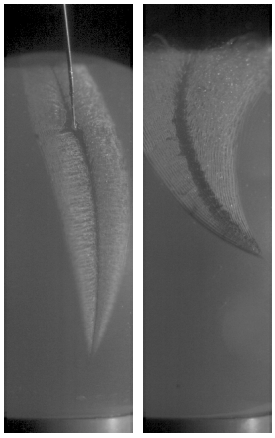

(a) (b)

Figure 5.7: The path of crack propagation in 130 mm spherical balloons initially ruptured away from the top. On the same side as the rupture **(a)**, the crack travelled in a straight line; on the opposite side **(b)**, the crack deviated sharply to one side, before continuing horizontally. Note that these images are of two separate balloons, though both ruptured in an identical way.

considered, so that $\boldsymbol{a} = (a(t, X), 0, 0)$. The strip lies in the region $0 < X < L$ in its undeformed configuration, and is held stationary, stretched at length $(1+\epsilon)L$, before the end at $X = L$ is released at $t = 0$. The assumption of incompressible plane stress in a thin bar then leads to the momentum equation

$$\rho a_{tt} = 3\mu_{XX} = E a_{XX} \qquad \text{for } 0 \leq X \leq L. \tag{5.37}$$

The initial conditions are

$$u_X(0, 0 \leq X \leq L) = \epsilon, \tag{5.38}$$

$$u_t(0, 0 \leq X \leq L) = 0. \tag{5.39}$$

For the boundary conditions, the strip is fixed at $X = 0$, while the end at $X = L$ becomes stress free instantaneously at $t = 0$. The first condition gives

$$a(t > 0, 0) = 0. \tag{5.40}$$

Using the stress tensor as given by (5.15),

$$\tau_{XX} = 3\mu a_X. \tag{5.41}$$

implying the other boundary condition to be

$$a_X(t > 0, L) = 0. \tag{5.42}$$

The solution, as given by James and Guth [1944], is then easy to find:

$$a(t, X) = \begin{cases} \epsilon X & X \leq L - Vt, \\ \epsilon(L - Vt) & X > L - Vt. \end{cases} \tag{5.43}$$

where $V = \sqrt{E/\rho}$ is the speed of the quasi-longitudinal stress wave as given in (5.12). For such waves in a thin plane membrane, $V = \sqrt{E/\rho(1-\nu^2)} = (2/\sqrt{3})\sqrt{E/\rho}$ as in (5.9). This solution may be interpreted as the imposition of the stress-free condition at $X = L$ causing a stress wave to travel through the material (or mathematically as the discontinuity in the initial and boundary conditions propagating through the material) at longitudinal wave speed c_{ql} that is independent of the initial strain. This wave takes the form of a shock wave: all the material in front of it is stretched to strain ϵ and stationary, while all the material behind it is unstretched and in motion at velocity $-\epsilon V$. The stress wave reaches $X = 0$ at time L/V, at which time the material has returned to its unstressed configuration (though still traveling at velocity $-\epsilon V$). Experiments on rubber strips by numerous authors, such as Stambaugh [1944], Mrowca et al. [1944] and Vermorel et al. [2007], have shown a good agreement with this theory: the retraction was observed to be non-dispersive to a good approximation, with acceleration limited to a very narrow region behind the wavefront, behind which all material travelled at the same speed.

It is worth noting here that this theory provides support for our statement that retraction occurs through quasi-longitudinal wave motions: if the rubber band was deforming due to compressible longitudinal waves, we would expect the acceleration wave to travel at $c_p = 1420$ m/s, and the end of the rubber band at $\epsilon V = 1420\epsilon$ m/s. This predicts that a rubber band stretched beyond 50 % of its initial length would break the sound barrier as it retracts! Yet this is not what was observed, both in our experiments and those of others: the rubber is in fact deforming due to quasi-longitudinal waves, and thus the end of the rubber is traveling closer to $\epsilon V = 45.4\epsilon$ m/s. The rubber would therefore need to be stretched to around eight times its initial length to break the sound barrier in air as it retracts, and while linear theory would no longer apply in such a situation, this at least appears physically reasonable. As stated previously, any pure compressional waves that did appear when the free end was released rapidly decayed in amplitude, becoming negligible within a few membrane thicknesses of the free end.

We conducted a small number of experiments to examine the behaviour of our balloon rubber when retracting from uniaxial initial stretches. These experiments were performed on strips 10×100 mm cut from a cylindrical 646 balloon, along which equally spaced parallel lines were drawn with a ball point pen. The strip was held clamped stationary at one end, with a rigid tube pushing down on the clamp to hold it in place. The final 5 mm of the other end was held above it in a clamp attached to a stand. This second clamp could then be moved up and down to change the initial stretch. The free end was then released by hand as smoothly as possible, causing the strip to retract. The whole process was recorded by the high-speed camera, in the range $20,000$ fps to $108,000$ fps. From the resulting video, the displacement of the lines on the strip could be tracked over time, and compared to the predictions of theory. Mason [1963] explained how the strain may also be determined by measuring the width of the strip, due to incompressibility. However, difficulties in cleanly cutting the strip out of the balloon meant that the width was not sufficiently uniform pre-stretch, so that using the width as a measure of strain was subject to a high degree of inaccuracy.

As a balloon would not rupture when the stretch was sufficiently small for linear theory to hold ($\lambda < 2$), we did not perform extensive tests as described above on such small initial stretches. However, figure 5.8 does show one such experiment for an initial stretch of 1.3, with the material clearly displaying the predicted near shock-like behaviour. The speed of the wavefront as estimated from figure 5.8 is $c_{ql} = 27$ m/s. This is at least of similar order to the theoretical value derived earlier,

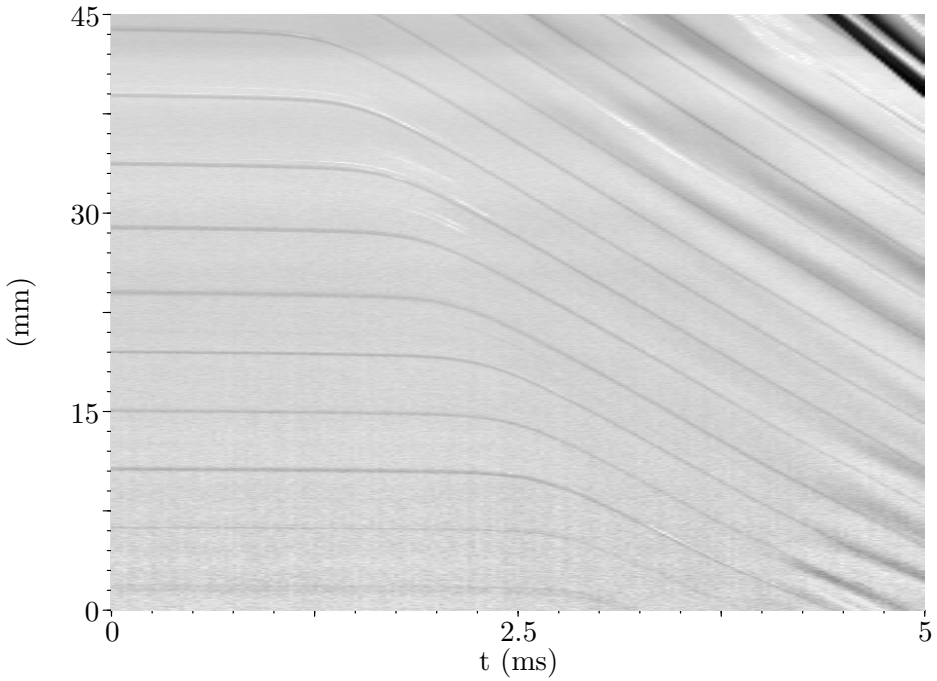

Figure 5.8: The displacement over time of lines marked on a latex strip retracting from an initial stretch $\lambda_0 = 1.3$. In this linear region, there is very little dispersion. The material undergoes full retraction and acceleration to its maximum speed over a very short time period relative to the total time of retraction.

$c_{ql} = 59$ m/s. The difference between the two values is likely due to the assumed value for the shear modulus μ, found by other authors, being inaccurate for our rubber. The small amount of dispersion in the unloading wave seen in figure 5.8 may also play a role in causing the inaccuracy.

Effect of viscoelasticity

We briefly discuss here the effects viscoelasticity could have on the retraction of rubber strips. The main viscoelastic effect that would affect the retraction of rubber is known as internal friction: frictional forces generated within the material as the long chains of molecules move past one another. The effects of internal friction were considered by James and Guth [1944] who, using the Kelvin-Voigt model discussed in section 5.2.1, derived the momentum equation to be

$$\rho a_{tt} = E a_{XX} + \eta a_{tXX}. \tag{5.44}$$

In the limit of high internal friction, the inertial term is neglected, and the solution becomes

$$a \approx \epsilon X \exp(-(E/\eta)t). \tag{5.45}$$

The retraction is therefore highly disperse; such behaviour is seen many types of rubber in retraction, including Butyl tread (see Mrowca et al. [1944]). However, several authors studying the retraction

of stretched rubber, including Mason [1963], Gent and Marteny [1982], and Bogoslovov and Rowland [2007], found that such viscoelastic effects were unimportant in natural rubber. Combined with our own experiments on retracting linear rubber strips showing no evidence viscoelasticity, we therefore neglect such effects in future work.

Non-linear retraction

If we wish to make direct comparisons with our retracting balloon membranes, we must consider non-linear theory. First we consider Mooney-Rivlin theory, then Ogden's theory, as they were shown in chapter 2 to be the most accurate for our rubber in quasi-static extension. However, as shall be discussed in the following section, neither model provides a good fit for rubber in retraction.

As we are considering only quasi-longitudinal deformations in the X direction, we consider a deformation of the form $\boldsymbol{a} = (a(t,X), b(t,X,Y), c(t,X,Z))$, where a deformation has been imposed in the X-direction independent of Y and Z, with no deformation or stress imposed in the other two directions (though there will be some stretching in those directions, to ensure that the condition of incompressibility is satisfied). By considering such a deformation imposed on a thin strip, we may examine how the wave speed in non-linear materials depends on the imposed stretch, in contrast to the linear situation discussed previously.

The principal stretches are $\lambda_x = (1+a_X)$, $\lambda_y = (1+b_y)$, $\lambda_z = (1+c_z)$. The deformation is assumed symmetric in the $Y$and Z directions, so that incompressibility implies $\lambda_y = \lambda_z = \lambda_x^{-1/2}$. The stresses in the reference configuration are given by equation (2.25),

$$[\tau_R]_{ii} = \frac{\partial W}{\partial \lambda_i} - \lambda_i^{-1} P,$$

for some hydrostatic pressure P. The plane stress assumption implies $[\tau_R]_{YY} = [\tau_R]_{YY} = 0$, leading to

$$P = \lambda_y \frac{\partial W}{\partial \lambda_y}. \tag{5.46}$$

The equation of motion is then given by equation (5.1) while neglecting $[\tau_R]_{xy}$ and $[\tau_R]_{xz}$ using the plane stress assumption, leading to

$$\rho a_{tt} = \frac{\partial}{\partial x}[\tau_R]_{xx}. \tag{5.47}$$

For a Mooney-Rivlin material, the strain energy density is, by equation (2.34),

$$W = \frac{\mu_1}{2}\left(\lambda_x^2 + \lambda_y^2 + \lambda_z^2 - 3\right) + \frac{\mu_2}{-2}\left(\lambda_x^{-2} + \lambda_y^{-2} + \lambda_z^{-2} - 3\right),$$

leading to the equation of motion,

$$\rho a_{tt} = \left[\mu_1(1 + 2(1+a_X)^{-3}) - 3\mu_2(1+a_X)^{-4}\right] a_{XX}. \tag{5.48}$$

This is a wave equation, with wave speed c given by $\rho c^2 = \mu_1(1 + 2\lambda_x^{-3}) - 3\mu_2\lambda_x^{-4}$ that agrees with the linear wave speed (5.19) as $a_X \to 0$. As the wave-speed depends on the strain, the waves are dispersive. However, for the retraction of a strip of Mooney-Rivlin rubber, only the speed of the stress wave is different from the behaviour for a linear strip. As before, a shock travels from the free end at

a constant speed, behind which the material is fully retracted; such behaviour, with a shock forming near-instantaneously upon release, was observed by Niemczura and Ravi-Chandar [2011c], amongst others. That this happens despite the dispersion is because the wave speed c_{ql} is monotone decreasing in the strain a_X for all (positive) values of a_X, so that stress waves for smaller strains travel faster than those for high strains. However, the rubber must pass through the higher strains to reach the lower ones, the waves for different strains therefore collapsing on the wavefront for the highest strain. Consequently, a shock forms, as the material passes through all strains to zero at the same moment. The same occurs for the linear, non-dispersive case as wave speeds for all strains travel at the same speed, and are all started at the same time when the free end is released. As a consequence of this, it is impossible to tell whether the behaviour seen in figure 5.8 is linear or Mooney-Rivlin purely from the presence of the shock.

Consideration of an Ogden's material reveals different behaviour, however. Now the strain energy density is given by equation (2.36),

$$\begin{aligned} W &= \frac{\mu_1}{1.3}\left(\lambda_1^{1.3}+\lambda_2^{1.3}+\lambda_3^{1.3}-3\right)+\frac{\mu_2}{5}\left(\lambda_1^{5}+\lambda_2^{5}+\lambda_3^{5}-3\right) \\ &\quad +\frac{\mu_3}{-2}\left(\lambda_1^{-2}+\lambda_2^{-2}+\lambda_3^{-2}-3\right). \end{aligned}$$

Following the same method as above, the equation of motion is given by

$$\begin{aligned} \rho a_{tt} &= \left[\mu_1(0.3(1+a_X)^{-0.7}+1.65(1+a_X)^{-2.65})\right. \\ &\quad \left.+\mu_2(4(1+a_X)^{3}+3.5(1+a_X)^{-4.5})-\mu_3(1+a_X)^{-4}\right]a_{XX}, \end{aligned} \tag{5.49}$$

where here the wave speed c_{ql} is given by $\rho c_{ql}^2=\mu_1(0.3\lambda_x^{-0.7}+1.65\lambda_x^{-2.65})+\mu_2(4\lambda_x^{3}+3.5\lambda_x^{-4.5})-\mu_3\lambda_x^{-4}$. For physically relevant values of the material constants, this is not monotone decreasing: as the stretch increases, the wave speed is initially decreasing, as for the Mooney-Rivlin model, but for high stretches (over $\lambda_x = 2.1$ for our rubber), the wave speed is increasing with stretch. This means that for a strip stretched to below $\lambda_x = 2.1$, the behaviour in retraction will be as for the linear and Mooney-Rivlin cases (and thus it is also possible that the behaviour seen in figure 5.8 obeys Ogden's theory). However, for an initial stretch above 2.1, the acceleration pulse will no longer all be contained within an infinitesimal region, but broadened out over a finite area, as the higher stretch stress-waves travel faster than the lower stretch waves. A shock will then eventually form when the stretch reaches the value associated with the minimum wave speed, behind which the material will be fully retracted.

The dispersion in the retraction of rubber just described is a consequence of the non-linear stress-strain behaviour of rubber, not of any viscoelastic effects. No dispersion was observed by Stevenson and Thomas [1979], but this was likely due to the low resolution of their experimental images. Dispersion was, however, previously observed experimentally in the retraction of rubber strips from large initial strains by Mason [1963], who showed that it matched with purely elastic theory. However, the author did not attempt to match it with any of the non-linear theories for rubber in extension discussed in this section. This is likely because such models are poor predictors of the rubber in retraction for any choice of the material constants, as discussed in section 2.13.3. Even worse, Bogoslovov and Rowland [2007] found that the stress-strain behaviour of rubber in free (and therefore dynamic) retraction differed significantly from the behaviour in quasi-static retraction. This discrepancy in behaviour was a consequence of strain-induced crystallisation in rubber (as discussed in 2.1).

More detailed experiments on the retraction of rubber strips from high initial stretches were performed by Niemczura and Ravi-Chandar [2011c], who also observed disperse behaviour. They provided no comparison of their results with standard non-linear models of rubber, but stated that attempts by them to do so were unsuccessful. This led them to propose a phenomenological model for the early stages of retraction based on a power law stress-strain relationship that did match their data well. Their model was 1D, and related the strain in the X-direction ϵ to the stress in the same direction τ as

$$\tau = \tau_0 - \mu_r(\epsilon_0 - \epsilon)^{n_r} \tag{5.50}$$

for a uniform strain ϵ_0 and stress τ_0 at $t = 0$, and material parameters $\mu_r > 0$ and $0 < n_r < 1$. The only restriction on ϵ is that $0 < \epsilon < \epsilon_0$. The wave speed in the X-direction is then

$$c_{ql}(\nu) = \sqrt{\frac{1}{\rho}\frac{d\tau}{d\epsilon}} = \left(\frac{n_r\mu_r}{\rho}\right)^{1/2}(\epsilon_0 - \epsilon)^{(n_r-1)/2},$$

and thus monotone increasing in the strain ϵ, so that high strains travel faster than low strains, at least initially. The initial behaviour of the rubber in retraction is therefore dispersive, as an expansion fan or simple wave spreads through the material. The full solution for the dispersive region, for a rubber strip initially in $0 < X < \infty$ and released at $X = 0$, is

$$a(X,t) = \lambda_0 X - \frac{1-n_r}{1+n_r}\left(\frac{n_r\mu_r}{\rho}\right)^{1/(1-n_r)}\frac{t^{2/(1-n_r)}}{X^{(1+n_r)/(1-n_r)}}. \tag{5.51}$$

This is, in fact, a similarity solution for equation (5.1) with the stress as in (5.50). This theory may then, in principle, be matched to experiments by fitting the two parameters n_r and μ_r. In practice, however, Niemczura and Ravi-Chandar [2011c] found that the initial stress τ_0 had to be treated as a free parameter too.

This model therefore predicts that $c_{ql} \to \infty$ as $\epsilon \to \epsilon_0$, so that the wave speed at the initial strain is infinite; there is no wave front, as all the material starts retracting at $t = 0$. Consequently, this model is only truly valid for semi-infinite strips of rubber, as it cannot satisfy the condition $a(t, 0) = 0$. An infinite wave speed corresponds to the stress-strain curve being vertical, something that theoretically should only occur at $\tau = \tau_0$. However, as stated previously, Niemczura and Ravi-Chandar [2011c] fitted with their experiments by using τ_0 as a free parameter, often finding the best fit with τ_0 less than the actual stress used to hold it in tension. This meant that their theoretical stress-strain curves had a finite-length vertical region.

Niemczura and Ravi-Chandar [2011c] performed experiments for a range of different initial stretches. For initial stretch $\lambda_0 > 5.5$, only a simple wave was observed that could be matched to equation (5.51). However, for $3 < \lambda_0 < 5.5$ both a shock and a simple wave were observed, while for $1 < \lambda_0 < 3$, only a shock was observed. This is in agreement with both the work of earlier authors (such as Stambaugh [1944]) and with linear theory. The reason the authors suggested for this change in behaviour was different from that given earlier: the presence and location of the shock for initial strain rates between 0 and 4.5 was argued to be a consequence of the maximum dissipation criterion, that states that the rubber will retract by the path that maximizes the amount of energy dissipated (as heat). By considering the extensional stress-strain curve of the rubber, the energy dissipated is given by the area between this curve, and the curve for the rubber in retraction. This condition then manifests itself

during the dynamic retraction in the following way: when retracting, the rubber has two distinct ways to do so, either through a simple wave or through a shock. On the stress-strain graph, the simple wave is equivalent to following the kind of curve as given by (5.50), whereas a shock is equivalent to a straight line from the pre-shock stress and strain to a point on the strain axis where the stress is zero (though not necessarily at the origin). The maximum dissipation criterion effectively states that the retraction will follow whichever combination of these two paths that provides the maximum dissipation, which is the same as the maximum area between the extension and retraction stress-strain curves. For low initial strains, the initial curvature of the retraction stress-strain curve will be positive or zero, so that a shock will occur immediately; for intermediate initial strains, the curvature will initially be negative, then change to positive at some lower stretch, so that a simple wave will occur initially, followed by a shock; for high initial strains, the curvature will always be negative, so only simple waves will occur. These behaviours are demonstrated in figure 5.9. It should be noted that this behaviour is different from that suggested by the non-linear Ogden's model: here, the shock occurs at the point where a straight line from the point of zero stress is tangent to the stress-strain curve, whereas for the Ogden's model shock occurs where the curvature changes sign. Nevertheless, for typical forms of the stress-strain curves seen for rubber, the difference will be small, and in both cases, the presence of a shock corresponds to a change in curvature of the stress-strain curve.

The experiments of Niemczura and Ravi-Chandar [2011c] revealed that, in all cases, the rubber reaches a stress- and strain-free final state in finite time. The values of n_r and μ_r varied greatly, n_r going from 0.7 at $\lambda_0 = 2$ to 0.3 at $\lambda_0 = 6$, with μ_r between 0.63 MPa to 0.95 MPa over the same range.

We conducted our own experiments, to examine the behaviour of our rubber in retraction, and compare it to that observed by other authors. These experiments used the same method outlined in section 5.4.1. We focused our attention on the range of stretches seen when balloons rupture: $4 < \lambda_0 < 7$. In this region, we would expect to see significant dispersive behaviour - and this was exactly what was observed, with shocks occurring after most of the strain had been relaxed, if at all. The fitting of one such experiment to equation (5.51) is shown in figure 5.10, demonstrating a very good agreement, and so suggesting that the model is appropriate to apply to experiments using the rubber in our balloons. However, the parameters found to provide this match were not in close agreement with those found by Niemczura and Ravi-Chandar [2011c] for similar initial stretches. As we were also interested in the behaviour of the fluid surrounding the rubber, it was also important to determine the speed of the rubber's response, the speed of the material itself. This velocity was determined by tracking the free end immediately after release. The results, for a range of initial stretches, are given in figure 5.11. No attempt was made to measure the wave speed, as unlike for linear retractions, there was no shock and no sharp acceleration, but instead the material was smoothly accelerated. The dispersive nature of the retraction therefore meant that it was impossible to determine when retraction actually began, which would determine the wavefront. Also shown are the predictions of equation (5.51) for the edge speed, assuming no shock occurs and using the parameters given by Niemczura and Ravi-Chandar [2011c]. This final velocity is found by determining the speed when the strain is zero, and is

$$c_{\text{end}} = \left(\frac{2}{1+n_r}\right)\left(\frac{n_r\mu_r}{\rho}\right)^{1/2}(\lambda_0 - 1)^{\frac{1+n_r}{2}}. \tag{5.52}$$

Figure 5.11 shows this theory to overestimate the retraction speeds of our experiments by a factor

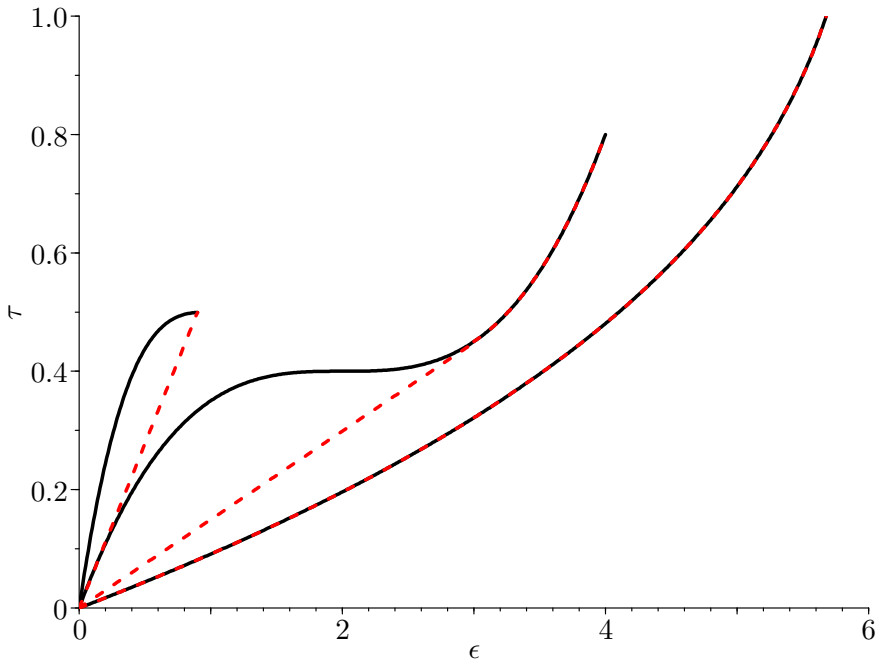

Figure 5.9: The dynamic retraction behaviour of rubber for a range of initial stretches. The black lines represent the full stress-strain relationship for the rubber in dynamic retraction, the dashed red lines represent the actual behaviour of the rubber. Where the two lines separate, it represents a shock forming, as the stress and strain jumps to zero along the shown straight line. This occurs due to the maximum dissipation criterion: the behaviour of the rubber follows the combination of following the stress-strain behaviour and shock such that the area between the line giving the actual behaviour and that giving the stress-strain behaviour in extension (not shown, but above that for retraction) is maximised. This area gives the energy dissipated as a result of the stretch and release, and the rubber always behaves so as to maximise the energy dissipated.

of around 3. Though this does mean that it would be inappropriate to model our rubber using the values of Niemczura and Ravi-Chandar [2011c], it clearly shows the importance of non-linearity (as captured by the model of Niemczura and Ravi-Chandar [2011c]) in determining the behaviour of our rubber balloons in dynamic retraction. If the material behaved linearly to such an extension, the free-edge speed would be $V = (\lambda_0 - 1)c_{ql} \approx 227$ m/s, far higher than what is actually observed; the presence of dispersion in the retraction wave thus acts to reduce the final speed of the material. Also included in figure 5.11 is end speed data for retractions in water and glycerin. It shows that while water has little effect at lower, linear stretches, it does become significant for initial stretches above $\lambda = 2$. At an initial stretch of 5 it reduces the final speed by at least a third, and suggests the reduction will be more at higher stretches. In contrast, the high viscosity of glycerin means that it has a strong influence on the retraction for all stretches, with velocities at the highest initial stretches one-tenth of those found in air.

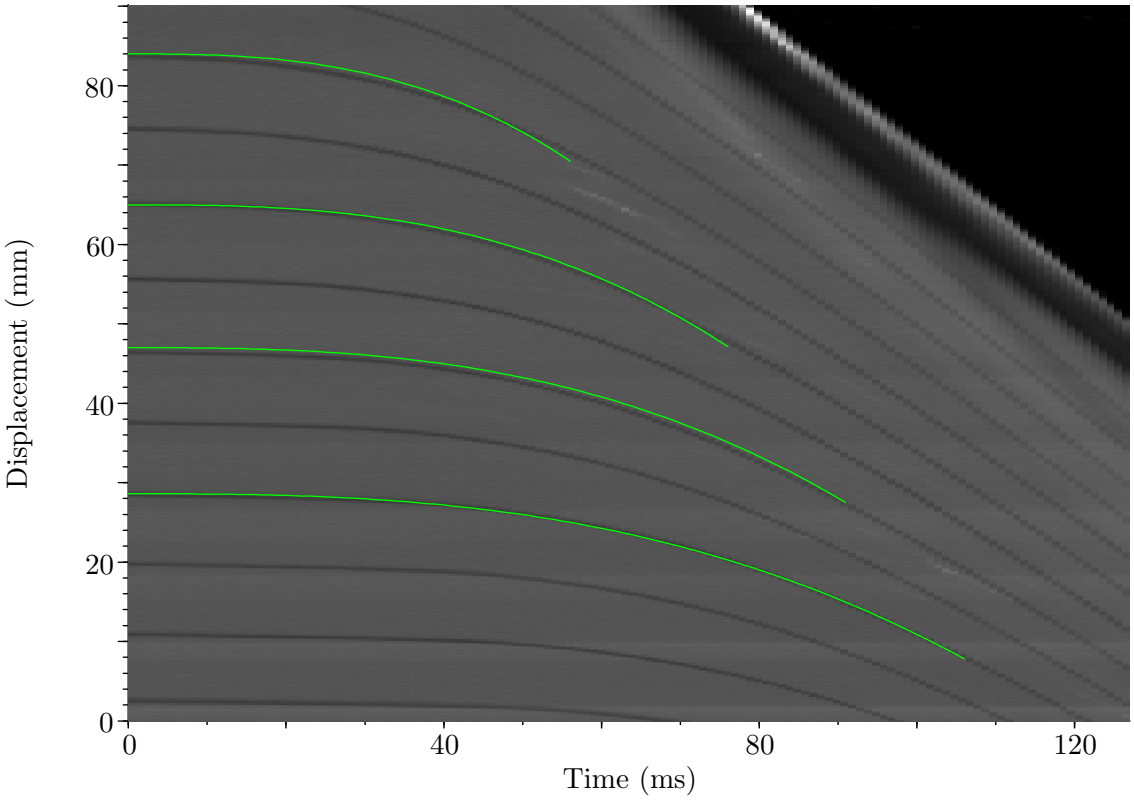

Figure 5.10: Particle trajectories for the retraction of a rubber strip in air with $\lambda_0 = 6$. The strip was released at time 0. The green lines represent the power law behaviour fitted using equation (5.51), with $n = 0.27$, $\mu_r = 1.5$ MPa. By way of comparison, Niemczura and Ravi-Chandar [2011c] found, for $\lambda_0 = 6$, $n = 0.3$ and $\mu_r = 0.95$ MPa.

We also detected a residual deformation, as the strip buckled (implying zero tension) before the strip had returned to its original length. The phenomena was noticed by other authors studying the free retraction of rubber, with Mason [1963] finding this residual stretch to be up to 23%. He, as other authors, attributed this effect to the viscoelastic nature of rubber, with the viscous part of retraction taking place over far longer timescales than the elastic part.

It should be noted that the model of Niemczura and Ravi-Chandar [2011c] was derived based on experimental observations of retraction from an initial uniaxial stretch, while the bursting of a balloon is closer to retraction from an initial biaxial stretch. As the behaviour of rubber is far from straightforward, it is therefore possible that the presence of a biaxial stretch could significantly alter the behaviour. However, testing this using the equipment available to us was not possible. As the presence of a stretch parallel to the free edge changed little significant for both the linear and other non-linear cases (other than an adjustment to the wave-speed), it seems reasonable to expect this uniaxial model to provide an approximate picture of the behaviour of rubber in dynamic retraction

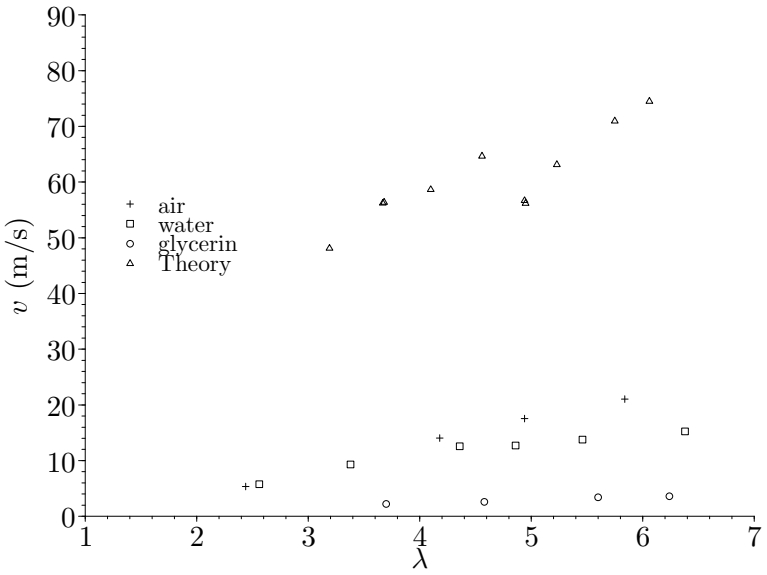

Figure 5.11: The average speed of the end of a retracting rubber strip in air (crosses), water (squares), and glycerin with kinematic viscosity 0.001 m^2/s (circles)

from high initial strains. By way of comparison, using the experiments performed to examine the speed of crack propagation in air, we measured the speed at which the material retracted away from the crack opening. For $\lambda_0 = 4.4$, the speed was $c_{ql} = 51$ m/s, and so approximately in agreement with the results for the uniaxial case (as in figure 5.11). Similarly, we may use our uniaxial experimental data to estimate the total time for a 130 mm balloon full of air ($\lambda_0 = 6$) to retract. The time is given by $t = \pi * R/c \approx 3$ ms. Experimental measurements found the equivalent total retraction time for balloons filled with air, in air, to be 2 ms. Our uniaxial experiments therefore are of the right order, yet do underestimate the speed of the rubber. The reason for this underestimation will be discussed in section 5.4.3, but is a consequence of the biaxial nature of the initial stress state.

It is therefore clear that rubber retracting from a burst balloon comes nowhere near the speed of sound in air (330 m/s), as it is unlikely to much exceed 100 m/s. The loud 'popping' noise heard when an air-filled balloon bursts is simply a pressure wave created by the difference in pressure between the inside and outside of the balloon when the membrane ruptures.

Another phenomenon noticed in these experiments was that the zero stress state did not correspond to the same strain as before the extension. This phenomena was noted by Mason [1963], who determined this 'residual' strain to be up to 23% and claimed it to be a consequence of the viscoelasticity of rubber. In our experiments the same effect was noted of varying effect depending on initial stretch λ_0, up to nearly 100% for $\lambda_0 = 6$. It was also noted for retractions in all surrounding fluids (air, water, and glycerin). We made no measurement of how long it took for this residual strain to disappear, but Mason [1963] determined it to take around three times as long as the elastic retraction.

Reflected wave

Niemczura and Ravi-Chandar [2011c] only theoretically considered a semi-infinite strip, so stopped their experimental analysis before any reflected waves from the fixed end of the rubber strip interacted with the observed section of material. To model the full behaviour of a retracting balloon, however, we must consider what happens once the wavefront has reflected from the fixed end. This mirrors the behaviour of the stress waves once they reach the point diametrically opposite the crack path, when due to the axisymmetry of the balloon they meet an equivalent wave travelling in the opposite direction and so reflect back around the balloon.

The predictions of linear theory were examined by Vermorel et al. [2007]. For rubber initially stretched to λ_0, once the retraction is complete, the wavefront reflects. Behind the reflected wavefront the material will be stationary and in uniform compression (negative stress), with stretch given by

$$\lambda = \frac{1}{\lambda_0}. \tag{5.53}$$

However, as discussed in section 2.9, a thin piece of rubber cannot support significant negative stresses and so will deform out-of-plane, a phenomenon known as buckling. This buckling occurs behind the reflected wavefront, so first occurs near the fixed end.

For a non-linear material as described above, the material immediately behind the initial wavefront is far from stress or strain-free. Consequently, the material will not be in compression behind a reflected wavefront. It will, however, behave differently than if the reflected wave had not passed: the reflected wave carries information of the condition $u = 0$ at $x = 0$, so the material behind the reflected wavefront must adjust its behaviour accordingly. Consequently, once the reflected wave has passed, the behaviour of the material becomes far more complicated: not necessarily in compression, but not following the behaviour predicted by equation (5.51) either. We have not considered this behaviour in detail, however, as it turns out that the effect of water surrounding the rubber changes the behaviour significantly. This is discussed in the following section.

However, one interesting consequence of this non-linear behaviour that appears not to have be mentioned in the literature, is that for high enough initial strain in a long-enough strip retracting in air, buckling first occurs in the middle of the strip. This is likely because the reflected stress wave causes the strip to buckle where the stress is zero but the material is in motion towards $x = 0$; but while the material near the fixed end has not had time to fully retract thus has positive stress, somewhere nearer the free end the material will be stress-free and in motion by the time the reflected wave passes. This will lead to negative stresses being created there, so the strip will buckle. This has been seen both experimentally and by solving numerically the equation

$$\rho u_{tt} = \mu_r n_r (\nu_0 - u_X)^{n_r - 1} u_{XX}, \tag{5.54}$$

as shown in figure 5.12.

5.4.2 Retraction in water

It was demonstrated in section 5.3 that the presence of water around the membrane has a significant effect on its behaviour in retraction: both the crack speed and initial speed of the retracting membrane were reduced. Figure 5.4(b) also showed that the presence of water reduced the retraction speeds

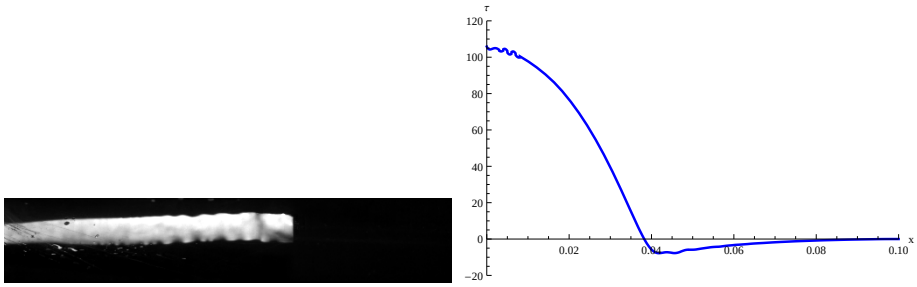

(a) Experiment (b) Theory

Figure 5.12: The buckling of a non-linearly stretched strip after release. As seen in **(a)**, this first occurred near the middle of the strip, when the strip first felt the effect of the fixed end. This is predicted by the theory of Niemczura and Ravi-Chandar [2011c] for finite strips, as given by equation (5.54). This equation was solved numerically using Mathematica, with stress at one moment during retraction shown in **(b)**. The oscillating behaviour seen near $x = 0.05$ is the result of a numerical instability. It can be seen to first become negative (and hence cause the strip to buckle) in the middle of the strip, before it has fully retracted near the fixed end ($X = 0$).

of uniaxial strips at high initial stretches. Consequently, we examined the retraction of uniaxially stretched strips of rubber immersed in water in detail as in section 5.4.1, but with the strips held within a clear perspex tank 0.1 m by 0.6 m by 0.45 m, that was filled with fresh water. Compared with the experiments of the previous section featuring strips retracting in air, retraction in water showed clear qualitative, as well as quantitative, differences in behaviour. A comparison between the two is displayed in figure 5.13.

Initially, the behaviour underwater was similar to that in air, with the wavefront traveling through the material from the free end, behind which the strain was decreasing as a simple wave, while the material itself was accelerating. However, after around 1 ms, the water began to significantly influence the behaviour: around this time, the material attained its maximum velocity, and began to slowly decelerate. This deceleration continued until the strip had fully retracted, at which point it buckled. The displacement of the rubber appears to decay approximately exponentially, similar to the behaviour suggested by James and Guth [1944] for rubber of high internal friction; however, experiments on retraction in air, as in the previous section, showed no such behaviour, nor did the work of other authors such as Mason [1963], Gent and Marteny [1982], and Bogoslovov and Rowland [2007]. It therefore seems clear that the change in behaviour is due to drag on the strip by the water.

The retraction of rubber bands in water was considered, briefly, by Vermorel et al. [2007], who found that for $\lambda_0 < 2$ the influence of the water compared to air on the band was negligible. Notably, however, they found that water-glycerol mixtures of viscosities $\mu = 0.04$ Pa s and greater did have a significant effect on the rubber. We, in contrast, are considering retraction from higher stretches, thus at greater speeds, when the drag would be more significant. We are also considering thinner strips than Vermorel et al. [2007], so the mass of water per unit length, and hence drag, is more significant.

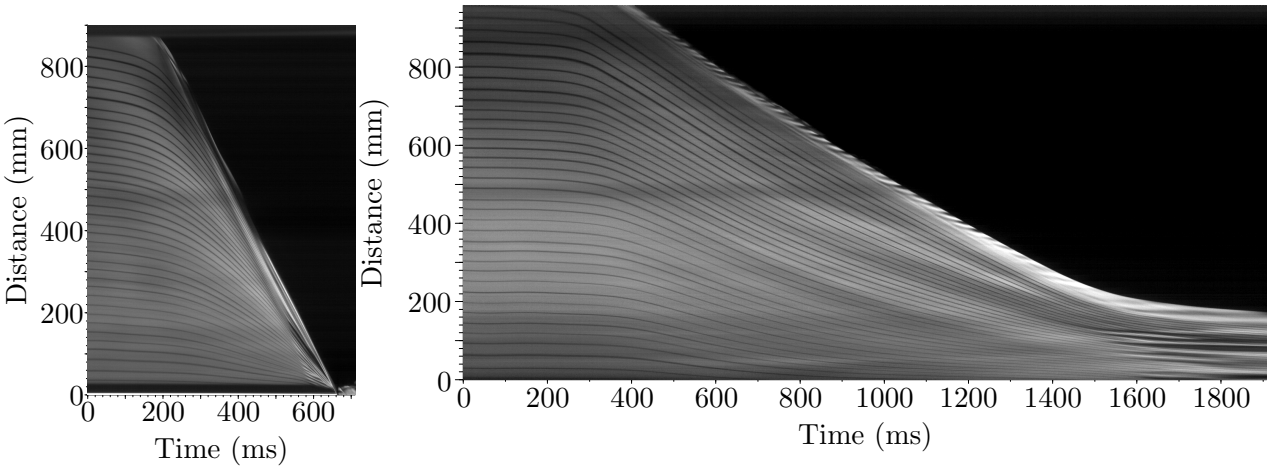

(a) Air (b) Water

Figure 5.13: The displacement of lines drawn on a rubber strip during its retraction. Image **(a)** is for the strip retracting in air, image **(b)** is for the same strip retracting in water. In both cases, the initial stretch was $\lambda_0 = 6.0$.

Drag on a retracting membrane

The force a fluid exerts on an object within a flow may be separated into two components, drag and lift. Drag acts parallel to the direction of flow relative to the body, whereas lift acts transverse to it. In this section, we are only considering the longitudinal motion of the strip and thus will only consider drag. Lift will be considered in section 5.5 when examining the transverse waves seen near the end of the strip.

There are two forms of drag: skin friction (or viscous drag) and form (or pressure) drag. Skin friction arises from net fluid shear stresses on the object's surface; form drag arises from net fluid normal stresses on the object's surface. The strength of both types of drag depends on the nature of flow in the boundary layer near the object: the transition from turbulent to laminar flow increases the skin friction, but may decrease the form drag. If the drag on an object is dominated by the skin friction, it is referred to as streamlined. If the drag is dominated by form drag, it is referred to as blunt.

Skin friction

We first consider skin friction. Physically, the no-slip condition at the rubber's surface creates a boundary layer of fluid being dragged along by the strip, and the more viscous the fluid, the wider the boundary layer and so the more fluid is dragged along. Consequently, the more viscous the fluid, the more drag on the strip.

We consider here a uniaxially stretched strip of width b, thickness h, and density ρ, retracting in the x direction along $z = 0$, in a surrounding fluid of viscosity μ and density ρ_f. The frictional drag per unit length of the rubber strip, τ_f, is given by the width of the strip multiplied by the tangential stress within the fluid at the rubber's surface, τ_{xz}. Neglecting all out of plane motions in the z directions,

τ_f may be written as

$$\tau_f = -2b\mu \left[\frac{\partial u}{\partial z}\right]_{z=0}. \tag{5.55}$$

Vermorel et al. [2007] used PIV to examine the nature of flow within the boundary layer for glycerin of viscosity 0.001 m^2/s, and found that it was laminar. Furthermore, they showed that, at position x, the flow field matched the form given by Batchelor [1967] for a flat plate initially at rest and impulsively started in motion at constant speed $U(x,t)$ when the stress wavefront passes at time $t = x/c$,

$$u(x,z,t) = U(x,t)\left[1 - \text{erf}\left(\frac{z}{\sqrt{4\nu(t-x/c)}}\right)\right]. \tag{5.56}$$

Using equation (5.55), this gives the shear stress per unit length as

$$\tau_f = -\frac{2b\rho_f\sqrt{\nu}}{\sqrt{\pi(t-x/c)}}U(x,t). \tag{5.57}$$

For the experiments we conducted, the movement of the strip near its fixed end was always slow, and thus the boundary layer there was always laminar. However, it was not obvious that the flow was laminar everywhere in the boundary layer, in particular near the fast-moving free end: the viscosity of the surrounding fluid, water, was orders of magnitude less than that of glycerin, while the strips were retracting from a greater initial stretch and thus were traveling faster. The effect of turbulence within the boundary layer on the retracting strip is a lot harder to quantify, particularly as the flow would have to transition from laminar to turbulent at a point of the strip. However, some insight into its effect can be gained by considering the high Reynolds number flow past a stationary flat plate parallel to the flow. Drag is typically calculated using the drag equation,

$$F_d = \frac{1}{2}C_d\rho_f A U^2, \tag{5.58}$$

where U is the flow velocity relative to the body, A is some relevant reference area, and C_d is a drag coefficient that depends on Re. When considering skin friction, A is the surface area of the body. Hoerner [1965] then gives approximate values for the drag coefficient as follows: $C \approx 6.8Re^{-1}$ for laminar flow when $Re < 100$, $C \approx 0.664Re^{-1/2}$ for laminar flow when $10^3 < Re < 10^6$, and $C \approx 0.059Re^{-1/5}$ for turbulent flow when $Re > 10^6$. The laminar drag is relatively greater at lower flow speeds as the whole flow is affected, and a large amount of fluid is affected by the presence of the plate. At higher Reynolds numbers, a boundary layer forms, and the influence of the plate is limited to that thin region of fluid. The experiments of Vermorel et al. [2007] were within the very low Reynolds number region, whereas ours had much higher Reynolds numbers. Notably, for the transition value of $Re = 10^6$, laminar flow gives $C \approx 0.0007$ whereas turbulent flow gives $C \approx 0.0047$. Turbulent flow therefore leads to a five-fold increase in the skin friction. It is thus important for us to consider the nature of flow within the boundary layer on the strip.

Theoretically, we may estimate whether the flow is laminar of turbulent by considering, as above, the transition point between laminar and turbulent behaviour for flow past a stationary, parallel flat

plate. Transition between laminar and turbulent flow is determined by the Reynolds number. For an outer flow of speed U, this is defined to be

$$Re \sim \frac{UL}{\nu}. \tag{5.59}$$

How the length-scale L is defined then determines the critical value of Re. If L is taken to be the characteristic width of the boundary layer δ, then $Re_c \approx 10^3$. An alternative critical Reynolds number may be obtained by observing that the boundary layer grows in width with distance down the plate; therefore, assuming all the strip is in motion, we may obtain Re_c using the length of the strip, $Re_c \approx 10^6$. The monotone relationship between boundary layer width and distance down the plate mean that the two values are equivalent.

We are considering the retraction of rubber when surrounded by water. The viscosity of water is $\nu = 10^{-6}\mathrm{m}^2\mathrm{s}^{-1}$; from figure 5.4, we see the speed of the rubber in our balloons when in retraction surrounded by water is typically around 30 m/s; the length of strip used was 0.1 m. This gives a Reynolds number of

$$Re = 3 \times 10^6, \tag{5.60}$$

and thus near, but slightly above, the boundary for transition between laminar and turbulent flow. Considering the alternate definition of Re, if the boundary layer were laminar, equation (5.56) gives the thickness as $\delta = \sqrt{4\nu t} \approx 0.0002$ m. This implies a Reynolds number of

$$Re = 6 \times 10^3, \tag{5.61}$$

again just over the transition between laminar and turbulent for a flat plate. These estimates for Re suggest that the boundary layer could well have been turbulent. However, they far from confirm it, as the situation is significantly different from that of flow over a flat plate. For one, the boundary layer will always start off laminar, before developing into turbulence. This process takes time, whereas the strip is only in motion for one hundredth of a second. It is therefore far from clear whether a turbulence will have time to fully develop. Indeed, this whole discussion of laminar and turbulent flow is something of a simplification: flow does not change immediately from fully laminar to fully turbulent flow, but instead it will pass through a period of transition, where small sections of the flow may become turbulent while the rest does not. The fact that the calculated Reynolds numbers are on the boundary between laminar and turbulent flow does suggest that the flow on the strip may well be in this transition region. This will affect the nature of drag on the strip, though the change (compared with laminar flow) is even harder to quantify than for fully turbulent flow.

There is also some evidence that compliant boundaries, such as rubber, delay the onset of turbulence in boundary layers adjacent to them, by suppressing the initial waves in the fluid from which turbulence develops. This effect is greatest when the material is of similar density to the fluid, highly flexible, but with low internal damping, all of which apply to rubber in water. A full discussion of this effect is given in Riley et al. [1988] and Babenko et al. [2012]. Hoerner [1965] states that a compliant boundary may delay the onset of turbulence to $Re \approx 10^7$ (for Re defined in terms of distance down the plate). Part of the evidence for this comes from observing the swimming of fish: for reasons of efficiency, they want to ensure the boundary layer next to their skin remains laminar, yet have been observed swimming at speeds such that the Reynolds number of the flow exceeds that usually associated with the transition to turbulence. While most of the work in this area has focused on flow past

compliant materials attached to a solid substrate, it does suggest that the critical Reynolds numbers discussed earlier may not be the most relevant to the retraction of our rubber strips.

In conclusion, standard theory was unable to determine whether the boundary layer flow on our retracting rubber strips and membranes in water was laminar or turbulent. To investigate further, we conducted experiments using Particle Image Velocimetry (PIV). These experiments are described in section 5.4.2.

Form drag

The form drag F_d may again be estimated using the drag equation (5.58) but with A as the cross-sectional area of the body (equal to bh here), and C_d a different drag coefficient that again depends on Re.

For low Reynolds number flows, $C_d \propto 1/Re$, a relation used by Vermorel et al. [2007] to estimate the drag on a linearly-stretched rubber strip retracting in glycerin. They found the form drag to be of the order of 10^{-2} N, whereas the skin friction was of the order of 1 N and thus dominant. For our strips, the higher Reynolds number ($Re \approx 10^6$ compared to 10^2 for laminar strips in glycerin), means assuming $C_d \propto 1/Re$ is likely to be no longer appropriate. However, it is easy to see that we still would expect the form drag to be small, almost insignificant, in comparison with the skin friction. If we ignore the waves near the free end of the strip, the shape of our retracting rubber strips may be well approximated by a cuboid parallel to the direction of motion. The form drag will therefore be given purely by the normal fluid forces on the free end - the fixed end and fluid around it is not in motion, and the other surfaces are parallel to the motion. While the strength of the drag will depend on the Reynolds number Re of the flow (including whether it is laminar or turbulent), it will still scale with the area of the free end $bh \approx 10^{-6}$ m^2. The skin friction will be given by the tangential fluid forces on the surfaces parallel to the direction of motion, and thus will scale with the area of the strip $bl \approx 10^{-3}$ m^2. The skin friction will therefore likely be far larger than the form drag. This was the assumption used by Dowling [1988], de Langre et al. [2007] and others when considering the behaviour of thin cylinders in axial flow.

Another comparison between drag forces may be found in the work of de Langre et al. [2007] on thin, flexible cylinders in high Re axial flow. There, they give the total skin friction F_s on a cylinder of radius a as

$$F_s = C_T \rho_f a L U^2, \tag{5.62}$$

with C_T estimated as being around 0.01. The form drag F_d is given by

$$F_d = 2 C_b \rho_f a^2 U^2, \tag{5.63}$$

where C_b varies from 0 for a streamlined end, to $\pi/4$ for a blunt end. Assuming that the end is blunt, and thus giving the maximum possible form drag, the ratio between the two is

$$\frac{F_d}{F_s} = \frac{2 C_b a}{C_T L} \approx 150 \frac{a}{L}. \tag{5.64}$$

For our strips, $a \approx 10^{-4}$ m/s and $L \approx 10^{-1}$ m/s, implying

$$\frac{F_d}{F_s} \approx 0.1 \tag{5.65}$$

and therefore that the form drag is likely to be far smaller than the skin friction.

The presence of waves near the free edge on the retracting membranes (see figure 5.1) also supports the notion that the form drag at the free end is small: if the form drag were large, this would induce tension in the membrane that would suppress these waves. The work of de Langre et al. [2007] supports this idea, finding that having a blunt end (and thus significant form drag) on a thin, flexible cylinders in axial flow suppresses transverse waves near the free end.

These transverse waves could complicate the drag situation, however, as there may be a form drag associated with the waves themselves. This arises from flow separation: whether the boundary layer stays attached to the strip as it passes over the transverse deformations of the strip. If it does stay attached, then the waves will cause far less drag on the retracting strip than if the boundary layer does separate. Taneda [1968], Carruthers and Filippone [2005], and Morris-Thomas and Steen [2009] have all studied the fluttering of flags in air experimentally, and found that fluttering typically occurs at a Reynolds number around 10^4. Taneda [1968] was the first, and found that fluttering increased the drag coefficient by a factor of around 20. Morris-Thomas and Steen [2009] studied the drag on flags in the transition regime $10^4 < Re < 10^6$, and found that for flags of large aspect ratio ($b \ll L$) the drag coefficient was ten times larger than that expected for a turbulent boundary layer over a flat plate, confirming the earlier work of Carruthers and Filippone [2005]. This discrepancy was attributed to the flutter of the flags. Similarly, Hoerner [1965] found a five-fold increase in drag for a flapping flag, as a result of flow separation and consequent momentum transfer to the outer flow.

We may estimate the relative significance of drag from the waves near the free edge by using the results of Morris-Thomas and Steen [2009]. The drag due to skin friction (assuming a turbulent boundary layer) is given by both Morris-Thomas and Steen [2009] and de Langre et al. [2007] as $F_s = 0.01(bL)\rho_f U^2$. For the drag due to fluttering, the relevant reference area is the region in which the waves are present, approximately 10 mm from the end of the strip. The drag is therefore given by $F_f = 0.1(0.01b)\rho_f U^2$. The ratio between the two is $F_f/F_s = 1$, suggesting that the drag caused by these waves near the free end is non-negligible. Indeed, it will be shown in section 5.4.2 that this form drag likely does have a significant effect on the behaviour of the strip in retraction.

The strength of this form drag will also be affected by the nature of the boundary layer: a turbulent boundary layer round a cylinder is well-known to separate later than a laminar one for the same flow speed, and thus leads to less form drag. The form drag on our retracting strips will therefore be most significant when the boundary layer is laminar everywhere, as then the skin friction is least but the form drag greatest. As will be discussed in section 5.4.2, we conducted PIV experiments on retracting strips in water. While these experiments proved to be unclear as to the nature of the boundary layer, they did suggest laminar flow. This is yet another reason why the form drag from the waves at the free edge should not be neglected.

Laminar drag displacement equation

Vermorel et al. [2007] found the momentum equation for the displacement of the strip in the x direction under the assumptions of linear elasticity and laminar flow in the boundary layer, and so using (5.57) for the drag. By taking $U(x,t) = \frac{\partial a}{\partial t}$, the equation was

$$\rho h \frac{\partial^2 a}{\partial t^2} = Eh \frac{\partial^2 a}{\partial x^2} - \frac{2\rho_f \sqrt{\nu}}{\sqrt{\pi(t - x/c)}} \frac{\partial a}{\partial t}. \tag{5.66}$$

This equation has no analytic solution. However, they examined the asymptotic behaviour as $t \to \infty$, which represented the behaviour of the material behind and away from the wavefront, but before the reflected wavefront had arrived. Effectively this limit represented the behaviour of a semi-infinite strip, similar to that found by Niemczura and Ravi-Chandar [2011c] for non-linear rubber. In this limit, $t \gg x/c$ and inertia is neglected. Equation (5.66) then becomes

$$\frac{1}{\sqrt{t}}\frac{\partial a}{\partial t} = \frac{Eh\sqrt{\pi}}{2\rho_f\sqrt{\nu}}\frac{\partial^2 a}{\partial x^2}. \tag{5.67}$$

As this is equivalent to the motion of a semi-infinite strip, there is no length-scale. The equation is therefore solved using similarity variable $\eta = x/t^{3/4}$ as

$$a(x,t) = (\lambda_0 - 1)x\mathrm{erf}\left(\frac{x}{2Dt^{3/4}}\right) + \frac{2(\lambda_0 - 1)Dt^{3/4}}{\sqrt{\pi}}\exp\left(-\frac{x^2}{4D^2t^{3/2}}\right), \tag{5.68}$$

where $D = \sqrt{Eh\sqrt{\pi}/(3\rho_f\sqrt{\nu})}$. This solution implies that as $t \to \infty$, the material displacement goes like $t^{3/4}$. This matched the results of experiments performed Vermorel et al. [2007] for retracting linear rubber bands in highly viscous fluids.

As stated previously, Vermorel et al. [2007] found the influence of water surrounding retracting rubber bands to be negligible, with the surrounding fluid only becoming significant for $\nu \geq 4 \times 10^{-5}$ $\mathrm{m^2 s^{-1}}$. However, they were only considering small initial extensions, $\lambda_0 < 2$, and thus material speeds below 20 m/s; we are considering retractions from λ_0 up to 6 and so material speeds up to 40 m/s, in water of kinematic viscosity 10^{-6} $\mathrm{m^2/s}$. The drag term in equation (5.66) scales like $\sqrt{\nu}a_t$, so that a forty-times increase in viscosity is equivalent to only a six-times increase in velocity. Thus, while we would not expect our retractions (with speeds around twice those of linear retraction) to be as influenced by drag as those of linear retraction in highly viscous fluids, we would still expect drag to be relevant. That this is true is clearly seen in figure 5.13. Furthermore, our strips are significantly thinner (around 0.2 mm) than those used by Vermorel (from 0.3-1.2 mm). As both the inertia and tension in the strip scale with thickness but the drag does not, the drag will be more significant for thinner strips such as ours.

PIV experiments in water

To gain some insight into the nature of the fluid boundary layers on our strips retracting in water, we conducted our own PIV experiments, similar to those of Vermorel et al. [2007]. As before, the experiments were conducted within a clear perspex tank, 0.1 m by 0.6 m by 0.45 m, that was filled with fresh water. Small, approximately neutrally-buoyant 70-100 μm diameter Pliolite particles were then mixed into the water. A 0.1 m by 0.01 m strip was used, cut out of a 646 cylindrical balloon. One end of the strip was held firmly in a clamp on the floor of tank, with a rigid tube pushing down on the clamp to hold it in place. The final 0.005 m of the other end was held above it in a clamp attached to a stand. This second clamp could then be moved up and down to change the initial stretch. The water was then stirred vigorously to ensure the particles were spread evenly, before being left to settle for a few minutes to allow most of the motion in the water to die away. Illumination was provided by two vertically-aligned 300 W lamps, both aimed at the same region and projecting light through a slit formed on the tank's side using two blackened metal strips and black, self-adhesive film. The light

sheet created was aligned with the centre of the strip, and thus illuminated flow on only one side of the strip while the rubber was present, while both sides were illuminated in the wake. The high-speed camera was aligned perpendicular to the light sheet, and recorded at either $5,400$ fps or $10,000$ fps. After the images had been saved to hard-disk, they were analysed using the PIV facility within the program DigiFlow.

The main difficulty with regards to these experiments was the thinness of the boundary layer. From the theory of Lamb [1932] for an impulsively accelerated strip, the boundary layer thickness is estimated as only $\sqrt{4\nu t} \approx 0.2$ mm. Though the equipment detailed above were the best available, they ultimately proved inadequate to determine the whether the flow was laminar or turbulent - the spatial resolution of the boundary layer was inadequate, and so there was simply not enough boundary layer visible to draw any definitive conclusions. Nevertheless, several observations could still be made. During the early stages of retraction, there was almost no evidence of flow near the rubber strip, as the boundary layer was still too thin to be visible. It was only during the later stages, as the end of the strip neared, that flow could be detected. Then, variation perpendicular to the strip in the velocity component parallel to the strip was observed, that was of the same approximate shape as would be expected for a laminar boundary layer, as shown in figure 5.14. However, significant motion perpendicular to the strip was seen, and the layer was also much thicker, around 2 mm as opposed to 0.2 mm for laminar flow. This would appear to suggest turbulent motion, as while the thickness of a laminar boundary layer over a plate is given by Hoerner [1965] as

$$\delta \approx \frac{5.5L}{Re^{1/2}} = 0.6 \text{ mm}, \tag{5.69}$$

the thickness of a turbulent boundary layer over a plate is

$$\delta \approx \frac{0.15L}{Re^{1/7}} = 2 \text{ mm}, \tag{5.70}$$

and so in good agreement with our experimental observations. However, the detection of perpendicular motion and increased boundary layer thickness are likely linked, and there is another explanation for the apparent perpendicular motion, beyond turbulence in the water. The flow field is determined by tracking the small particles in the water. After the water has been stirred and left to settle, some of the particles adhere to the rubber strip, with no fluid between them and the rubber. They are thus carried along by the rubber when it retracts. However, although the main motion of the rubber was in the direction of retraction, it was impossible to remove all out-of-plane motions from the strip. When the strip was traveling at high velocity, these motions would project the particles near the strip away from the strip. The particles would thus pass through and out of the boundary layer, not due to motion of the water but due to that of the strip. This phenomena could be easily observed by tracking individual particles by eye, and indeed, it appeared to be the case for most of the particles experiencing vertical motion.

In summary, it was not possible to conclusively determine whether the fluid boundary layer near a rubber strip retracting from a high initial stretch remained laminar through out the motion. It would certainly have been laminar during the early stages of motion, and velocity profiles for the later stages do match, in shape at least, those expected of linear motion (as shown in figure 5.14). Yet significant perpendicular motion in the boundary layer in the later stages was detected, along with a thickening of

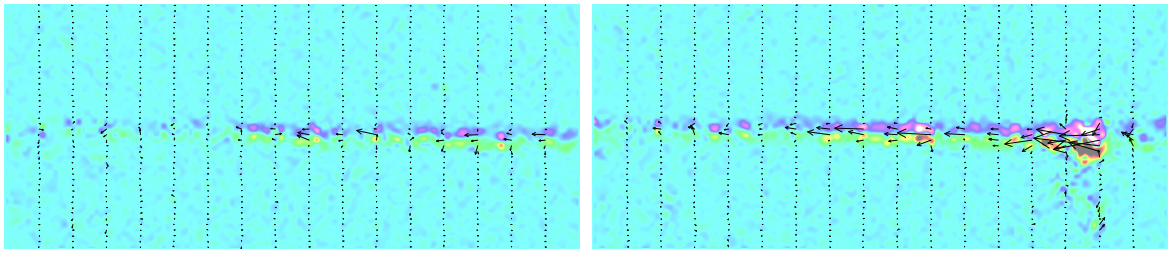

(a) $t = 4$ ms (b) $t = 7$ ms

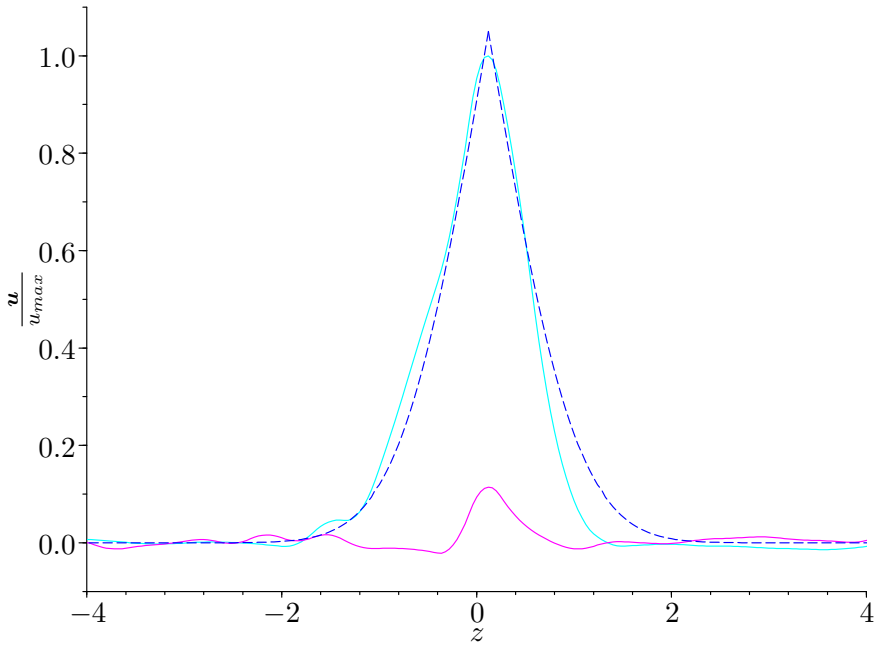

(c)

Figure 5.14: The results of PIV on a retracting rubber strip in water. The arrows show the velocity field, with the colors showing the vorticity: purple negative, cyan zero, and green positive. Both experimental images are taken at the same point in the laboratory frame, with the field of view approximately 50 mm by 20 mm. The times given are the time after release of the strip. Image **(a)**, taken soon after release, shows only a very thin boundary layer. In image **(b)**, at a later time near the free end of the strip, the boundary layer is thicker, though still only a couple of millimetres thick. Figure **(c)** shows how both the parallel (cyan) and perpendicular (magenta) velocity distributions vary with perpendicular distance to the strip in mm, after averaging over the length of the strip visible in **(b)**. The horizontal distribution is matched with a fitted error function profile (blue). Due to the thinness of the boundary layer, and hence the small number of particles within it, these velocity profiles should be regarded as approximate.

the boundary layer, that would suggest turbulence; however, this may have been due to the particles being directly propelled by the rubber, and not due to motion in the fluid. Ultimately, all we can say is that our experiments did not find anything to conclusively contradict the idea that the motion was laminar throughout. Furthermore, figure 5.13 shows that the material speeds near the fixed end were at all times small; thus if there were a transition to turbulence somewhere along the strip, it would likely be in a small region near the free end. This turbulent region would thus have limited effect on the overall motion of the rubber strip. Thus, from now on, we shall work on the assumption that it was laminar throughout the motion.

Assuming the boundary layer remained laminar everywhere, we can therefore apply the theory of Vermorel et al. [2007]. Note that this theory neglects form drag, so this is a test of its significance. In particular, we can consider the asymptotic solution for $t \gg x/c$, but with a slight change. They considered only the behaviour before the reflected wavefront arrived, which made sense considering the wavefront was of comparable speed to the material speed in the linear limit. For the high initial strains we are considering, the wave speed is far greater than the material speed, and so the reflected wavefront will already have traveled all the way back through the strip during the early parts of the motion. It thus makes sense to ignore individual wavefronts, but to consider the long-time behaviour when the whole strip has knowledge of the fixed end at $x = 0$ and has adjusted to it.

We therefore wish to solve equation (5.67),

$$\frac{1}{\sqrt{t}}\frac{\partial a}{\partial t} = \frac{Eh\sqrt{\pi}}{2\rho_f\sqrt{\nu}}\frac{\partial^2 a}{\partial x^2}, \tag{5.71}$$

but now we have a length-scale: the length of the strip, L. The boundary conditions are therefore

$$a(0, x) = \epsilon x, \tag{5.72}$$

$$a(t, 0) = 0, \tag{5.73}$$

$$a_x(t, L) = 0. \tag{5.74}$$

The solution, using separation of variables and the last two boundary conditions, is

$$a(t, x) = \sum_{k=0}^{\infty} A_k \sin\left(\left(\left(k + \frac{1}{2}\right)\frac{\pi x}{L}\right)\right) \exp\left(-\left(\left(k + \frac{1}{2}\right)\frac{\pi}{L}\right)^2 D^2 t^{3/2}\right) \tag{5.75}$$

with D defined as before. The A_k are unknown constants that may may be determined using (5.72) to be

$$A_k = \frac{8(-1)^k}{\pi^2(2k+1)^2}\epsilon L. \tag{5.76}$$

At late times, the $k = 0$ term will become dominant. An asymptotic solution for the behaviour of a finite length strip as $t \to \infty$ is therefore

$$a(t, x) \approx \frac{8\epsilon L}{\pi^2}\sin\left(\frac{\pi x}{2L}\right)\exp\left(-\frac{\pi^2 D^2}{4L^2}t^{3/2}\right). \tag{5.77}$$

Figure 5.15 shows how this theory compares to experiment for the free end of a strip with initial stretch $\lambda = 6$. Of all the physical constants, the one we have least knowledge of is E, due to the complicated

non-linear behaviour of rubber in dynamic retraction. The experimental data is therefore plotted against theory assuming both $E = 285,000$ Pa as implied by our experimentally determined values in chapter 2, and $E = 570,000$ Pa to try to account for the fact that the Young's modulus decreases in the non-linear regime. Both theories, however, show very poor agreement with the experiments, underestimating the total time of retraction more than four-fold.

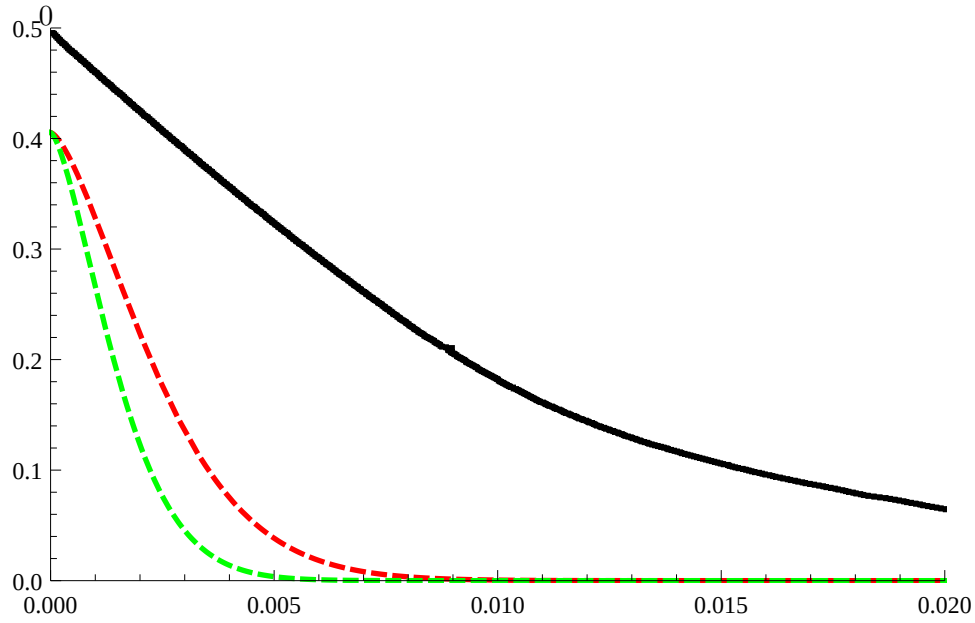

Figure 5.15: The displacement over time of the free end of a rubber strip retracting from initial stretch $\lambda_0 = 6$ in water. The black line is the result of experiment, the green line shows the theory of equation (5.77) with $E = 570,000$ Pa as predicted for the linear regime in chapter 2, the red line the theory with $E = 285,000$ Pa.

One possible reason for this inaccuracy may be the neglect of non-linearity in the rubber, both in terms of the stress-strain relationship and the change in shape of the strip. The change in shape matters because the drag on the strip is assumed here to be primarily due to skin friction, that is proportional to the Eulerian surface area. The inertial and stress terms are proportional to the Lagrangian cross-sectional area. The Lagrangian cross-sectional area does not change when the strip is stretched, but the Eulerian surface area does. This is not an issue in the linear limit, where the difference between frames is negligible, but becomes significant as the deformations become non-linear. If we consider a section of strip of width b and thickness h between X and $X + \delta X$, in the deformed configuration the length of the section is given by $l_d = (1 + a_X)\delta X$; by the condition of incompressibility, the width is then given by $b_d = (1 + a_X)^{-1/2} b$ and the thickness by $h_d = (1 + a_X)^{-1/2} h$. The surface area parallel to the direction of motion (the X direction) is therefore $2(l_d b_d + l_d h_d) = 2\sqrt{1 + a_X}(b + h)\delta X$. This means that as the strip retracts, the surface area decreases. Consequently, the skin friction will decrease too. For an initial stretch of $\lambda = 6$, therefore, the drag will decrease by a factor of $\sqrt{7} \approx 2.6$ over the course of the retraction, a significant amount.

A better model would therefore include both this change of surface area and the non-linearity of the rubber. We therefore combine all these effects, including the stress-strain relationship suggested by Niemczura and Ravi-Chandar [2011c], to give a fuller equation of motion

$$bh\rho\frac{\partial^2 a}{\partial t^2} = bh\mu_r n_r \left(\lambda_0 - 1 - a_X\right)^{n_r-1} a_{XX} - b\sqrt{1+a_X}\frac{2\rho_f\sqrt{\nu}}{\sqrt{\pi t}}\frac{\partial a}{\partial t}. \tag{5.78}$$

with the boundary conditions

$$a(0,x) = \epsilon x \tag{5.79}$$

$$a_t(0,x) = 0, \tag{5.80}$$

$$a(t,0) = 0, \tag{5.81}$$

$$a_x(t,L) = 0. \tag{5.82}$$

This equation is not found in any previously published literature. There is no analytical solution to this equation, but it may be solved numerically, using values of n_r and μ_r for the equivalent retraction in air. This was done using Mathematica's NDSolve function, and a comparison is given in figure 5.16 of this solution with the experiment previously shown in figure 5.15. While the fit is slightly better than for the linear models above, it is still far from accurate, predicting the retraction to occur approximately twice as fast as was observed experimentally.

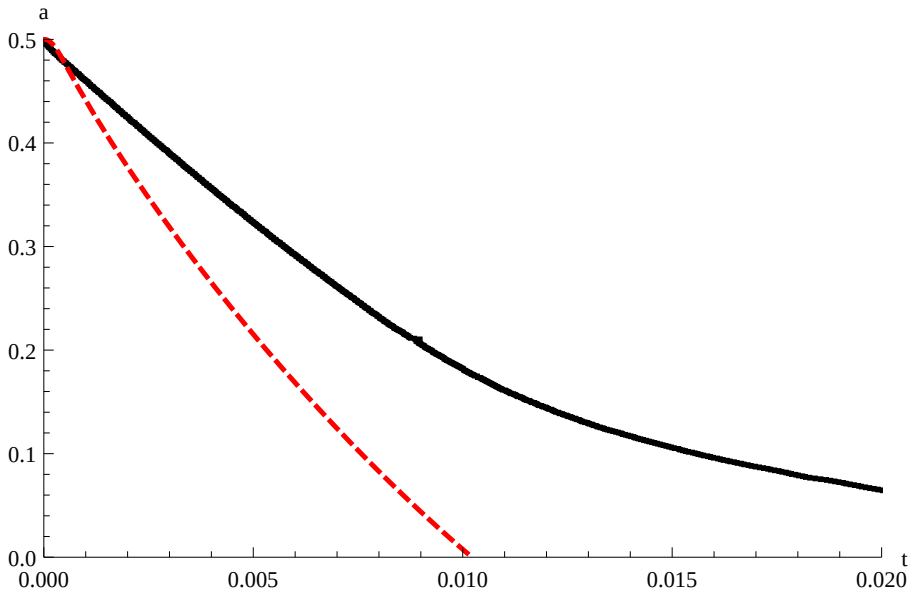

Figure 5.16: The displacement over time of the free end of a rubber strip retracting from initial stretch $\lambda_0 = 6$ in water. The black line is the result of experiment, the red line shows the theory of equation (5.78) with $n_r = 0.27$, $\mu_r = 1.5$ MPa as found for the equivalent retraction in air.

The source of this inaccuracy could be one of several factors. To get a better understanding of it, we considered the strain in the retracting strip. Through the boundary conditions on either end of the

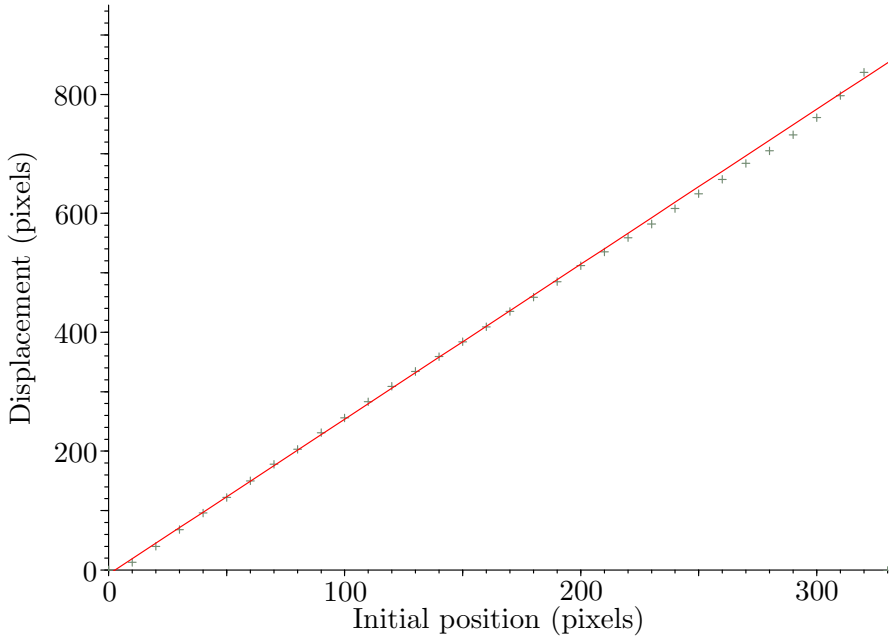

Figure 5.17: The experimental strain for a strip retracting in water from $\lambda_0 = 6$. The crosses show, for a single moment half-way through the retraction (9 ms after release), the displacement of lines that were equally spaced on the strip when the strain was zero. The red line is a fitted straight line.

strip, the strain must be maximum at the fixed end, and zero at the free end. Equation (5.77) therefore predicts it to decrease sinusoidally between the two points. However, experimental measurements of the strain on our retracting strips, as shown in figure 5.17, show it to be far more uniform away from the free end than predicted, in fact it is almost constant. While this could be a consequence of the non-linear stress-strain relationship in rubber, it may also be a consequence of differences in drag from that derived from the assumption of laminar flow in the boundary layer. It may be that, as the material moves faster the closer it is to the free end (from 0 m/s at the fixed end to around 40 m/s at the free end), the boundary layer transitions from laminar to turbulent flow somewhere near the free end of the strip. As discussed in section 5.4.2, turbulent skin friction is significantly greater than laminar skin drag; if transition does occur, the free end of the strip will therefore be experiencing greater drag than the rest of the strip, thus making the strain more uniform away from the free end. More likely however, and as discussed previously in this section, this extra drag was caused by the waves near the free end. These waves were seen near the free edge of retracting balloon membranes (see figure 5.1), and also near the free edge of the retracting strips in water. They acted much like a flag, and as discussed in section 5.4.2, the fluttering of a flag may significantly increase the drag on it. This occurs through separation of the boundary layer and vortex shedding, with the consequent increase in momentum in the wake balanced by increased form drag on the membrane. This extra drag near the free end would stretch out the strip, making the tension (and thus strain) far more uniform than it would have been without the fluttering.

One final neglected source of drag arises from the finite width of the strip, something we have previously ignored. Vermorel et al. [2007] point out that the drag created by the sharp corners parallel to the direction of retraction at either side of the strip is significant for linear retractions in highly viscous fluids. Batchelor [1954] considered the impulsive acceleration of an infinite cylinder with sharp corners at speed U, and found that for a flat plate of finite width (equivalent to a 'flat' cylinder with two corners of angle π), the drag correct to order $\nu^{1/2}$ is

$$\tau_f = \frac{2\rho_f\sqrt{\nu}bU}{\sqrt{\pi t}}\left[1+\frac{\sqrt{\pi\nu t}}{2b}\right]. \tag{5.83}$$

Thus the drag from the corners becomes significant when the boundary layer thickness $\delta \approx \sqrt{\nu t}$ is of the same order as the strip width $b \approx 0.01$ m. For the most viscous fluids considered by Vermorel et al. [2007], and that considered in the next section, the viscosity was around 1×10^{-4} m^{2}s^{-1}. This would imply the drag from the corners would become significant at around $t \approx b^2/\nu \approx 0.01$ s, of the same order as the time taken for the strip to fully retract. The corner drag would therefore be significant. For our strips retracting in water, however, this would not be the case: the time for drag from the corners to become significant would be $t \approx 100$ s, and thus far longer than the time taken for the strip to fully retract. We are therefore justified in neglecting its influence here. Furthermore, our study of one dimensional strips retracting was motivated by attempting to gain some insight into the retraction of bursting spherical membranes, that of course have no such corners. Consequently, while we need to estimate the influence of the corners for the present discussion, it obviously does not play a role for the balloons themselves.

PIV experiments in glycerin

By way of comparison, we repeated the experiments of the previous section, but in glycerin of kinematic viscosity 0.001 m^2/s. For small stretches, this justs repeat the work of Vermorel et al. [2007]. We, however, considered large initial stretches.

Figure 5.18 shows the distribution of horizontal (u) and vertical (w) velocity through the boundary layer at a single point near the free end of a strip for which $\lambda_0 = 6$. The vertical velocity is very small everywhere in comparison to the horizontal velocity, that itself closely matches the error function profile of equation (5.56). We can therefore say with a high degree of certainty that for retractions in highly viscous fluid for large initial stretch, the boundary layer does remain laminar through out.

To model this retraction, we follow our analysis of the previous section, but now include the effects of drag from the corners given by equation (5.83). With this extra term, the equation for the behaviour of the retracting finite strip at long times becomes

$$\left(\frac{1}{\sqrt{t}}+\frac{\sqrt{\pi\nu}}{2b}\right)\frac{\partial a}{\partial t} = \frac{Eh\sqrt{\pi}}{2\rho_f\sqrt{\nu}}\frac{\partial^2 a}{\partial x^2}, \tag{5.84}$$

with the same boundary conditions as before. The full solution, taking only the leading order term in k that is dominant at late times, is

$$a(t,x) \approx \frac{8\epsilon L}{\pi^2}\sin\left(\frac{\pi x}{2L}\right)\left[\frac{2b}{2b+\sqrt{\pi\nu t}}\right]^{-\frac{6\pi^2D^2b^3}{L^2(\pi\nu)^{3/2}}}\exp\left(\frac{3\pi^2D^2b\sqrt{t}}{4L^2\pi\nu}(4b-\sqrt{\pi\nu t})\right). \tag{5.85}$$

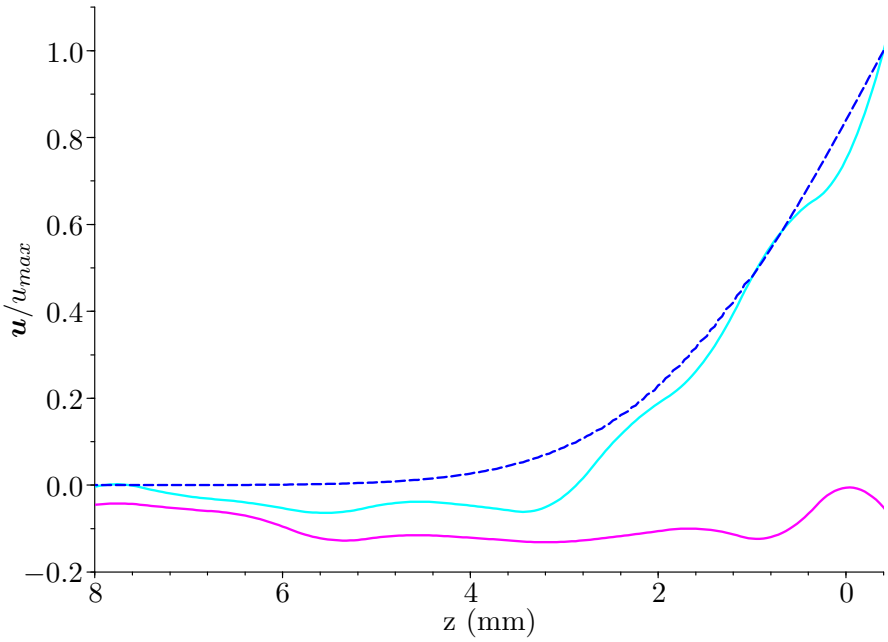

Figure 5.18: The results of PIV performed for a strip of rubber retracting from $\lambda_0 = 6$ in glycerin of kinematic viscosity 0.001 $\mathrm{m^2 s^{-1}}$. Shown are the experimentally-determined tangential (cyan) and perpendicular (magenta) velocity distributions varying with distance perpendicular to the strip for a single cross-section. The blue line shows the error function profile fitted to match the horizontal velocity distribution.

However, we may also use the extended analysis presented in the previous section, including the effects of non-linearity in the stress-strain relation and changing strip surface area, to obtain a more accurate model of the retraction in glycerin. The resultant equation of motion is

$$bh\rho\frac{\partial^2 a}{\partial t^2} = bh\mu_r n_r \left(\lambda_0 - 1 - a_X\right)^{n_r - 1} a_{XX} - 2b\rho_f\sqrt{\nu}\left(\frac{\sqrt{1+a_X}}{\sqrt{\pi t}} + \frac{\sqrt{\pi\nu}}{2b}\right)\frac{\partial a}{\partial t}, \tag{5.86}$$

that is just equation (5.78) with the additional term relating to drag from the corners. This equation, that again is new, must also be solved numerically.

The predictions of equations (5.85) and (5.86) are matched against experimental data in figure 5.19. The fit for both is reasonable, with both estimating the time and speed of retraction accurately. That the theory is more accurate here than for retracting strips in water is because there was no possible source of extra drag: the effect of the corners was accounted for, the slow speed of retraction meant that the boundary was sure to remain laminar throughout the retraction, and no transverse waves were observed near the free edge of the membrane.

With that said, it must be noted that the full, numerically-determined theory is not perfectly accurate. The reason for this is likely to be our use of the model of Niemczura and Ravi-Chandar [2011c], and in particular our use of the constants n_r and μ_r found for retracting strips in air. It has been shown both by those authors and Bogoslovov and Rowland [2007] that the stress-strain

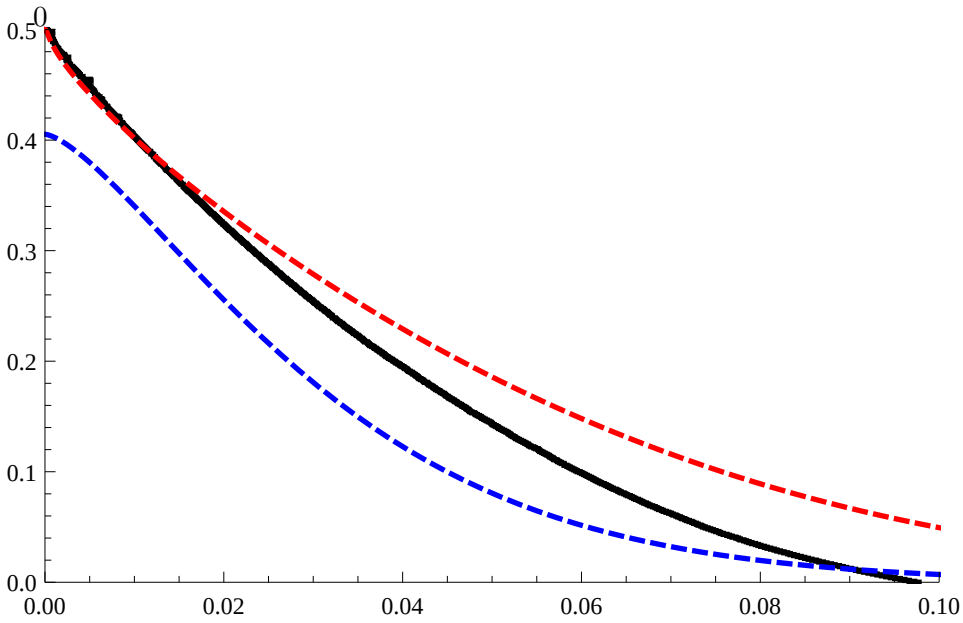

Figure 5.19: The displacement of the free end of a rubber strip retracting from $\lambda_0 = 6$ in glycerin of kinematic viscosity $\nu = 0.001$ m^{2}s^{-1}. The black line is taken from an experiment. The blue line shows the prediction of equation (5.85) including the influence of the corners with $E = 285,000$ Pa, with the red line giving the numerically-determined solution to the full equation of motion (5.86), including the corners, the change in surface area of the strip and the non-linear stress-strain relation. The parameters used were the same as those given previously.

relationship for rubber is dependent on the strain-rate (the rate at which the strain changes). The presence of water or glycerin slowed the material down. This, in turn, meant that the strain-rate decreased, and so the stress-strain relationship likely changed. While it was not possible for us to determine the exact nature of this effect, it was likely to have been small (particularly for water) and purely quantitative. It also possible that the absorption of water by the rubber may somewhat alter the non-linear stress-strain behaviour of the rubber.

Vorticity created by retraction

It was stated in chapter 3 that the late-time growth of the interfacial amplitude was driven by vorticity in a thin layer at the interface, and it was shown in chapter 4 how that vorticity was created by the pre-burst waves. However, the rapid retraction of the rubber led to viscous shear with the external fluid, and so also created vorticity at the interface. Assuming the boundary layer created by the retraction remained laminar, equation (5.56) gives the flow field at late-time for a strip moving at speed $U(x,t)$ in a fluid of kinematic viscosity ν as

$$\boldsymbol{u} = (U(x,t)\left[1 - \text{erf}\left(\frac{|z|}{\sqrt{4\nu(t)}}\right)\right], 0, 0) \tag{5.87}$$

and hence the vorticity as

$$\omega = (0, \mathrm{sgn}(z)\frac{U(x,t)}{\sqrt{\pi\nu t}}\exp\left(-\frac{z^2}{4\nu t}\right), 0). \tag{5.88}$$

The circulation density on one side of the membrane is thus

$$\gamma_r = \int_0^\infty \omega_y dy = \mathrm{sgn}(z)U(x,t), \tag{5.89}$$

though when both sides of the strip are taken into account, the total circulation density is zero.

This result may also be obtained by using the argument of Batchelor [1967] and noticing that the total velocity shear between the stationary outer flow and the moving strip was simply the velocity of the strip. Therefore, for a strip moving at constant speed once impulsively started, vorticity is only created at $t = 0$ at the rigid boundary. Over time, that same amount of vorticity then just diffuses out into the fluid. For a strip retracting in water, γ_r is thus of the order of 30 m/s. As the vorticity passes into the wake, there will be some diffusion across the line of symmetry, as the velocity profile rapidly converts from error function-like to Gaussian (see section 5.6). The flapping of the membrane near its free edge also affects the vorticity field in the wake, as will be discussed in section 5.5. Neither phenomenon, however, will significantly affect either the strength or direction of the vorticity created by retraction, just the distribution.

In chapter 4, the circulation density due to the pre-burst waves, γ_w, was found to be $4\pi fB/k \approx 1$ m/s, and hence much smaller. The two vorticities are also restricted to similar regions. The pre-burst vorticity lies in a region near the interface of thickness $\sqrt{2\nu/\omega} \approx 0.1$ mm, whereas the thickness of the shear vorticity region is given by $\sqrt{4\nu t} \approx 0.2$ mm. Note, however, that for the standard crack direction, traveling from top to bottom of the balloon (see figure 5.6 **(a)**), the vorticities were in different directions most places on the interface: that created by the pre-burst waves lay in the θ direction, whereas that created by shear during retraction lies in the ϕ direction.

As discussed previously, the shear instability on the interface was a consequence of the vorticity created by retraction. It was discussed in chapter 3 how the late-time instability was a consequence of the vorticity created by the pre-burst waves. There was therefore potential for interference between the two. An example of such interference is shown in figures 5.20(a) and 5.20(b), for an oscillation and rupture with water both inside and outside the balloon. The crack propagated down the right-hand side of the balloon, in line with the light sheet. As the membrane did not retract past the interface there, there was no vorticity from retraction created. The interface therefore evolved purely as a consequence of the pre-burst vorticity, a situation examined in more detail in chapter 6. The situation was different on the left-hand side of the balloon, where the membrane ended up after fully retracting (as may be seen in figure 5.20(a)). On that side, the vorticity created by retraction was in the same direction as that from the pre-burst waves, and therefore dominated the flow post-rupture (as is clear from figure 5.20(b)). Consequently, no large-scale, late-time growth of the interface was seen on that side. A similar effect was seen for all the ruptures in water: growth according to the pre-burst waves was dominant on the half of the balloon nearest the initial crack path, growth according to the shear instability was dominant on the half nearest the membrane after it had fully retracted.

For ruptures in air, as shown in figures 5.21(a) and 5.21(b), the development of the late-time interfacial amplitude was not affected by the retraction of the membrane, with both effects occurring on nearly the whole interface. This was because for such a large density difference across the interface,

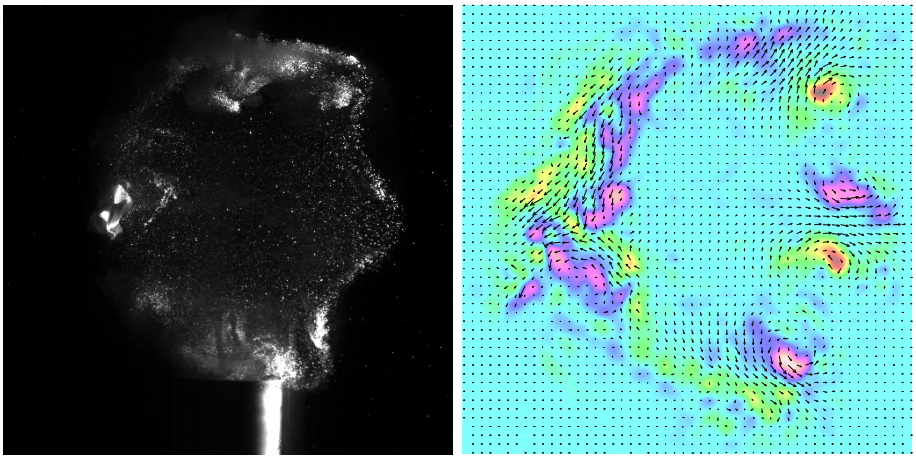

(a) Experimental image (b) Vorticity

Figure 5.20: The full flow created by the rupture of a 130 mm balloon after being oscillated at 50 Hz underwater. The images were taken at 0.4 s after rupture. Image **(a)** shows the actual experimental image, with the membrane visible half-way up the image on the left-hand side. The flow was seeded with particles, so that PIV could be performed. From this PIV, the vorticity field was found, as shown in image **(b)**.

the late-time interfacial growth was not governed by the interfacial vorticity, but by momentum in the outer flow. This will be discussed further in chapter 6.

5.4.3 Application of 1D theory to the bursting of balloons

The theory discussed above has given us a valuable insight into the behaviour of rubber in retraction from high initial stretches in the presence of water. However, the bursting of a water balloon is clearly not a purely 1D effect, and so there are a number of other factors to take into account.

Retraction in a spherical geometry

So far, our analysis has been restricted to the retraction of uniaxially-stretched rubber. A balloon is, approximately, a biaxially-stretched membrane in spherical geometry. The bursting and subsequent retraction of a spherical membrane therefore introduces added geometrical complications when compared with a one-dimensional uniaxially-stretched strip. To elucidate the differences, we consider three linear situations of increasingly accurate approximation to a balloon: a biaxially-stretched square membrane, a biaxially-stretched circular membrane, and a biaxially-stretched (or inflated) spherical membrane. Introducing non-linearity here would greatly increase the complexity of the algebra, while changing little of importance apart from a small adjustment to the retraction speed.

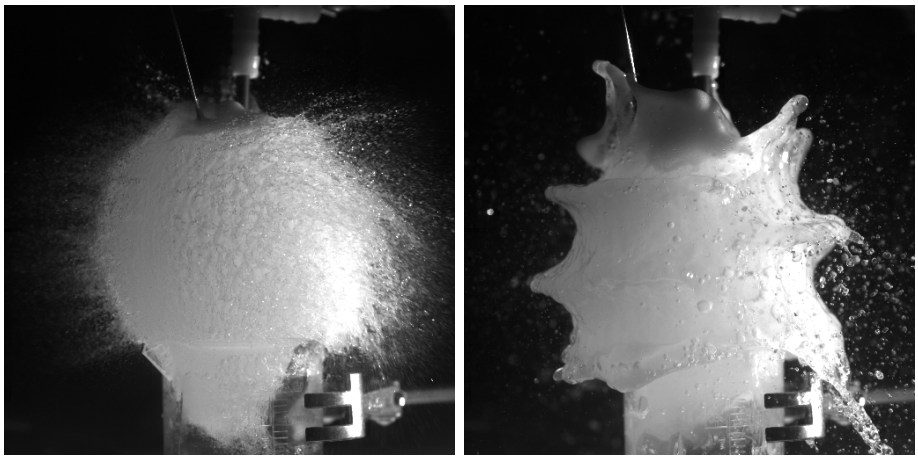

(a) $t = 7$ ms (b) $t = 54$ ms

Figure 5.21: The flow created when a 130 mm balloon was burst after being oscillated at 120 Hz in air. Time $t = 0$ ms was the moment rupture began. In image **(a)**, soon after rupture, the shear instability may be seen everywhere on the interface. Later, in image **(b)**, the shear instability is no longer visible, but the large-scale growth of the interfacial amplitude is present everywhere - even in the bottom right, to where the membrane ended up after fully retracting.

Flat membrane

We first consider a membrane biaxially stretched in the x and y directions. The equation of motion is given by the linear momentum equation, the Navier equation (5.5), that limited to longitudinal motions is

$$\boldsymbol{a}_{tt} = c_{ql}^2 \nabla \boldsymbol{a} \tag{5.90}$$

where c_{ql} is the quasi-longitudinal wave speed for a thin sheet given in section 5.2.1, $c_{ql} = \sqrt{4\mu/\rho}$. The motion is therefore identical in nature to that outlined for a uniaxial strip, with a stress wave traveling through the material at speed c_{ql}, acting as a shock-wave behind which the material is stress-free in the direction of motion. Here, however, that is not the same as being strain-free. The stress in the direction of retraction is, from section 5.2.1,

$$\tau_{XX} = -p + 2\mu u_X = 4\mu u_X + 2\mu(\lambda_y - 1). \tag{5.91}$$

For the material to be stress-free, $\tau_{XX} = 0$ and hence $u = -\frac{1}{2}(\lambda_y - 1)x;$. The material is therefore contracted from its reference configuration. However, the time for retraction will be the same as for uniaxial extension, only the length of the rubber when 'fully' retracted in the X-direction will be less than its length in the reference configuration, due to the strain remaining in the y direction.

Flat circular membrane

We now consider a circular membrane of radius R, where the material displacement is given by a_r in the r direction and a_θ in the θ direction. The rubber is stretched in the r direction before being

released at $t = 0$; this situation does not appear to have been considered in any published literature. This is a biaxial displacement, but with with axisymmetry so that the only displacements are in the r direction. However, the strains, as given by Sadd [2005], are

$$\epsilon_{rr} = \frac{\partial a_r}{\partial r}, \tag{5.92}$$

$$\epsilon_{\theta\theta} = \frac{a_r}{r}, \tag{5.93}$$

and thus this deformation represents a biaxial strain (or stretch).

The stress components are then given by

$$\tau_{rr} = -p + 2\mu \frac{\partial a_r}{\partial r}, \tag{5.94}$$

$$\tau_{\theta\theta} = -p + 2\mu \frac{a_r}{r}, \tag{5.95}$$

$$p = -\frac{2\mu}{r} \frac{\partial}{\partial r}(r a_r). \tag{5.96}$$

The equation of motion in cylindrical coordinates is given by Sadd [2005] as

$$\rho \frac{\partial^2 a_r}{\partial t^2} = \frac{\partial \tau_{rr}}{\partial r} + \frac{1}{r}(\tau_{rr} - \tau_{\theta\theta}), \tag{5.97}$$

which is equivalent here to

$$\frac{\partial^2 a_r}{\partial t^2} = \left(\frac{4\mu}{\rho}\right)^2 \left(\frac{\partial^2 a_r}{\partial r^2} + \frac{1}{r}\frac{\partial a_r}{\partial r} - \frac{a_r}{r^2}\right). \tag{5.98}$$

The boundary conditions are now a_r finite and smooth at $r = 0$, and $\tau_{rr} = 2\mu\left(2\frac{\partial a_r}{\partial r} + a_r/r\right) = 0$ for $r = R$, $t > 0$, with initial conditions $a_r = \epsilon r$, $\partial a_r/\partial t = 0$ at $t = 0$. This situation is depicted in figure 5.22. No simple analytical solution to this equation exists. Consequently, while it likely permits an infinite series solution, we solved it numerically, as for the results given in figure 5.23. These results reveals that, as before, a stress wave propagates from the stress-free edge into the material at speed $\sqrt{4\mu/\rho}$. However, the material is not uniformly strain and stress-free behind the wave front, but in fact in compression, with negative stresses everywhere between the wavefront and the free edge. The compression is greatest near the wavefront, before tailing off to zero near the free end, and arises because as the wavefront passes through the material, it releases the stress in the r-direction but not the stress in the θ direction. The Poisson effect therefore leads to negative stresses behind the wavefront that force the material to retract in the r direction, just as in the previous section. Unlike in the previous section, however, this perpendicular stress is constantly changing (decreasing) as the material moves inwards, thus complicating the motion. As a consequence of this, the material is not fully retracted and stress-free when the wave front reaches $r = 0$, but instead is in compression almost everywhere.

In section 5.2.2, it was shown that the stress-wave speed for non-linear theories of rubber may depend on the perpendicular stretch, which may mean a changing wave speed here. However, equation (5.93) shows that for initial displacement $a_r = \epsilon r$, the strain $\epsilon_{\theta\theta} = \epsilon$ and therefore is independent of r. The wave speed should therefore be constant.

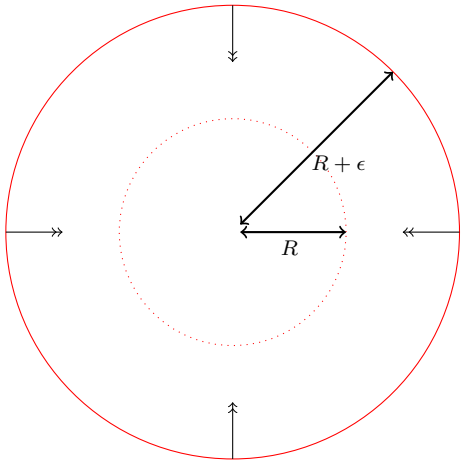

Figure 5.22: Diagram showing the stretch then release of a circle of material in the radial direction. The dotted red line shows the stress-free configuration, the solid red line the stretched configuration at $t = 0$.

Spherical membrane

As shown previously, a balloon is well approximated by a thin spherical membrane of rubber stretched radially. The rupture of a balloon may therefore be modelled by considering such a membrane, and instantaneously applying a stress-free condition about a great circle, for instance $\phi = \pi/2$, at $t = 0$. As before, we can find no evidence in the literature of linear elasticity theory being applied in this way to model the bursting of a balloon.

The geometrical situation here shows strong similarities with those discussed previously in this section, as the membrane will retract from an initial state of biaxial stress, with the stress perpendicular to the direction of retraction decreasing as the membrane retracts. Indeed, viewing the retraction from above $\phi = 0$, it will look like the retracting flat circular membrane discussed previously, with water present either side of the membrane, the two situations are qualitatively highly similar. However, with air both sides of the membrane, the situation changes significantly. The stresses within the rubber prior to rupture apply a net inward force on the fluid inside that is balanced by pressure within the fluid. After rupture, there will be a sharp pressure gradient between the fluid inside and that outside the membrane. In both air and water, the speed of sound is far greater than the speed of sound in the stretched rubber for all but the highest stretches, so that information of the pressure gradient in the fluid will reach the material before the wavefront in the rubber (that represents the pressure gradient at the rubber's free edge). Once this happens, the fluid pressure will start to decrease and so will no longer balance the stresses in the membrane, causing the membrane to contract radially. However, this drop in fluid pressure occurs by the fluid inside the balloon being accelerated to move to the outside, and thus depends on the inertia of the fluid. With water either inside or outside the membrane (or both), its high inertia resists movement, meaning that the flow of fluid from inside to outside will take place over a far longer timescale than that taken by the membrane to retract. Changes in the deformation in the radial direction are therefore not significant, so the membrane is restricted to its initial sphere. With air both sides of the membrane, the inertia is far less, so the fluid

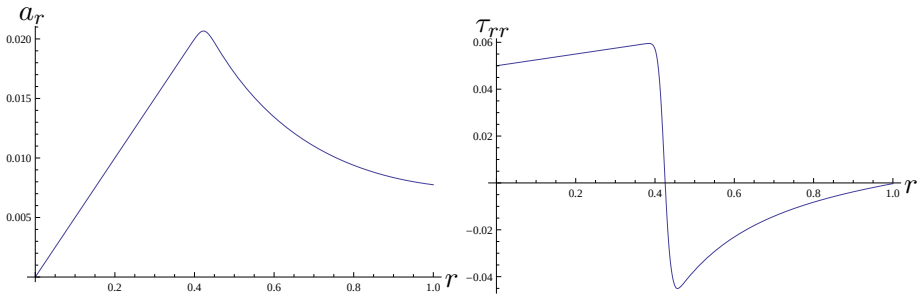

(a) Displacement (b) Stress

Figure 5.23: Results from the numeric solution to equation (5.98) for the linear retraction of a radially-stretched circle of rubber. The strip was released at $r = 1$ at $t = 0$, with the above figures taken at $t = 0.6$. The wave speed is $c_{ql} = 1$.

is quickly accelerated and moves to the outside. The membrane may therefore start retracting inwards before retraction in the ϕ direction is completed. Changes in deformation in the radial direction must therefore be taken into account.

We considered here a thin, spherical membrane of radius A in the reference configuration, that is stretched uniformly to radius $A + \epsilon A$ before $t = 0$. Axisymmetry is assumed, so that the material displacement in the radial direction is given by $a_r = a_r(t, \phi)$ such that $r = R + a_r(t, \phi)$. The displacement in the ϕ direction is $a_\phi = a_\phi(t, \phi)$, with no displacement in the θ direction. As before, this is a uniaxial displacement but biaxial strain, as the strains are given by

$$\epsilon_{\theta\theta} = \epsilon_{\phi\phi} = \frac{a_r}{R}. \tag{5.99}$$

The stress components are then given by

$$\tau_{rr} = \tau_{r\theta} = \tau_{\phi\theta} = 0 \tag{5.100}$$

$$\tau_{\theta\theta} = -p + 2\mu \left(\frac{a_r}{R} + \frac{a_\phi \cot\phi}{R} \right), \tag{5.101}$$

$$\tau_{\phi\phi} = -p + 2\mu \left(\frac{1}{R}\frac{\partial a_\phi}{\partial \phi} + \frac{a_r}{R} \right), \tag{5.102}$$

$$\tau_{r\phi} = \mu \left(-\frac{1}{R} a_\phi + \frac{1}{R}\frac{\partial a_r}{\partial \phi} \right), \tag{5.103}$$

$$p = -\frac{2\mu}{R} \left(\frac{2}{R} a_r + \frac{1}{\sin\phi}\frac{\partial}{\partial \phi}(\sin\phi a_\phi) \right). \tag{5.104}$$

The equations of motion in spherical polar coordinates are given by Sadd [2005] as

$$\rho \frac{\partial^2 a_r}{\partial t t} = \frac{1}{R}\frac{\partial \tau_{r\phi}}{\partial \phi} + \frac{1}{R}\left(\tau_{r\phi}\cot(\phi) - \tau_{\phi\phi} - \tau_{\theta\theta} \right), \tag{5.105}$$

$$\rho\frac{\partial^2 a_\phi}{\partial tt} = \frac{1}{R}\frac{\partial \tau_{\phi\phi}}{\partial \phi} + \frac{1}{R}\left((\tau_{\phi\phi} - \tau_{\theta\theta})\cot\phi + 3\tau_{r\phi}\right), \tag{5.106}$$

that for our thin, axisymmetric spherical membrane are equivalent to

$$\rho\frac{\partial^2 a_r}{\partial tt} = \frac{\mu}{\rho A^2}\left(\frac{1}{\sin(\phi)}\frac{\partial}{\partial\phi}\left(\sin(\phi)\frac{\partial a_r}{\partial\phi}\right) - 12a_r - \frac{7}{\sin(\phi)}\frac{\partial}{\partial\phi}\left(\sin(\phi)a_\phi\right)\right), \tag{5.107}$$

$$\frac{\partial^2 a_\phi}{\partial t^2} = \left(\frac{4\mu}{\rho A^2}\right)\left(\frac{\partial^2 a_\phi}{\partial\phi^2} + \cot(\phi)\frac{\partial a_\phi}{\partial\phi} - (1+\cot^2(\phi))a_\phi + 2\frac{\partial a_r}{\partial\phi}\right). \tag{5.108}$$

The boundary conditions now require a_ϕ finite and smooth at $\phi = 0$, along with

$$a_\phi(t,0) = 0, \tag{5.109}$$

$$\frac{\partial a_r}{\partial\phi}(t,0) = 0, \tag{5.110}$$

$$\tau_{\phi\phi}(t,\pi/2) = \left[-p + 2\mu\left(\frac{1}{A}\frac{\partial a_\phi}{\partial\phi} + \frac{a_r}{A}\right)\right]_{\phi=\pi/2} = 0, \tag{5.111}$$

$$\tau_{r\phi}(t,\pi/2) = \left[-\frac{1}{A}a_\phi + \frac{1}{A}\frac{\partial a_r}{\partial\phi}\right]_{\phi=\pi/2} = 0. \tag{5.112}$$

The initial conditions are:

$$a_r(0,\phi) = \epsilon, \tag{5.113}$$

$$a_\phi(0,\phi) = 0, \tag{5.114}$$

$$\frac{\partial a_r}{\partial t}(0,\phi) = \frac{\partial a_\phi}{\partial t}(0,\phi) = 0. \tag{5.115}$$

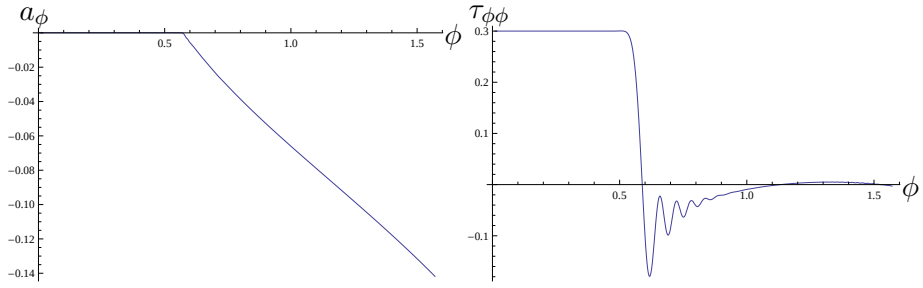

(a) Displacement (b) Stress

Figure 5.24: Results from the numeric solution to equation (5.108), representing the bursting of a water-filled membrane, so that there was no displacement in the r direction. The strip was released at $\phi = \pi/2$ $t = 0$, with the above figures taken at $t = 1$. The wave speed is $c_{ql} = 1$. The displacement is negative here, as the initial stretch is in the radial direction, but the membrane retracts in the the ϕ direction. The oscillation in the stress between $\phi = 0.6$ and $\phi = 1.0$ displayed **(b)** is the result of numerical error.

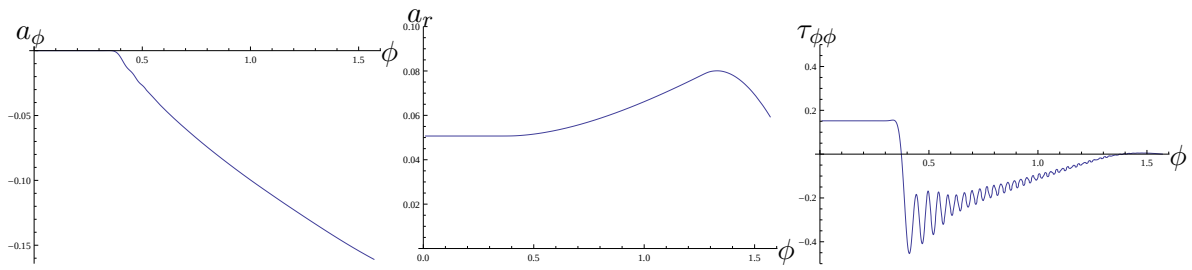

(a) Polar displacement (b) Radial displacement (c) Stress

Figure 5.25: Results from the numeric solution to equations (5.107) and (5.108), representing the bursting of an air-filled membrane. The free edge was released at $t = 0$, with the above figures taken at $t = 1.2$. The wave speed is $c_{ql} = 1$. The waviness in **(c)** is the result of numerical error.

We first consider the simpler situation, with water either one or both sides of the membrane. Note that we neglect drag here, as we are primarily interested in geometrical effects. Due to the relatively significant inertia of water in comparison with that of the retracting rubber, we make the approximation that the radial displacement is fixed at $a_r = \epsilon A$ with water present, and so we need only consider equation (5.108) along with suitable boundary conditions. This problem must be solved numerically, for which we used the inbuilt NDSolve tool in Mathematica. Results are displayed in figure 5.24, and show much the same phenomenology as for the retracting circle: the stress wave propagating at speed $\sqrt{4\mu/\rho}$, behind which the material is in compression away from the free edge due to the Poisson effect. This compression then relaxes as the material nears full retraction.

For retraction in air, the behaviour is different. Now the radial displacement a_r must be taken as an unknown, so a_r and a_ϕ must be solved for using the full range of coupled equations above. As before, this was done numerically in Mathematica, and results are shown in figure 5.25. The behaviour of a_ϕ is similar to the previous situation, with the material in compression behind a wavefront traveling at speed $\sqrt{4\mu/\rho}$. The behaviour of a_r shows two main features: simultaneous retraction everywhere in the r direction starting at $t = 0$, and a shear wave propagating in from the free edge at speed $\sqrt{\mu/\rho}$. This shear wave is is given by the first term on the right-hand side of equation (5.107), and is a consequence of applying the condition $\tau_{r\phi}$ instantaneously at $t = 0$. It travels through near stress-free material far behind the longitudinal wavefront, and leads to a positive radial displacement. The simultaneous retraction everywhere is due to the assumed instantaneous release of pressure at $t = 0$ and neglecting of the air's momentum, meaning there is nothing to balance the stresses $\tau_{\phi\phi}$ and $\tau_{\theta\theta}$ that, as discussed in chapter 2, are the stresses than balance the pressure difference across a thin balloon. From equation (5.107), this retraction is controlled by the second term $(-12\mu/\rho)a_r$. The third term in equation (5.107) affects the radial displacements due to gradients in the polar displacement a_ϕ. Such gradients affect $\tau_{\phi\phi}$ and $\tau_{\theta\theta}$ and hence the radial displacement.

The retraction of a balloon in air is therefore more complex than that in water (when neglecting drag), as it is given by the coupling of the polar and radial displacements. Nevertheless, the behaviour in the direction of retraction is highly similar; it is only the radial displacements that change significantly, with a shrinking of the radius everywhere accompanied by a shear wave propagating in from the free edge.

For the rest of this thesis we are considering only bursting water balloons, and so shall not be concerned about the changes in radial displacement; both the shear wave and uniform radial retractions may be neglected. Furthermore, while the stress behind the wavefront was shown to be compressive (unlike uniaxially-stretched rubber strips), it was shown experimentally that the behaviour of non-linearly stretched rubber was highly dispersive behind the wavefront. Consequently, such compressive stresses will not appear during retraction of a non-linearly stretched balloon. The added geometrical effects of a retracting spherical membrane as opposed to a retracting strip will therefore likely be insignificant, adding only quantitative, rather than qualitative, changes to the material behaviour. The same, therefore, will be true if the balloon's initial shape is not perfectly spherical, as was shown to be the case in chapter 2.

We may attempt to quantify the effect of the different geometry (and the uniaxial or biaxial initial stress state) by comparing the total retraction time for a balloon underwater, and a strip retracting underwater from the same initial strain. Defining retraction to have ended when buckling waves have spread over the whole piece of rubber, typical retraction times for a strip with $\lambda_0 = 6$ was 12 ms. For a balloon with $\lambda_0 = 6$, it was around 4 ms. The retraction was therefore significantly faster. A similar, if less significant, difference was also noted for retractions in air in section 5.4.1.

Other factors

It must also be acknowledged here that we should not necessarily expect the model of Niemczura and Ravi-Chandar [2011c] be applicable to the retraction of balloon membranes. The model was phenomenologically-derived based on the behaviour of rubber in uniaxial retraction. As was demonstrated in section 5.2.2 for Mooney-Rivlin and Ogden's models, the behaviour of non-linear rubber in biaxial retraction may be significantly different from uniaxial retraction. Consequently, the phenomenological model of Niemczura and Ravi-Chandar [2011c] may be inaccurate to describe the stress-strain relationship for the retraction of rubber membranes from an initial biaxial strain, as for a burst balloon. As it was not possible for us to measure the stress-strain behaviour of rubber in dynamic retraction, we cannot be sure how significant the differences would be; however, section 5.2.2 did show that the differences were small and quantitative for Mooney-Rivlin and Ogden's models, and so it seems highly likely that that would be the case for the non-linear model of Niemczura and Ravi-Chandar [2011c] too.

Further inaccuracies may arise from approximating the crack formation as instantaneous. Experiments on non-linear retracting rubber strips showed the wave speed to be very high, far higher than the crack speed. Consequently, stress waves created by the crack could travel all round the balloon faster than the crack itself, and so affect the stress conditions at the tip later in time, as it propagated. This was especially significant for a bursting balloon as opposed to a retracting strip, as for a strip the crack would only have to travel the width of the strip, likely to be far less than the material traveled; for a bursting balloon, the crack would be traveling around a diameter of the balloon, and thus a similar distance to the material. The crack would, relatively, be in motion far longer. For a full description of the crack behaviour in a bursting balloon, therefore, this interference should be taken into account. However, to a large extent, the dispersion in the stress-wave justified our approximating the crack formation as instantaneous. This meant that even in material the wavefront had passed, the strain and stress were likely to still be close to their initial values over the timescale on which the crack propagated. By the time the crack had finished propagating, most of the material would

not have experienced significant displacement. Approximating the crack formation as instantaneous would therefore not have a significant effect on the material behaviour. This discrepancy between crack and material speeds was especially pronounced for retraction in water (see figure 5.2), our main topic of study.

In summary, our investigations into the retraction of 1D strips have uncovered the main physical phenomena that occur both in the rubber and the flow surrounding it during retraction after bursting. Consequently, we may now qualitatively describe the process of retraction well. However, the results do not appear to carry over into the more complicated geometry of a bursting balloon, with our qualitative predictions from 1D accurate only to the nearest order of magnitude. To obtain better predictions for the retraction behaviour of a bursting rubber balloon, a large-scale computational study is likely to be necessary.

5.5 Waves near the free edge

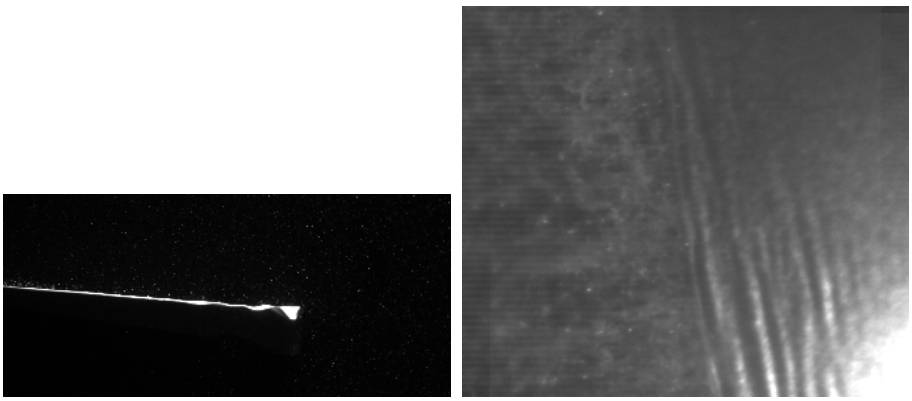

(a) Strip (b) Balloon

Figure 5.26: Waves seen near the free edge for a balloon membrane underwater.

During our experiments on the dynamic retraction of the rubber in water, small waves were seen near the free edge, as shown in figure 5.26. This was the case for both the instantaneously-released uniaxially-stretched strips, and the bursting water balloons in water or air. Far smaller (in both wavelength and amplitude) versions of such waves were seen for retractions of strips in air, while none were seen for retractions in glycerin. In water, these waves had a typical wavelength on the order of one millimetre, approximately the same wavelength as seen for the buckling waves created once the material has fully retracted and enters compression. The amplitude of these waves was also typically less than half the wavelength (as shown in figure 5.26), and so may reasonably be assumed to be linear. The linearity of the waves is assumed in all the following discussion.

The appearance of such waves on retracting rubber strips does not appear to have been noted before in the literature, likely due to most being conducted in air, and using thicker strips so that bending forces would suppress waves of such a short wavelength. The only example of work on the retraction of rubber in water, that of Vermorel et al. [2007], makes no mention of such waves. However, their work was limited to retraction from linear initial stretches, which was shown in the previous sections

to be significantly different (in particular, slower) from the behaviour of rubber in retraction from non-linear initial stretches. Their strips were also significantly thicker than ours.

Despite the lack of work done on this particular situation, much work has been done on the more general case of fluid flowing past elastic membranes. In particular, these waves appeared to show similarity to flapping flags, by which we mean thin sheets of flexible but inextensible material that oscillate out-of-plane in response to a flow parallel to their length. Despite the apparently simple situation, the flags display a range of behaviours: they may remaining flat and parallel to the flow, or flutter (oscillate periodically perpendicular to the flow), or diverge (non-oscillatory transverse motion), as described by de Langre et al. [2007]. The type of motion seen depends on both the material properties and fluid properties, but for a set flag and fluid, the motion goes from flat to flutter to divergence as the flow speed increases. The range of behaviours was first studied experimentally by Taneda [1968], since which time a wide range of experimental, theoretical and numerical investigations have been conducted.

Some research has also looked at flow out of elastic tubes, as reviewed by Paıdoussis and Li [1993]. Tubes in such a situation are known to display what is known as the 'garden hose instability', that takes the form of asymmetric waves near the tube exit. This is the cause of the writhing around of an unsupported garden hose that gives the phenomenon its name.

More relevant to us, however, is the inverse situation: that of fluid flowing past an elastic sheet or cylinder. This topic has been the subject of significant research as it relates to the behaviour of streamers - long, thin elastic cylinders housing hydrophones that are towed underwater through the ocean, and used to survey the sea floor and beneath by the oil industry. Significant work on this problem has been done by Dowling [1988] and de Langre et al. [2007], amongst others; a complete review is given by Paidoussis [2003].

The waves displayed in figure 5.26 are examples of flutter: periodic oscillations perpendicular to the flow. In the following sections, we shall describe the physical mechanisms behind their growth, before describing our experimental investigations into the phenomena. No matching of these experiments to theory was performed, due to our uncertainty in the stress-strain relationship for rubber in free retraction.

5.5.1 Lift on a retracting membrane

The modeling of streamers, as by Dowling [1988], starts from the work of Lighthill [1960] on the swimming of slender fish. In this work, the author considers axial flow at speed U in the x direction past a so-called slender body whose centre line is given by $\zeta(x,t)$. If the flow does not separate, the inviscid fluid-loading, or lift force, $L(x,t)$ per unit length on the object from the fluid is given for a one-dimensional displacement by

$$L(x,t) = \rho_f A_f(x) \left(\frac{\partial}{\partial t} + U \frac{\partial}{\partial x} \right)^2 \zeta(x,t) = \rho A(x) \left(\frac{\partial^2 \zeta}{\partial t^2} + 2U \frac{\partial^2 \zeta}{\partial x \partial t} + U^2 \frac{\partial^2 \zeta}{\partial x^2} \right), \tag{5.116}$$

where ρ_f is the density of the fluid, and $A_f(x)$ is the 'virtual' cross-section of the object. $A_f(x)$ has the dimensions of area, and for a circular cylinder is equal to the cylinder's cross-section. For a flat, two-dimensional plane, however, Coene [1992] showed that $A_f = \lambda/\pi$ and thus depends on the wavelength of waves on the body. Similarly, for a two-dimensional strip of width b, the cross-section

is $A_m = bh$, while the virtual cross-section is $A_f = 2b/k$ (as above and in Vermorel et al. [2007]). The first term on the right-hand side of (5.116) is the added-mass, that arises from the inertia of the fluid displaced when the object is displaced. The second term is the Coriolis load, giving the object's resistance to rotation or change in gradient. The third term is the centrifugal load, that arises from the deflection of the fluid round curvature in the object.

If viscous drag is included (as in Dowling [1988]), it will also have a component acting normally to the plane of the membrane. This term is given in full later, in equation (5.126). However, while this viscous lift may have a small influence on the waves formed, it does not explain their generation, as given by de Langre et al. [2007]. Further, as our strips are smooth and traveling at high speed in (low-viscosity) water, we expect this lift to be small compared with the inviscid forces. We therefore neglect it in the following explanation of the generation mechanism for the waves, though it is included in the later description of work by Dowling [1988].

5.5.2 Transverse deformation of a retracting membrane

The equation of motion for transverse linear deformations of a one-dimensional body of thickness h neglecting the surrounding fluid was given in chapter 2, equation (2.8), based on Euler-Bernoulli beam theory. This may be combined with equation (5.116) to describe the transverse deformations with added inviscid axial flow,

$$\rho_m A_m \frac{\partial^2 \zeta}{\partial t^2} = \frac{\partial}{\partial x}\left(T(x)\frac{\partial \zeta}{\partial x}\right) - \frac{Eh^2}{12}\frac{\partial^4 \zeta}{\partial x^4} - \rho_f A_f \left(\frac{\partial^2 \zeta}{\partial t^2} + 2U\frac{\partial^2 \zeta}{\partial x \partial t} + U^2 \frac{\partial^2 \zeta}{\partial x^2}\right), \tag{5.117}$$

where here ρ_m is the density of the body and A_m is its cross-section (that is not necessarily the same as its 'virtual' cross-section A_f). This equation may be rearranged in the more useful form

$$(\rho_m A_m + \rho_f A_f)\frac{\partial^2 \zeta}{\partial t^2} = (T(x) - \rho_f A_f U^2)\frac{\partial^2 \zeta}{\partial x^2} - \frac{Ebh^3}{12}\frac{\partial^4 \zeta}{\partial x^4} - 2\rho_f A_f U \frac{\partial^2 \zeta}{\partial x \partial t} + \frac{\partial T}{\partial x}\frac{\partial \zeta}{\partial x}. \tag{5.118}$$

Assuming T constant, Coene [1992] looked for harmonic solutions to this equation of the form

$$\zeta(x,t) = B\exp(i(kx - \omega t)). \tag{5.119}$$

Substituting this solution into equation (5.118) leads to the dispersion relation

$$-(\rho_m A_m + \rho_f A_f)\omega^2 = -(T - \rho_f A_f U^2)k^2 - \frac{Ebh^3}{12}k^4 - 2\rho_f A_f U w k. \tag{5.120}$$

Writing $\rho_f A_f = \alpha_f$, $\rho_m A_m = \alpha_m$ and solving for ω gives

$$\omega = \frac{k}{\alpha_f + \alpha_m}\left(\alpha_f U \pm \sqrt{\left(T + k^2\frac{Eh^2}{12}\right)(\alpha_f + \alpha_m) - \alpha_f \alpha_m U^2}\right). \tag{5.121}$$

If ω is real, the waves on the body will be steady, of fixed amplitude. However, if ω is complex, the wave amplitudes will be growing exponentially in time. The nature of these waves will change when ω goes from real to complex, a critical point given by the equation

$$T + k^2\frac{Eh^2}{12} - \frac{\alpha_f \alpha_m}{\alpha_f + \alpha_m}U^2 = 0. \tag{5.122}$$

When $U = 0$, this reduces to the equation for bending waves discussed in section 2.9, with steady waves for $T > 0$ (as for the pre-burst tension-driven waves discussed in chapter 4) and exponentially growing waves for $T < 0$ (as for the buckling of a membrane after it has fully retracted). As our membranes are thin, the magnitude of the bending stresses will usually be far less than that of the tension, meaning the behaviour when $U = 0$ may be approximated as follows: when in extension, steady, tension-driven waves are present; when in compression, exponentially growing waves appear from a balance between tension and bending stresses.

However, when $U \neq 0$, the membrane does not need to be in compression for exponentially growing waves to appear: as both α_f and α_m are always positive, such waves may appear when the flow speed U is great enough in comparison to the tension and bending stiffness. In such a situation, it is the centrifugal force from the fluid, given by $-\rho_f A_f U^2 \zeta_{xx}$ in equation (5.118), that acts like a compressive force to create these waves. However, it is not a true compression, as it does not actually create compressive stress in the body, but instead acts to increase the curvature (increase in curvature is also a by-product of compressive stresses). Note that a clear parallel may be drawn with purely fluid shear instabilities, such as Kelvin-Helmholtz instability, where here the membrane plays the role of the shear layer in allowing a velocity discontinuity to form between the fast-moving flow near the strip, and the stationary outer flow. The instability growth then proceeds in a similar way for both the retracting membrane and pure fluid instabilities. Further discussion of this similarity is given in section 5.6.3.

This theory can then be used to explain why we saw waves on our retracting balloon membranes and strips, but only near the free edge. As the stress wave created by the zero stress condition at the free edge is highly dispersive, the membranes did not experience compressive stresses anywhere before they had fully retracted. For most of the membrane, therefore, tension was large enough to overcome the fluid loading, so any transverse growth was suppressed. However, the tension would necessarily decrease to zero near the free edge, and thus there would be a region near the free edge where $T - \frac{\alpha_f \alpha_m}{\alpha_f + \alpha_m} U^2 < 0$, causing transverse waves to grow from a balance between fluid loading, the remaining tension in that region, and also bending stiffness. As retraction continued, it was shown in section 5.4.2 that the membrane speed varied little while the strain and hence stress decreased greatly. Consequently, the size of the region in which $T - \frac{\alpha_f \alpha_m}{\alpha_f + \alpha_m} U^2 < 0$ would grow. This was indeed observed for bursting balloons, as is shown in figure 5.27.

Of course, this analysis ignored several important features, most notably variation in the tension T. While this is significant, as it provides the force causing the rubber to retract in the first place, gradients in T will be of the order of one over the strip length, whereas the other terms will be of the order of one over the (far smaller) transverse wavelength. The term $T_x \zeta_x$ will thus be far smaller than all other terms in equation (5.118) and so its inclusion will change little of significance.

An example of the inclusion of tension variation was given by Dowling [1988] when studying inextensible flexible cylinders in outer flow at fixed speed U, who also included the effects of viscous drag. With the tangential and normal viscous forces per unit length on the cylinder given by F_T and F_N, respectively, the first order axial equation of motion is

$$F_T + \frac{\partial T}{\partial x} = 0, \tag{5.123}$$

with the sum of the forces equal to zero as the cylinder is inextensible and fixed at its upstream end. This shows the tension is derived purely from viscous drag with the fluid (form drag neglected here

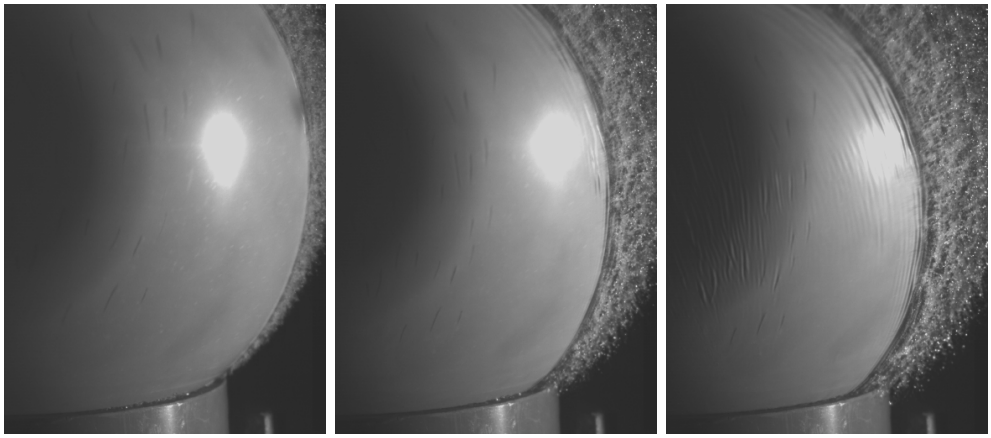

(a) $t = 0.85$ ms (b) $t = 1.35$ ms (c) $t = 1.60$ ms

Figure 5.27: The growth of the region in which transverse waves near the free edge appeared, over the course of a retraction. Time $t = 0$ ms is when the crack started propagating. Some buckling waves are also present near the centre of the retracting membrane, on the left-hand side of the images.

as the body is slender), something that was not true for our retracting strips. The equation of motion in the transverse direction is then

$$(\rho_m A_m + \rho_m A_f)\frac{\partial^2 \zeta}{\partial t^2} = (T(x) - \rho_f A_f U^2)\frac{\partial^2 \zeta}{\partial x^2} - \frac{Eh^2}{12}\frac{\partial^4 \zeta}{\partial x^4} - 2\rho_f A_f U \frac{\partial^2 \zeta}{\partial x \partial t} + \frac{\partial T}{\partial x}\frac{\partial \zeta}{\partial x} + F_T \frac{\partial \zeta}{\partial x} - F_N. \quad (5.124)$$

Note that the inclusion of the penultimate term was remarked upon by Dowling, who points out that its presence ensures that the tangential viscous force acts in the instantaneous tangential direction, and not simply in the x-direction. Following the work of Taylor [1952], Dowling [1988] gave the forces per unit length as

$$F_T = \rho_f \pi a U^2 C_T, \quad (5.125)$$

$$F_N = \rho_f \pi a U C_N \left(\frac{\partial \zeta}{\partial t} + U\frac{\partial \zeta}{\partial x}\right), \quad (5.126)$$

where C_T and C_N are drag coefficients and a is the radius of the cylinder. Equation (5.123) may then be solved, assuming the end of the cylinder is free, to give

$$T(x) = \rho \pi a U^2 C_T (l - x), \quad (5.127)$$

thus suggesting the tension varies linearly along the cylinder. Conveniently, this also means that the gradient in the tension $T_x \zeta_x$ in equation (5.124) is cancelled out by the term $F_T \zeta_x$. With the body cylindrical (so $A_f = A_m = \pi a^2$) and neutrally-buoyant ($\rho_f = \rho_m = \rho$), equation (5.124) may be rewritten as

$$2\pi a^2 \frac{\partial^2 \zeta}{\partial t^2} = (T(x) - \rho \pi a^2 U^2)\frac{\partial^2 \zeta}{\partial x^2} - \frac{E\pi a^4}{4}\frac{\partial^4 \zeta}{\partial x^4} - 2\rho\pi a^2 U \frac{\partial^2 \zeta}{\partial x \partial t} + \rho \pi a U C_N \left(\frac{\partial \zeta}{\partial t} + U\frac{\partial \zeta}{\partial x}\right). \quad (5.128)$$

A more comprehensive equation was given by de Langre et al. [2007], who also considered the effects of the shape of the free edge. However, as discussed in section 5.4 the strips we are concerned with are very thin, and so may regarded as streamlined, meaning that drag and lift from the free end may be neglected.

Equation (5.128) was solved by Dowling [1988] using matched asymptotic expansions. The nature of this equation changes at the critical point given by $T(x)-\rho\pi a^2U^2$ (given by $x = l-a/C_T$): upstream of this point, the tension is larger, whereas downstream the fluid loading term is dominant. This leads to a significant change in behaviour of the body as this critical point is crossed. Upstream of the critical point, the lengthscale for variations in displacement are of the order of l, the total length of the cylinder. Downstream, however, there exist wavelike solutions with wavelengths of the order of $(Ea^3/l^3\rho U^2C_T)^{1/3}$, that is a small parameter for a slender body. As before, these waves arise from a balance between fluid-loading wanting to increase the curvature, and tension and bending stiffness wanting to suppress it. Upstream of the critical point, the tension is dominant and so suppresses such waves completely.

The behaviour uncovered by Dowling [1988], of small amplitude waves restricted to a region near the free edge of a moving slender body, is clearly analogous to what we have observed on retracting rubber membranes. No direct quantitative comparisons may be made, however, as two assumptions have been made that do not apply for retracting membranes: the material was assumed inextensible, and the tension was assumed solely as a result of shear stress with the surrounding fluid. As stated above, we can find no evidence of work on retracting rubber strips, where the tension is initially applied then released at the free end. The extensibility of flexible cylinders in axial flow was taken into account by Modarres-Sadeghi et al. [2005]. However, axial displacements were assumed to be an order of magnitude smaller than transverse displacements, and the tension, as above, was determined by shear with the outer fluid. In contrast, for our retracting strips, the tension present is primarily due to that arising when the strip is initially stretched. The model of Dowling [1988] shows that the wavelength of these waves depends on C_T and thus on the tension. To get an estimate for the wavelength of the waves near the free edge, we would need to know the tension there. However, as discussed in the previous section, the non-linearity of rubber prevents accurate estimation of the stress distribution in the retracting strip. It is therefore not possible for us to give accurate theoretical estimations of the waves near the free edge.

The above theory was also derived for uniaxial stretches. When burst, a balloon membrane is retracting from a state of biaxial stress, so that there is significant tension parallel to the free edge. There is some evidence that this cross-strip tension can also affect the fluttering of flags, as in Chang and Moretti [2002].

This theory, however, does explain why only significant waves were seen near the free end of the membranes and strips when retracting in water. These waves were a consequence of balance between bending stresses trying to suppress transverse displacements, and centrifugal fluid loading trying to increase them. This fluid loading is given by $\rho 2bk^{-1}U^2$, so when either the density of surrounding fluid was low (retraction in air) or the flow velocity was low (retraction in glycerin), the generation mechanism for these waves was diminished. As this is an inviscid effect, we would perhaps expect glycerin to display the same behaviour as water. Yet, for the free retraction we are considering here, the speed U of the strip is closely linked to the viscosity of the surrounding fluid, and so increasing viscosity decreases U, and thus the fluid loading. For the fluids we have considered, it is water that

provides the best balance between density and viscosity for the waves to grow.

Despite the lack of directly applicable theory, measurements were made of the waves mid-way through retraction in water, including of their wavelength, amplitude, and speed relative to the strip, for three different retractions from $\lambda_0 = 6$. Waves were observable on the 30 mm near the free edge, and traveled in the direction of retraction, but slower than the strip itself (as predicted by the theory of Coene [1992]), at around 77% of the retraction speed. Wavelengths were consistently around 10 mm. The amplitudes increased from zero over time, reaching a maximum when the waves coincided with the free edge of the strip. This maximum was typically around 1.5 mm, much smaller than the wavelength, thus supporting the notion that the waves were linear.

We also noticed a significant cross-strip component to these waves. For the size of strip we were using, the maximum transverse motion was seen at the edges parallel to retraction, with little significant transverse motion near the centre. Similar behaviour was seen for retracting balloon membranes, with the waves near the free edge displaying a wavelength parallel to the free edge of order 10 mm. This, noticeably, was the same wavelength as seen for the waves on the membrane before rupture. That was no coincidence, as the restoring force for both was tension of similar strength in the membrane. Due to the biaxial stress applied before rupture, the creation of the crack only caused relaxation of the stress perpendicular to it. The stresses parallel to it therefore remained (at least in the initial stages of retraction), and thus acted as the restoring force for any transverse displacements, such as the waves near the free edge, that formed on the membrane.

5.6 Shear instability in the water

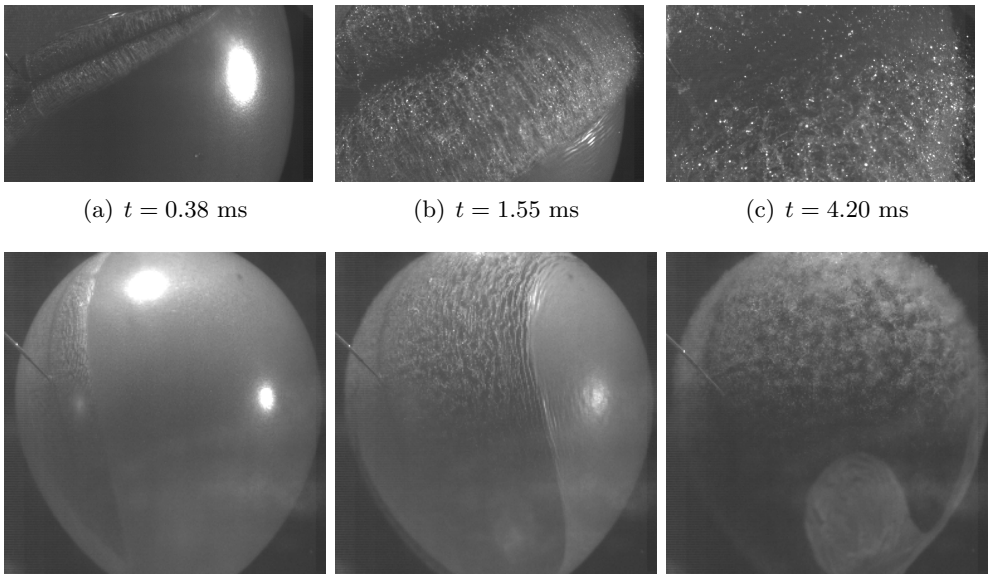

(a) $t = 0.38$ ms (b) $t = 1.55$ ms (c) $t = 4.20$ ms

(d) $t = 0.65$ ms (e) $t = 2.20$ ms (f) $t = 7.5$ ms

Figure 5.28: The wake behind a retracting water balloon membrane in air, **(a)** - **(c)**, and water, **(d)** - **(f)**. Time $t = 0$ is when the cracks started propagating.

When the balloon was ruptured, the membrane retracted rapidly. Behind it, growth of the interfacial amplitude was seen on a timescale and lengthscale less than that for the larger growth of the interfacial amplitude, as seen in figure 5.28 for both the air-water and water-water cases. Typically, wavelengths immediately following the retraction were around 1 mm, with full development of the instability taking around 1 ms. For an air-water interface, this interfacial growth was asymmetric (non-Boussinesq), with thin sheets or spikes of water penetrating into the air, angled toward the direction of membrane retraction. For the water-water interface, the growth was symmetric and so Boussinesq.

5.6.1 Flat membrane in water

As in the previous section, while no work can be found on the wake behind retracting rubber strips, much research has been published on closely related topics. We first consider the wake behind a retracting strip without waves on the free end; the effect of the fluttering will be considered in the following section.

Theory

The creation of the instability in the wake arises from the change in boundary conditions on the interface when the membrane retracts. While the membrane is retracting, the boundary condition at the interface was continuity of velocity with the membrane. Once the interface passed into the wake, the boundary conditions became continuity of velocity and shear stress between the fluids either side of the interface. The velocity condition did not lead to any change, as the velocity in both fluids was set, by the no-slip condition, by the speed of the membrane. They were therefore the same at the interface when the membrane was present, and so remained the same at the interface in the wake. However, the shear stress condition does lead to significant changes in the flow field. Assuming laminar flow, the velocity distribution in the fluid as the membrane was retracting along a water-water interface at speed U is given by Stokes solution (5.56),

$$u(z,t) = \begin{cases} U\left[1 - \operatorname{erf}\left(\frac{y}{\sqrt{4\nu t}}\right)\right] & (y > 0), \\ \\ U\left[1 - \operatorname{erf}\left(\frac{-y}{\sqrt{4\nu t}}\right)\right] & (y < 0). \end{cases} \tag{5.129}$$

The shear stress in the fluid is given by

$$\tau_{xz} = \mu u_z. \tag{5.130}$$

For the same fluid either side of the membrane, and thus with the density and viscosity the same in both fluids, the shear stress at $z = 0$ is therefore $-\rho\sqrt{\nu}U/\sqrt{\pi t}$ in the upper fluid, and $\rho\sqrt{\nu}U/\sqrt{\pi t}$ in the lower fluid. There is therefore a clear discontinuity in shear stress across the membrane (that is supported by tension in the membrane) with the shear stress on one side the negative of the shear stress on the other. In the wake, this discontinuity may no longer exist, and so due to symmetry between the upper and lower fluids, the shear stress $\tau_{xz} = 0$ at $z = 0$. By equation (5.130), this is

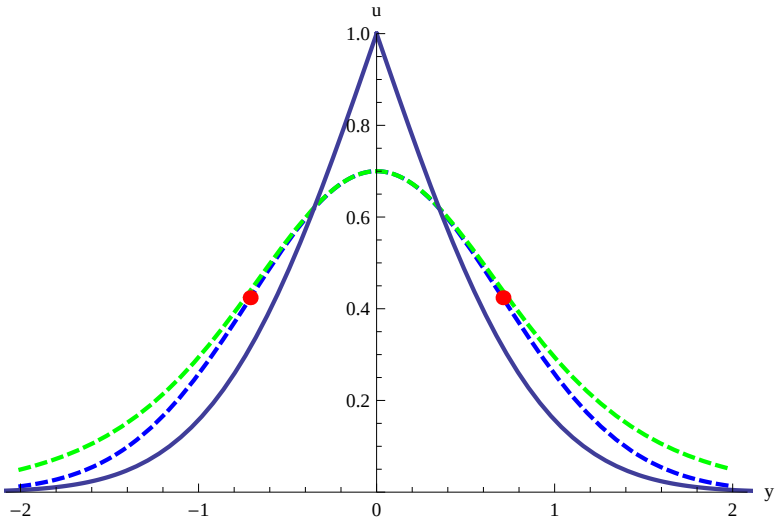

Figure 5.29: The form of the velocity profiles next to a retracting membrane (solid blue line), in a plane wake (dashed blue line), and in a plane jet (dashed green line). The red dot denotes the location of inflection points in the velocity profile for a plane wake.

then equivalent to $u_z = 0$ on $z = 0$, a distinct change from the situation when the membrane was retracting. The velocity profile therefore flattens out at $z = 0$.

In fact, the flow within a wake behind a thin plate may be solved exactly when the flow remains laminar, and shows strong similarities with a laminar plane (also known as Bickley) jet. A derivation of the flow field for both in the laminar regime is given by Ockendon and Ockendon [1995]. When the flow remains laminar, the horizontal flow in a thin plane jet aligned with the x-axis may be derived using Prandtl's boundary layer equations to be of the form

$$u(x, y, t) = Ax^{-\frac{1}{3}} \operatorname{sech}^2\left(\frac{Bz}{x^{2/3}}\right), \tag{5.131}$$

where A and B are constants depending on the viscosity, density and momentum flux. The width of the jet therefore scales with $x^{2/3}$. For a circular laminar jet, the width scales with x (see Bird et al. [2007]). The boundary layer equations may also be used to derive the flow field in a thin laminar wake,

$$u(x, y, t) = Cx^{-\frac{1}{2}} \exp\left(-\frac{Dz^2}{4x}\right), \tag{5.132}$$

with C and D constants as above. The width of the wake thus scales with $x^{1/2}$. If the flow becomes turbulent, the velocity fields obviously deviate from those given above. However, Lesieur [2008] states that, using mixing-length theory, it may be shown that the averaged behaviour still takes the same form: $\operatorname{sech}^2(z)$ for the jet, and $\exp(-z^2)$ for the wake. The plane jet width now goes like x, with the plane wake width going like $x^{1/2}$ as before.

These two flow profiles, along with that with the membrane present given by (5.56), are shown in figure 5.29. The differences between the wake and jet are small, and indeed the two situations

show similar behaviour with regards to their stability. There is no simple condition that determines whether a particular inviscid shear velocity profile is unstable, yet there are two necessary conditions as described by Lesieur [2008]: the Rayleigh inflection point condition, and the Fjortoft condition. The Rayleigh condition states that a flow may only become unstable if there exists a point $z*$ such that

$$u_{zz}(z*) = 0. \tag{5.133}$$

This is equivalent to saying that the velocity u must have an inflection point somewhere. The classic inviscid shear-flow instability, Kelvin-Helmholtz, has a typical velocity profile of the form $u \sim \tanh(z)$, so that there is one inflection point at $z = 0$. For the plane jet and wake, consideration of the velocity profiles (5.131) and (5.132) depicted in figure 5.29 reveals that both velocity profiles have two inflection points, one either side of $z = 0$. This suggests a tendency to become unstable. The flow field during retraction can be seen not to have any inflection points, however, showing that it must be stable to shear instabilities and explaining why flow instability only occurs in the wake.

The second necessary condition, the Fjortoft condition, is stronger. It states that for a shear flow to become unstable, there must exist a point $\tilde{z}$ within the flow such that

$$u_{zz}(\tilde{z})[u(\tilde{z} - u(z*)] < 0, \tag{5.134}$$

where $z*$ is, as above, the location of an inflection point in the velocity. While not straightforward, it may be shown that this condition is satisfied almost everywhere within the plane jet and wake.

The plane jet and wake velocity profiles thus satisfy the necessary conditions to become unstable. That the plane jet is theoretically unstable was shown by Sato [1960], with the plane wake later shown by Sato and Kuriki [1961] to follow the same behaviour. Experimental evidence of the wake instability was found by Taneda [1958]. In both cases, the dominant mode of the instability is that of asymmetric sinuous deformations to the wake path (see figure 5.30), that soon break down into patches of alternating sign vorticity that form a von Karman vortex street. This breakdown occurs because of velocity-induction effects, due to velocity differences across the wake. For a deformation in the positive z direction, the flow nearer $z = 0$ will be moving faster in the negative x direction than will that further out. This will then cause the wake to roll-up clockwise, creating negative vorticity. The opposite will occur for deformations below $z = 0$, and thus positively-signed vorticity will be created. This is in contrast to classical Kelvin-Helmholtz instability, where there is only one turning point in the velocity profile, and so only vorticity of one sign is created. As the deformations are out-of-phase (see figure 5.30 **(a)**), the patches of different sign will also be out-of-phase. This arrangement is shown in figure 5.30 **(b)**, along with the consequent flow field. This diagram implies flow out of the plane of the wake, angled toward the plate - much as was seen for the wake behind our retracting membranes. These vortex patches will be advected with the flow, but as the outer flow is stationary here, they remain approximately stationary in the laboratory flow (though not in the frame of the membrane). Later on, as found by Sato and Kuriki [1961], the flow becomes three-dimensional and fully turbulent.

The wavelength of the sinusoidal perturbations to a plane jet must be found numerically, and is given by Lesieur [2008] to be

$$\lambda \approx 6.54\delta, \tag{5.135}$$

where δ is the half-width of the jet. Similarly, the work of Sato and Kuriki [1961] suggests a wavelength around 7.55δ for a plane wake. However, as will be discussed in section 5.6.2, the wavelength will

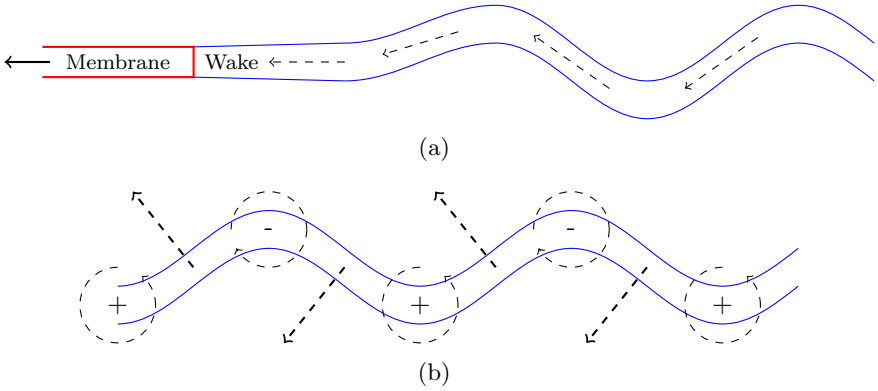

Figure 5.30: Diagram depicting instability in the wake behind a retracting thin plate. The edge of the wake is given by the blue line, and the direction of flow by the dashed black lines. In **(a)**, sinusoidal waves begin to form in the wake. Later on, **(b)** shows the development of alternately signed vortex patches from the sinusoidal perturbations, and consequent flow field.

change as it passes along the wake, as the wake itself decelerates due to the surrounding fluid. It is thus wrong to consider a single wavelength for this perturbation. Nevertheless, we would expect the value $\lambda \approx 8\delta$ to be approximately accurate when the waves first form.

Experiments

To examine the flow field created in the wake of our retracting strips, we may use the PIV experiments of section 5.4.2 for both water and glycerin. Sample flow fields are shown in figure 5.31 for the light sheet directed onto the centre of the strip, thus where the free edge waves were minimal in amplitude. For water, the wake was initially laminar, symmetric and Gaussian, as predicted by equation (5.132). The velocity field, averaged over the visible length of the wake, is shown in figure 5.32, along with a fitted Gaussian, to which the agreement is excellent. Almost immediately, the wake began to show evidence of the asymmetric instability described previously. Measurements were made of the wavelength of the instability in the wake. As shall be discussed in the following section, there was not a unique wavelength, as the deceleration of the mean flow over time stretched out the wake, and so increased the wavelength. For an initial stretch of $\lambda_0 = 6$, the initial wavelength was 3.64 mm, with half-thickness of the wake, as determined by fitting a Gaussian to the velocity profile, at 1.1 mm. We therefore found $\lambda = 3.3\delta$, similar to the theory derived above. Patches of alternating sign vorticity were then formed, with the flow field similar to that depicted in figure 5.30 with out-of-plane flow angled towards the membrane. The vortex patches themselves remained approximately stationary. Eventually, the patches of vortices interacted and deformed, and the flow became fully turbulent.

5.6.2 Membrane on air/water interface

As was demonstrated in the previous chapter, the differences between flow near a free-surface and a fluid-fluid interface can be significant. Figure 5.28 shows this to be the case for the shear instability too, with the asymmetric behaviour on an air/water interface indicative of a non-Boussinesq flow, where

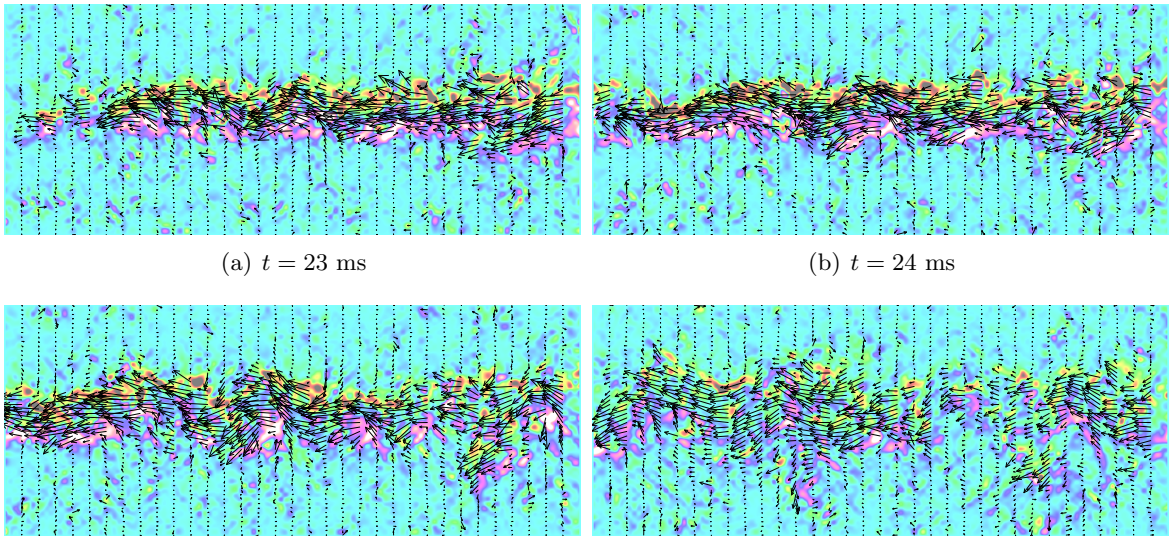

(a) $t = 23$ ms (b) $t = 24$ ms

(c) $t = 26$ ms (d) $t = 33$ ms

Figure 5.31: The results of PIV on a retracting strip in water. The field of view was approximately 50 mm by 20 mm, and the strip was released at $t = 0$ ms. Image **(a)** shows the wake as initially approximately laminar and symmetric, though 1 ms later in **(b)** there was evidence of sinusoidal asymmetry. Image **(c)** shows this instability being amplified over time. Eventually, this instability lead to the wake becoming fully turbulent, as shown in **(d)**.

the difference in densities between the phases is important, despite the influence of gravity being insignificant. The surface tension at an air/water interface may also act to stabilize the interface, suppressing or slowing the growth of waves of short wavelengths; it clearly plays a role at late times, when the sheets ejected from the water's surface break up into droplets. Differences in viscosity and density between the phases will also affect the flow profile in the wake, so that it is less obvious that it is Gaussian.

However, despite the visual and quantitative differences, the generation mechanism for the interfacial instability is the same: the change in shear stress condition at the interface. The shear stress in the water will be the same as for the water/water case while the membrane retracts, and thus have an error function profile. In the wake, the effect of the air on the water will be negligible due to its much lower density. In the limit of the density of one fluid going to zero, the interfacial conditions on the other phase reduce to those for a free surface (continuity of velocity will still hold, but tell us nothing about flow in the water), for which the shear stress condition is $\tau_{xz} = 0$ on $z = 0$. For the water-water case, symmetry between the upper and lower fluids reduced the condition of continuity of shear stress to the same thing. We would therefore expect the flow in the water of an air/water wake to have a similar form to the Gaussian profile seen in a water/water wake. In particular, having $u \neq 0$, $u_z = 0$ at $z = 0$ and error function-like flow away from the interface necessitates the presence of an inflection point somewhere in the velocity profile. The flow in the water behind a membrane retracting across an air/water interface therefore satisfies at least the Rayleigh inflection-point theorem (and, due to similarities with the water/water case, likely the Fjortoft condition too) and so is likely to be unstable.

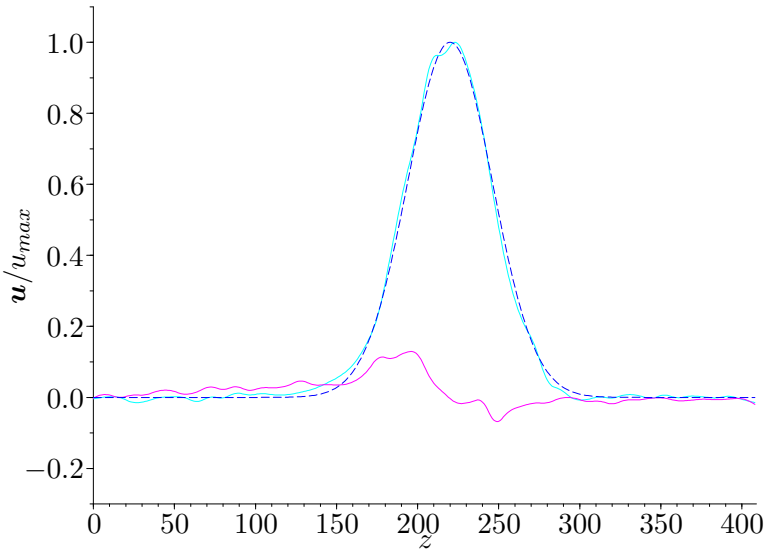

Figure 5.32: The horizontal (cyan) and vertical (magenta) velocity fields averaged over the length of the visible wake in figure 5.31(a). The dashed blue line represents a fitted Gaussian curve, the shape predicted by (5.132).

Performing experiments on the retraction of a membrane across an air/water interface are more difficult than those on a water interface. Instead of simply submerging the whole apparatus underwater, the strip must be aligned with an existing air/water interface. Though far from impossible, this added difficulty meant that we did not perform any such experiments ourselves.

As for the other membrane retraction phenomena, no work appears to have been published on this exact problem. However, the strong similarities between a wake and jet suggest consideration of a situation on which a significant amount of work has been done: the high-speed flow of a laminar water jet discharging from a nozzle into air. Hoyt and Taylor [1977] were among the first the study this situation. They found that the jet was initially smooth, before axisymmetric instability waves appeared within a single jet diameter of the nozzle exit. As the flow is high-speed, this is not an example of Rayleigh-Plateau instability, surface tension playing no significant role - the instability in fact causes the surface area to increase, rather than decrease, and so surface tension is probably stabilizing. The instability waves were then amplified further downstream, culminating in the ejection of spray droplets. Though not discussed explicitly, their experimental images also appear to show the interfacial growths angled towards the nozzle. It is these stages that are clearly analogous to the spray ejected behind a membrane retracting across an air/water interface. The water jets then underwent a helical instability due to drag between the air and water that appears not to have any relation to what we are interested in here.

The growth of the axisymmetric waves and consequent instability of the air/water surface was considered in more detail theoretically by Portillo and Blaisdell [2006], and experimentally by Portillo et al. [2011]. Portillo and Blaisdell [2006] found that the most unstable modes are initially amplified in a region of absolute instability near the nozzle exit, that is a region where the waves may travel both

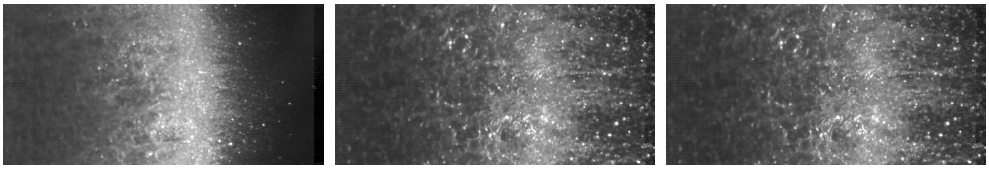

(a) $t = 3$ ms (b) $t = 6$ ms (c) $t = 20$ ms

Figure 5.33: The late-time development of the shear instability on an air/water interface.

directions along the jet. They only grow significantly and become visible once they continue down the jet into a region of convective instability - a region where the instability waves are convected with the flow. Thus the waves seen on the jet move with the mean flow of the jet. Portillo et al. [2011] studied experimentally flow out of a tube of diameter 6.35 mm. The relevant Reynolds number was defined to be $Re = U\delta_m/\nu$ where U was the mean flow speed and $\delta_m = 0.664\sqrt{\nu L/U}$, the momentum thickness of the wall boundary layer at the tube exit. As this itself was set by the flow speed, defining the speed defined the Reynolds number, and vice versa. They considered mean flow at speeds of between 10 and 40 m/s, the same range of velocities (and hence Reynolds numbers) as seen for retracting balloon membranes. They found the waves being stretched as they convected downstream, the wavelength increasing, as the speed of the surface was accelerated by the mean flow downstream. The wavelengths all lay in the range 0.25 mm to 0.9 mm, similar to the wavelengths we observed behind retracting balloon membranes. These waves were so small that the authors argued that the diameter of the jet was irrelevant. They were also found to scale with the momentum thickness δ_m and so inversely with the Reynolds number and mean flow velocity. Though the relation was not linear, the wavelengths could be approximated by

$$\lambda = 30\delta_m. \tag{5.136}$$

We note here that this is significantly (around four times) larger than that predicted for a laminar wake on a water/water interface.

Though it proved difficult to do a systematic study of retracting membranes on an air/water interface, we can at least compare this prediction with rough measurements of the wavelengths of the shear instabilities seen behind membranes on burst water balloons. Based on section 5.4, for water $\delta_m \approx 0.03$ mm and thus equation (5.136) predicts $\lambda \approx 1$ mm. This is of a similar order to the waves seen experimentally on bursting balloons, but drawing any deeper conclusions is not possible due to the high degree of error in our measurements. We could also see that the interfacial growths were angled towards the retracting membrane, much as those on jets were angled towards the nozzle. The changing speed of the membrane, together with spray droplets obscuring the interface, also made it impossible to determine the wavelength at later times. In particular, we expect the stationary flow away from the interface decelerated the wake, causing the wavelengths to lengthen over time. However it was not possible to tell whether this did actually occur.

The above discussion focused on the initial formation of the shear instability. However, the late-time behaviour is also shown in figure 5.28. In water, as there is no density difference between the fluids, the growth remained symmetric at all times, with non-linearity leading to a region of turbulence forming near the interface. In air, however, the behaviour was significantly different, as shown in figure 5.33. At later times, the behaviour became highly non-linear, as the amplitude of the

interfacial perturbations grew far larger than their wavelength. At this point, surface tension began to play a role. Previously, surface tension has been neglected, as it was insignificant at early times compared to shear with the retracting membrane and consequent inertia in the water. However, at late times did it become important, smoothing the interface and causing the growths in interfacial amplitude to become unstable (as a result of Rayleigh-Plateau instability) and separate into droplets. It is these droplets that caused the 'spray' typically associated with bursting stationary balloons. Once the growths became completely unstable and had broken up, surface tension then returned the interface to approximately its pre-burst shape.

How far down the jet the waves first appear also varied for Portillo et al. [2011] depending on the momentum thickness, but lay between 2 and 6 mm. For our bursting balloons, however, waves appeared immediately behind the retracting membranes. The reason for this was the flapping of the membrane, the effect of which will be discussed in the next section.

5.6.3 Wake behind a flapping membrane in water

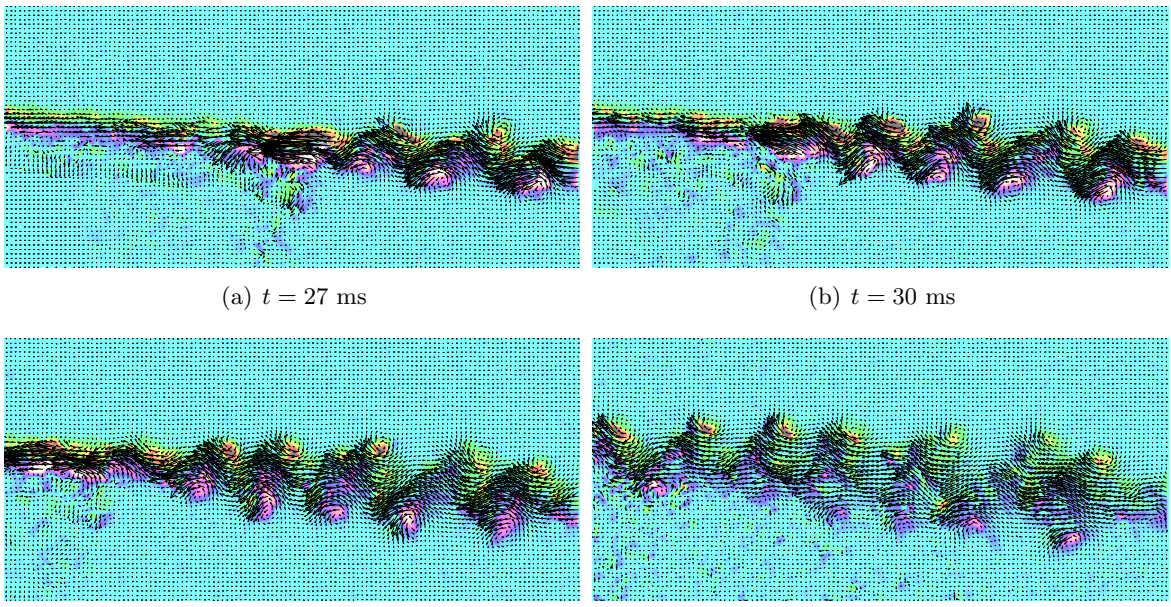

(a) $t = 27$ ms (b) $t = 30$ ms

(c) $t = 33$ ms (d) $t = 43$ ms

Figure 5.34: The effect of flapping on the wake behind a retracting rubber strip in water. As before, the arrows represent the flow field, the colours vorticity, with the field of view approximately 50 mm by 20 mm, and the strip released at $t = 0$ ms. The end of the strip is half way across the field of view in **(a)**.

It was demonstrated in section 5.5 that small waves were created on retracting balloon membranes near their free edge. These waves were also seen on retracting rubber strips in water, with maximum amplitude near the edges of the strip. The PIV experiments of section 5.4.2 may be used to determine the influence of the waves on the flow in the wake, by aligning the light sheet near one edge. Typical results are shown in figure 5.34. They reveal that the edge waves had a clear influence on the flow in

the wake: the wake was now immediately unstable, rolling up into discrete patches of alternating-sign vorticity whose average separation was half the wavelength of the waves on the membrane, and whose radius was of similar order to the boundary layer thickness. The flow field then created was of the same form as for the plane wake after breaking down, shown in figure 5.29, with fluid in the wake being pushed out-of-plane and in the direction of the membrane. This was therefore another driving mechanism for the instability seen in the wake of retracting balloon membranes. The flow then later became fully turbulence before any other coherent behaviour was observed. As argued in the previous section, the fact that waves were seen in the wake immediately behind the membrane suggests that they were caused by its flapping. The wavelength of the waves in the wake caused by flapping of the membrane was measured at 5.3 mm for a wake of thickness 1.6 mm, and thus almost double the wavelength seen without flapping.

Similar behaviour was observed by Zhang et al. [2000], who studied the 2D flow around thin filaments fixed in a moving soap film. They observed the same stationary, flapping, and chaotic behaviours for flags as observed by other authors, but also had the ability to observe the flow around the filament and in its wake. When the flow speed was low, the filament remained stretched straight and parallel with the flow. Vortices of alternating sign were shed from the trailing edge of the filament, forming a narrow von Karman vortex street. These vortices began to form within a couple of wake-thicknesses of the free edge. Their typical radius was the same as the boundary layer thickness. At higher flow speeds, when the filament began to flutter, the amplitude of the oscillations was far larger than the wake thickness. Vortices of the same size as before were shed from the free end, but now their sign depended on the phase of the wave on the filament. For half the period of the flapping, vortices of one sign were shed, and for the other half-period, vortices of the alternate sign were shed. This shows a clear connection with what we have observed for the wake behind a flapping, retracting strip: the sign of vorticity shed depended on the phase of the wave near the free-edge, with it changing every half-period. For the flapping filament, a row of similarly-signed vortices was shed, as the amplitude of flapping was much thicker than the boundary layer. For the retracting membranes, as the amplitude of the waves was of the same order as the boundary layer thickness, the vorticity shed each half wavelength rolled up into a single patch of vorticity. This notion of the shed vorticity having the same frequency as the waves near the free edge was also used by Argentina and Mahadevan [2005] in their investigation of fluttering flags, whose theoretical results showed good agreement with experiments.

As waves were observed near the free edge on all our retracting balloon membranes, it therefore seems that it was these waves that drove the shear instability, rather than an instability in the wake itself. However, we showed in the previous section that even without this flapping, we would expect some kind of shear instability, of a similar wavelength and behaviour. These two situations, flapping near the free end and instability in the wake, were closely related: both were, ultimately, forms of shear-driven inviscid instability. In both cases, there was a thin fast-moving region (the membrane and the wake, respectively) within a stationary outer fluid, and it was the difference in momentum between the two that caused waves to form. Any perturbations to the shape of this thin region created centrifugal forces that acted to amplify the disturbance, leading to instability. This connection between the flapping of a flag and inviscid shear instability has been noted by many authors before, such as Argentina and Mahadevan [2005]. The two situations were not identical, of course: the flow fields within the central viscous boundary layers were similar but different (error function and Gaussian, respectively), and where the membrane was present, tension and bending stiffness modulated the

growth of the instability. For a perfectly rigid membrane (a flat plate), no flutter would occur, so the instability only begins in the wake. For our membranes, the tension decreased to zero at the free end, and the bending stiffness was very small. Consequently, there was a region on the membrane near the free end where, as for a flag, forces within the membrane were not great enough to stop the shear instability causing transverse growth.

As discussed in previous sections, we were not able to obtain a good model for the waves near the free end of the membrane, due to our lack of knowledge of the stress-strain relationship in the rubber. However, we can use the parallel with the shear instability discussed above to estimate at least the order of wavelength. In both cases, while the ultimate instability mechanism is inviscid, it arises due to flow profiles of viscous origin. The lengthscale for both flow profiles, whether the instability starts on the strip or in the wake, is set by the boundary layer thickness, that itself depends on the fluid viscosity and retraction speed (that are both approximately independent of whether flapping occurs or not). Consequently, the lengthscale driving the shear instability in the wake in both cases is the same (the boundary layer thickness), so we would expect the instability length scales to be of similar order. Indeed, as discussed above, while the wavelength was larger with flapping, it was of a similar order to that seen without flapping.

This flapping of the membrane is also likely to be responsible for the significant drag on the free end detected in section 5.4. It is clear from figure 5.34 that the flapping has a significant impact on the wake, imparting significant momentum to it, while the effect of a flag flapping has been noted by other authors, including Taneda [1968], Carruthers and Filippone [2005], and Morris-Thomas and Steen [2009], to increase the drag significantly.

5.6.4 Effect of high viscosity

The PIV experiments in glycerin did not show evidence of instability in the wake. As discussed previously, no waves were seen near the free edge of the membrane, and the high viscosity of the glycerin caused all motion to decay away before instability of the wake itself could occur. Instead, the velocity profile of the wake was laminar and Gaussian, as shown in figure 5.35, for all time, while decaying rapidly. Note that we may estimate the width of the wake by assuming it is the same as the width of the two boundary layers at the free end of the strip. As given by the Stokes solution, equation (5.56), the half-width δ for the wake shown in figure 5.35 should therefore be

$$\delta \approx \sqrt{4\nu t} \approx 20\text{mm}, \tag{5.137}$$

where t was the time taken from release until the end of the strip reached the centre of the field of view. This is in excellent agreement with the wake width shown in figure 5.35, though given that this was only a very rough approximation, we may only be sure that the experiment and theory are of similar order.

Some insight into the effect of viscosity on the wake may be gleaned from the work of Soto and Belmonte [2009]. In their paper, they show images of air-filled balloons bursting when submerged in three different fluids: acetone of dynamic viscosity 0.3 Pa s, water of dynamic viscosity 1 mPa s, and oil of dynamic viscosity 89 mPa s that, while large, is significantly less than the viscosity of glycerin used in our experiments. As the authors themselves remarked, the effect of increasing viscosity is to make the wake 'smoother', and while it is impossible to know the amplitude of the surface deformations

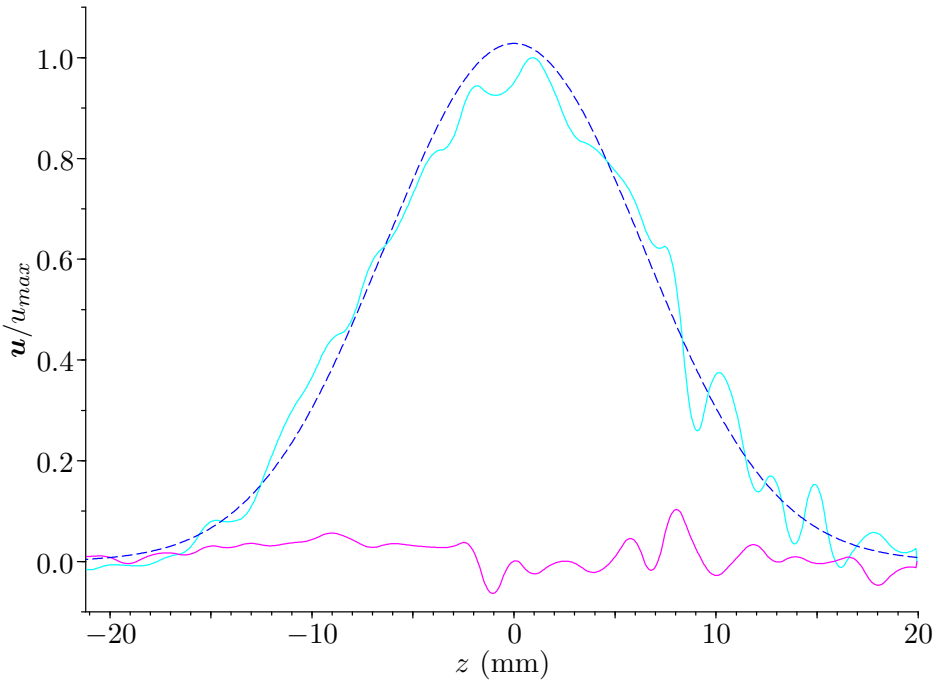

Figure 5.35: For a strip retracting from $\lambda_0 = 6$ in glycerin, the graph shows the distribution of tangential (cyan) and perpendicular (magenta) velocities, relative to the motion of the strip, for a single (unaveraged) cross-section. The blue line shows the best-fit Gaussian for the tangential velocity u.

in their images, that effect of increasing viscosity does appear to increase their wavelength to around 5 mm. From the work of Portillo et al. [2011], the wavelength of these instability waves was shown to scale with the momentum thickness as $\lambda \approx 30\delta_m$. For the data given by Soto and Belmonte [2009] for oil, we estimate the momentum thickness to be 0.35 mm and thus the predicted wavelength as 10 mm, of the same order as that observed in the experiments of Soto and Belmonte [2009]. Unfortunately, it is impossible to tell from the images of Soto and Belmonte [2009] whether any flapping of the membrane occurred for the retraction of oil, nor is any mention made of it for any case, including water, in the text. Consequently, it is not possible for us to say how the flapping of the membrane may affect the instability of a viscous wake, if it occurred at all.

5.7 Buckling of the membrane

Whatever the fluid outside the membrane, once it had fully retracted, transverse waves spread fully across the membrane over a very short period of time relative to the total time of retraction. Examples of these waves are shown in figure 5.36 for both a strip and a balloon membrane in water. Images of a strip buckling in air were given in figure 5.12.

The waves were an example of what is known as buckling, where negative tension (compression)

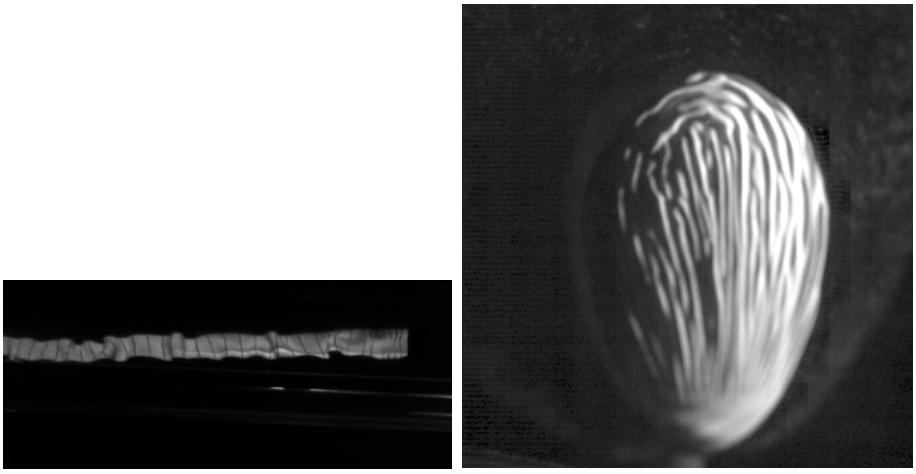

(a) Strip (b) Balloon

Figure 5.36: The buckling of retracting membranes in water after retraction.

in the direction of retraction is balanced by bending forces. The negative tension arose in a retracting strip or membrane due to the strip's inertia causing it to continue moving in the direction of retraction once fully relaxed. The material then became compressed compared to its reference state, and thus experienced negative stresses. As the membranes were thin, they could not support significant compressive stresses, and thus deformed out-of-plane. This was different from the flutter waves seen nearing the free edge of retracting membranes, where fluid loading was balanced by tension and bending forces. That these waves were examples of buckling and not fluttering is suggested by the fact they spread over the whole membrane, including near the fixed end where the membrane speed was always zero. There was thus little to no fluid loading there, and yet waves were still observed. That said, once buckling began, no obvious change in behaviour near the free edge was observed. The flutter waves appeared to persist, only increasing in amplitude. This was likely because the true buckling waves had a similar wavelength to the flutter waves, thus the flutter waves became buckling waves without a noticeable change in behaviour.

The nature of these transverse waves may be determined mathematically. As discussed both in chapter 2 and section 5.5, the relevant equation of motion for linear transverse displacement c (as given by Vermorel et al. [2007] based on the Euler-Bernoulli hypotheses) is

$$\rho bh\frac{\partial^2 c}{\partial t^2} = \frac{\partial}{\partial x}\left(T\frac{\partial c}{\partial x}\right) - \frac{Ebh^3}{12}\frac{\partial^4 c}{\partial x^4}, \tag{5.138}$$

where T is the tension, E the Young's modulus, b the width of the strip and h the thickness. Supposing a wave-like solution of the form $c(x,t) = c_0\exp(i[kx - \omega t])$ and that T is constant, the dispersion relation is

$$\omega^2 = \frac{Eh^2}{12\rho}k^2\left[k^2 + \frac{12T}{Ebh^3}\right]. \tag{5.139}$$

When $T < 0$, there exits a range of wavenumbers for which ω is imaginary, and thus for which the amplitude of the waves grows exponentially. For a thin rod retracting from a small (and thus

linear) initial strain ϵ_0, Vermorel et al. [2007] found the most amplified waves, those that have the largest growth rate. As it is these wave that grow fastest, it is they that dominate the out-of-plane waves seen on strips buckling from a linear initial stretch. This analysis they based on linear theory to predict the stress-strain behaviour. As noted in section 5.4, linear theory for a retracting strip predicts a stress wave to travel down the strip at constant speed, behind which the material is fully retracted. Once the wave reaches the fixed end, it reflects. Behind this reflected wave, the material is in uniform compression, with strain given by $-\epsilon_0/(1+\epsilon_0)$ and tension given by $T = -Ebh\epsilon_0/(1+\epsilon_0)$. To determine the buckling behaviour, they assumed that the growth-rate was small enough relative to the wave speed, so that the wave front had traveled at least one wavelength from the fixed end before significant growth could occur. Under these assumptions, the most amplified wave had wavelength

$$\lambda = \pi h \sqrt{\frac{2}{3}} \sqrt{\frac{1+\epsilon_0}{\epsilon_0}}, \tag{5.140}$$

notably independent of E (a consequence of the compressive stress T depending linearly on E). The growth rate for these waves is given by

$$\sigma = \sqrt{3} \frac{\epsilon_0}{1+\epsilon_0} \frac{c_{ql}}{h}, \tag{5.141}$$

where c_{ql} is the quasi-longitudinal wave speed of the material. It is therefore clear the role that the thickness h plays: increasing h means increasing the wavelength but decreasing the growth rate. Thus, transverse waves will grow whatever the thickness of the strip, but it will happen slower the thicker the strip is.

In terms of the initial stretch ϵ, for $\epsilon = 0$, $\lambda \to \infty$ but $\sigma = 0$. As ϵ increases, so does the growth-rate while the wavelength decreases. If we naively (neglecting all the evidence of non-linear stress-strain behaviour) use equation (5.141) to predict the buckling wavelength λ of our most stretched-strips ($\epsilon = 5$) retracting in air, it estimates $\lambda = 0.4$ mm. However, Vermorel et al. [2007] noted that, even if the stress-strain behaviour were to remain linear at such a high initial stretch, their model would no longer be valid as it relied upon the assumption that $kh \ll 1$; for an initial stretch of $\epsilon = 5$, $kh = 2.2$. In fact, Vermorel et al. [2007] found equation (5.141) to be inaccurate for initial stretches above 0.3, as then the growth-rate of the waves was of similar order to the wave speed. In this case, the wave has not traveled at least one half-wavelength before significant growth occurs, causing the wavelengths observed experimentally to be shorter than predicted.

Vermorel et al. [2007] also modeled the effect of a surrounding fluid of non-negligible density and viscosity on the buckling strip. The dispersion relation for the buckling waves was derived from the linear Navier-Stokes equations as in chapter 4, coupled with the Euler-Bernoulli model for the strip, as in equation (5.138). The dispersion relation was

$$\left(\rho_m bh + 2\frac{\rho_f b}{k}\right)\omega^2 + 2b\mu\left(k + \sqrt{k^2 + \frac{\rho_f \omega}{\mu}}\right)\omega + \frac{Ebh^3}{12}k^4 - Tk^2 = 0. \tag{5.142}$$

In comparison to the dispersion relation for the waves near the free edge given by equation (5.120), equation (5.142) includes terms related to the fluid's viscosity, but neglects those related to the mean flow U. The authors solved this equation numerically, and found that the external fluid had only a limited effect on the wavelength, the added mass effect tending to increase the wavenumber by a

small amount. However, the added mass effect did significantly reduce the growth rate, by a factor of 1.6 for water, and 2 for the more viscous glycerol. Note that these differences were almost entirely a consequence of the increased density of fluid surrounding the strip (glycerol being denser than water); the influence of the increased viscosity was negligible. They did find in their experiments that the buckling wavelength increased significantly for retraction in more viscous fluid, but ascribed this to the drag of the fluid on the strip during retraction. As described in section 5.4.2, the external fluid slowed the strip down and made the stress conditions in the strip non-uniform. However, there still existed a clear stress wave front, with buckling starting when it reached the fixed end as before. By assuming the stress profile was linear behind the front, and that buckling began only when the reflected wavefront reached half the wavelength selected for buckling, they derived the estimate

$$\lambda = 2\left[\frac{\pi^2 h^2 l}{12\epsilon}\right]^{1/3}. \tag{5.143}$$

The wavelength thus scaled with $\epsilon^{-1/3}$, a prediction which matched their experimental observations of linear retractions in glycerol.

Unfortunately, the nature of these buckling waves make them very difficult to model for strips retracting from large initial stretches. As we are considering faster retractions, we could include the fluid loading terms, that would lead to a correction in the most unstable wavelength. However, that would require accurate knowledge of the strip velocity U, which we do not have. The dispersive nature of the retraction also meant that the strip velocity was not uniform along the strip. The fluid loading and hence the linear estimate of the buckling wavelength would therefore vary along the strip. This, in itself, is possible to calculate, and possible to measure on our buckled strips. The larger problem, as before, is that these buckling waves arise from a balance between bending and tension, and thus knowledge of the stress state of the rubber at the moment of buckling is essential to model the behaviour. We cannot use the work of Vermorel et al. [2007], as they were considering retraction from small initial stretches, and thus where the stress-strain behaviour was linear and there were clear stress wave fronts traveling at finite speed. For a disperse non-linear retraction, there were not two separate regions of constant stress, but instead the stress everywhere on the strip would be varying both in time and space, as predicted by equation 5.77. The situation was thus qualitatively, as well as quantitatively, different. Added to this, it has been shown by Niemczura and Ravi-Chandar [2011c] that the stress at any given time depends on the strain history for dynamic retraction. Thus, even if we were to assume that the stress-strain relation was linear when buckling occurred, it is not clear what the correct Young's modulus would be. It would likely vary depending on the initial stretch, and even the amount of drag during retraction.

There are other complications when considering buckling after retraction from non-linear stretches. While it was noted above that the stress during buckling is difficult to determine, the same is true for the strain. In the linear model of Vermorel et al. [2007], buckling begins once the elastic strain, and hence stress, reaches zero. However, it was revealed in chapters 1 and 2 that for retraction from non-linear initial stretches, the material reached a state of zero stress before the strain returns to its pre-stretch level. This phenomenon was due to the viscoelasticity of rubber, as the viscous component of the strain relaxed over a far longer timescale than the elastic component. The exact strain when the elastic stress reached zero depended on the strain history of the material, and was as high as 100 %. Consequently, accurately determining even the strain at which buckling occurs was difficult.

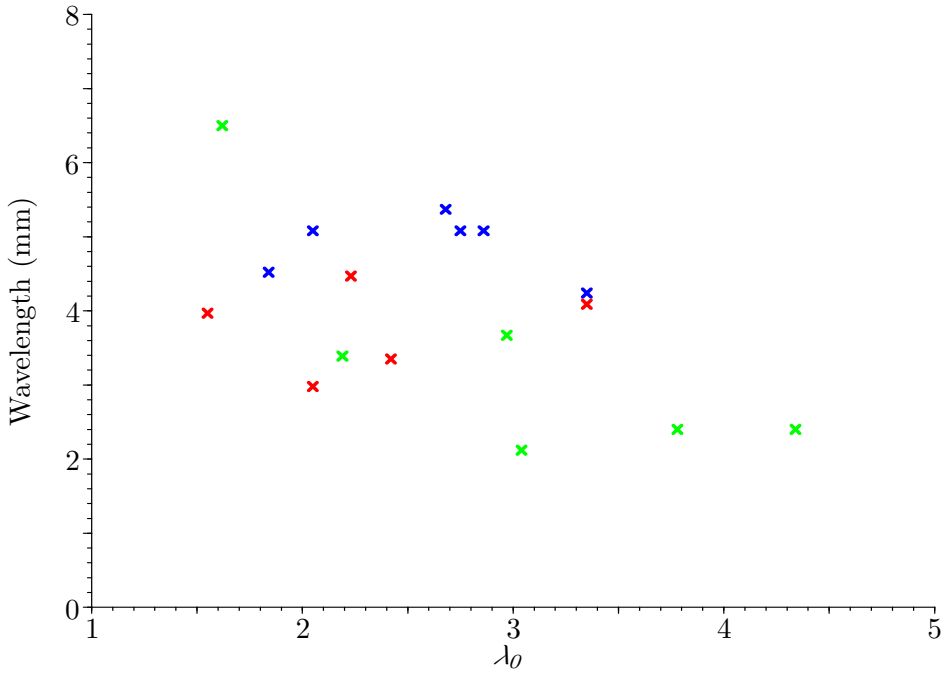

Figure 5.37: The buckling wavelength for rubber strips retracting from a range of initial stretches. The green marks are for retractions in air, blue for retractions in water, and red for retractions in glycerin.

Experimental measurements of buckling wavelength for strips retracting in air, water, and glycerin plotted against their initial stretch are given in figure 5.37. We note here that we are only considering, both theoretically and experimentally, the first buckling waves that appear. It was observed both by ourselves and by Vermorel et al. [2007] that after the initial waves formed, the axial stress then relaxed as the wavelength increased. For retractions in air, the wavelength did appear to decrease with increasing initial stretch, though not linearly. For retractions in water and glycerin, however, the buckling wavelength appeared to be independent of initial stretch, being around 4.5 mm in both cases. This similarity in behaviour was likely due to dispersion in the strip's motion during retraction meaning that by the late time at which buckling occurred, any effects of the initial conditions had, to a large extent, been lost. Note that the wavelengths for the buckling waves were comparable to those seen for the waves on the free edge during retraction, suggesting that bending stiffness did play a role for the waves near the free edge.

The models of Vermorel et al. [2007] predict the first buckling to occur near the fixed end of the strip, and this was indeed what they observed for linear retractions in all surrounding fluids. However, the first buckling waves for non-linear retractions in air were shown in section 5.4.1 to occur near the centre of the strip. For retractions in water and glycerin, the first buckling usually occurred near the centre of the strip, though its location varied. Once the first wave had formed, they spread quickly over membrane, taking around 1 ms to spread over the whole membrane. This was far faster than

the quasi-longitudinal wave speed c_{ql} as predicted by linear theory (where the waves form behind the reflected wave front traveling at c_{ql}), as the disperse nature of non-linear retraction in water and glycerin meant that the whole strip entered compression almost simultaneously. Unlike linear retractions, the material away from the fixed end did not need to wait so long for the reflected wave front to arrive, as the slow speed of the material in comparison to that of the stress waves meant it had already arrived during retraction. All the strip therefore already 'knew' about the fixed end by the time the strip had fully retracted, so experienced compressive stress simultaneously with the rest of the material.

5.8 Summary

In this chapter, we have examined the behaviour of rubber membranes during retraction as a water balloon burst, and the consequent creation of a shear instability on the interface, as revealed in section 5.1. In contrast to the quasi-static theory of rubber discussed in chapter 2, the dynamic theory of rubber was introduced in section 5.2, as a background to the following discussions. Retraction of the membrane began after a crack had propagated through it, a phenomenon discussed in section 5.3, where it was shown that the speeds of the cracks exceeded the predictions of linear theory, but were in line with the work of others on cracks in non-linearly stretched rubber. The movement of the membrane itself was examined in section 5.4, where both the non-linear initial stretch and drag from the water on the membrane were shown to introduce significant dispersion. This drag was shown to result from both skin friction with a (probably) laminar boundary layer, and form drag on the free end associated with the appearance of transverse waves. These waves were explored in more detail in section 5.5, and shown to arise due to lift exerted on the membrane by the surrounding water, in much the same way that flags flutter. Section 5.6 dealt with the wake behind the retracting membrane, where the shear instability occurred. Whether transverse waves appeared on the membrane or not, an instability would appear on the surface. This instability was an inviscid shear instability that ultimately derived from the velocity difference between the wake and the stationary surrounding fluid, and led to vorticity in the wake rolling up into patches of alternating sign, before breaking down into turbulence. Waves on the membrane appeared only to enhance this process. Finally, section 5.7 discussed the transverse waves that appeared on the membrane once it had fully retracted. These waves were buckling waves, as the thinness of the membrane meant that it could not support the compressive stresses created by the inertia of the strip. The wavelength of these buckling waves was shown to be same for a range of retractions in air or water, likely due to the dispersive effects of non-linearity and drag on retraction.

Chapter 6

Late-time growth

In this chapter, we consider the late-time growth of the interfacial amplitude seen when a balloon bursts with waves present on the membrane. The experimental method outlined in chapter 4 is used again, only now with the membrane eventually ruptured. Experimental observations of the phenomenon are described, and we explain why this interfacial growth may be regarded as closely related to the Richtmyer-Meshkov mechanism (RMM), one that may occur even with no density difference between the phases. An analytical model is derived to model the non-linear stages of growth for the zero Atwood number (water/water) case. This, together with a basic numerical simulation, is then matched to experimental measurements, before reasons for the discrepancies are explored.

6.1 Experimental method

The same experimental method as that detailed in section 4.1 was used pre-burst. To study the post-rupture behaviour, the membrane was oscillated for at least 1 s to allow a regular pattern of standing waves to form, before a long pin was pushed through the membrane at a point along the radial plane normal to the camera's axis, and at approximately $\phi = \pi/4$. The membrane would then retract rapidly, allowing the interfacial growth to occur. As we wished to measure the growth of the interfacial amplitude without influence from the retracting balloon, and as the camera was set up horizontally level with the centre of the balloon, the results of any experiments for which the crack was not vertical were discarded. This constituted approximately a quarter of the experiments run. PIV was also performed as described in chapter 4. In all experiments used to examine the late-time growth, the camera was operated at either 2000 fps or 5400 fps.

6.2 Qualitative experimental results

The late-time growth of the interfacial amplitude was discussed in both chapter 1 and 3, in relation to the bursting of water balloons dropped in air. Then, significant growth occurred only when capillary-like waves were present on the interface at the moment of rupture. The growth developed over approximately one-twentieth of a second, with wavelength the same as that of the waves present at the moment of rupture. The growth soon lost symmetry between the phases, taking the form of thin,

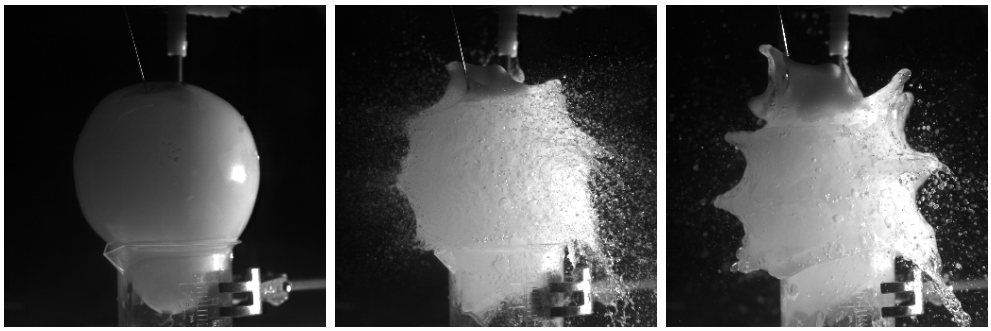

(a) $t = 0$ ms (b) $t = 17$ ms (c) $t = 53$ ms

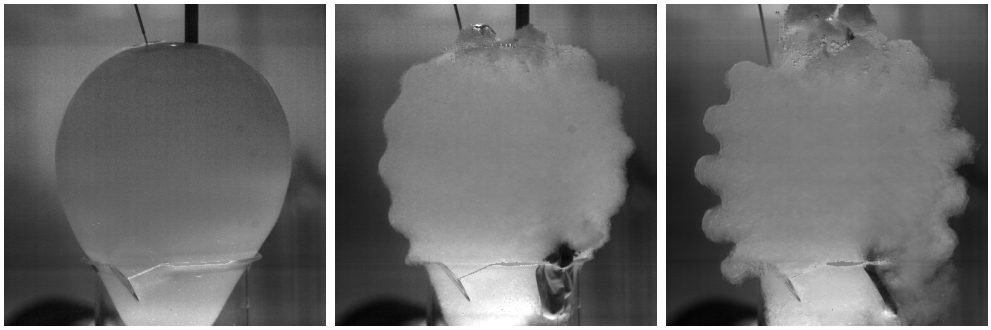

(d) $t = 0$ ms (e) $t = 11$ ms (f) $t = 72$ ms

Figure 6.1: The late-time growth of the interfacial amplitude for water balloons in air **(a)** - **(c)**, and water **(d)** - **(f)**. The balloon in air was oscillated at 120 Hz prior to rupture, the one in water at 170 Hz prior to rupture. The water inside the balloons contained milk powder to aid visualisation.

circular sheets of water penetrating rapidly into the air, with wide sections of air penetrating far more slowly into the water. The tips of the thin water sheets were rounded off by surface tension, and eventually became unstable due to capillary effects and separated into droplets of water.

Examples of the late-time growth for forcibly oscillated then ruptured balloons with both air and water external to the balloon are show in figure 6.1. For the forced balloons in air (figure 6.1, (a) - (c)), the behaviour was nearly identical to that seen for the dropped balloons: the denser water penetrated into the air as thin 'spikes' as the air penetrated more slowly into the water as wide 'bubbles', behaviour typical of both Rayleigh-Taylor instability (RTI) and Richtmyer-Meshkov instability (RMI) for Atwood numbers close to 1. The only real difference was that the growths were predominantly of a single wavenumber, whereas for a dropped balloon they were of a range of wavenumbers. This difference arose because of the nature of the interfacial waves present on the membrane at rupture, being of only a single wavenumber set by the forcing of only a single frequency for the forced balloons, but of all wavenumbers for the sudden impact of a dropped balloon (as discussed in chapter 3).

The late-time growth from balloons forced underwater (figure 6.1, (d) - (f)) shows further significant differences from the the case of a dropped balloon in air, beyond having waves of only a single wavenumber. Now, the growth is symmetric between the phases inside and out, initially taking the form of growing sinusoidal perturbations. Eventually, however, the interface rolls up into vortex rings,

(a) $t = 8$ ms (b) $t = 81$ ms (c) $t = 198$ ms

Figure 6.2: The roll-up of the interface after rupture for a 130 mm balloon oscillated at 100 Hz. The cross-section was obtained by shining a thin light sheet through the flow, with the fluid inside containing sodium fluorescein to allow its visualisation.

as shown in figure 6.2, whose axis of symmetry is the straight line from the top to the open end of the balloon ($\phi = 0$, π), and thus the same as for the preburst waves. The vorticity within each ring is of a single sign, with the sign alternating between adjacent rings. The distance between adjacent rings is far smaller (typically around 1 mm) than the radius of each ring (typically around 50 mm). Consequently, the coupling between neighbouring rings is much stronger than the self-induced motion of each ring. The rings therefore propagate away from the interface in pairs, driving the interfacial growth further. Eventually, these vortex rings break down, as the flow becomes fully turbulent. The total time between rupture and breakdown into turbulence was typically around 0.5 s.

In all cases, the timescale for development of the late-time amplitude growth, at least 50 ms, was significantly greater than that for phenomena associated with the retraction of the membrane as discussed in chapter 5, being typically of the order of 1 ms. This would suggest that the late-time growth was unrelated to flow created by the retraction of the membrane. This is supported by considering the energy within the flow, as shown in figure 6.3. This figure shows the total root-mean-squared velocity (and hence the square root of the kinetic energy) within one wavelength, as found using PIV experiments on a 130 mm balloon oscillated at 105 Hz then ruptured. It oscillates preburst with the same frequency as the forcing, before slowly decaying after rupture. Notably, no jump in the kinetic energy is observed at rupture, with the energy driving the late-time growth deriving from that present prior to rupture. This suggests that the retraction of the membrane does not put significant energy into the flow, and so does not greatly impact the late-time growth. Consequently, we shall consider the late-time growth as entirely separate to the phenomena associated with retraction of the membrane. This is also supported by considering the physical mechanisms driving the late-time growth, as in the next section, which do not depend at all on the retraction of the membrane. The analysis is equally valid for the membrane being instantaneously removed without retracting over the interface.

We tracked the maximum interfacial displacement after rupture from the unperturbed situation for 130 mm balloons over a range of frequencies and tensions, with the results shown in figure 6.4. The experimental data was taken by bursting water-filled balloons underwater, with the water inside dyed with milk powder. No measurements were taken for water balloons burst in air, as the spray caused by

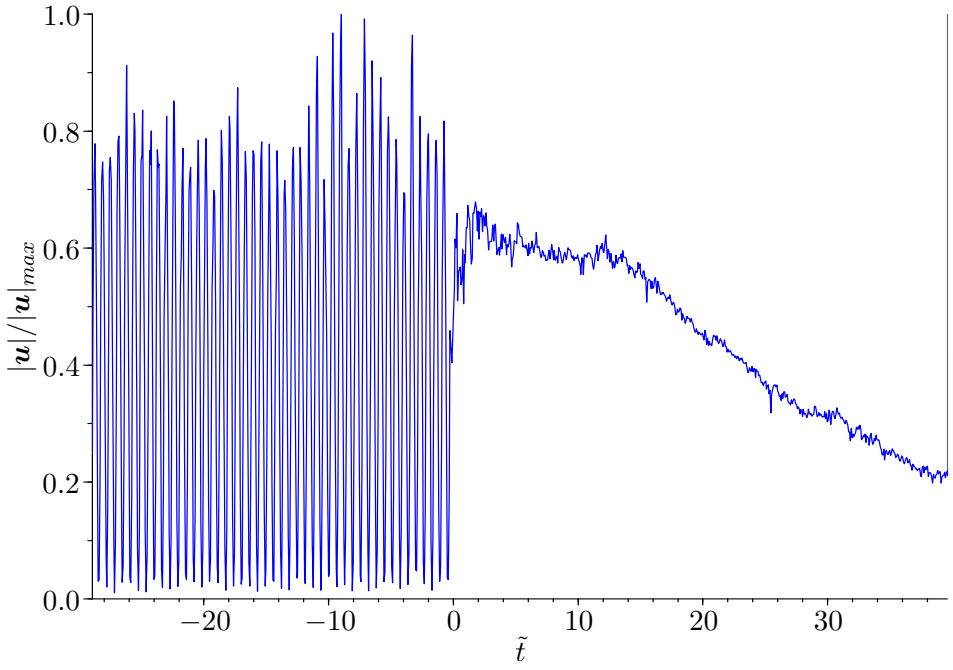

Figure 6.3: RMS velocity within a single wavelength, scaled against the maximum, plotted against non-dimensionalised time $\tilde{t}$ for flow within a 130 mm water balloon held underwater, and oscillated at 105 Hz prior to rupture. Rupture occurred at $\tilde{t} = 0$.

the retracting membrane obscured the early time growth, and gravity dominated the late-time growth. The membrane was ruptured so that the crack propagated in the plane perpendicular to the optical axis of the camera. The flow was then recorded at 5400 fps. Using the program Digiflow, the greatest interfacial displacement was then tracked relative to its starting point. The results are scaled as in Jacobs and Sheeley [1996], with scaled time $\tilde{t}$ given by $\Gamma k^2 t/4$ where Γ is the initial circulation within each half-wavelength and $k = k/R$ the dimensional wavenumber, and scaled displacement $\tilde{a}$ given by kh/R. After scaling, the results collapse down to one curve, within the margin of experimental error. The initial growth is approximately linear, before the flow decelerates at later time. Beyond $\tilde{a} = 30$, the flows lost structure and broke down into turbulence.

6.3 Initial development of the interfacial growth

The basic physical mechanism behind the late-time interfacial growth was discussed briefly in chapter 3, but shall be explored in more detail here. It is directly responsible for the behaviour in the linear stages growth, with little difference in behaviour depending on the density ratio between the phases. This is not the case for non-linear stages of growth, which shall be considered separately, in the next section.

The simplest explanation for the growth of the interfacial amplitude is that it occurs because

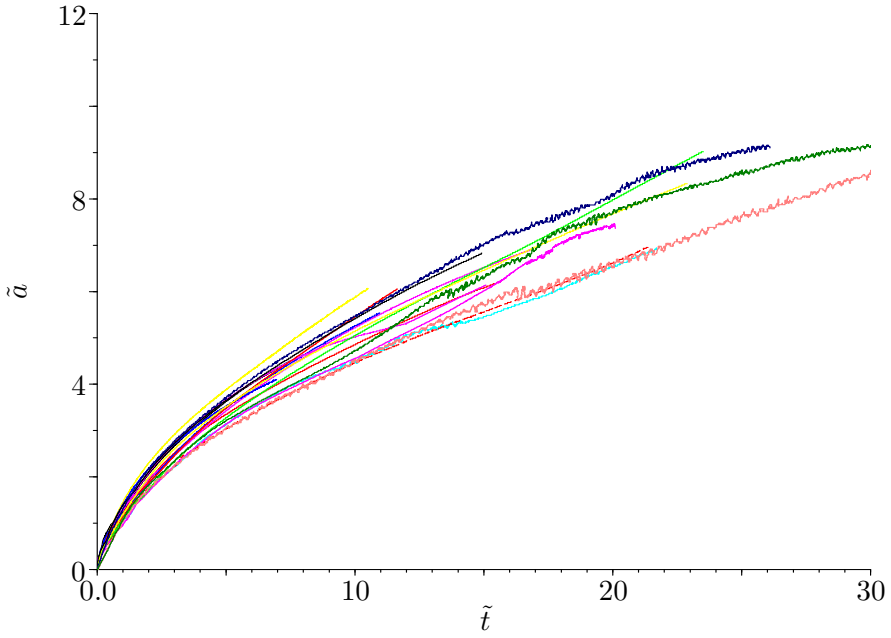

Figure 6.4: The growth rate of the interfacial amplitude for 130 mm balloons oscillated then burst with water both inside and outside. The inner fluid contained milk powder to allow easy tracking of the interface. Experiments were performed for frequencies in the range 60 Hz to 180 Hz, and membrane tension between 100 N/m and 250 N/m. The growth is shown up to $ka = 30$, when the vortex rings broke down into smaller structures as the flow became fully turbulent.

the bursting of the balloon is a near-instantaneous removal of the restoring force (tension in the membrane) for the pre-burst, capillary-like waves. The flow present at the moment of rupture then continues without an acceleration acting on it, implying a linear initial growth rate for the interfacial amplitude. This argument may be made more rigorous by performing a linear stability analysis. We consider the simplest case, that of a linear, incompressible, inviscid, and irrotational flow at a planar interface between two fluids. Though, as will discussed later, such an analysis has previously been applied to study other interfacial flows, there is no evidence in the published literature of it having been applied to bursting balloons.

The quantities associated with the fluid beneath the interface will have subscript 1, those above subscript 2. This flow may be modeled using velocity potential functions ϕ_1 (below the interface) and ϕ_2 (above the interface), both of which satisfy Laplace's equation,

$$\nabla^2 \phi_i = 0. \tag{6.1}$$

Assuming a 2D, Cartesian interface, the interfacial boundary conditions at the interface $z = \eta(x, t)$ are then the kinematic condition

$$\frac{\partial \eta}{\partial t} = \frac{\partial \phi_1}{\partial z}, \tag{6.2}$$

$$\frac{\partial \eta}{\partial t} = \frac{\partial \phi_2}{\partial z}, \tag{6.3}$$

and the dynamic condition

$$\rho_1 \frac{\partial \phi_1}{\partial t} - \rho_2 \frac{\partial \phi_2}{\partial t} + (\rho_1 - \rho_2)\eta g(t) = -\sigma(t)\frac{\partial^2 \eta}{\partial x^2}, \tag{6.4}$$

where here both the gravitational acceleration g and surface tension σ are taken to be functions of time. These equations imply the potentials and interface have the form

$$\phi_1 = b(t)e^{ky}\cos kx, \tag{6.5}$$

$$\phi_2 = -b(t)e^{-ky}\cos kx, \tag{6.6}$$

$$\eta = a(t)\cos kx, \tag{6.7}$$

for wavenumber k and amplitudes $a(t)$ and $b(t)$. The interfacial boundary conditions then give

$$\dot{a}(t) = kb(t), \tag{6.8}$$

$$\dot{b}(t) = -\frac{k^2}{\rho_1 + \rho_2}\sigma(t)a(t) - Aa(t)g(t), \tag{6.9}$$

where

$$A = \frac{\rho_1 - \rho_2}{\rho_1 + \rho_2} \tag{6.10}$$

is the Atwood number. Combining these two equations leads to

$$\ddot{a}(t) = -\left(\frac{k^3}{\rho_1 + \rho_2}\sigma(t) + kAg(t)\right)a(t). \tag{6.11}$$

Different choices of $g(t)$ and $\sigma(t)$ in the above equation then determine the initial growth of the interfacial amplitude for the different situations. For the bursting of a balloon, $g(t) = 0$ but $\sigma(t) = H(-t)$. In practice, the acceleration will only be applied to the interface for a finite time, but as long as that time is significantly longer than a single wave period, it may be appropriately modelled as a semi-infinite step function. Equation (6.11) thus becomes

$$\ddot{a}(t) = -\frac{k^3}{\rho_1 + \rho_2}H(-t)a(t). \tag{6.12}$$

Integrating the above equation between $-\epsilon$ and t (where both ϵ and t are positive) gives

$$\dot{a}(t) - \dot{a}(-\epsilon) = -\frac{k^3}{\rho_1 + \rho_2}\int_{-\epsilon}^{0} a(t)dt. \tag{6.13}$$

Taking the limit $\epsilon \to 0$ therefore implies

$$\dot{a}(t) = \lim_{\epsilon \to 0}\dot{a}(-\epsilon) = \dot{a}_0 \tag{6.14}$$

where $\dot{a}_0$ is the normal velocity of the interface at that moment of rupture. This implies, as argued above, that the initial interfacial growth after rupture will be linear, going at the velocity of the interface at the moment of rupture. This linearity was supported by experimental measurements of the interfacial growth for water/water ruptures, as shown in figure 6.4. The initial gradient is 1, as the scalings used are equivalent to $\tilde{t} = (k/R)\dot{a}_0 t$ and $\tilde{a} = (k/R)a$. This linear behaviour persists until approximately $\tilde{t} = 2$, when it starts to decelerate as the flow becomes non-linear. This theory also predicts that interface retains its initial sinusoidal shape in the initial linear stage of growth, and so that the shape remains symmetric (and so independent of the relative densities of the two fluids). This was indeed the case, as seen in figures 6.1(b) and 6.1(e).

The above analysis has been conducted without specifying the densities of the fluids either side of the interface. Consequently, while our focus is on the cases with water inside the balloon (due to the relative ease of conducting such experiments, and the fact that compressibility of the fluids may be neglected in such cases), the same mechanism for growth will still occur with air inside and water outside, or even air both inside and outside, provided there are waves on the balloon at the moment of rupture.

It was argued in chapter 3 that this growth of the interfacial amplitude was related to RMM (unlike most authors, we refer to it as a mechanism as it does not feature the exponential growth needed to be a true instability). To be clear, when we refer to RMM we refer to the definition of Jacobs and Sheeley [1996], that it is the impulsive acceleration of a density interface. Impulsive accelerations of the whole flow may only occur on an interface between incompressible fluids. For compressible fluids, impulsive acceleration is given by a shock wave passing through the interface. Other authors, including Velikovich et al. [2000], define RMI to be when a shock wave passes through a interface, thus excluding the possibility of RMI for incompressible flow in which shocks cannot occur. Despite this, the incompressible case is then referred to by Velikovich et al. [2000] as 'Richtmyer-Meshkov-like', as it does feature the same deposition of initial localized vorticity at the interface that causes the growth.

The connection between RTI, RMM and growth of the interface due to a bursting balloon becomes clear by repeating the previous analysis for the initial growth rate. This was first done by Taylor [1950] for RTI, for an interface with gravitational acceleration: $g(t) = g\,\mathrm{sgn}(-t)$, and $\sigma(t) = 0$. Equation (6.11) thus becomes

$$\ddot{a}(t) = -kAga(t), \tag{6.15}$$

and so the initial interfacial growth is exponential in time. This is distinct from the balloon and RMM cases, as the interface is being constantly accelerated throughout growth of the interfacial amplitude. In the other two, no acceleration is applied once growth has begun.

The linear stability analysis for RMM was first considered by Richtmyer [1960], where it was modeled as the impulsive limit of RTI. Though the author was concerned with the compressible case, his model is actually best applied to the incompressible case. The acceleration on the interface is $g = \triangle V \delta(t)$ (where $\triangle V$ is the difference in normal velocity either side of the shock) and $\sigma(t) = 0$, thus equivalent to the situation discussed in section 4.6 but with an impulsive gravitational acceleration. Equation (6.11) thus becomes

$$\ddot{a}(t) = -kA\triangle V \delta(t) a(t). \tag{6.16}$$

Integrating up once gives the growth-rate for $t > 0$ as

$$\dot{a}(t) = \dot{a}(0) - kA\triangle V a(0), \tag{6.17}$$

showing that the initial interfacial growth is linear in time, its speed being constant as for the bursting balloon case. Note that as we are considering the incompressible, impulsively accelerated case, $a(0)$ is well-defined - this is not the case for the compressible, shock-accelerated case.

The connection to RMM through initial linear growth is more than just coincidence. In fact, the flow is identical between an impulsively accelerated interface after the acceleration, and the balloon interface once the membrane has ruptured. This is best seen by considering vorticity. It is well-known that the basic driving mechanism for interfacial growth is the baroclinic deposition of vorticity at the interface by the impulsive acceleration. The relevant version of vorticity equation, including the baroclinic term, is

$$\frac{D\omega}{Dt} = \frac{1}{\rho^2}\nabla\rho \times \nabla p. \tag{6.18}$$

When the interface is impulsively accelerated, ∇p will be normal to it. If there are any perturbations to the interface, $\nabla\rho$ will not be normal to the interface. The density and pressure gradients will therefore be misaligned, leading to the creation of vorticity. In the inviscid limit, this vorticity will be restricted to an infinitely-thin sheet at the interface. The flow associated with this vorticity will then cause the interfacial amplitude to increase, as shown in figure 6.5. This is true wherever the vorticity actually is, even for an air/water interface where the vorticity is in the air (as shown in section 4.6). We may therefore refer to the Richtmyer-Meshkov mechanism as the instantaneous creation of vorticity at an interface.

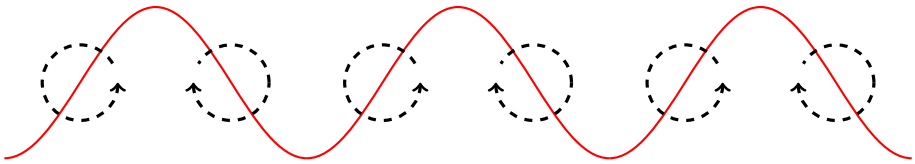

Figure 6.5: Diagram of the flow induced by an interfacial vortex sheet deposited on a sinusoidal interface by an impulsive acceleration.

For the interfacial growth of a bursting balloon, it was shown in chapter 4 how the preburst waves create vorticity localised near the interface, that in the limit of small viscosity may be approximated by a vortex sheet. Once the balloon bursts, this vortex sheet is left at the interface. The situation is now identical to that for an interface has been impulsively accelerated: the flow implied by the vortex sheet causes the interfacial amplitude to grow, as depicted in figure 6.5. The growth is therefore linear, as for RMM.

It should be noted that, in our above argument for the interfacial growth in the balloon case, the fact that the interfacial waves were capillary waves was not important. We would therefore also expect interfacial growth to occur if the restoring force for gravity waves was present for a finite time before being instantaneously removed. The initial growth rate would then be given by equation (6.11) with $g(t) = gH(-t)$ and $\sigma(t) = 0$, and hence $\dot{a}(t) = \dot{a}(0)$. Such a situation could be created by forming gravity waves on a tray of water, that is then released into free fall.

Both definitions of RMM given previously defined it to be a consequence of the impulsive, or instantaneous, acceleration of an interface. Through our experiments on bursting water balloons, we have shown that this definition is arguably imprecise: the growth of the interfacial amplitude is

a consequence of the instantaneous removal of the acceleration (or equivalently, the instantaneous removal of the restoring force for waves). It does not matter whether that acceleration is applied instantaneously (classical RMM) or for a finite time (as for balloon). Indeed, it is noticeable that in our previous linear stability analysis for bursting balloons that the growth of the interface is independent of the time for which the acceleration was applied to the interface pre-burst. After removal of the acceleration, the flow evolves according to that present at the moment of removal, the interfacial amplitude growing linearly in time due to the vorticity present at the interface. For balloon bursts with standing waves on the interface, the interfacial growth does, of course, depend on the exact time of rupture: the phase of the waves at the moment of rupture will determine the normal velocity of the interface, and therefore the initial growth rate. It does not, however, depend on how long the waves have been present.

The only difference between a balloon burst and RMM is in how the vorticity is created. For RMM (and gravity waves), it is baroclinically generated at the interface. Consequently, no growth will occur when the densities of the two fluids are the same, when $A = 0$. This is a clear distinction with the balloon case, where the interfacial waves are generated by a form of surface tension. The creation of these waves, and hence the interfacial vorticity and consequent interfacial growth after their removal, will therefore occur even when $A = 0$.

In summary, the growth of interfacial amplitude after a balloon bursts is closely related to the Richtmyer-Meshkov mechanism. In RMM, vorticity at a density interface produced by impulsive gravitational acceleration leads to growth of the interfacial amplitude at constant speed. Our experiments on bursting water balloons, however, show that vorticity produced at an interface by capillary waves can also lead to growth of the interfacial amplitude, if and when the restoring force for those waves is instantaneously removed. In fact, similar to how Kelvin-Helmholtz instability may be simply regarded as the instability of a vortex sheet of constant vorticity, so RMM may be regarded as the instability of a vortex sheet of sinusoidal sections of alternating sign. Under such a definition, the rupture of a balloon would indeed be a example of RMM.

6.4 Non-linear interfacial growth

The linear stability analysis above is only valid when the interfacial amplitude was small in comparison to the wavelengths of the perturbation. Once they were of a similar order, it could no longer be regarded as accurate. In the non-linear stages of growth, and unlike the linear stages, the relative densities of the two fluids became important. Once again, it closely mirrored the behaviour of both RTI and RMM for the equivalent density ratio.

6.4.1 Air/water interface

For the air/water interface, $A \approx 1$ and thus the relative density difference between the fluids was large. As seen in figure 6.6 (and in figures 6.1(a) to 6.1(c)), the process then became non-Boussinesq, as the interfacial growth lost symmetry between the phases. Thin sheets of water penetrated into the air, while thicker intrusions of air moved into the water at a far slower rate. This behaviour closely mirrored that of RTI and RMM at high Atwood number, where the wide intrusions of the less dense fluid are referred to as bubbles, and the thin sheets of denser fluid are referred to as spikes. Notably,

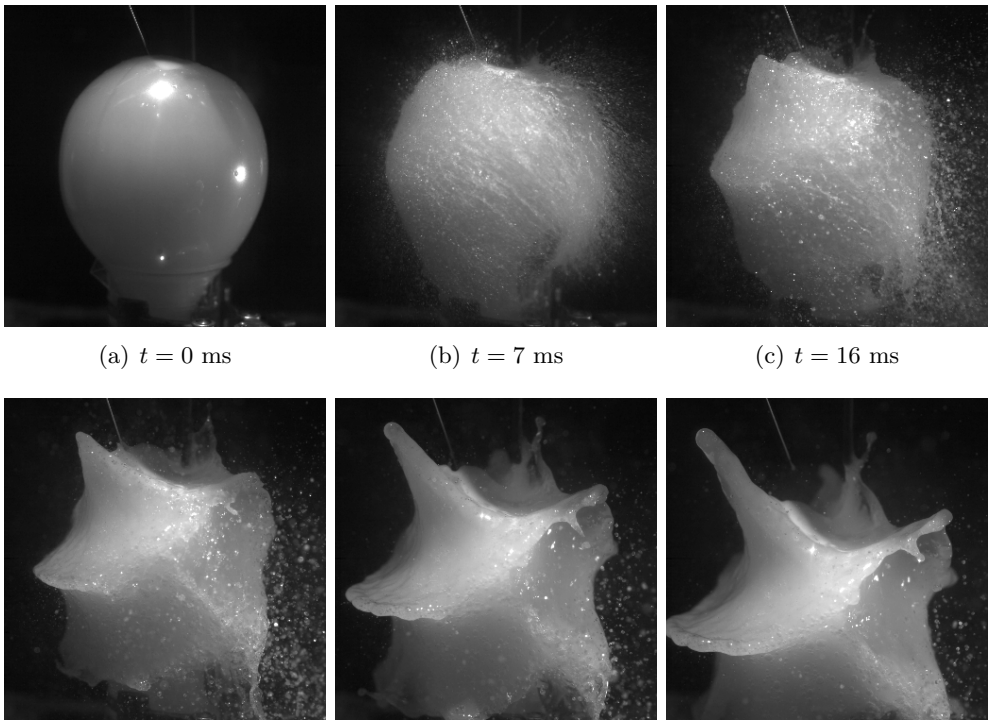

(a) $t = 0$ ms (b) $t = 7$ ms (c) $t = 16$ ms

(d) $t = 36$ ms (e) $t = 67$ ms (f) $t = 94$ ms

Figure 6.6: The late-time growth of the interfacial amplitude for a water-filled 130 mm balloon oscillated at 80 Hz prior to rupture. The water inside the balloons contained milk powder to aid visualisation. The instability is only clearly visible on the left side of the balloon, as that was where the crack propagated. On the right side, vorticity created by the retracting membrane dominated the flow instead. At the later times, the effect of gravity can clearly be seen, causing the entirety of the water to slump down.

and unlike for the water/water case below, no roll-up of the interface occurred. This happened because the large density difference between the phases lead to a mismatch in momentum between the phases. The vortex sheet was therefore stretched out along the interface as it rapidly grew in area, so that it could not form the tight spirals typical of roll-up.

We demonstrated in chapter 4 how the presence of the membrane changes the structure of the interfacial vorticity. While in all cases it may be approximated by an infinitely thin sheet in the inviscid limit, physically that is not possible, with the actual location of the vorticity depending on the nature of the interface. For the water/water case when $A = 0$ this did not matter, as there was no difference between the phases. However, for the air/water case when $A = 1$, it may have mattered. For a true air/water free surface as for RMM, whether impulsively accelerated or accelerated for a finite time, and whether due to gravity or capillary forces, the vorticity will be in the air. For a membrane-covered interface, the vorticity will be split, with approximately half in the air and half in the water. This could, potentially, have lead to differences in the late-time behaviour. However, the structure of the instability displayed in figure 6.6 for a bursting balloon did match that seen for RTI and RMM for $A = 1$, indicating that the location of the vorticity was not significant in determining the general form of the interfacial growth. At such low viscosities, the approximation of the vorticity as a sheet at the interface was still accurate, suggesting that its exact location did not matter. This does, however, raise the possibility of the flow structure being significantly different if the fluid within the balloon is not water but something far more viscous. Unfortunately, we did not carry out any such experiments.

The location of the interfacial vorticity, if not important in determining the overall structure of the interfacial growth, could still have impacted the growth rate. Unfortunately, it was not possible for us to accurately measure the growth rate of the bubbles and spikes in the non-linear regime, as at such late-times gravity came to dominate the flow. This caused the water to slump down, introducing further non-linear complications to the motion of the fluids, and meaning the interfacial growths no longer traveled along simple, straight paths.

6.4.2 Water/water interface

For the water/water interface, when $A = 0$, the behaviour was distinctly different. Now there was no mismatch of momentum and the growth was Boussinesq, as the interfacial vorticity rolled up into discrete vortex rings of alternating sign on lines of constant latitude. Similar behaviour (though with straight vortex tubes instead of vortex rings) has been noted before for both RTI and RMM at low Atwood numbers, including by Jacobs and Sheeley [1996] for incompressible RMM on a planar interface. Distinct from most previous studies, however, the vortex rings were of varying radius and circulation due to the spherical shape of the interface. Consequently, mutual interaction between these rings caused them to separate into pairs and propagate away from the interface. As the vortex rings were a mix of both fluids, they took the interface with them, and so were the primary driving mechanism behind the non-linear interfacial growth at very late-times. This process is clearly seen in figure 6.7 through the use of PIV on an oscillated water balloon rupturing underwater. Eventually, these vortex rings broke down into smaller scales as the flow became fully turbulent. This typically occurred before a scaled time $\tilde{t} = 30$. Note that this behaviour was only observed on the half of the interface closest to the initial path of crack propagation. Elsewhere, vorticity created by the retracting membrane (as discussed in the previously chapter) dominated the behaviour, causing the

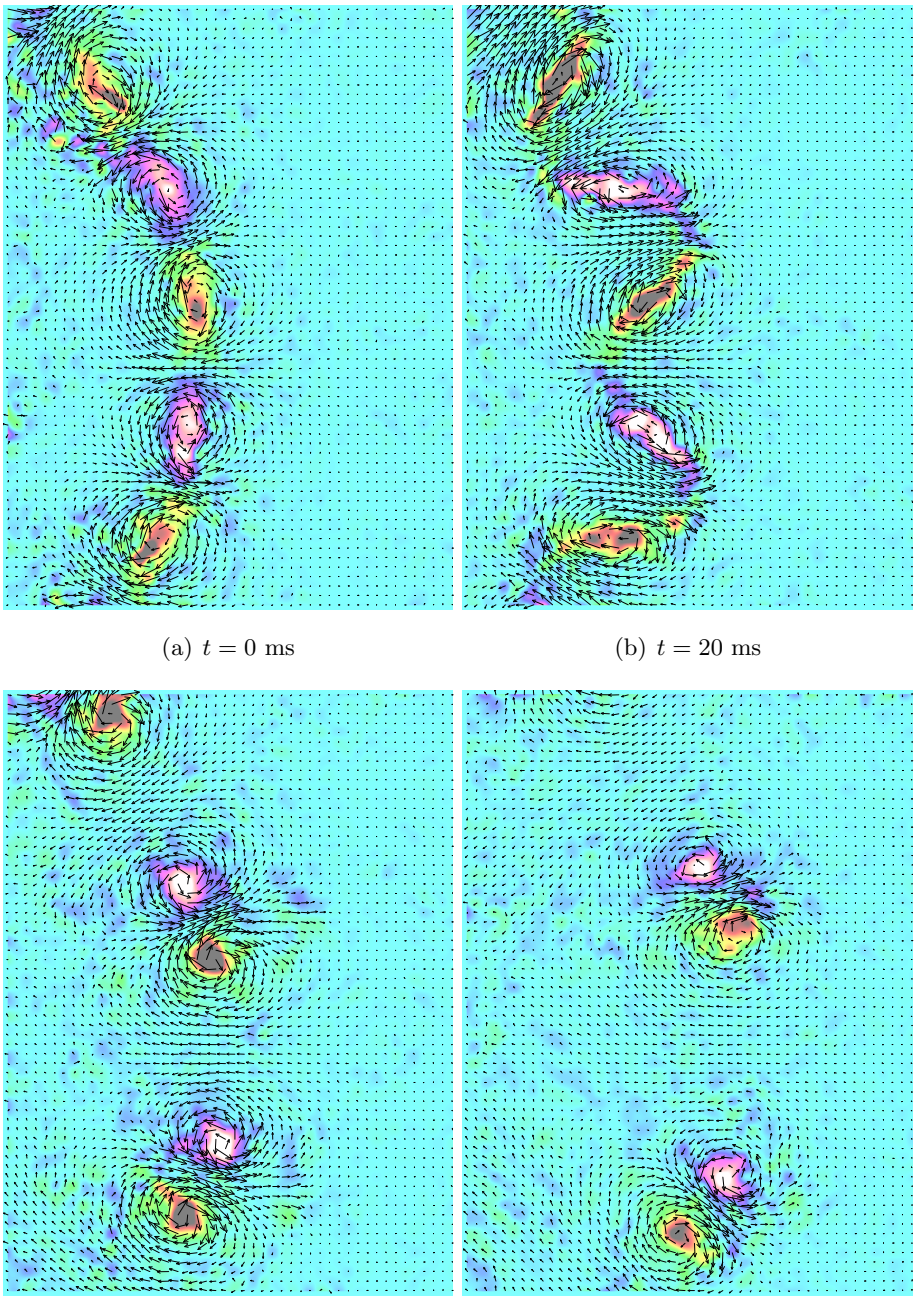

(a) $t = 0$ ms (b) $t = 20$ ms

(c) $t = 117$ ms (d) $t = 221$ ms

Figure 6.7: The results of PIV on a cross-section of the flow created by a 130mm balloon forcibly oscillated at 105Hz before being ruptured by a pin. The arrows represent the velocity field and the colours represent the vorticity, with purple positive, cyan zero and red negative. Prior to rupture, the vorticity was restricted to a narrow region near the interface. Post-rupture, the vorticity rolled up into discrete rings. These rings then separated into pairs of opposite sign, and propagated away from the initial interface. Image (d) shows two such pairs.

flow to become turbulent almost immediately after rupture ($\tilde{t} < 1$). This also meant that the vortex rings were not fully closed. However, enough of the interface did roll up into the rings for them to be the dominant structures in the flow on one side of the balloon at late times.

Growth rates for the water/water case were shown in figure 6.4. In particular, they show that the growth rate decelerates as it enters the non-linear regime. However, this deceleration does not last for long, with the growth becoming approximately linear once again, albeit at a slower speed than immediately after rupture. This is different from the behaviour of incompressible RMI at low Atwood numbers studied by Jacobs and Sheeley [1996], who found that the interfacial amplitude grew like $\log(k\dot{a}_0 t)$ at late-times. However, as stated previously, their experiments were conducted on flat interfaces, whereas ours were conducted on spherical interfaces. It therefore seems that the unperturbed shape of the interface plays a key role in determining the non-linear interfacial growth rate.

6.5 Vortex model for non-linear growth when $A = 0$

Jacobs and Sheeley [1996], in their previous work on RMI in the low Atwood number number regime, developed a theory to match their experimental results that was referred to as the Vortex model. This model was based on the idea that the late-time behaviour was dominated by the interfacial vorticity. As they were considering a 2D horizontal (though perturbed) interface, the initial distribution of vorticity given by linear theory was

$$\omega = -2\dot{a} \sin kx$$

for $-\infty < x < \infty$, $z = 0$, with $\omega = 0$ elsewhere. The model assumed that the sinusoidal distribution of vorticity present on the interface at time $t = 0$, when the shock passed through the interface, instantaneously rolled up into discrete vortices. As the initial distribution of vorticity was assumed to extend to plus and minus infinity, all of the vortices would remain in their initial position. They could thus find an analytical expression for the stream-function of the flow, and thus for the growth of the maximum amplitude of the interface. The expression for the stream-function found was

$$\psi = \frac{\Gamma}{4\pi} \ln \frac{\cosh ky + \sin kx}{\cosh ky - \sin kx}, \tag{6.19}$$

for vortices of circulation $\pm\Gamma$ separated by a distance $\frac{\pi}{k}$, k being the wavenumber of the interfacial perturbation at $t = 0$. The consequent expression for the growth of the amplitude $a(t)$ was

$$a(t) = \frac{1}{k} \sinh^{-1} \left(\frac{2}{\pi} k\dot{a}_{0+} t + \sinh ka_0 \right). \tag{6.20}$$

Consequently, as $t \to \infty$, $a \sim \ln t$ and $\dot{a} \sim 1/t$. This expression, when matched with experimental data, showed a good qualitative agreement but predicted growth-rates below those observed experimentally. As the authors noted, as the growth-rate is reduced by the coalescence of vorticity, which occurs gradually, it is reasonable to expect the vortex model to always yield a lower growth rate than that of experimental measurements.

A similar model was derived by Likhachev and Jacobs [2005] to model bubble and spike growth on a low Atwood number interface. They did this by assuming the oppositely-signed vortices were

not equally spaced along the interface at $t = 0$. Consequently, the vortices did not remain stationary, but propagated away from the initial interface, affecting the late-time growth rate of the interface. As $t \to \infty$, the interface speed would approach that of the vortices.

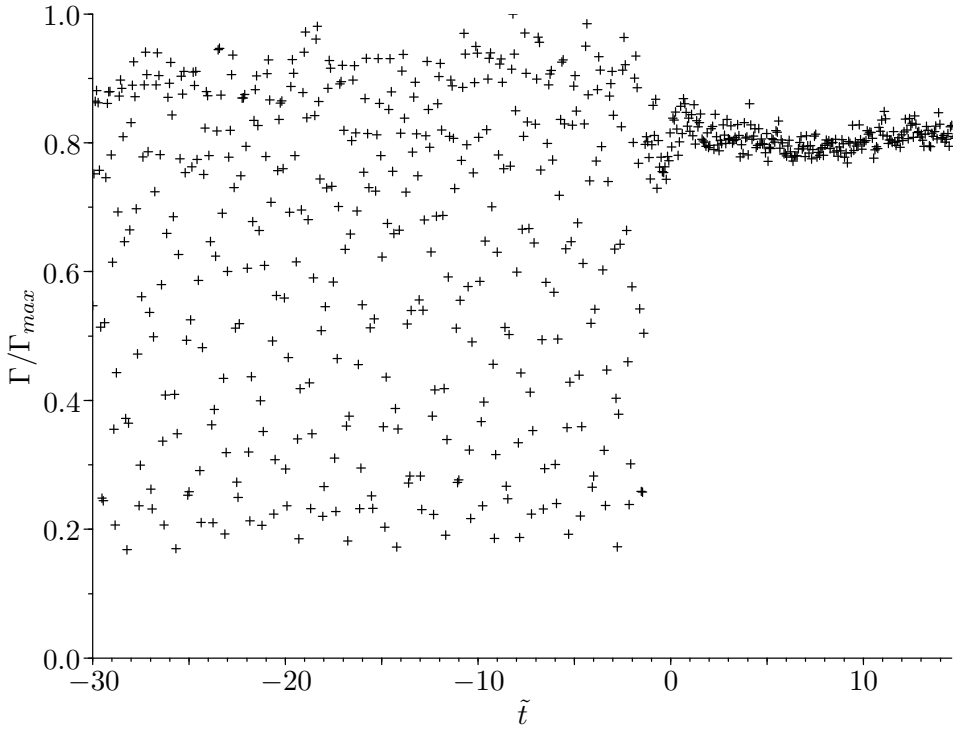

Figure 6.8: The total circulation in one half wavelength (equivalently, one vortex after rupture) plotted against time for a 130 mm balloon forced at 105 Hz. These values were attained using PIV on the water within a filled balloon both before and after rupture. The circulation is initially periodic as the balloon is oscillated, until rupture at $\tilde{t} \approx 0$, where after it remains constant despite the motion of the vortex ring. The apparent drop in vorticity at $\tilde{t} = 0$ is just a consequence of the phase at which the balloon was ruptured not being that for which the interface had maximum vorticity.

As discussed previously, and much like incompressible RMM, the late-time interfacial growth after a balloon bursts is also driven by a vortex sheet at the interface. For bursting balloons, however, this was in a different geometrical configuration: instead of a 2D interface, upon bursting of the balloon the vorticity is initially restricted to a spherical interface, but quickly coalesces into vortex rings. These vortex rings are of alternating sign and centred on the vertical axis of the balloon. Under their own influence, they then spread axisymmetrically outwards as, due to the initial arrangement, each core has an initial net velocity towards one of its neighbours. Once the initial circular symmetry is broken, the velocity contribution from its 'partner' comes to dominate, and the two vortices behave similar to a pair of translating vortices of equal strength but opposite sign (as discussed by Batchelor [1967], page 531).

The rings were of finite inner radius that decreased as they expanded. However, by Kelvin's

circulation theorem, we expected their circulation to remain constant as they propagated away from the interface. This is clearly demonstrated in figure 6.8 for the initial stages of growth, where $k\dot{a}_{0+}t < 10$. However, later on, as the vortex rings approach one another, the vorticity was annihilated at the centre-line between the rings, and the circulation decreased linearly. This effect will discussed in section 6.8.

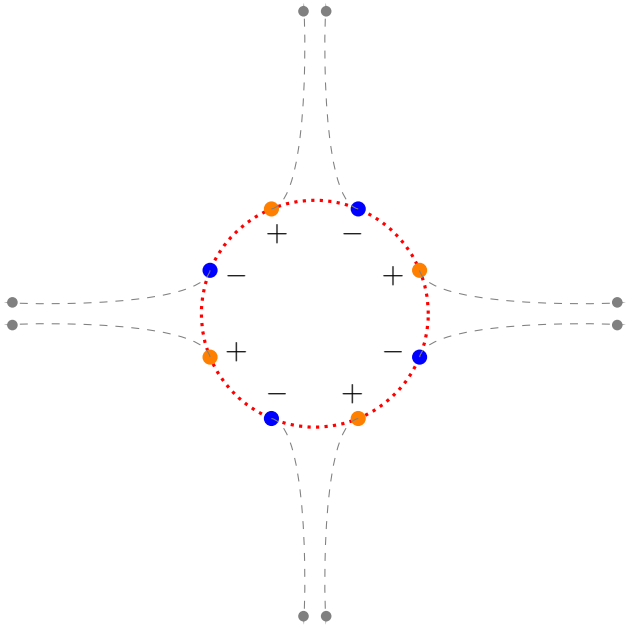

Figure 6.9: The approximate motion of 8 vortices of alternating sign initially arranged on a circle. They separate off into adjacent pairs that head off to infinity together.

To model the non-linear stages of interfacial growth when $A = 0$, we therefore extend the work of Jacobs and Sheeley [1996] and Likhachev and Jacobs [2005] by assuming the interfacial vorticity concentrated at the interface at the moment of burst instantaneously rolls up into discrete vortex rings. Due to axisymmetry, we simplify the problem by considering a 2D cross-section of the system, where each vortex ring is replaced by a pair of oppositely-signed point vortices, as shown in 6.5. For a single vortex ring, it is known that such an approximation does not give the correct translation speed for the ring, as it does not account for the curvature of the ring (see Saffman [1992]). However, as the distance between adjacent rings is far smaller than the diameter of each ring, we expect the point vortex approximation to be valid, with any correction for the curvature of each ring to be insignificant. It is further assumed that each ring has the same strength circulation. Though this assumption was shown to be technically incorrect in chapter 4, it is reasonable for high-wavenumber bursts near the balloon's equator, as for all our experimental measurements. The assumption that this circulation is constant over time is also used.

In summary, we shall attempt to model the late-time interfacial growth by assuming that the interfacial vorticity instantaneously rolls-up into vortex rings. These rings form a system equivalent

to an even number (as each ring contributes two vortices) of point vortices of equal, constant strength circulation but alternating sign arranged in a circle in a 2D plane. This model is explored in the following sections, before its predictions are matched against the experimental data. This model, an application of the method of Jacobs and Sheeley [1996] to a circular geometry, is new and original work.

6.5.1 Motion of the vortices

We first wish to determine the motion of the vortices, from which we may then determine the stream-function and hence the overall flow field. For such a system of n vortices, we thus have $2n$ unknowns to find, the x and y coordinates of each vortex. However, we may use the inherent symmetry of the initial conditions (and subsequent motion) to reduce the problem to one of finding the x and y coordinates of just one vortex. By symmetry, the motion of all the other vortices will then be same, only rotated, reflected, or both. In fact, this situation is analogous to a single vortex in a wedge, as its motion may be solved using the method of images, leading to a consideration of the situation we have here. This situation was first considered by Greenhill [1878], who found the polar equation of the motion. However, he did not solve for the motion in terms of time, which we require. We thus rederive the equations of motion, and solve for both radius and polar angle in terms of time.

We work in polar coordinates with radial coordinate r and polar angle ζ, taking $\zeta = 0$ along the positive x-axis. The vortices are initially distributed on the circle $r = r_0$ at positions $\zeta = \frac{\pi(2j-1)}{n}$ for $j = 1, .., n$, with circulation

$$\Gamma_j = (-1)^{j+1}\Gamma$$

for some positive constant Γ. The vortices then separate into pairs whose motion is symmetric across the lines $\zeta = \frac{4\pi m}{n}$ for $m = 1, .., \frac{n}{2}$.

We assume, as is usual, that the motion of each vortex solely due to the sum of the velocity fields induced by the other vortices. The stream function ψ_j created by a vortex of strength Γ_j at position $z_j = r_j e^{i\zeta}$ in the complex plane is, as in Batchelor [1967],

$$\psi_j = -\frac{\Gamma_j}{2\pi} \ln |z - z_j|,$$

meaning that the stream function for the flow at vortex 1, $\tilde{\psi}$, is

$$\begin{aligned} \tilde{\psi} &= -\frac{\Gamma}{2\pi} \left(\sum_{j=1}^{\frac{n}{2}-1} \ln |z - z_{2j+1}| - \sum_{j=1}^{\frac{n}{2}} \ln |z - z_{2j}| \right), \\ &= -\frac{\Gamma}{2\pi} \left(\ln \prod_{j=1}^{\frac{n}{2}-1} |z - z_{2j+1}| - \ln \prod_{j=1}^{\frac{n}{2}} |z - z_{2j}| \right). \end{aligned} \tag{6.21}$$

6.5.2 Equations of motion of a vortex

Taking the position of vortex 1 to be $(a(t), \phi(t))$ (functions of t alone), with consequent complex position $z_1 = a(t)e^{i\phi(t)}$, symmetry then gives the complex positions of the other vortices as

$$z_{2j} = ae^{i(\theta_j - \phi)},$$

$$z_{2j+1} = ae^{i(\theta_j+\phi)},$$
$$\theta_j = \frac{4\pi j}{n}.$$

The θ_j represent the $\frac{n}{2}$-th roots of unity. Taking $z = re^{i\zeta}$, equation (6.21) may then be written as

$$\begin{aligned}
\tilde{\psi} &= -\frac{\Gamma}{2\pi}\left(\ln\prod_{j=1}^{\frac{n}{2}-1}|re^{i\zeta}-ae^{i(\theta_j+\phi)}| - \ln\prod_{j=1}^{\frac{n}{2}}|re^{i\zeta}-ae^{i(\theta_j-\phi)}|\right), \\
&= -\frac{\Gamma}{2\pi}\left(-\ln a + \ln\prod_{j=1}^{\frac{n}{2}-1}|\frac{r}{a}e^{i(\zeta-\phi)}-e^{i\theta_j}| - \ln\prod_{j=1}^{\frac{n}{2}}|\frac{r}{a}e^{i(\zeta+\phi)}-e^{i\theta_j}|\right). \qquad (6.22)
\end{aligned}$$

(6.23)

As the θ_j represent the $\frac{n}{2}$-th roots of unity, we have for any x

$$\prod_{j=1}^{\frac{n}{2}}(x-e^{i\theta_j}) = x^n - 1.$$

We may thus rewrite equation (6.22) as

$$\begin{aligned}
\tilde{\psi} &= -\frac{\Gamma}{2\pi}\left(-\ln a + \ln\left|\frac{\left(\frac{r}{a}e^{i(\zeta-\phi)}\right)^{\frac{n}{2}}-1}{\frac{r}{a}e^{i(\zeta-\phi)}-1}\right| - \ln\left|\left(\frac{r}{a}e^{i(\zeta+\phi)}\right)^{\frac{n}{2}}-1\right|\right) \\
&= -\frac{\Gamma}{2\pi}\left(-\ln a + \ln\left|\left(\frac{r}{a}e^{i(\zeta-\phi)}\right)^{\frac{n}{2}}-1\right| - \ln\left|\frac{r}{a}e^{i(\zeta-\phi)}-1\right| - \ln\left|\left(\frac{r}{a}e^{i(\zeta+\phi)}\right)^{\frac{n}{2}}-1\right|\right) \\
&= -\frac{\Gamma}{4\pi}\left(-2\ln a + \ln\left[1+\left(\frac{r}{a}\right)^n - 2\left(\frac{r}{a}\right)^{\frac{n}{2}}\cos\frac{n}{2}(\zeta-\phi)\right]\right. \\
&\quad -\ln\left[1+\left(\frac{r}{a}\right)^2 - 2\left(\frac{r}{a}\right)\cos(\zeta-\phi)\right] \\
&\quad \left.-\ln\left[1+\left(\frac{r}{a}\right)^n - 2\left(\frac{r}{a}\right)^{\frac{n}{2}}\cos\frac{n}{2}(\zeta+\phi)\right]\right). \qquad (6.24)
\end{aligned}$$

From the stream function we may find the velocity using the relations

$$v_r = \frac{1}{r}\frac{\partial\tilde{\psi}}{\partial\zeta}, \qquad (6.25)$$
$$v_\zeta = -\frac{\partial\tilde{\psi}}{\partial r}. \qquad (6.26)$$

Using equation (6.24),

$$\begin{aligned}
\frac{1}{r}\frac{\partial\tilde{\psi}}{\partial\zeta} &= -\frac{\Gamma}{4\pi r}\left(\frac{n\left(\frac{r}{a}\right)^{\frac{n}{2}}\sin\frac{n}{2}(\zeta-\phi)}{1+\left(\frac{r}{a}\right)^n - 2\left(\frac{r}{a}\right)^{\frac{n}{2}}\cos\frac{n}{2}(\zeta-\phi)} - \frac{2\left(\frac{r}{a}\right)\sin(\zeta-\phi)}{1+\left(\frac{r}{a}\right)^2 - 2\left(\frac{r}{a}\right)\cos(\zeta-\phi)}\right. \\
&\quad \left.-\frac{n\left(\frac{r}{a}\right)^{\frac{n}{2}}\sin\frac{n}{2}(\zeta+\phi)}{1+\left(\frac{r}{a}\right)^n - 2\left(\frac{r}{a}\right)^{\frac{n}{2}}\cos\frac{n}{2}(\zeta+\phi)}\right). \qquad (6.27)
\end{aligned}$$

At vortex 1, $(r,\zeta)=(a,\phi)$ and $v_r=\frac{da}{dt}=\dot{a}$. Initially setting just $r=a$ into equation (6.27) gives

$$v_r=\dot{a}=-\left[\frac{\Gamma}{4\pi a}\left(\frac{n\sin\frac{n}{2}(\zeta-\phi)}{2-2\cos\frac{n}{2}(\zeta-\phi)}-\frac{\sin(\zeta-\phi)}{1-\cos(\zeta-\phi)}-\frac{n\sin\frac{n}{2}(\zeta+\phi)}{2-2\cos\frac{n}{2}(\zeta+\phi)}\right)\right]_{\zeta=\phi}.$$

It is easy to show that

$$\frac{\sin x}{1-\cos x}=\cot\frac{x}{2},$$

giving

$$\dot{a}=\left[-\frac{\Gamma}{4\pi a}\left(\frac{n}{2}\cot\frac{n}{4}(\zeta-\phi)-\cot\frac{1}{2}(\zeta-\phi)-\frac{n}{2}\cot\frac{n}{4}(\zeta+\phi)\right)\right]_{\zeta=\phi}. \tag{6.28}$$

Now the Taylor expansion of $\cot Ax$ near $x=0$ is

$$\cot Ax=\frac{1}{Ax}+O(x).$$

Consequently, the first two terms of equation (6.28) may be written as

$$\begin{aligned}-\frac{\Gamma}{4\pi a}\left(\frac{n}{2}\cot\frac{n}{4}(\zeta-\phi)-\cot(\zeta-\phi)\right) &= -\frac{\Gamma}{4\pi a}\left(\frac{n}{2}\left(\frac{4}{n(\zeta-\phi)}+O(\zeta-\phi)\right)\right.\\ &\quad\left.-\left(\frac{2}{\zeta-\phi}+O(\zeta-\phi)\right)\right)\\ &= O(\zeta-\phi).\end{aligned}$$

Thus in the limit $\zeta\to\phi$, these two terms cancel. This is to be expected, as these terms represent the motion induced by other vortices of the same sign, equally spaced on the circle $r=a$. It is a well-known result (see Acheson [1990] p. 196) that in such a situation the vortices just rotate about the centre of the circle with angular velocity

$$\Omega=(n-1)\frac{\Gamma}{4\pi a^2}.$$

Hence, we would expect no contribution to the radial velocity of vortex 1 from these vortices.

The equation for the radial motion is therefore

$$\dot{a}=\frac{\Gamma}{4\pi a}\left(\frac{n}{2}\right)\cot\frac{n\phi}{2}.$$

Similarly, we may find $\dot{\phi}$ using equation (6.26),

$$a\dot{\phi}=[v_\zeta]_{(a,\phi)}=\left[-\frac{\partial\tilde{\psi}}{\partial r}\right]_{(a,\phi)}.$$

This gives

$$a\dot{\phi} = \left[\frac{\Gamma}{4\pi}\left(\frac{\frac{nr^{n-1}}{a^n} - \frac{nr^{\frac{n}{2}-1}}{a^{\frac{n}{2}}}\cos\frac{n}{2}(\zeta-\phi)}{1+\left(\frac{r}{a}\right)^n - 2\left(\frac{r}{a}\right)^{\frac{n}{2}}\cos\frac{n}{2}(\zeta-\phi)} - \frac{\frac{2r}{a^2} - \frac{2}{a}\cos(\zeta-\phi)}{1+\left(\frac{r}{a}\right)^2 - 2\left(\frac{r}{a}\right)\cos(\zeta-\phi)}\right.\right.$$
$$\left.\left. - \frac{\frac{nr^{n-1}}{a^n} - \frac{nr^{\frac{n}{2}-1}}{a^{\frac{n}{2}}}\cos\frac{n}{2}(\zeta+\phi)}{1+\left(\frac{r}{a}\right)^n - 2\left(\frac{r}{a}\right)^{\frac{n}{2}}\cos\frac{n}{2}(\zeta+\phi)}\right)\right]_{(a,\phi)}. \tag{6.29}$$

Setting $r = a$ gives

$$\begin{aligned} a\dot{\phi} &= \left[\frac{\Gamma}{4\pi}\left(\frac{\left(\frac{n}{a}\right)(1-\cos\frac{n}{2}(\zeta-\phi))}{2-2\cos\frac{n}{2}(\zeta-\phi)} - \frac{\frac{2}{a}(1-\cos(\zeta-\phi))}{2-2\cos(\zeta-\phi)}\right.\right. \\ &\quad \left.\left. - \frac{\left(\frac{n}{a}\right)(1-\cos\frac{n}{2}(\zeta+\phi))}{2-2\cos\frac{n}{2}(\zeta+\phi)}\right)\right] \\ &= \left[\frac{\Gamma}{4\pi}\left(\frac{n}{2a} - \frac{1}{a} - \frac{n}{2a}\right)\right] \\ &= -\frac{\Gamma}{4\pi a}. \end{aligned} \tag{6.30}$$

Hence we end up with the two equations

$$\dot{a} = \frac{\Gamma}{4\pi a}\left(\frac{n}{2}\right)\cot\frac{n\phi}{2}, \tag{6.31}$$

$$\dot{\phi} = -\frac{\Gamma}{4\pi a^2}. \tag{6.32}$$

6.5.3 Solving for the motion of a vortex

We may now proceed to solve for the motion of vortex 1, by dividing equation (6.31) by equation (6.32) to give

$$\frac{\dot{a}}{\dot{\phi}} = \frac{da}{d\phi} = -a\left(\frac{n}{2}\right)\cot\frac{n\phi}{2}. \tag{6.33}$$

Solving (6.33) for $a(\phi)$ gives

$$a(\phi) = A\csc\left(\frac{n\phi}{2}\right) \tag{6.34}$$

for some constant A. At $t = 0$ we have $a = r_0$ and $\phi = \frac{1}{2}\frac{2\pi}{n} = \frac{\pi}{n}$, and thus the initial condition

$$a\left(\frac{\pi}{n}\right) = r_0. \tag{6.35}$$

Equations (6.34) and (6.35) together then lead to

$$a(\phi) = r_0\csc\left(\frac{n\phi}{2}\right). \tag{6.36}$$

This is the equation given by Greenhill [1878]. However, he does not go on to solve for the dependencies of a and ϕ on t, as we require.

Substituting (6.36) into equation (6.32) gives

$$\dot{\phi} = -\frac{\Gamma}{4\pi r_0^2}\sin^2\left(\frac{n\phi}{2}\right).$$

Solving this together with the initial condition $\phi(0) = \frac{\pi}{n}$, we get ϕ as a function of t,

$$\phi(t) = \frac{2}{n}\cot^{-1}\left(\frac{\Gamma n}{8\pi r_0^2}t\right). \tag{6.37}$$

This may be rearranged to

$$\cot\left(\frac{n\phi}{2}\right) = \frac{\Gamma n}{8\pi r_0^2}t,$$

so that equation (6.31) becomes

$$\dot{a} = \frac{\Gamma}{4\pi a}\frac{n}{2}\left(\frac{\Gamma n}{4\pi r_0^2}t\right).$$

Using the initial condition $a(0) = r_0$, we find

$$a(t) = r_0\left[1 + \left(\frac{\Gamma n}{8\pi r_0^2}t\right)^2\right]^{\frac{1}{2}}. \tag{6.38}$$

We can easily deduce from equations (6.37) and (6.38) that as $t \to \infty$, $a \to \infty$ and $\phi \to 0$ as we would expect. However, what is of greater interest is the distance between the vortices in each pair and their velocity as $t \to \infty$. If we denote the distance between the vortices as $l(t)$ and their displacement along their centre line as $x(t)$, the distance $l(t)$ is given by

$$l(t) = 2\,a\sin(\phi) = 2\,r_0\csc\left(\frac{n\phi}{2}\right)\sin(\phi) = 2\,r_0\frac{\sin(\phi)}{\sin\left(\frac{n\phi}{2}\right)}.$$

As we know already that as $t \to \infty$, $\phi \to 0$, we see (using L'Hopital's rule)

$$\begin{aligned}\lim_{t\to\infty} l(t) &= \lim_{\phi\to 0} 2\,r_0\frac{\sin(\phi)}{\sin\left(\frac{n\phi}{2}\right)} \\ &= \lim_{\phi\to 0} 2\,r_0\frac{\cos(\phi)}{\frac{n}{2}\cos\left(\frac{n\phi}{2}\right)} \\ &= \frac{4r_0}{n}.\end{aligned} \tag{6.39}$$

To find the velocity of the vortices as $t \to \infty$, we note that the x-coordinate of vortex 1 is given by

$$x(t) = a(t)\cos(\phi).$$

The velocity of the vortices as $t \to \infty$ is therefore

$$\begin{aligned}
\lim_{t\to\infty} \dot{x}(t) &= \lim_{t\to\infty} \left[\dot{a}\cos(\phi) - a\dot{\phi}\sin\phi\right] \\
&= \lim_{t\to\infty} \left[\frac{\Gamma n}{8\pi a}\cot\left(\frac{n\phi}{2}\right)\cos(\phi) + \frac{\Gamma}{4\pi a}\sin(\phi)\right] \\
&= \lim_{\phi\to 0} \left[\frac{\Gamma n}{8\pi r_0}\cos(\phi)\cos\left(\frac{n\phi}{2}\right) + \frac{1}{r_0}\sin(\phi)\sin\left(\frac{n\phi}{2}\right)\right] \\
&= \frac{\Gamma n}{8\pi r_0} \\
&= \frac{\Gamma}{2\pi\left(\frac{4r_0}{n}\right)} \\
&= \frac{\Gamma}{2\pi l_\infty}, \qquad (6.40)
\end{aligned}$$

where subscript infinity denotes the limit as $t \to \infty$. This result is no surprise, as we expect that the late-time motion of any one vortex will be primarily determined by its partner. Influence from other vortices will wane, as the distance between different vortex pairs increases with time.

We expect the interface to travel at the same velocity as the vortices at late-times, just as for Likhachev and Jacobs [2005], thus approximately following the relation

$$r(t) = \frac{\Gamma n}{8\pi r_0} t + C, \qquad (6.41)$$

for some constant C that depends on k. It will therefore be linear in time, in contrast to the behaviour for a flat interface found by Jacobs and Sheeley [1996], where the growth is asymptotically logarithmic. We define the dimensional wavelength of the disturbance on the interface at time $t = 0$ as

$$\lambda = \frac{2\pi}{\frac{n}{2}} r_0 = \frac{4\pi r_0}{n},$$

and hence the dimensional wavenumber as

$$k = \frac{2\pi}{\lambda} = \frac{n}{2r_0}. \qquad (6.42)$$

Equation (6.41) then becomes

$$kr(t) = \frac{\Gamma k^2}{4\pi} t + kC.$$

Taking the scalings as used in Jacobs and Sheeley [1996], we write

$$\tilde{t} = \frac{\Gamma k^2}{4} t,$$

$$\tilde{r} = kr,$$

leading to the equation

$$\tilde{r}(\tilde{t}) = \frac{1}{\pi}\tilde{t} + \tilde{C}.$$

6.5.4 Full solution for the flow-field

The analysis presented in section 6.5.1 can be extended to find a theoretical prediction for the flow at any point. We then proceed to use this information to find a prediction for the interfacial displacement for all of $0 < t < \infty$.

6.5.5 Stream function

Following the analysis given in section 6.5.1, the stream function for the flow away from any of the vortex cores is

$$\begin{aligned}\psi &= -\frac{\Gamma}{4\pi}\left(-2\ln a + \ln\left[1+\left(\frac{r}{a}\right)^n - 2\left(\frac{r}{a}\right)^{\frac{n}{2}}\cos\frac{n}{2}(\zeta-\phi)\right]\right.\\ &\quad\left.-\ln\left[1+\left(\frac{r}{a}\right)^n - 2\left(\frac{r}{a}\right)^{\frac{n}{2}}\cos\frac{n}{2}(\zeta+\phi)\right]\right), \qquad (6.43)\end{aligned}$$

where a and ϕ are as derived in section 6.5.1. This is the stream function used previously but with the addition of the term representing vortex 1.

The maximum displacement of the interface in the direction of increasing r will occur on the centre line between two vortices in a pair. Due to the rotational symmetry of the problem, we may just consider the motion along the line $\zeta = 0$ so as to simplify the analysis.

The angular velocity of any point along the line $\zeta = 0$ is given by

$$\begin{aligned}r\dot{\zeta} &= \left[-\frac{\partial\psi}{\partial r}\right]_{(r,0)}\\ &= \frac{\Gamma}{4\pi}\left[\frac{\frac{n}{a}\left(\left(\frac{r}{a}\right)^{n-1} - \left(\frac{r}{a}\right)^{\frac{n}{2}-1}\cos\frac{n}{2}(0-\phi)\right)}{1+\left(\frac{r}{a}\right)^n - 2\left(\frac{r}{a}\right)^{\frac{n}{2}}\cos\frac{n}{2}(0-\phi)}\right.\\ &\quad\left.-\frac{\frac{n}{a}\left(\left(\frac{r}{a}\right)^{n-1} - \left(\frac{r}{a}\right)^{\frac{n}{2}-1}\cos\frac{n}{2}(0+\phi)\right)}{1+\left(\frac{r}{a}\right)^n - 2\left(\frac{r}{a}\right)^{\frac{n}{2}}\cos\frac{n}{2}(0+\phi)}\right]\\ &= 0. \qquad (6.44)\end{aligned}$$

This is as expected, due to the symmetry of the problem. Consequently we need only consider the radial component, given by

$$\begin{aligned}\dot{r} &= \left[\frac{1}{r}\frac{\partial\psi}{\partial\phi}\right]_{(r,0)}\\ &= -\frac{\Gamma}{4\pi r}\left[\frac{n\left(\frac{r}{a}\right)^{\frac{n}{2}}\sin\frac{n}{2}(0-\phi)}{1+\left(\frac{r}{a}\right)^n - 2\left(\frac{r}{a}\right)^{\frac{n}{2}}\cos\frac{n}{2}(0-\phi)} - \right.\\ &\quad\left.\frac{n\left(\frac{r}{a}\right)^{\frac{n}{2}}\sin\frac{n}{2}(0+\phi)}{1+\left(\frac{r}{a}\right)^n - 2\left(\frac{r}{a}\right)^{\frac{n}{2}}\cos\frac{n}{2}(0+\phi)}\right]\\ &= \frac{\Gamma}{2\pi r}\left[\frac{n\left(\frac{r}{a}\right)^{\frac{n}{2}}\sin\frac{n}{2}\phi}{1+\left(\frac{r}{a}\right)^n - 2\left(\frac{r}{a}\right)^{\frac{n}{2}}\cos\frac{n}{2}\phi}\right]. \qquad (6.45)\end{aligned}$$

Using equation (6.42), we now define the function $\hat{a}(t)$ to be

$$\begin{aligned}\hat{a}(t) &= \frac{a(t)}{r_0} \\ &= \left(1+\left(\frac{\Gamma k^2}{2\pi n}t\right)^2\right)^{\frac{1}{2}}.\end{aligned}$$

Using this definition, together with equation (6.36), equation (6.45) may be rearranged to

$$\dot{r} = \frac{\Gamma\, k}{\pi \hat{a}^2}\frac{\left(\frac{2k\,r}{n\hat{a}}\right)^{\frac{n}{2}-1}}{1+\left(\frac{2k\,r}{n\hat{a}}\right)^n - 2\left(\frac{2k\,r}{n\hat{a}}\right)^{\frac{n}{2}}\left(1-\frac{1}{\hat{a}^2}\right)^{\frac{1}{2}}}. \tag{6.46}$$

Together with the initial condition

$$r(0) = r_0 = \frac{n}{2k},$$

this equation may be solved numerically to give a theoretical prediction for the maximum interface displacement as a function of time t.

6.5.6 Special Cases

We can also solve equation (6.46) analytically for two special cases, $n = 2$ and $n = \infty$. These cases are the lower and upper limits for n, and feature the great simplification that the spacing between the vortices remains constant.

n=2

The $n = 2$ case represents the situation of just two vortices of opposite sign, located at $(r_0, \frac{\pi}{2})$ and $(r_0, -\frac{\pi}{2})$ for $t = 0$. As is well-known (see Batchelor [1967]), these two vortices should then maintain their spacing for all time t and move parallel to the line $\zeta = 0$ at speed

$$\begin{aligned}v &= \frac{\Gamma}{4\pi r_0} \\ &= \frac{\Gamma k}{4\pi},\end{aligned} \tag{6.47}$$

where here

$$k = \frac{1}{r_0}.$$

In non-dimensional coordinates, this becomes

$$\tilde{v} = \frac{d\tilde{r}}{d\tilde{t}} = \frac{1}{\pi}.$$

The velocity at the point x on the line $\zeta = 0$ will be given by the sum of the velocities induced by the two vortices,

$$\begin{aligned} \dot{x}(t) &= 2\left[\frac{\Gamma}{4\pi}\left(\frac{2\,r_0}{(x(t)-vt)^2+r_0^2}\right)\right] \\ &= \frac{\Gamma}{\pi}\frac{k}{(kx-kvt)^2+1}. \end{aligned} \tag{6.48}$$

If we return to equation (6.46), putting $n = 2$ gives

$$\hat{a} = \left(1+\left(\frac{\Gamma k^2}{4\pi}t\right)^2\right)^{\frac{1}{2}},$$

$$\begin{aligned} \dot{r} &= \frac{\Gamma k}{\pi \hat{a}^2}\frac{1}{1+\left(\frac{kr}{\hat{a}}\right)^2-2\left(\frac{kr}{\hat{a}}\right)\left(1-\frac{1}{\hat{a}^2}\right)^{\frac{1}{2}}} \\ &= \frac{\Gamma}{\pi}\frac{k}{\hat{a}^2+(kr)^2-2kr(\hat{a}^2-1)^{\frac{1}{2}}} \\ &= \frac{\Gamma}{\pi}\frac{k}{1+(kvt)^2+(kr)^2-2(kr)(kvt)} \\ &= \frac{\Gamma}{\pi}\frac{k}{(kr-kvt)^2+1}. \end{aligned}$$

This acts as support that equation (6.46) is correct.

This equation, together with the initial condition

$$r(0) = \frac{1}{k},$$

may be solved analytically to give the implicit solution

$$kr - \frac{4\sqrt{3}}{3}\tanh^{-1}\left(\frac{\sqrt{3}}{3}\left(kr-\frac{\Gamma k^2}{4\pi}t\right)\right) = 1 - \frac{4\sqrt{3}}{3}\tanh^{-1}\left(\frac{\sqrt{3}}{3}\right).$$

Scaling as before gives

$$\tilde{r} - \frac{4\sqrt{3}}{3}\tanh^{-1}\left(\frac{\sqrt{3}}{3}\left(\tilde{r}-\frac{1}{\pi}\tilde{t}\right)\right) = 1 - \frac{4\sqrt{3}}{3}\tanh^{-1}\left(\frac{\sqrt{3}}{3}\right). \tag{6.49}$$

n$\rightarrow \infty$

We can also find an analytical solution to equation (6.46) in the case of $n \to \infty$ while k remains constant and finite. As

$$k = \frac{n}{2r_0}$$

this means we are taking r_0 to infinity too. Physically, this corresponds to an infinite row of vortices at a distance

$$\lambda = \frac{2\pi}{k}$$

apart, the same situation as considered by Jacobs and Sheeley [1996]. As we shall see, we end up with the same equation.

We start by defining the function

$$x(t) = r(t) - r_0$$

and hence the function

$$\begin{aligned} \tilde{x}(\tilde{t}) &= k\,x(t) \\ &= \tilde{r}(\tilde{t}) - k\,r_0 \\ &= \tilde{r}(\tilde{t}) - \frac{n}{2}. \end{aligned}$$

It follows that

$$\tilde{r} = \frac{n}{2} + \tilde{x}, \tag{6.50}$$

$$\frac{d\tilde{r}}{d\tilde{t}} = \frac{d\tilde{x}}{d\tilde{t}}, \tag{6.51}$$

$$\tilde{x}(0) = 0. \tag{6.52}$$

As $n \to \infty$, $\hat{a} \to 1$ so that equation (6.46) becomes

$$\begin{aligned} \frac{d\tilde{x}}{d\tilde{t}} &= \frac{4}{\pi} \frac{\left(1 + \frac{2\tilde{x}}{n}\right)^{\frac{n}{2}-1}}{1 + \left(1 + \frac{2\tilde{x}}{n}\right)^{n}} \\ &= \frac{4}{\pi} \left(\frac{1}{1 + \frac{2\tilde{x}}{n}} \right) \frac{\left[\left(1 + \frac{2\tilde{x}}{n}\right)^{n}\right]^{\frac{1}{2}}}{1 + \left(1 + \frac{2\tilde{x}}{n}\right)^{n}}. \end{aligned} \tag{6.53}$$

It is well-known (see Korovkin [1968]) that for all finite A,

$$\left(1 + \frac{A}{n}\right)^{n} \to e^{A} \qquad \text{as} \quad n \to \infty \tag{6.54}$$

Thus in the limit $n \to \infty$ keeping t and $\tilde{x}$ fixed, equation (6.53) becomes

$$\begin{aligned} \frac{d\tilde{x}}{d\tilde{t}} &= \frac{4}{\pi} \frac{e^{\tilde{x}}}{1 + e^{2\tilde{x}}} \\ &= \frac{4}{\pi} \frac{1}{e^{\tilde{x}} + e^{-\tilde{x}}} \\ &= \frac{2}{\pi} \frac{1}{\cosh \tilde{x}}. \end{aligned} \tag{6.55}$$

Putting this back into unscaled coordinates,

$$\begin{aligned} k\tfrac{4}{\Gamma k^2}\dot{x} &= \frac{2}{\pi}\frac{1}{\cosh kx} \\ \Rightarrow \qquad \dot{x} &= \frac{1}{2\pi}\frac{\Gamma k}{\cosh kx}, \end{aligned} \tag{6.56}$$

the same equation found by Jacobs and Sheeley [1996]. They go on to solve this equation, which in scaled coordinates becomes

$$\tilde{x}(t) = \sinh^{-1}\left(\frac{2}{\pi}\tilde{t} + \sinh x_0\right). \tag{6.57}$$

It is notable that this solution behaves like $\ln(2t)$ at infinity, whereas all solutions for finite n behave like $\frac{1}{\pi}\tilde{t}$ at infinity.

6.6 Comparison with experiments

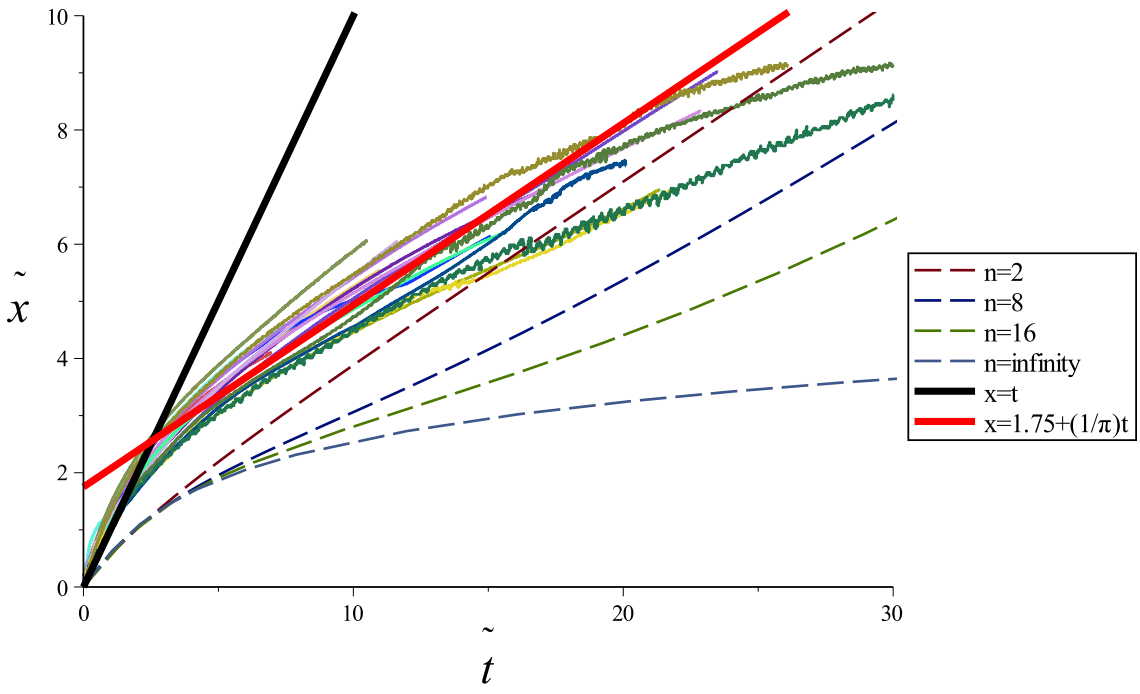

Figure 6.10: The interfacial displacement $\tilde{x}$ plotted against time $\tilde{t}$. Shown are theoretical predictions for $n = 2$, $n = 8$, $n = 16$, and $n = \infty$ (the model of Jacobs and Sheeley [1996]), together with the experimental data, and the lines $\tilde{x} = \tilde{t}$ (black) and $\tilde{x} = 1.75 + (1/\pi)\tilde{t}$ (red).

Theoretical solutions for $n = 2, 8, 16$ and ∞ plotted on figure 6.10, along with our experimental data and the lines $x = t$ and $x = (1/\pi)t$. The solutions for $2 < n < \infty$ lie between those for $n = 2$ and $n = \infty$, eventually tending to parallel with $\frac{1}{\pi}\tilde{t}$.

When compared with this experimental data, the theoretical predictions appear to have the correct shape, but lie below the experimental data. This was also observed by Jacobs and Sheeley [1996], (with the initial gradient out by the same factor of $2/\pi$) and is due to the different initial distributions of vorticity. With the vorticity initially distributed sinusoidally, 2D potential theory (as discussed in chapter 4) predicts the initial velocity to be greater than that for point vortices by the factor $2/\pi$. Rescaling the theoretical predictions so that the initial velocity is the same provides a better match at early times. However, this rescaling is equivalent to increasing the vorticity, and thus doing so means the theoretical models now over-estimate the final, constant late-time velocity. As stated before, our model also assumes the same circulation within each ring, when in reality it will be a function of polar angle ϕ. This may also have led in inaccuracy, though for the large k in our experiments ($k > 6$ so that $n > 12$) our model should still be accurate near $\phi = \pi/2$ where our measurements were taken, so we do not anticipate this difference being a source of significant inaccuracy.

Also plotted in figure 6.10 is the best fit for the asymptotic behaviour $\tilde{a} = \tilde{C} + (1/\pi)\tilde{t}$ with $\tilde{C} = 1.75$. Here, $\tilde{C}$ is a rough measure of the time taken for the interface to roll-up, and compares well with the value found by Jacobs and Sheeley [1996], $\tilde{C} = 2$. This best fit asymptotic behaviour provides a good fit with the data between $\tilde{t} = 5$ and $\tilde{t} = 20$. However, it does appear to overestimate the asymptotic growth rate, $\dot{\tilde{a}} = \frac{1}{\pi}$. The reason for this will be discussed in section 6.7, but is a combination of the initial interfacial vorticity being an overestimate for the circulation within the rings, and the rings approaching so closely that the modeling of them as point vortices is no longer valid.

No attempt is made to compare our data to other models for non-linear incompressible RMM as detailed by Niederhaus and Jacobs [2003], as all are only applicable for flat interfaces. On such interfaces, the vortex patches remain stationary under their mutually induced action, whereas for our axisymmetric spherical interface they do not. Comparing the models therefore makes little sense, save for noting that the asymptotic growth rate for $A = 0$ on a flat interface is proportional to $1/t$, decaying over all time, whereas for a spherical interface it tends to a constant value, and so does not decay.

To show that it is indeed the movement of the vortex rings that drives the later growth, we have used the PIV technique described in chapter 4 to track the rings after the rupture of a balloon on a water/water interface. Two rings are followed, with the location of the rings determined by the positions of minimum and maximum vorticity. Results for the distance between the rings L and their displacement from the initial interface $R - R_0$ over time is given in figure 6.11, along with theoretical predictions, for which the circulation of each vortex was chosen to be the circulation within the half-wavelength at the moment of rupture. Both L and $R - R_0$ agree well with theory, when adjusted to allow for the time taken for the vorticity to roll up into discrete rings. In particular, they show that both the distance between the rings and their speed approaches the correct asymptotic value for $\tilde{t} < 25$. At later time, however, the speed of the vortices decreases away from the theoretical asymptotic value. The reason for this, as will be discussed in section 6.8, is that the circulation within each rings decays over time.

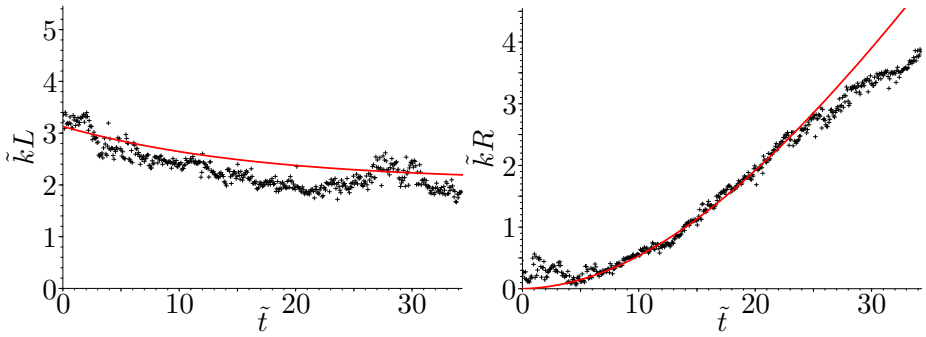

(a) L (b) R

Figure 6.11: The behaviour over time of **(a)** the distance between two vortices, and **(b)** their displacement from the interface at the moment of rupture, for a 130 mm balloon forced at 50 Hz with water both inside and outside the balloon. The black marks denote the experimental data, while the red line gives the theoretical prediction. Due to the time taken for the vorticity to roll-up, time $\tilde{t} = 0$ is not the moment of rupture but chosen to be 5.3 after to give the best fit to the data.

6.7 Simulations

We also simulated the experiment using a 2D vorticity-stream function scheme, in which vorticity was conserved. The flow was assumed inviscid, so that the evolution of the flow in time was found using

$$\frac{D\omega}{Dt} = 0, \tag{6.58}$$

that was solved using a SHARP (see Leonard [1988]) third-order upwind scheme, together with an explicit first-order time step, on a staggered grid. To determine the flow field at each time step, the stream function ψ was found using

$$\nabla^2\psi = -\omega. \tag{6.59}$$

This equation was solved numerically using a second-order multigrid method.

Our simulations were run on a grid of size 512 by 512, with rigid boundaries (so that there was no flow normal to the boundary). To valid the code, simple tests were run, initiated with a pair of small vortex patches of equal magnitude but opposite sign circulation, whose behaviour should be approximated by that of two point vortices. The behaviour of the two patches within the code then closely matched the linear propagation speed as predicted by point vortex theory (see equation 6.40).

To simulate our bursting balloons, we used a radius for the interface $R = 50$. Consequently, the finite size of the computational domain did not play a significant role until the vortex rings had propagated far from the initial interface, by which time their propagation speed was approximately constant, in accordance with their expected asymptotic behaviour. The number of half-wavelengths and hence vortex patches $n(= 2k)$ was then varied between 4 and 32, a similar range to that observed in our experiments. Using polar coordinates (r, θ), each run featured a sinusoidal initial vorticity distribution ω of the form

$$\omega = \begin{cases} \sin\frac{n\theta}{2} & R-1 < r < R+1 \\ \\ 0 & \text{otherwise} \end{cases} \tag{6.60}$$

This distribution of vorticity is different from that seen in experiments, where the vorticity depended instead on spherical harmonics $P_k(\cos(\phi))$. However, it was shown in chapter 4 how, for large k, $P_k(\cos(\phi) \asymp \sqrt{2/k\pi}\cos(k\phi)$. Thus, these simulations may again be regarded as accurate for large k. The fluid inside and outside this circle was the same, only with the fluid inside carrying a tracer to allow determination of the interface. Unlike our experiments, these simulations were not axisymmetric but 2D. This would not affect the circulation of each ring (by Kelvin's circulation theorem), but it did mean the simulations would not capture the decrease in core cross-sectional area with increasing distance from the initial interface. However, as the distance travelled by the vortex rings in our experiments was typically small compared with their initial radius, the influence of such changes in core size would also likely be small. By performing these simulations, we hoped to understand whether indeed the interfacial vorticity could drive the late-time growth, and if so, gain greater understanding of the process.

Sample images produced by these simulations are seen in figure (6.12). These clearly demonstrate the same phenomena as observed in experiments, as the initial vorticity distribution rolls up into vortex cores that then propagate outwards in pairs, with little vorticity elsewhere. We may then attempt to match the simulations to experiments, by comparing the interfacial displacement (figure 6.13). This shows a good, if approximate, agreement between theory and experiments, strongly suggesting that it was indeed the interfacial vortex that drove the late-time growth of the interfacial amplitude. Comparisons with the theory is provided by tracking the motion of the vortex cores (figure 6.14) for both the distance between the cores and their displacement from the initial interface, as was performed for experiments in figure 6.11. Both figures shows a pleasing agreement with the theory, if allowance is made for the time taken for the vorticity to roll up.

The most useful outcome of these simulations, however, was that they showed how, even with no viscosity or experimental error, our point vortex model overestimates the final speed of the vortex dipoles by around 20%, based on assuming the circulation of each point vortex is equal to that initially present on the interface in each half-wavelength. A small amount of vorticity was shed during roll-up and left behind as the vortices propagated away, accounting for around $10-15\%$ of the difference. The remaining deficit was likely due to the close approach of the vortex patches at late-times meaning that the point vortex approximation was no longer valid. These two phenomena shall be discussed in the following sections. Both issues are consequences of the movement of the vortex rings away from the interface, thus would not be issues for roll-up of a 2D interface.

6.7.1 Roll-up

How vortex sheets roll up is a very complicated problem, as discussed by Saffman [1992]. As our focus is on the asymptotic behaviour of the interface, we do not consider the process by which the interfacial vorticity rolled up in detail. However, there is one aspect of the roll up that is important later on: how much of the initial vortex sheet was actually carried with the vortex rings as they propagated away from the interface, and thus contributed to their circulation. Figure 6.15 shows an example of

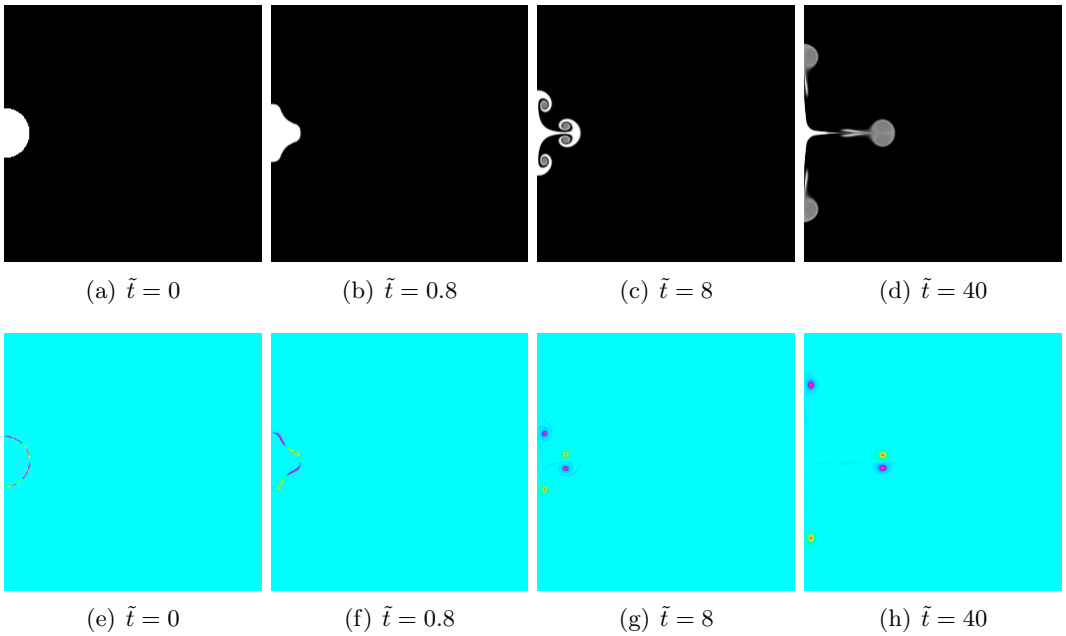

(a) $\tilde{t} = 0$ (b) $\tilde{t} = 0.8$ (c) $\tilde{t} = 8$ (d) $\tilde{t} = 40$

(e) $\tilde{t} = 0$ (f) $\tilde{t} = 0.8$ (g) $\tilde{t} = 8$ (h) $\tilde{t} = 40$

Figure 6.12: Typical images from the vorticity-stream function simulations. The initial condition was a sinusoidal vorticity distribution restricted to the interface. Images **(a)** - **(d)** show the white tracer carried by the inner fluid to permit visualisation, but there is otherwise no difference between the phases. Images **(e)** - **(h)** show the vorticity, with purple negative, cyan zero, and orange positive.

the late-time vorticity distribution for a simulation of the $n = 4$ case, with a significant amount of the vorticity not rolled up into the vortex patches. As shown in the previous sections, the translation speed for each pair of vortex rings tended to that for a pair of oppositely-signed point vortices, that was linearly dependent on the circulation of each vortex. Consequently, any reduction in the circulation caused an equivalent decrease in the final speed of the vortices.

The behaviour of pairs of vortex patches has been studied by a number of authors. In particular, Trieling et al. [1998] studied the motion of 2D vortex dipoles in strain flow, which is flow where the two vortices were either being pushed together (cooperative) or pulled apart (adverse) by the externally-applied flow. For any vortex pair in our initial arrangement (as seen in figure 6.5), the flow induced by the other vortices takes a similar form to a cooperative strain flow, thus suggesting comparison with their work. Notably, Trieling et al. [1998] discuss the concept of the dipole having an atmosphere, that is the fluid elements dragged along with the dipole. For a dipole with no external flow, the atmosphere is an ellipse that remains constant in time. However, Trieling et al. [1998] found that for a dipole in cooperative strain flow, the atmosphere changes, becoming smaller, so that of the fluid initially within the atmosphere before the external flow is applied, most is retained in an approximately elliptical head, but with a long, thin tail stretching out behind it. This is closely mirrored by the behaviour of our vortex patches at later times, as displayed in figure 6.15.

To the best of knowledge, no studies have been published examining the behaviour of alternately-signed vortex patches in the cooperative strain flow created by their mutual interaction when arranged

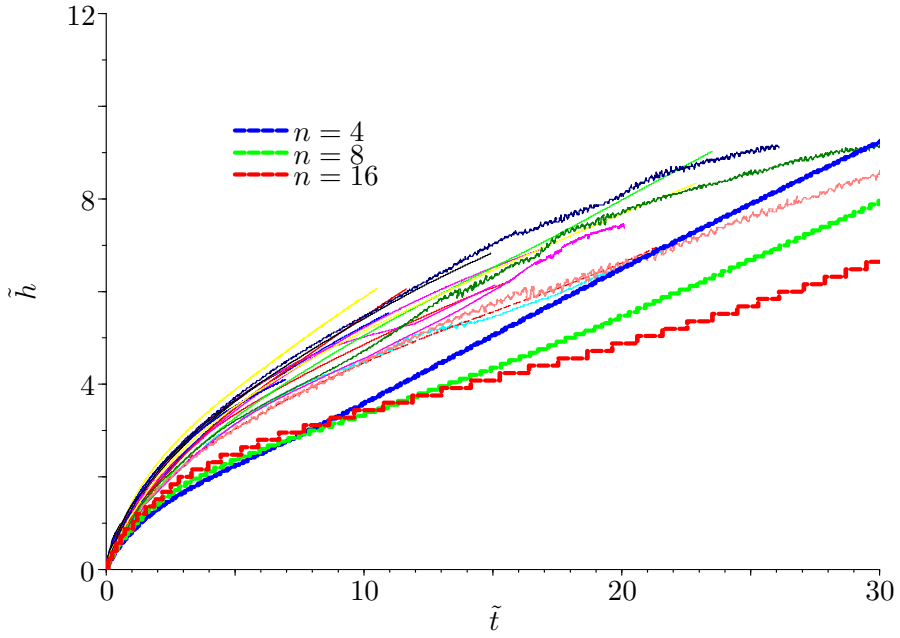

Figure 6.13: The interfacial growth rate of our simulations scaled as before, compared with our experimental data. The number n is the number of vortex patches that form after rupture, $n = 2k$.

on a circle. To observe the process more closely, we used the program Maple to tracking material points initially arranged on a circle, in the flow given by four point vortices of alternating sign initially positioned on the same circle, thus simulating the movement of the interface for the $n = 4$ case. The results are shown in figure 6.16. As seen for our simulations using a continuous distribution of vorticity, while most of the points ended up in the head as it propagated away from the interface, a significant amount of the initial interface was left behind. There were two main contributions to this tail: first, a section of the initial interface near $\phi = 0$ ended up near the line $\phi = \pi/2$, before a section of interface initially adjacent to $\phi = \pi/2$ was left near the initial interface. That this effect occurred when considering point vortices shows that it was not the result of numerical error or of the finite thickness of the initial vorticity distribution, but of the form of the vorticity distribution itself.

This loss of the initial interface to the wake corresponded in our simulations to a loss of circulation, as the initial vorticity was restricted to the interface. As the circulation directly determined the speed, if this loss to the tail was steady over time, it would lead to the vortex patches completely decaying within finite time. Distinct from the observations of Trieling et al. [1998] or any other work in the literature, however, the tail was not evenly distributed, but largest near the initial interface, becoming smaller as the vortices moved away from it. The reason for this was that the rate of strain on each vortex pair was set by the other vortices. As they moved apart, the strain decreased, so less of the initial interface was shed into the tail. This meant that in the simulations, the rate of strain decreased fast enough such that the circulation within each vortex patch did not tend asymptotically to zero, but a non-zero constant value. They therefore would still asymptotically travel at constant, non-zero

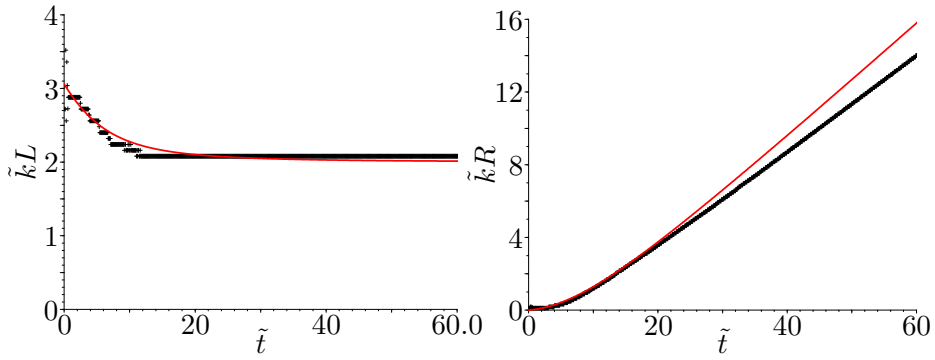

Figure 6.14: The results of 2D vorticity-stream function simulations (black marks) are plotted against theoretical predictions corrected for roll-up (red line) for the $n = 8$ case, for (a) the distance between vortices in a pair and (b) the displacement of their midpoint from its initial position. Unlike for the experiments, no time has been allowed for the vortices to roll-up.

speed, but one smaller than that predicted by considering the circulation to be that within each half-wavelength at $t = 0$.

Obtaining a universally accurate estimate of the amount of vorticity left behind theoretically is difficult. However, our vorticity-stream function simulations revealed that between 11% and 17% of the initial vorticity was left behind, with the proportion increasing for higher k (or equivalently, higher n). However, it is possible that this range was a consequence of resolution issues, as in the limit $n \to \infty$, the configuration approaches that of alternately signed vortices on a straight line (as discussed in section 6.5). Tests on such a flat interface showed that none of the vorticity was left behind, as the vortices remain stationary at all times. Consequently, it is possible that increasing the resolution would reveal different behaviour to that which we observed at higher k. Note that whatever the vorticity left behind, as it was the same for each vortex, the paths of the vortex patches will not significantly change. This is because the paths were shown, for point vortices at least, to be independent of the circulation of each vortex. The circulation left behind will have an influence on the motion of the vortex rings, but it will be weak, as the circulation left behind was far less than that carried with each ring.

Though difficult to see in figure 6.7, this leaving behind of vorticity was also observed for our experiments, and of a similar order. For the experiment shown in figure 6.7, where $k = 10$, the calculated amount of vorticity left behind by the vortex rings at $\tilde{t} = 27.4$ was 15% of the amount within the rings, and thus well within the range found in our simulations.

6.7.2 Finite core size

It was assumed during the derivation of our point vortex model that the radius of the vortex ring cores remained small compared to the distance between different rings over all time. Yet for both experiments (figure 6.7) and simulations (figure 6.12) this was clearly not the case. Instead they approached each other closely, so that each core was deformed by the presence of the other as they formed a dipole. The structure of this dipole depended on how closely the rings approached each other,

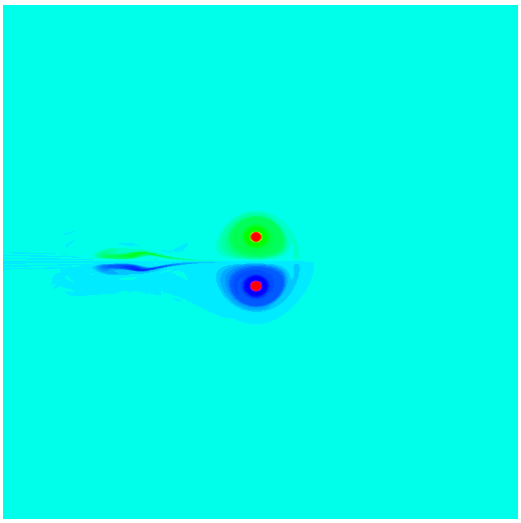

Figure 6.15: The distribution of vorticity for the simulation with $n = 4$ at $\tilde{t} = 32$. A significant amount of vorticity was left behind by the vortex patches as they propagated away from the interface, amounting to 13 % of the total vorticity in the flow.

varying from something approximating the elliptic dipole described by Kizner and Khvoles [2004] for well-separated vortices (for low k) to, for high wavenumber and hence close approach, the circular Lamb-Chaplygin dipole as described by Meleshko and Heijst [1994]. Most lay somewhere in between. Changing the thickness of the initial vortex sheet also influenced the final vorticity structure, with a thicker sheet mirroring the effects of closer approach, making the final distribution more like that of the Lamb-Chaplygin dipole. Such a variation of core size was also seen experiments, though detailed no qualitative study was undertaken. Note, though, that the core size would not simply change linearly with wavelength of the preburst waves, as it was show in chapter 4 how the wavelength $\lambda \propto \omega^{-2/3}$ but the boundary layer thickness $\gamma \propto \omega^{-1/2}$.

The nature of a dipole may be characterised by the relationship between the stream function and vorticity, or by the vorticity distribution in the core. Examples of the stream function-vorticity relationships are shown in figure 6.17 for some simulations, from the linear relationship of a Lamb-Chaplygin dipole to the more sinh-like relationship for the elliptic dipoles described by Kizner and Khvoles [2004]. This range was also found by Trieling et al. [1998] for dipoles in cooperative strain flow. Figure 6.17 also shows the vorticity distribution in both elliptic and circular dipoles, with former taking a Gaussian form and the later that of a Bessel function. Again, the same behaviour was found by Trieling et al. [1998]. As there is no analytical expression for the dipole found by Kizner and Khvoles [2004], it is difficult to calculate the adjustment to the final velocity it would create. However, an exact analytical expression is known for the Lamb-Chaplygin dipole, so the final velocity may be calculated. Indeed, as most of our experiments were conducted with high wavenumber, we would expect most observed dipoles to be closer to this form.

The Lamb-Chaplygin dipole is a solution to the steady two-dimensional Euler equations, with the vorticity distribution (ω) within the dipole taken to be linearly-related to the stream function moving with the dipole (ψ') within a circle of radius R, and zero elsewhere.

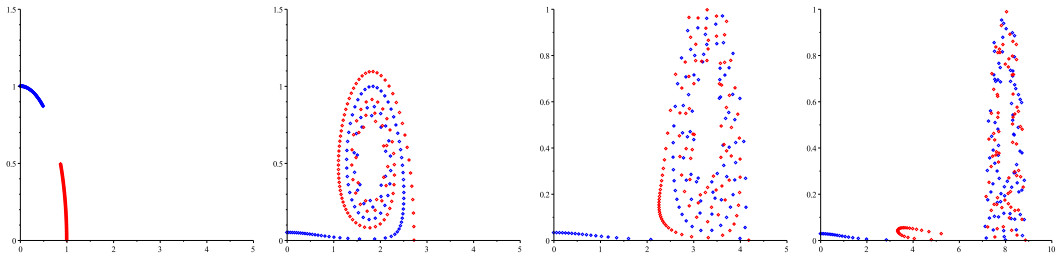

(a) $\tilde{t} = 0$ (b) $\tilde{t} = 10$ (c) $\tilde{t} = 20$ (d) $\tilde{t} = 50$

Figure 6.16: Results from using Maple to solve for the motion of four point vortices of equal strength but alternating sign circulation arranged in a square, so simulating the $n = 4$ case. The blue and red marks represent material points that initially lie on the interface near $\phi = 0$ and $\phi = \pi/2$, respectively. As time progresses, and the interface rolls up, we see that first a section of interface near $\phi = 0$ is left behind, then a section of the interface near $\phi = \pi/2$.

Consider a dipole moving with velocity $U = (U_x, U_y)$, with stream function ψ. Then $\psi' = \psi - U_x y + U_y x$, and

$$\omega = \begin{cases} k^2 \psi', & r \leq R \\ 0, & r > R \end{cases} \tag{6.61}$$

for some constant k. Solving for ψ' and ω leads to

$$\omega = \begin{cases} \frac{-2|U|k}{J_0(kR)} J_1(kr) \sin\theta, & r \leq R \\ 0, & r > R \end{cases} \tag{6.62}$$

$$\psi' = \begin{cases} \frac{-2|U|}{kJ_0(kR)} J_1(kr) \sin\theta, & r \leq R \\ |U| \left(r - \frac{R^2}{r} \right) \sin\theta, & r > R \end{cases} \tag{6.63}$$

where J_i is the ith-order Bessel function of the first kind.

Requiring that the vorticity is zero on $r = R$ needs $J_1(kR) = 0$ and hence $kR = 3.83$. The points of maximum as minimum vorticity are located at $(r, \theta) = (0.48R, \pm\pi/2)$.

This solution has two unknowns, $|U|$ and R. To solve for them, we suppose that the circulation within one half of the dipole (Γ) is known (based on the surface waves present on the balloons at rupture) and that the distance d between the points of maximum and minimum vorticity is known. These conditions may be written mathematically as

$$\Gamma = \frac{2|U|k}{J_0(3.83)} \int_0^\pi \int_0^R J_1(kr) \sin(\theta) r \, dr \, d\theta, \tag{6.64}$$

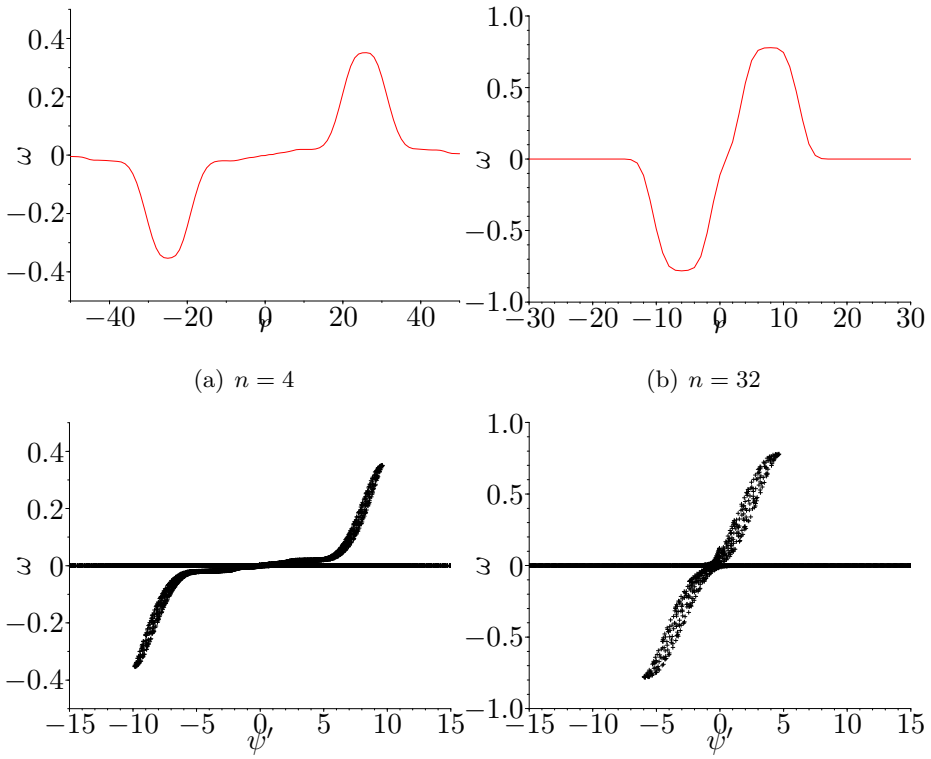

(a) $n = 4$ (b) $n = 32$

(c) $n = 4$ (d) $n = 32$

Figure 6.17: The two limiting late-time forms of the vortex patches seen in simulations. The top two images show the vorticity distribution along a line passing through the centre of both patches. The bottom two images show the relation between the vorticity and the adjusted stream function $\psi' = \psi - U_x y + U_y x$, where the velocity of the vortices is $U = (U_x, U_y)$. These relations were taken at a very late time, when the patches were traveling at near-constant velocity. Images **(a)** and **(c)** are for two patches that do not approach closely, the vorticity distribution approximately Gaussian and the stream function-vorticity relation non-linear. Images **(b)** and **(d)** are for two patches that do approach closely, the vorticity distribution well-approximated by a Bessel function and the stream function-vorticity relation approximately linear.

$$0.96R = d. \tag{6.65}$$

Equation (6.64) may be simplified to

$$\begin{aligned} \Gamma &= \frac{4|U|R}{3.83}\frac{\int_0^{3.83} rJ_1(r)dr}{J_0(3.83)} \\ &\approx 6.83|U|R. \end{aligned} \tag{6.66}$$

Combining equations (6.65) and (6.66) thus gives

$$\begin{aligned} |U| &= \frac{\Gamma}{6.83R} \\ &= \frac{0.96}{6.83}\frac{\Gamma}{d}. \end{aligned} \tag{6.67}$$

It is well known that the speed V of two vortices of strength $+\Gamma$ and $-\Gamma$ a distance d apart is

$$V = \frac{1}{2\pi}\frac{\Gamma}{d},$$

and thus the relative difference is

$$\begin{aligned} \frac{|U|}{V} &= \frac{0.96}{6.83} * \left(\frac{1}{2\pi}\right)^{-1} \\ &\approx \frac{0.035}{0.040} \\ &= 0.88. \end{aligned} \tag{6.68}$$

Should the vortices form a Lamb-Chaplygin dipole, therefore, the velocity will be reduced by approximately 12%. For the more elliptical dipole shapes found by Kizner and Khvoles [2004], the difference with the point vortex velocity is likely to be less, though still significant. Together with the loss of vorticity during roll-up, this explains the discrepancy in final velocity between the theory and simulation, and goes some way to explaining the discrepancy with experiments.

6.8 Vorticity annihilation

In the previous section, reasons behind the discrepancy between the simulations and model were given. Both, however, show significantly different behaviour to the experiments at late-time, meaning $k\dot{a}_0 t > 20$. The model and simulations both predict the growth to approach constant speed as $t \to \infty$. Our experiments, however, show significant decay in the growth rate at later time, even before the dipoles lose structure and the flow becomes fully turbulent. The reason for this is that both the model and simulations neglect viscosity; because of it, the circulation within each vortex ring decays over time once it gets close enough to its partner. This is clearly displayed in figure 6.18 with data from an experiment, where the circulation remains constant while the initial vortex sheet rolls-up, before it then decreases linearly until the flow breaks down. Such a linear decay has been noted before,

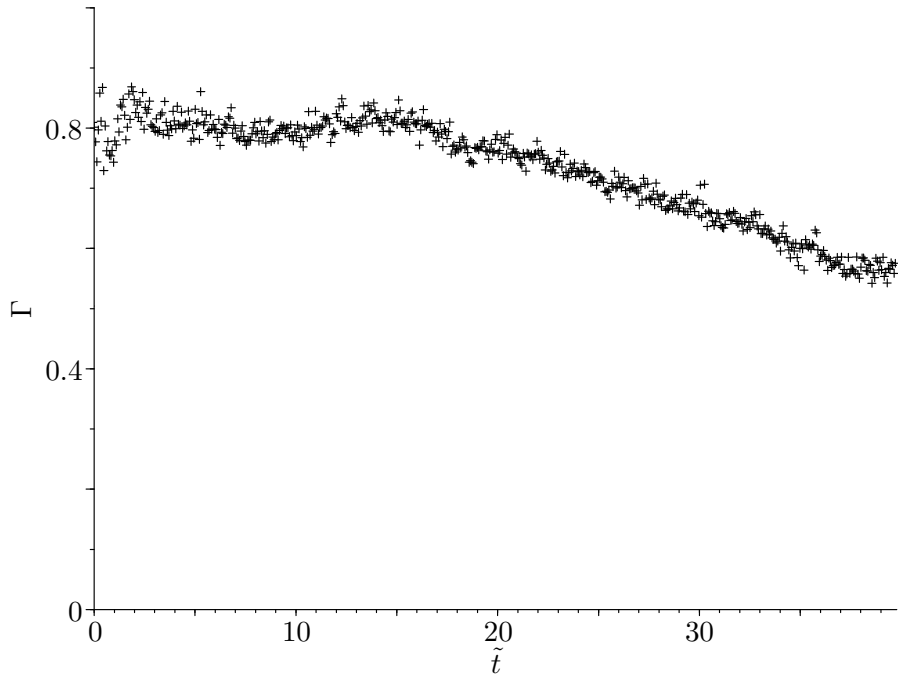

Figure 6.18: The total circulation within one half wavelength (equivalently, one vortex after rupture) plotted against time for a 130 mm balloon forced at 105 Hz. This is the extension of figure 6.8 to later times, where we see the circulation within each vortex ring decrease linearly. Note that this includes any vorticity potentially left behind by the vortex ring during roll-up.

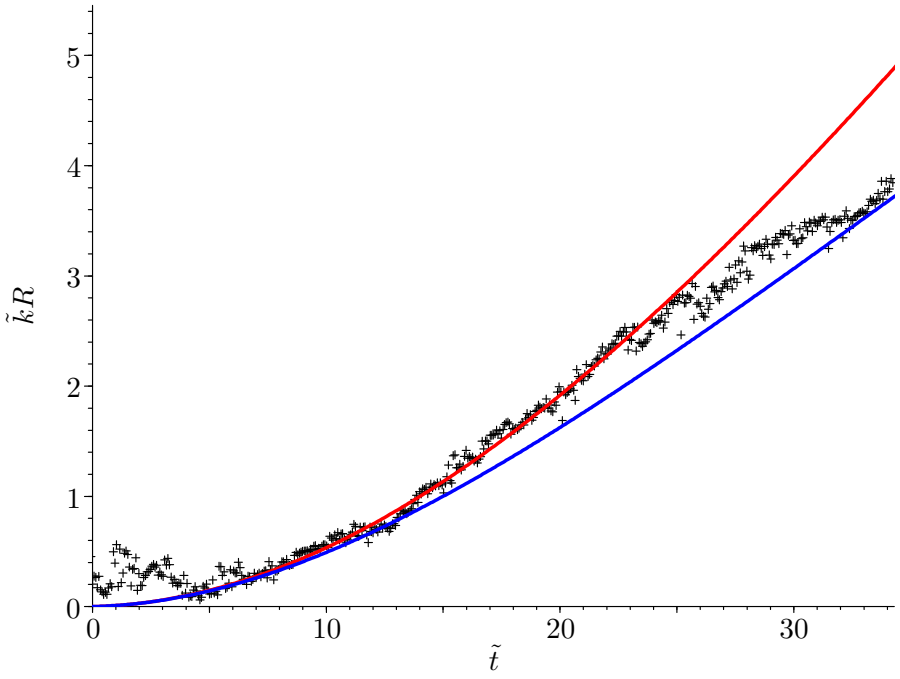

Figure 6.19: The results of PIV for an experiment on a 130 mm balloon oscillated at 104 Hz prior to rupture, in particular the displacement of the midpoint of the two vortex rings from its initial position. Also plotted are the theoretical predictions for both constant circulation (red line) and linearly decaying circulation (blue line) as from equations (6.69) and (6.70). The mid-point is given by $a(t)\cos(\phi(t))$. For constant circulation, $\tilde{A} = (\Gamma_0 k^2/4a^2)^{-1}A = 0$, while for the decay $\tilde{A} = 0.009$ as found from the data in figure 6.18.

including by Stanaway et al. [1988] for colliding viscous vortex rings, and by Archer et al. [2010] for a simulation of a vortex ring colliding with a stationary free surface (thus simulating the collision of two vortex rings due to the free slip condition at the interface, and the image of the vortex ring in that interface). Both state that this loss of circulation is down to vorticity annihilation at the mid-line between the vortex rings, as the positive vorticity on one side diffuses over the centre line between the rings, where it meets and cancels with the negative vorticity from the other side. Neither, however, give a reason why this should mean that the decay is linear. This effect was also present in our simulations due to numerical diffusion, but the effect of such diffusion was almost negligible when compared to that of viscosity in the experiments.

It is relatively straightforward to incorporate this linear decay into our point vortex model, something that does not appear to have been done before by other authors for any similar model. We do this by specifying the circulation as a function of time, perhaps $\Gamma = \Gamma_0(1 - At)$ for suitable constants Γ_0 and A (not the Atwood number). This then implies

$$\phi(t) = \frac{2}{n}\cot^{-1}\left(\frac{\Gamma n t(2 - At)}{16\pi r_0^2}\right), \tag{6.69}$$

$$a(t) = r_0 \left(1 + \left(\frac{\Gamma n t}{16 \pi r_0} \right)^2 (2 - At)^2 \right)^{1/2}. \tag{6.70}$$

The asymptotic interfacial displacement therefore behaves like $t^2(2-At)^2$. Obviously, this assumption of linear decay only applies up to the time when Γ reaches zero, so does not predict negative growth in the interfacial amplitude.

Figure 6.19 shows the displacement of the vortices as in figure 6.11 **(b)**, matched with the theory for both constant circulation and linear decay of the circulation, using A as found from figure 6.18. The theory including decay of the circulation is far better beyond $\tilde{t} = 20$, suggesting that it is indeed decay of the circulation that drives the late-time slow down of the vortex patches seen in experiments. No attempt is made to match the predictions of linearly decaying circulation to the interfacial amplitude growth, as in figure 6.10, as very little of our experimental data goes beyond $\tilde{t} = 20$, when decay appears to become significant. However, for the three experiments that did extend that far, two did show sign of decay in the growth rate that could be quadratic.

6.9 Summary

In this chapter, we have examined the late-time growth of the interfacial amplitude seen when capillary-like waves are present on the balloon at the moment of rupture. In section 6.1 we described the experimental method used to examine this phenomena, with qualitative results described in section 6.2. The initial linear stages of growth were discussed in section 6.3, and shown to be dominated by the outer, potential flow present at the moment of rupture. This growth was closely related to the Richtmyer-Meshkov mechanism. The initial growth rate of the interface was therefore linear, as confirmed through comparisons with our experiments. The later, non-linear stages of growth were described in 6.4 and shown to be determined by vorticity present at the interface at the moment of rupture due to the pre-burst waves. In section 6.5, a model was derived based on the assumption that the interfacial vorticity instantaneously rolls up into discrete, point vortices. The predictions of this model were compared to experiments in 6.6, and show good qualitative but weak quantitative accuracy. This growth differed from that for a flat interface due to the initial circular arrangement of the vorticity. Once the initial vorticity has rolled-up into alternately-signed rings, they propagated away from the interface in pairs, driving the interfacial amplitude further than it would go for a flat interface. The asymptotic growth was therefore linear, and not logarithmic as for a flat interface. Vorticity-stream function simulations were described in section 6.7, and shown to be approximately in agreement with both experiments and the model. The discrepancies with the model were then discussed, and shown to be due to both the finite core size of the rings, and the fact that they left some of the initial interfacial vorticity behind. Both issues were also present in our experiments, as further sources of inaccuracy with the theory. Finally, in section 6.8 we briefly discussed the viscous decay of the vortex rings at late times, showing the circulation decaying linearly once the two vortex rings came into close proximity with one another.

Chapter 7

Conclusion

The principle aim of this thesis was to explore the behaviour of both the water and rubber when a water-filled balloon was dropped onto a flat, rigid surface so that the balloon ruptured - there was no evidence in the published literature of this process having been studied before. Using high-speed photography, we were able to observe the process in detail, and uncovered a number of significant phenomena, as detailed in chapter 3. Initially, the balloon accelerated as it fell. Upon impact, the balloon deformed through the appearance of waves on the surface, and if the consequent increase in surface area was great enough, the balloon ruptured as a crack propagated through it. A fine spray was then ejected from the water's surface due to the rapid retraction of the balloon over the water's surface. A slower but larger-scale growth of the interfacial amplitude was then observed, of the same wavelength as the pre-burst waves.

Three distinct stages therefore emerged: the pre-burst waves oscillating with a typical timescale of 10 ms and lengthscale of 10 mm; the rupture and retraction of the membrane taking around 1 ms, and consequent ejection of spray occurring on a timescale of 1 ms and lengthscale of 1 mm; and the later growth of the interfacial amplitude on a typical timescale of 100 ms and lengthscale of 10 mm. It was this late-time growth that was our most significant finding. The behaviour during the first two stages, while not previously studied, did mirror some other, better-known flows. For instance, one may think to draw an analogy between the pre-burst waves on a balloon with capillary waves on a water droplet oscillating in air. This approximation indeed proved to be appropriate both physically and mathematically (at least to first order in the viscosity). Similarly, as a first approximation to model the spray created by the retracting membrane, one may think of the flow in the wake past a flat plate parallel to the flow. This, again, proved to be an appropriate analogy, revealing in particular the physics behind the creation of the shear instability. Furthermore, both the first two stages may be clearly observed in videos easily found on the Internet, the first for bouncing water balloons, and the second for the bursting of stationary water balloons. The third stage, however, is both not easily observed, and has no clearly analogous situation. It required both the presence of the pre-burst waves, and the rupture of the balloon, something that only normally occurs when a balloon ruptures after being dropped. Obtaining clear images of the phenomenon is therefore difficult; taking qualitative data from it nearly impossible. However, we showed in this thesis how this late-time growth could be accurately observed using a different experimental method, and how it was, in fact, a manifestation of the Richtmyer-Meshkov mechanism.

Static behaviour

All three of the stages discussed above were a direct result of the presence of the rubber balloons, as without them, none of the phenomena we observed would occur. It was therefore important to have a clear understanding of the behaviour of the rubber. To obtain this understanding, in chapter 2 we examined the rubber under static and quasi-static conditions, with a particular focus on determining its stress-strain behaviour when experiencing non-linear stretches. We found that, for any fixed inflation, the tension around an inflated balloon could be approximated as constant in both air and water, a useful result when considering both the pre-burst waves and retraction of the membrane. We also found that the stress-strain relationship for quasi-static inflation of our balloons was well-fitted by standard models for non-linear rubber. This was relevant to the pre-burst waves, but not to the retraction of the membrane, when the the behaviour was not quasi-static extension but dynamic retraction. Experiments on quasi-static retraction showed the behaviour to deviate significantly from the case of inflation. Furthermore, it has been shown by several authors that the dynamic behaviour of rubber may be significantly different to the quasi-static behaviour, as the stress-strain relationship may be strain-rate dependent.

Preburst waves

To examine the dynamic behaviour of a bursting balloon in detail, we developed a new experimental method, in which the balloon was held stationary and forced at a set frequency from a point near its top. This method had several advantages over simply dropping the balloon, most notably keeping the balloon stationary so that the location of certain phenomena could be determined in advance, and examining the flow with water on both sides of the balloon. It also meant standing waves of only a single frequency were created, pre-burst. This method was outlined in chapter 4, along with an exposition of our theory describing the pre-burst waves. The model was based on the assumption of linearity of the waves, something that proved to be accurate for the forcing we used in our experiments. The equations of motion for the fluids were therefore the linearised Navier-Stokes equations. To model the rubber, we assumed that the membranes were thin, and thus could neglect shear stresses. As we were considering initial stretches up to 800 %, it was not appropriate to apply the standard linear theory of rubber. However, the linearity of the waves meant that we could approximate the tension in the balloon as being given by the sum of a large constant value and small (linear) deviation to it, that was proportional to the change in surface area. There is no evidence in the literature that such a model of rubber has been previously used to analyse waves on a water-filled balloon. Coupling the models of the water and rubber through the boundary conditions at the interface, the analysis proved highly similar to that for an oscillated water droplet in air. Indeed, to a good approximation, the tension acted much like a (constant) fluid surface tension; changes in tension in the membrane caused by changing interfacial area were insignificant in setting the wavelength of the waves, for a given frequency (a statement backed up by experimental measurements). However, the analysis did suggest that the elasticity of the membrane played an important role in determining the flow field near the interface. For any waves on an interface between two viscous fluids, continuity of tangential stresses necessitate the presence of a boundary layer at that interface, which contains the vorticity created by the tangential velocity shear across the interface between the outer, inviscid flows in the two fluids.

The flow within this viscous boundary layer also determines the decay rate of the waves. For a pure air/water interface, the low density of the air means that it has little effect on the water. The vorticity is therefore concentrated in the air, and so the decay rate of the waves is low. The presence of the membrane, however, changes the situation. Now, the stresses created in the membrane by changing the surface area are far greater than the equivalent fluid stresses, and the membrane therefore suppresses tangential flow at the interface. Consequently, the vorticity is now shared equally between the air and water phases, as the shear between the interfacial and outer flows in the denser water is now much stronger, and so the decay rate of the waves is much higher. With water on both sides of the membrane, the symmetry between the phases means that the vorticity is shared equally between the phases, whether or not the membrane is present. The presence of the membrane therefore has little effect on either the distribution of the vorticity, or the decay.

If we were only studying the pre-burst waves, the distribution of vorticity would be unimportant, as the viscosity of both water and air is so small that little vorticity would diffuse into the outer flow. However, we were also interested in the behaviour after rupture, in which vorticity at the interface played a significant role.

Rupture and retraction

To study the late-time growth of the interfacial amplitude, one could simply model the bursting of the balloon as the instantaneous removal of the membrane. Doing so, however, would not only ignore some interesting and previously unnoticed physical phenomena, but would also neglect the vorticity created by the retracting membrane, vorticity that proved to significantly suppress the late-time growth of the interfacial amplitude.

The rupture and retraction of the membrane was explored in chapter 5. Rupture was initiated by the propagation of typically one crack through the membrane at speeds around 50 m/s. The faces of the crack were stress-free, so the gradient in stress created with the rest of the membrane caused it to retract. This process was examined using the simpler geometry of a uniaxially-stretched then released strip. While the linear model of rubber predicts this retraction to occur through the passage of a shock, we were looking at non-linear stretches, and found the material behaviour to be disperse. This was partly due to the non-linearity of the initial stretches, as found by Niemczura and Ravi-Chandar [2011c] for high-stretch rubber retractions in air, and to the presence of water providing drag on the membrane, as found by Vermorel et al. [2007] for linear retractions in viscous fluids. There was, however, no published work in which the two were combined. This we did, and the equation we derived modelled the retraction of non-linear strips in high viscosity glycerin well. It proved less accurate for retractions in water, predicting the retraction to be approximately twice as fast as was observed in experiments. This discrepancy, we argued, was a consequence of form drag associated with transverse waves seen near the end of the strip. These waves were similar to a flapping flag, created due to centrifugal fluid-loading forces. They only appeared near the free end of the strip, as that was where the tension (that acted to suppress transverse deformations) was lowest and but the speed, and hence fluid-loading effects, were greatest.

The vorticity associated with the retraction of the membrane was found using Particle Image Velocimetry (PIV) experiments, and shown to be of the same order and location as that created by the pre-burst waves. This vorticity was then significant in creating the shear instability in the wake

behind the retracting membrane. The instability arose because the Gaussian flow profile within the wake was inviscidly unstable. Soon after the membrane passed, sinusoidal waves appeared on the wake, that grew in amplitude. The vorticity created by the retraction then broke down into patches of alternating sign, with the flow field associated with these vorticity patches projecting fluid out of the wake. For retractions with water both sides of the membrane, this process was nearly symmetric, as the wake region soon lost all structure and became fully turbulent. For retractions on an air/water interface, the instability lost symmetry as it became non-linear, with thin sheets of water projected into the air. These sheets soon became unstable to capillary forces and so broke down into the droplets visible in our experimental images, and that we refer to as the spray. This asymmetry of behaviour is typical of many interfacial instabilities, including the late-time growth observed on bursting balloons.

The shear instability arose for retractions in water whether or not flapping of the free end was observed (though the flapping did have a small influence on the instability's wavelength). This was no surprise, as both effects had the same origin: centrifugal forces that were a consequence of a thin, fast moving region of fluid surrounded by a much larger, stationary region. If tension or bending forces in the retracting membrane were great enough (as for a rigid plate), they would suppress any growth until the flow entered the wake. If they were not great enough, however, the growth would occur before the membrane had fully passed, as thus appear as waves on the membrane.

Once the membrane had fully retracted, its momentum caused it to continue further in its direction of motion. This caused the membrane to become compressed. As our membranes were so thin, however, they could not support significant compressive stresses, and so quickly buckled, as transverse waves grew everywhere on the membrane almost simultaneously.

Late-time growth

The final phenomenon we considered in detail was the late-time growth of the interfacial amplitude in chapter 6, something that has not previously been mentioned in any published literature. This growth required both the presence of the capillary waves on the membrane, and for the membrane to rupture. A simple summary of the process would be to say that the bursting of the balloon was equivalent to the instantaneous removal of the restoring force on the pre-burst waves. After rupture, therefore, while the momentum within the water remained, there was no force to restrain it, and so the water kept moving as it was at the moment of rupture. The initial growth rate, with no significant forces acting on the flow, was therefore linear. At later times, the non-linear evolution of the flow depended on the density of the two fluids. For an air/water interface, symmetry was soon lost: the momentum mismatch between the fluids caused thin regions of the denser water to penetrate into the air, while wide regions of the less-dense air penetrated more slowly into the bulk of the water. For a water/water interface, however, there was no momentum mismatch, so the flow remained symmetric for longer. The interface rolled up symmetrically into vortex rings of alternating sign, with the flow created by these rings driving the non-linear growth.

From the above description, we can see how this interfacial growth relates to other, previously-studied interfacial instabilities. In particular, the driving mechanism behind this interfacial growth is the the same as that driving Richtmyer-Meshkov instability (RMI), that occurs when a shock wave passes through a perturbed density interface. If the fluids either side of interface are incompressible, RMI is equivalent to an acceleration being instantaneously applied to, then removed from, the interface.

For our bursting balloons, the acceleration (tension in the membrane) is applied to the interface for a finite time. Yet in both cases, the subsequent flow after removal of the acceleration is identical, as all that matters is the flow at the moment of removal. It does not matter whether that acceleration is applied instantaneously, for a finite time, or indeed for an infinite amount of time prior to removal. All that matters is that it was present to create the waves, whose momentum then causes the interfacial amplitude to grow after removal.

As reasoned earlier, the initial growth of the interface was predicted to be linear. Though it proved difficult to measure the growth of an air/water interface due to the spray created by the retracting membrane and the influence of gravity, this prediction of linear growth was borne out by measurements on bursts with water both sides of the membrane. Mushroom-like shapes then formed on the interface, as the vorticity left by the preburst waves rolled up into vortex rings on lines of latitude, of alternating sign. It was at this point that the flow lost symmetry between inside and outside, as the mutual interaction between these rings caused them to separate into pairs and propagate outwards, away from the initial interface. This behaviour has not been observed before, so we created a model to describe it, based on the work of Jacobs and Sheeley [1996]. This model assumed that all the vorticity initially at the interface instantaneously rolled up into thin vortex rings of alternating sign. Since vortex stretching does not change the total circulation as the rings expand, and the self-induced motion of each ring was insignificant compared with the motion induced by neighbouring vortex rings, a 2D axisymmetric model proved appropriate. Consequently, each vortex ring was modelled by a pair of oppositely-signed point vortices initially arranged on a circle. Tracking the consequent motion of the vortices predicted the late-time growth of the interfacial amplitude to again be linear, though slower than the initial growth by a factor of $1/\pi$. This matched the behaviour seen in experiments well, though attempts to obtain more accurate theoretical predictions of the behaviour by finding the exact motion of the interface proved less successful.

We also performed vorticity-stream function simulations of the flow at a water/water interface, that again were 2D and not axisymmetric, but were initiated by specifying a sinusoidal vorticity distribution on the interface (instead assuming the vorticity was concentrated into point vortices). Tracking the motion of the interface in these simulations matched our experimental results reasonably well. The simulations also provided a good way to examine the assumptions used to derive the point vortex theory, and showed two important considerations that had previously been neglected. First, they showed how not all of the vorticity at the interface at rupture became part of the rings propagating away from the interface, as typically around 15 % was left behind. This decreased the speed of the expanding vortex rings, as their speed depended on the total circulation within each ring. Secondly, the assumption of the vortex rings as thin was inaccurate at late-times, when each ring was pushed toward its partner, so that their cores deformed. Consideration of the idealised case of a Lamb-Chaplygin dipole showed how the finite cross-section of the vortex rings could reduce the propagation speed of each pair (for a given total circulation) by up to 12 %.

One final consideration, that was not accounted for in either the model or simulations, was viscous decay of the circulation within each ring. This occurred primarily through the annihilation of vorticity on the contact plane between each vortex ring in a pair, as vorticity of one sign in one ring diffused over the plane, where it met vorticity of equal strength and opposite sign from the other ring, and thus was canceled out. The consequent decay of circulation within each ring was shown, using PIV, to be approximately linear, in agreement with the work of other authors. Adjusting the point vortex

model for this linear decay in circulation did improve its accuracy when matched to experiments.

Themes

The full process of the impact and rupture of a water-filled balloon may be understood by following certain important themes. One way of doing so is by tracking the dominant form of energy within the flow, particularly for the ruptures with air outside the balloon. At the moment of release, the balloon contains both elastic potential energy (within the membrane) and gravitational potential energy. The gravitational potential energy is converted into kinetic energy as the balloon falls. As it lands and deforms, the kinetic energy of the balloon as a whole is converted into energy associated with the pre-burst waves, so that the energy is partitioned between kinetic energy in the water and rubber, and increased elastic energy due to perturbations (and hence stretching) of the membrane. When the balloon ruptures, the elastic potential energy is converted into kinetic energy within both the rubber as it rapidly retracts, and the water in the boundary layer around the retracting membrane, that leads to the shear instability in the wake behind it. Meanwhile, the kinetic energy in the flow due to the preburst waves persists, causing the late-time growth of the interfacial amplitude. This energy is then converted into surface energy as the area of the interface increases, and heat due to viscous effects. All the while this process is going on, the flow maintains some of its kinetic energy from its initial fall, along with a small amount of gravitational potential energy that is also converted into kinetic energy as the flow slumps down due to gravity.

For ruptures conducted using our new experimental method, with the balloons oscillated at a fixed frequency causing approximately standing waves to form, the process is slightly different. Preburst, the energy is shared between kinetic energy within the water and rubber, and increased elastic potential energy within the membrane caused by deformations to the interface, oscillating between the two at the same frequency as the waves themselves. Consequently, the phase of the waves at the moment of rupture is important in determining the late-time growth. For instance, if rupture occurs when the interface is flat, that is when the flow has the most kinetic energy, but least potential energy; consequently, the late-time growth will be fastest. However, if the rupture occurs when the perturbations to the interface are greatest, that is when there is no kinetic energy within the flow; consequently, no late-time growth of the interfacial amplitude will occur, as the energy is all converted into forms associated with the retracting membrane. For ruptures in air, providing there is some wave kinetic energy present at the moment of rupture, the flow then evolves as described in the previous paragraph. For a rupture with water both sides of the membrane, the process is similar, only without gravity playing any role. Consequently, the kinetic energy in the water is not directed downwards at late time, but continues to evolve according to the preburst flow until it is all dissipated due to viscosity.

The flow created by the rupture of a water balloon may also be understood by consideration of vorticity, as is most relevant for the ruptures with water both inside and outside the balloon. The preburst waves, though not driven explicitly by vorticity, do create significant vorticity in a thin boundary layer at the interface. The retraction of the membrane then creates further vorticity within boundary layers (of similar thickness to that created by the waves) on either side of it, that then rolls up in the wake of the membrane to create the shear instability. On regions of the interface where this retraction is significant (meaning regions away from the initial crack propagation path so that

the membrane retracts across it for a significant amount of time), the vorticity created by retraction is dominant, destroying that associated with the pre-burst waves. The interface therefore quickly becomes turbulent, and little late-time growth of the interfacial amplitude is observed. However, near the crack path, the vorticity from the preburst waves is dominant, and so the large-scale growth of the interfacial amplitude is observed. Seeing the late-time growth as being driven by the vorticity present in the flow at the moment of rupture also shows how it is related to RMI, as in both cases the flows evolves according to the vorticity distribution at an interface after the instantaneous removal of the restoring force. For ruptures underwater, this vorticity then rolls up into vortex rings that drive the non-linear growth of the interface, as previously explained. For bursts with air outside the membrane, however, the role of vorticity is greatly reduced, as the density mismatch between the phases means that the non-linear growth is dominated by the momentum of the flow in the water at the instant of rupture.

This understanding of the process as being driven by vorticity also explains the difference in length scale between the shear instability and late-time interfacial growth. Both flows are driven by vorticity concentrated in thin layers of approximately equal size. However, the vorticity driving the shear instability varies across the width of the layer, but not (significantly) with distance along it. Consequently, the relevant length scale is the width of the boundary layer, typically 0.1 mm or less. In contrast, the vorticity driving the late-time growth is in patches of alternating sign around the boundary layer, with little significant variation in vorticity across the layer. Consequently, the relevant length scale is the width of these patches, typically around 10 mm, rather than the width of the boundary layer.

Future work

There are a number of ways in which the work presented in this thesis may be extended. In general, we have focused on understanding the physics driving the process, and were, for the most part, successful. Consequently, future work would focus on providing accurate qualitative predictions of the process. To do so, the most important topic to understand in better detail would be the behaviour of rubber when in dynamic retraction. How this could be done for our rubber is not clear, though perhaps a better option is to conduct experiments using a type of rubber (or other material) that is sufficiently extensible, and about which more is known. Fortunately, the physical properties and behaviour of water and air are far better understood. Thus, once an accurate model of the rubber has been obtained, the best course of action may be to conduct a detailed numerical modelling of the flow, to capture the behaviour more accurately than our experiments were able to.

There are also several specific parts of our work that may be extended, to gain a deeper understanding of the flow. When studying the pre-burst waves, we concentrated only on the cases of low viscosity fluids, particularly air and water. It would be relatively straightforward to extend our experiments and analysis (at least numerically) to include fluids of intermediate and even large viscosity. Doing so would hopefully allow us some control over the strength and distribution of the interfacial vorticity created by the pre-burst waves, and thus more insight into how this vorticity influences the late-time growth of the interfacial amplitude. This would be especially useful for the cases with $A \approx 1$, where we currently have little idea of the impact on the late-time growth brought about by the change in location of vorticity due to the presence of the membrane, as opposed to a pure fluid-fluid interface.

Investigating the impact of the interfacial elasticity on the late-time growth is also something for which numerical modelling would be ideal, as then experimental factors such as the retraction of the membrane, and the weakness of air/water surface tension as opposed tension in a balloon membrane, could be neglected. It would also be interesting to investigate how finite values of the interfacial elasticity would affect both the pre-burst waves, and the consequent post-rupture evolution of the flow. As was discussed in chapter 5, intermediate values of elasticity would give rise to longitudinal waves in the membrane, that potentially could significantly alter the structure of the interfacial vorticity, and thus the post-rupture growth of the interfacial amplitude.

More detailed, qualitative investigations could be conducted of many of the phenomena associated with retraction, based on either a better model of the rubber elasticity or the assumption of a linear stress-strain relation. These investigations could include the boundary layer flow created by the retraction, using PIV with a better resolution than was available to us, and also the consequent flow in the wake, including the wake behind a membrane retracting across an air/water interface (a topic on which we did not perform any experiments). Perhaps the most interesting phenomenon to investigate would be the transverse waves seen near the free end. Using a similar method to Dowling [1988] and the assumption of linearity in the rubber, the problem would appear to be amenable to an analytical study.

One extension of our work looking at the late-time growth would be to consider the oscillation and rupture of 2D sheets of rubber. For such ruptures with the same fluid both sides of the membrane, the same roll-up of the interfacial vorticity will occur. Now, however, the pattern of vortex rings or tubes will be different, and thus so will the non-linear growth. Models similar to our own could then be derived, based again on the assumption that the tubes are thin. Through this analysis, perhaps the best and most useful extension of all our work may be performed: using our balloon rupture method to study classical RMI experimentally. The link between the two phenomena has been clearly established in this thesis, and while we can think of few other situations in which the late-time growth after rupture of an interfacial membrane occurs, there are a wide variety of well-documented and important situations in which RMI occurs. Studying RMI, however, is difficult, requiring the creation of perturbations on an interface, then passing a shock wave through it. This process is often difficult, and may require significant amounts of energy. The method we have discovered, of rupturing an oscillated membrane, is easy to set up and requires relatively little energy. It could also be used to extend the study of RMI to different geometrical configurations (varying both the shape of the interface, and the shape of the perturbations) that would be difficult to study experimentally using the classical, shock-generation method. Our work on spherical interfaces is an excellent example of this.

In summary, this thesis consists of the first published detailed investigation into the impact and rupture of a water-filled balloon on a rigid surface. This process, though apparently simple, was revealed by high-speed imaging to consist of a surprising range of phenomena. These included waves created on the membrane upon impact, a shear instability on the waters surface that manifested itself as a spray ejected from the water's surface, and a late-time growth of the interfacial growth. Though none of these phenomena have been studied before, it was this late-time growth that proved our most significant finding. We have argued that it is driven by the same mechanism as RMI; the primary use of our work, therefore, is that it suggests an alternative way to experimentally study the interfacial growth generated by RMI. Our work is therefore relevant to any examples of RMI, but particularly

those on a spherical interface, such as occurs during inertial confinement fusion (ICF). Furthermore, our work could also be applicable to any physical situation involving a fluid-filled membrane; examples include, but are not limited to, biological cells, and bursting paint balls.

Bibliography

M. Abramowitz and I.A. Stegun. Handbook of Mathematical Functions. Dover, 1970.

D.J. Acheson. Elementary Fluid Dynamics. OUP, 1990.

J.E. Adkins and R.S. Rivlin. Large elastic deformations of isotropic materials: Ix. the deformation of thin shells. Phil. Trans. R. Soc. Lond., 244:505–531, 1952.

H. Alexander. Tensile instability of initially spherical balloons. Int. J. Engng Sci., 9:151–162, 1971.

T.L. Anderson. Fracture mechanics: Fundamentals and applications. Taylor and Francis, third edition, 2004.

PJ Archer, TG Thomas, and GN Coleman. The instability of a vortex ring impinging on a free surface. Journal of Fluid Mechanics, 642:79, 2010.

Médéric Argentina and L Mahadevan. Fluid-flow-induced flutter of a flag. Proceedings of the National academy of Sciences of the United States of America, 102(6):1829–1834, 2005.

V.V. Babenko, H.H. Chun, and I. Lee. Boundary Layer Flow over Elastic Surfaces. Elseviour, 2012.

G. K. Batchelor. An Introduction to Fluid Dynamics. Cambridge University Press, 1967.

G.K. Batchelor. The skin friction on infinite cylinders moving parallel to their length. Quart. Journ. Mech. and Apllied Math., VII, 1954.

R Byron Bird, Warren E Stewart, and Edwin N Lightfoot. Transport phenomena. Wiley. com, 2007.

R.B. Bogoslovov and C.M. Rowland. Viscoelastic effects on the free retraction of rubber. J, Appl. Phys., 102, 2007.

K.B. Broberg. Cracks and Fracture. Academic Press, 1999.

M. Brouillette. The richtmyer-meshkov instability. Annu. Rev. Fluid Mech., 34:445–468, 2002.

M Brouillette and B Sturtevant. Experiments on the richtmyer-meshkov instability: single-scale perturbations on a continuous interface. Journal of Fluid Mechanics, 263:271–292, 1994.

Anna Carruthers and Antonio Filippone. Aerodynamic drag of streamers and flags. Journal of aircraft, 42(4):976–982, 2005.

A.L. Cauchy. Recherches sur lequilibre et le mouvement interieur des corps solides ou uids, lastiques ou non lastiques. Bull. Soc. Philomath., pages 9–13, 1832.

YB Chang and PM Moretti. Flow-induced vibration of free edges of thin films. Journal of fluids and structures, 16(7):989–1008, 2002.

EI Chebotareva, AN Aleshin, SG Zaytsev, and SV Sergeev. Investigation of interaction between reflected shocks and growing perturbation on an interface. Shock waves, 9(2):81–86, 1999.

CH Chen, HP Zhang, J Niemczura, K Ravi-Chandar, and M Marder. Scaling of crack propagation in rubber sheets. EPL (Europhysics Letters), 96(3):36009, 2011.

K.H. Christensen. Transient and steady drift currents in waves damped by surfactants. Phys. Fluids, 17, 2005.

R Coene. Flutter of slender bodies under axial stress. Applied scientific research, 49(1):175–187, 1992.

FE Condon and Michael Fryd. On the inflating of balloons. Journal of Chemical Education, 35(10): 518, 1958.

A.D.D. Craik. Wave Interactions and Fluid Flows. Cambridge University Press, 1985.

E. de Langre, M.P. Paidoussis, O. Doare, and Y. Modarres-Sadeghi. Flutter of long flexible cylinders in axial flow. J. Fluid Mech., 571:371–389, 2007.

R.D. Deegan, P.J. Petersan, M. Marder, and H.L. Swinney. Oscillating fracture paths in rubber. Phys. Rev. Lett., 88, 2002.

J. Diana, B. Fayolle, and P. Gilormini. A review on the mullins effect. Eur. Polym. J., 45:601–612, 2009.

J. Diani, B. Fayolle, and P. Gilmormini. A review on the mullins' effect. Eur. Polym. J., pages 601–612, 2009.

AP Dowling. The dynamics of towed flexible cylinders part 1. neutrally buoyant elements. Journal of Fluid Mechanics, 187(1):507–532, 1988.

S. Dutt, J. Glimm, J.W. Grove, D. Sharp, and Y. Zhang. Spherical richtmyer-meshkov instability for axisymmetric flow. Mathematics and Computer in Simulation, 65, 2004.

Daiki Endo, Katsuhiko Sato, and Yoshinori Hayakawa. Oscillatory instability in slow crack propagation in rubber under large deformation. Physical Review E, 86(1):016106, 2012.

N.H. Fletcher. The Physics of Rainclouds. Cambridge University Press, 1962.

M. Gaster. A note on the relation between temporally-increasing and spatially-increasing disturbances in hydrodynamic stability. J. Fluid Mech., 14:222–224, 1962.

A.N. Gent and P. Marteny. The effect of strain upon the velocity of sound and the velocity of free retraction for natural rubber. J. Appl. Phys., 53, 1982.

J.M. Gere and S.P. Timoshenko. Mechanics of materials. PWS, fourth edition, 1997.

G.I.Taylor. The instability of liquid surfaces when accelerated in a direction perpendicular to their planes. Proc. Roy. Soc., 201:192–196, 1950.

J. Glimm, J.W. Grove, and Y. Zhang. Three dimensional axisymmetric simulations of fluid instabilities in curved geometry. Avd. Fluid Mech., 2000.

A.G. Greenhill. Plane vortex motion. Quart. J. Pure Appl. Math., 15:10–29, 1878.

S.F. Hoerner. Fluid-Dynamic Drag. 1965.

R. Hooke. Lectures de Potentia Restitutiva, Or of Spring Explaining the Power of Springing Bodies. 1678.

JW Hoyt and JJ Taylor. Waves on water jets. J. Fluid Mech, 83(1):119–127, 1977.

J.W. Jacobs and V.V. Krivets. Experiments on the late-time development of single-mode richtmyer-meshkov instability. Phys. Fluids, 17, 2005.

J.W. Jacobs and J.M. Sheeley. Experimental study of incompressible richtmyer-meshkov instability. Phys. Fluids., 8:405–415, 1996.

H.M. James and E. Guth. Theory of the retraction of stressed rubber. Phys.Rev., 66:33, 1944.

D.F. Jones and L.R.G. Treloar. The properties of rubber in pure homogeneous strain. J. Phys. D: Appl. Phys., 8:1285–1304, 1975.

Z Kizner and R Khvoles. Two variations on the theme of lamb-chaplygin: supersmooth dipole and rotating multipoles. Regular and Chaotic Dynamics, 9(4):509–518, 2004.

P.P. Korovkin. Limits and continuity. Gordon and Breach, 1968.

W. Kuhn. Uber die gestalt fadenformiger molekule in losungen. Kolloidzeitschrift, 68:2, 1934.

W. Kuhn. Beziehungen zwischen molekulgrosse, statistischer molekulgestalt und elastischen eigenschaften hochpolymerer stoffe. Kolloidzeitschrift, 76:582, 1936.

S. Kyriakides and Y-C. Chang. On the inflation of a long elastic tube in the presence of axial load. Int. J. Solids Structures, 26:975–991, 1990.

R. Lakes. Viscoelastic Materials. Cambridge University Press, 2009.

H. Lamb. Hydrodynamics. Cambridge University Press, 1932.

BP Leonard. Simple high-accuracy resolution program for convective modelling of discontinuities. International Journal for Numerical Methods in Fluids, 8(10):1291–1318, 1988.

M. Lesieur. Turbulence in Fluids. Springer, 2008.

MJ Lighthill. Note on the swimming of slender fish. J. Fluid Mech, 9(2):305–317, 1960.

Oleg A Likhachev and Jeffrey W Jacobs. A vortex model for richtmyer–meshkov instability accounting for finite atwood number. Physics of Fluids, 17:031704, 2005.

Didier Long, Armand Ajdari, and Ludwik Leibler. Static and dynamic wetting properties of thin rubber films. Langmuir, 12(21):5221–5230, 1996.

Augustus Edward Hough Love. A treatise on the mathematical theory of elasticity. Cambridge University Press, 2013.

J Lucassen. Longitudinal capillary waves. part 1.theory. Trans. Faraday Soc., 64:2221–2229, 1968.

E.H. Lucassen-Reynders and J. Lucassen. Properties of capillary waves. Adv. Colloid Interfac., 2: 347–395, 1969.

M. Marder. Supersonic rupture of rubber. J. Mech. Phys. Solids, 54:491–532, 2006.

J.E. Mark. Polymer Data Handbook. Oxford University Press, second edition, 2009.

P. Mason. Finite elastic wave propagation in rubber. Proc. R. Soc. Lond. A, 272:315–330, 1963.

VV Meleshko and GJF van Heijst. On chaplygin's investigations of two-dimensional vortex structures in an inviscid fluid. Journal of Fluid Mechanics, 272(1):157–182, 1994.

E.E. Meshkov. Instability of the interface of two gases accelerated by a shock wave. Izv. Akad. Nauk SSSR Mekh. Zhid. i Gaza, 4:151–157, 1969.

K.H. Meyer and C. Ferri. Sur l'elasticite du caoutchouc. Chim. Acta, 29:570, 1935.

J. Miklowitz. The theory of elastic waves and waveguides. North-Holland, 1978.

C.A. Miller and L.E. Scriven. The oscillations of a fluid droplet immersed in another fluid. J. Fluid Mech., 32:417–425, 1968.

Y Modarres-Sadeghi, MP Païdoussis, and C Semler. A nonlinear model for an extensible slender flexible cylinder subjected to axial flow. Journal of fluids and structures, 21(5):609–627, 2005.

M. Mooney. A theory of large elastic deformation. J. appl. Phys., 11:582–592, 1940.

Michael T Morris-Thomas and Sverre Steen. Experiments on the stability and drag of a flexible sheet under in-plane tension in uniform flow. Journal of Fluids and Structures, 25(5):815–830, 2009.

B.A. Mrowca, S.L. Dart, and E. Guth. Retraction of stressed rubber. Phys.Rev., 66:30–32, 1944.

I. Muller and P. Strehlow. Rubber and rubber balloons: Paradigms of thermodynamics. Springer-Verlag, 2004.

L. Mullins. Softening of rubber by deformation. Rubber Chem. Technol., 42:339–362, 1969.

C.L.M.H. Navier. Sur le lois de lequilibre et du mouvement des corps solides lastiques. Bull. Soc. Philomath., pages 177–181, 1821.

C.E. Niederhaus and J. W. Jacobs. Experimental study of the richtmyer-meshkov instability of incompressible fluids. J. Fluid Mech., 485:243–277, 2003.

J. Niemczura and K. Ravi-Chandar. On the response of rubbers at high strain rates-i. simple waves. J. Mech. Phys. Solids, 59:423–441, 2011a.

J. Niemczura and K. Ravi-Chandar. On the response of rubbers at high strain rates-ii. shock waves. J. Mech. Phys. Solids, 59:442–456, 2011b.

J. Niemczura and K. Ravi-Chandar. On the response of rubbers at high strain rates-iii. effect of hysteresis. J. Mech. Phys. Solids, 59:457–472, 2011c.

H. Ockendon and J.R. Ockendon. Viscous Flow. Cambridge University Press, 1995.

R.W. Ogden. Large deformation isotropic elasticity: on the correlation of theory and experiment for incompressible rubberlike solids. Proc. R. Soc. Lond. A, 326:565–584, 1972.

R.W. Ogden. Non-linear elastic deformations. Ellis Horwood Limited, 1984.

M.P. Paidoussis. FluidStructure Interactions: Slender Structures and Axial Flow, vol. 2. Elsevier Academic Press, 2003.

MP Paıdoussis and GX Li. Pipes conveying fluid: a model dynamical problem. Journal of Fluids and Structures, 7(2):137–204, 1993.

R. Parnes. Solid Mechanics in Engineering. Wiley, 2001.

P.J. Petersan, R.D. Deegan, M. Marder, and H.L. Swinney. Cracks in rubber under tension exceed the shear wave speed. Phys. Rev. Lett., 93, 2004.

JE Portillo and GA Blaisdell. Spatial stability analysis of a high speed liquid jet. In ILASS-Americas 2006: 19th Annual ILASS-Americas Conference on Liquid Atomization and Spray Systems, 2006.

JE Portillo, SH Collicott, and GA Blaisdell. Measurements of axial instability waves in the near exit region of a high speed liquid jet. Physics of Fluids, 23(12):124105–124105, 2011.

KR Rajagopal. Conspectus of concepts of elasticity. Mathematics and Mechanics of Solids, 16(5): 536–562, 2011.

L. Rayleigh. On the capillary phenomena of jets. Proc. R. Soc. Lond., 29:71–97, 1879.

M. Rein. Phenomena of liquid drop impact on solid and liquid surfaces. Fluid Dynamics Research, 12, 1993.

D. Richard and D. Quere. Bouncing water drops. Europhys. Lett., 50:769–775, 2000.

R.D. Richtmyer. Taylor instability in shock acceleration of compressible fluids. Communs. Pure and Appl. Math., 13:297–319, 1960.

J.J. Riley, M. Gad el Hak, and R.W. Metcalf. Compliant coatings. Ann. Rev. Fluid Mech., 20:393–420, 1988.

R.S. Rivlin and D.W. Saunders. Large elastic deformations of isotropic materials vii. experiments on the deformation of rubber. Phil. Trans. R. Soc. Lond., 243:251–288, 1951.

P. Robertson. The Book of Firsts. Bramall House, 1978.

E.P. Rood. Vorticity interactions with a free surface. In S.I. Green, editor, Fluid Vorticies, chapter XVI. Kluwer Academic Publishers, 1995.

M.H. Sadd. Elasticity: Theory, Applications, and Numerics. Elsevier, 2005.

O. Sadot, L. Erez, U. Alon, L. A. Levin, G. Erex, G. Ben-Dor, and D.Shvarts. Study of nonlinear evolution of single-mode and two-bubble interaction under richtmyer-meshkov instability. Phys. Rev. Lett., 80:1654–1657, 1998.

Philip G Saffman. Vortex dynamics. Cambridge university press, 1992.

Hiroshi Sato. The stability and transition of a two-dimensional jet. Journal of fluid mechanics, 7(01): 53–80, 1960.

Hiroshi Sato and Kyoichi Kuriki. The mechanism of transition in the wake of a thin flat plate placed parallel to a uniform flow. J. Fluid Mech, 11(Pt 3), 1961.

E. Soto and A. Belmonte. Surface texture and pulsation due to balloon bursting in different liquids. Phys. Fluids, 21, 2009.

Narakorn Srinil, Marian Wiercigroch, and Patrick OBrien. Reduced-order modelling of vortex-induced vibration of catenary riser. Ocean Engineering, 36(17):1404–1414, 2009.

R.B. Stambaugh. Retraction of stretched rubber. Phys.Rev., 65:250, 1944.

Sharon K Stanaway, BJ Cantwell, and Philippe R Spalart. A numerical study of viscous vortex rings using a spectral method. NASA STI/Recon Technical Report N, 89:23820, 1988.

Richard S Stein. On the inflating of balloons. Journal of Chemical Education, 35(4):203, 1958.

A. Stevenson and A.G. Thomas. On the bursting of a balloon. J. Phys. D: Appl. Phys., 12, 1979.

Sadatoshi Taneda. Oscillations of the wake behind a flat plate parallel to the flow. Journal of the Physical Society of Japan, 13(4):418–425, 1958.

Sadatoshi Taneda. Waving motions of flags. Journal of the Physical Society of Japan, 24(2):392–401, 1968.

Geoffrey Taylor. The instability of liquid surfaces when accelerated in a direction perpendicular to their planes. i. Proceedings of the Royal Society of London. Series A. Mathematical and Physical Sciences, 201(1065):192–196, 1950.

G.I. Taylor. Analysis of the swimming of long and narrow animals. Proc. R. Soc. Lond. A, 214: 158–183, 1952.

L.R.G. Treloar. Stress-strain data for vulcanised rubber under various types of deformation. Trans. Faraday Soc., 40:59–70, 1944.

L.R.G. Treloar. Stresses and birefringence in rubber subjected to general homogeneous strain. Proc. Phys. Soc., 60:135–144, 1947.

L.R.G. Treloar. The Physics of Rubber Elasticity. Oxford University Press, third edition, 2005.

RR Trieling, JMA Van Wesenbeeck, and GJF Van Heijst. Dipolar vortices in a strain flow. Physics of Fluids, 10:144, 1998.

AL Velikovich, JP Dahlburg, AJ Schmitt, JH Gardner, L Phillips, FL Cochran, YK Chong, G Dimonte, and N Metzler. Richtmyer–meshkov-like instabilities and early-time perturbation growth in laser targets and z-pinch loads. Physics of Plasmas, 7:1662, 2000.

E. Ventsel and T. Krauthammer. Thin Plates and Shells. Marcel Dekker, 2001.

R. Vermorel, N. Vandenberghe, and E. Villermaux. Rubber band recoil. Proc. R. Soc. A, 463:641–658, 2007.

G.E. Wang and J. J. Lannutti. Static wetting of a liquid drop on a solid. J. Mat. Sci., 39, 1968.

A.M. Worthington. On impact with a liquid surface. Proc. Roy. Soc., 1882.

W-L. Yin. Non-uniform inflation of a cylinderical elastic membrane and direct determination of the strain energy function. J. Elasticity, 7:265–282, 1977.

Jun Zhang, Stephen Childress, Albert Libchaber, and Michael Shelley. Flexible filaments in a flowing soap film as a model for one-dimensional flags in a two-dimensional wind. Nature, 408(6814): 835–839, 2000.

Q. Zhang and S. Sohn. Nonlinear theory of unstable fluid mixing driven by shock wave. Phys. Fluids, 9:1106–1124, 1997.